UNIVERSIDADE DE SANTIAGO DE COMPOSTELA

FACULTADE DE FÍSICA

DEPARTAMENTO DE FÍSICA DA MATERIA CONDENSADA,
GRUPO DE FÍSICA NON LINEAL

PARAMETERIZATION OF TURBULENCE IN THE OCEAN AND APPLICATION OF A 3D BAROCLINIC MODEL TO THE RIA DE PONTEVEDRA.

Manuel Ruiz Villarreal

Xullo, 2000

D. VICENTE PÉREZ VILLAR, Catedrático do Departamento de Física da Materia Condensada da Universidade de Santiago de Compostela,
INFORMA:

Que a presente memoria titulada ”***Parameterization of turbulence in the ocean and application of a 3D baroclinic model to the Ría de Pontevedra***” foi realizada baixo a miña dirección no Departamento de Física da Materia Condensada da Universidade de Santiago de Compostela para optar ó grao de Doctor en Física

D. Vicente Pérez Villar

Santiago de Compostela, xullo de 2000

A Carmen

Agradecimientos

Llegar juntos es un comienzo, mantenerse juntos es progreso, trabajar juntos es éxito.
Henry FORD[1]

Siempre he pensado ingenuamente que el trabajo científico lo componían satisfacciones y algún que otro esfuerzo. Por lo menos en el accidentado camino hacia el doctorado esto no es así. Afortunadamente la cantidad de apoyos con los que he contado ha seguido una trayectoria exponencial.

Mi director, el profesor Vicente Pérez Villar, descubrió que las rías gallegas eran un campo abierto a la modelización, encontró los medios para que se empezara a hacer oceanografía con una visión de físicos y contó conmigo en este proyecto.

Pedro Montero y Juan Taboada son co-responsables de muchas de las ideas (y gráficas!) vertidas en este trabajo. Su constante esfuerzo ha supuesto una contribución a que la oceanografía gallega empezara a ser oceanografía física. Su visión constructiva, su escucha y la ilusión que me han transmitido me han permitido afrontar con calma los momentos de desesperación tanto cuando el modelo no iba como cuando los resultados eran espectaculares. Juntos hemos conseguido que la risa sea el mejor aliado para el trabajo en equipo. A Moncho Gómez Gesteira le agradezco que apoyara mi desembarco en la oceanografía, que es la línea de investigación que siempre me había atraído. A Vicente Pérez Muñuzuri le agradezco su ánimo y su estímulo para que hiciera una estancia en Lisboa en uno de los momentos en que más aire fresco necesitaba.

Hans Burchard es el máximo responsable de que mi paso por la turbulencia haya sido menos tormentoso de lo que se preveía en los inicios. Cuando más perdido estaba, me incluyo en su lista de distribución de ideas y modelos de turbulencia y me invitó al santuario de la turbulencia que tenía su sede en el pabellón 69 al pie del Lago Maggiore. Hans y los demás participantes en el proyecto GOTM de lanzar un modelo de turbulencia que pudiera ser usado libremente: Karsten Bolding y sus trucos mágicos, Pierre-Phillipe Mathieu, el creativo, que ha comprobado que soy un estusiasta redistribuidor de sus iniciativas, gráficas

---

[1] Citado por PP Mathieu en http://www.gotm.net

y visión pedagógica y Georg Umgiesser, han ayudado a que mantuviera la cordura gracias a las estimulantes discusiones e intercambios de ideas que tienen lugar en la constantemente bombardeada lista de desarrolladores del GOTM. A Adolf Stips le agradezco que me invitara a varias campañas en las que pude tomar contacto con las mediciones de la turbulencia.

En la meca del MOHID, los ’engenheiros’ del MARETEC (Ramiro Neves, Aires dos Santos, Paulo Chambel, Frank Braumsweig, Ricardo Miranda, Flavio Martins, Helder Martins, Pedro Pina y Claudia Lindim), los ’engenheiros’ de la HIDROMOD (Adelio Silva, Ze Chambel, Joao Delfino, Pedro Ferreira) y el ’físico’ de guardia (Henrique Coelho) han sido un apoyo valiosísimo en nuestra pelea con las rías gracias a su constante apoyo y estímulo. Cuando más necesitaba ordenar las ideas sobre el maremagnum de volumenes finitos, ´mapeamentos’ y condiciones de contorno, me ofrecieron un puesto de físico en prácticas en el Taguspark e hicieron lo que yo necesitaba: sentarse conmigo a discutir.

Ricardo Prego y su grupo del Instituto de Investigacións Mariñas me han mostrado las satisfacciones del trabajo de campo. Pese al choque químico-físico, parece que el proceso de mezcla ha sido enriquecedor para ambas partes. Manolo Varela y la tripulación del buque Mytillus han sido el referente de resistencia a las ’duras’ condiciones de trabajo en la ría.

En el Institut für Meereskunde en Hamburgo encontré un grupo que con paciencia me introdujeron en los secretos del modelado 3D y del alemán científico. Mi agradecimiento al profesor Sündermann, a Thomas Pohlmann, a Dagmar Hainbucher, a Susanne Rolinski, a Maik Thomas y al resto de gente que hizo que la falta de luz solar no fuera un obstáculo en mi formación.

Juan Alonso y Guillermo Díaz del Río, siempre entusiastas ante la perspectiva de que los modelos corrieran en las rías, me han brindado siempre su apoyo y su ayuda.

Nieves Lorenzo es una de las máximas responsables de que entrara en la hornada de doctores del curso 1999-2000, se puede decir que cogí la rueda buena, puesto que sigue rodando aunque la risa la atenace.

El resto de los miembros del grupo de física no lineal: Adolfo, Alberto, Bea, Carlos, Chus, Diego, Edu, Inés, Irene, Iván, Julio, Maite y Mónica han conseguido con su apoyo y su alegría que mi equilibrio mental no se viera nunca resentido por los acontecimientos, por los esfuerzos, por la superpoblación ni por el ruido de fondo. Por eso me siento mal sin dedicarles una frase especial a cada uno.

Varias personas me han acogido en mis múltiples exilios pre-tesis a lo largo de Europa y han hecho que no todo fuera ordenador y turismo individual, todos ellos han contribuido a este trabajo.

Javi, María y Manolo han ayudado a que consiguiera muchos momentos de despreocupación y desconexión. Han sido un referente para que la movilidad y los excesos de trabajo no me afectaran en exceso.

Mi madre y mis hermanos Gus y Miguel me han hecho sentir que están siempre cerca a pesar de las preocupaciones y separaciones que implica el tener un hijo/hermano científico y por encima becario (de los que no se puede vivir, Gus...).

A Carmen le va dedicado todo este trabajo. Ha puesto en él tanto o más esfuerzo e ilusión que yo sin plantearse las consecuencias, y esa facilidad de transmitir ilusión es lo que más me gusta de ella.

Este trabajo ha sido desarrollado con la ayuda de una beca predoctoral de la Secretaría Xeral de Investigación e Desenvolvemento de la Xunta de Galicia. Este mismo organismo y el Vicerrectorado de Investigación de la USC han proporcionado ayuda para la realización de distintas estancias en centros de investigación. Durante el transcurso de este trabajo me he visto beneficiado por la ayuda de los proyectos:

- ”La Ría de Pontevedra y el Ciclo Biogeoquímico del Silicio”, financiado por la CICYT (Comisión Interministerial de Ciencia y Tecnología), dentro del Programa Nacional de Ciencia y Tecnología Marinas (MAR96-1782).

- ”Ordenación Integral del Espacio Marítimo Terrestre de Galicia”, financiado por la Consellería de Pesca de la Xunta de Galicia.

Por último, me gustaría agradecer especialmente a toda gente que en el marco de estos proyectos o fuera de ellos han recogido y proporcionado los datos utilizados en esta memoria.

Resumen

En el presente estudio, se han dado varios pasos dirigidos a la aplicación de un modelo 3D baroclínico para la modelización de la ría de Pontevedra. La ría de Pontevedra es una de las rías gallegas, estuarios en la costa noroeste de la Península Ibérica. Su hidrodinámica sólo se conoce a rasgos generales, lo que dificulta el establecimiento de un modelo de circulación. Los resultados de un proyecto de monitorización de las propiedades químicas y termohalinas en la Ría durante los años 1997-1998 y la información disponible se han usado para identificar las escalas de variabilidad espacio-temporal relevantes. Un modelo 3D baroclínico se ha adaptado al área para la simulación de la hidrodinámica y finalmente, varios cierres de la turbulencia con diferentes niveles de complejidad se han programado en el modelo unidimensional de columna de agua GOTM (General Turbulence Ocean Model), que ha sido co-desarrollado por el autor y que puede descargarse del sitio http://www.gotm.net. El rendimiento de estos modelos se ha comparado en situaciones analíticas, estuáricas y de océano abierto. Los resultados de estas aplicaciones indican que el uso de un modelo de 2 ecuaciones puede llevarnos a una mejor descripción de los flujos en distintos ambientes, incluyendo la ría.

Las escalas de variabilidad relevantes en la ría de Pontevedra se han identificado y descrito con la ayuda de distintos conjuntos de datos de los que se dispone. El mayor forzamiento a corto plazo es la marea, que presenta un marcado carácter semidiurno. A escalas de días, el ciclo de mareas vivas-mareas muertas (quincenal), eventos meteorológicos y la variabilidad existente entre el gradiente de densidad río-plataforma dominan la variabilidad del sistema. El ciclo anual de las propiedades termohalinas ha sido determinado con la ayuda de medidas en distintos puntos de la ría en el período comprendido entre octubre de 1997 y octubre de 1998. Se han distinguido dos estaciones determinadas por el ciclo anual de radiación, precipitación y vientos predominantes: una estación de invierno, con estratificación halina y dominio de episodios de downwelling y una estación de verano, en la que la estratificación térmica es sustituida por una estratificación halina y suele haber condiciones de upwelling. Tanto en la estación de downwelling como en la de upwelling, existe una variabilidad en el régimen de vientos que resulta en episodios de upwelling o downwelling de una escala temporal típica de días. El estudio de la distribución espacial de las propiedades termohalinas en las distintas campañas nos ha permitido obtener una imagen de la variabilidad a lo largo del canal principal. Cerca de la desembocadura del río. la influencia

del agua dulce es mayor, mientras que la entrada de la ría es una zona de influencia oceánica, aunque la distribución real se ve influida por las condiciones del viento. Tambien es destacable el gradiente de densidad que aparece entre las orillas sur y norte.

Un conjunto de diferentes modelos para la descripción de la turbulencia ha sido recogido, programado y testeado en un modelo unidimensional de columna de agua en distintas situaciones analíticas, estuáricas y de mar abierto. Todos los modelos están basados en el principio de viscosidad turbulenta, que nos permite obtener los coeficientes de intercambio turbulento en función de propiedades medias del fluido. Los modelos más simples son los de 0 ecuaciones, donde los coeficientes de difusión turbulenta se obtienen de parametrizaciones ad hoc o empíricas. Muchos de estos modelos están basados en la hipótesis de la longitud de mezcla de Prandtl. En los modelos que consideran una ecuación de transporte para la energía cinética turbulenta (TKE) o dos ecuaciones, una para la TKE y otra para la longitud de escala característica de la turbulencia, se introduce más información sobre la evolución y la historia del flujo. El rendimiento de varios cierres de la turbulencia se ha evaluado comparando los resultados con predicciones analíticas o con datos observados.

En un experimento ideal en el que un fluido uniformemente estratificado es forzado por un viento constante, los modelos de dos ecuaciones proporcionan los mejores resultados. Entre estos, el modelo k-ε predice unos resultados más físicos, puesto que la ley de la pared cerca de los contornos se verifica automáticamente, sin necesidad de introducir restricciones adicionales. La elección de las funciones de estabilidad ha resultado desempeñar un papel determinante en las predicciones del modelo. Las funciones de estabilidad clásicas de *Mellor y Yamada [1982]* no presenta un comportamiento numérico estable, mientras que la versión de cuasiequilibrio derivada de ellas (*Galperin et al. [1988]*) predice un máximo no físico de la energía cinética turbulenta a una profundidad intermedia. Las funciones de estabilidad propuestas por *Canuto et al. [2000]* solucionan este problema puesto que consideran correlaciones de la presión en el cierre de las ecuaciones para las correlaciones de las magnitudes fluectuantes y funcionan de una forma estable.

El rendimiento de distintos modelos para la parametrización de la mezcla diapícnica se ha evaluado simulando el ciclo anual en los años 1961-62 para la estación Papa en el Pacífico Norte (145^o W 50^o N), donde distintos parámetros físicos y biológicos se han medido de forma continua desde los años 50. Clásicamente, se ha encontrado que los modelos de turbulencia locales sobreestiman la temperatura de la superficie del mar (SST) y la baja tasa de mezcla diapícnica ha sido considerada la causa de este mal comportamiento. En la literatura se encuentran varias parametrizaciones simples de este efecto en el contexto de los modelos de turbulencia locales que parecen mejorar la predicciones de estos modelos, especialmente la parametrización empírica de *Kantha y Clayson [1994]*. Usando las funciones de estabilidad de *Canuto et al. [2000]*, se obtiene que la SST deja de ser sobreestimada. Esto indica que la sobreestimación en la SST es inducida por una descripción incompleta de la física de la capa de mezcla. De todas formas, las parametrizaciones de la mezcla interna se requieren para una predicción de valores realistas de los coeficientes de intercambio turbulento en la región interna. Nuestros resultados indican que el modelo k-ε con las funciones de estabilidad de *Canuto et al. [2000]* y la parametrización de la mezcla diapícnica de *Large [1994]* puede usarse para el cálculo de coeficientes de intercambio turbulento físicamente realistas que proporcionen el forzamiento físico para estudios biogeoquímicos.

Una aplicación en un estuario en el que se habían realizado medidas de la tasa de disipación de la energía turbulenta nos han proporcionado una ilustración de las posibilidades que ofrece la intercomparación entre medidas de turbulencia y predicciones de modelos de turbulencia. En esta aplicación, el modelo se forzó con la tensión del viento, los flujos de calor y los gradientes de presión externos. La advección se parametrizó relajando los valores de la temperatura y la salinidad a los observados. De esta forma, las magnitudes turbulentas se diagnostican, lo que permite una intercomparación de las predicciones del modelo con las medidas de turbulencia. Se ha encontrado que la comparación de resultados de modelos numéricos con mediciones reales de la tasa de disipación de la energía turbulenta constituye un test exigente para los modelos, aunque estos estuadios ayudan a una mejor comprensión de los procesos de mezcla y del funcionamiento de los modelos en distintas condiciones. Otra conclusión del trabajo es que es necesario realizar más estudios para modelar situaciones de estratificación estable.

Los modelos numéricos constituyen una herramienta muy valiosa para el estudio y la gestión de estuarios y áreas costeras. El modelado constituye una tarea exigente, puesto que los requerimientos de un modelo que pueda ser utilizado como herramienta predictiva incluyen una documentación completa, una arquitectura estable y versátil que permita el trabajo multiusuario y la sencilla introducción de nuevas características y acoplamiento de nuevos modulos. Con estos requerimientos en mente, el modelo 3D baroclínico MOHID3D se ha adaptado para la simulación de los flujos en la Ría de Pontevedra a escalas de marea y residual. La elección y especificación de los diferentes parámetros se ha discutido y se han llevado a cabo algunas aplicaciones con forzamientos ideales. Se ha obtenido una descripción de las velocidades de marea y residuales en la ría, de la que no se disponía hasta el momento. El efecto combinado del gradiente de densidad entre el río y la plataforma y la batimetría induce el establecimiento de una circulación residual en doble capa. El agua circula en dirección al mar abierto por la capa de superficie y hacia el río en la capa del fondo. Se ha observado la aparición de una componente lateral de la componente residual que proporciona otra vía para la mezcla y que puede ser importante para comprender los ciclos de sedimentos y biogeoquímicos en el estuario. El mismo experimento en condiciones de verano ha proporcionado una predicción de una corriente residual reducida, lo que indica que otros forzamientos son necesarios para un modelizado adecuado de la hidrodinámica en condiciones de verano. Son necesarias más comparaciones con datos reales para correr el modelo en modo pronóstico. La monitorización de las condiciones en la plataforma es crucial para que las predicciones del modelo sean realistas. Asimismo, nuestros resultados sugieren que mediciones de circulación transversal son necesarios para la comprensión de la dinámica de las rías.

Finalmente, el modelo GOTM se ha aplicado a la ría de Pontevedra. Se ha mostrado cómo en condiciones de ligera estratificación y para los forzamientos de marea y viento característicos que actúan sobre el estuario, la capa de mezcla se extiende hasta la superficie. Los resultados sugieren que es necesarion analizar la respuesta de las corrientes en el estuario al forzamiento de escala sub-mareal antes de que se pueda evaluar la variabilidad en los procesos de mezcla en el estuario. La recogida de conjuntos de datos que contengan la mayor información posible sobre los forzamientos físicos es un requisito indispensable para avanzar en la comprensión de los procesos de mezcla en las rías.

Los modelos de turbulencia de dos ecuaciones han mostrado ser los más potentes para simular flujos complejos, pero su uso no está aún generalizado en aplicaciones 3D en el oceáno abierto y en áreas costeras y estuarios. La razón principal la constituye la mayor carga computacional de resolver dos ecuaciones adicionales, aunque esta complicación está siendo resuelta por los avances en potencia de cálculo. También la elección de los parámetros en los modelos y la dificultad de entender cómo un cierre complejo de la turbulencia influye en los resultados es una tarea compleja. El uso de modelos 1D como banco de pruebas de los modelos de turbulencia proporciona una ayuda en esta tarea. En este estudio, mediante la aplicación del modelo 1D GOTM a distintas situaciones, se ha mostrado que el cierre k-ε describe de forma realista la física de la capa de mezcla en el océano. El acoplamiento de este modelo de turbulencia de dos ecuaciones a nuestro modelo 3D nos permitirá mejorar la descripción de la hidrodinámica de la ría y evaluar la influencia de las variaciones en los distintos forzamientos en la respuesta de la ría.

Contents

1 Introduction

Coastal areas and estuaries constitute the link between land and ocean. In estuaries, freshwater collected over vast regions of the land flows into an ocean, which sends salt water upstream far beyond the river mouth. Mixing between the two fluids creates a unique environment, with large potential for life forms able to handle the associated large variability in environmental conditions. Often estuaries are also a place subject to great human influence, since many settlements and industries are placed on their margins.

Some efforts have been devoted to arrive to a consensuated definition of estuary. A classical definition of estuary, widely quoted in the literature, is that by (*Cameron and Pritchard, [1963]*):

An estuary is a semi-enclosed coastal body of water which has a free connection with the open sea and within which sea water is measurably diluted with fresh water derived from land drainage.

Estuaries described by this definition are known as positive estuaries. In his useful '*Shelf and Coastal Zone Lecture Notes*', Mathias Tomczac suggests a more general definition that directly include negative estuaries:

An estuary is a narrow, semi-enclosed coastal body of water which has a free connection with the open sea at least intermittently and within which the salinity of the water is measurably different from the salinity in the open ocean.

In estuaries the properties of water parcels are constantly changed by turbulent diffusion on all scales. The estuarine salinity field is determined by the balance between advection by the mean flow and turbulent tidal diffusion. The circulation in the deep ocean, for example, can be described as the sum of geostrophic movement, wind driven flow, tides and eddies. In estuaries, the nonlinear interaction among different forces induces that this separation is not a good approximation and all relevant forces must be considered. The dynamics of estuaries are therefore much more difficult to analyze than the dynamics of the open ocean.

The main driving agent for the turbulence is the tide. The type of turbulence which occurs in an estuary is determined by the strength of the tide, which can be expressed by the tidal volume, defined as the volume of water brought into the estuary by the flood tide (and again removed by the ebb tide during one tidal cycle.) By comparing this volume V with the fresh water volume R transported by the river over the same period, we can derive four main types of estuaries (this description is transcribed from *Tomczak,* '*Shelf and Coastal Zone Lecture Notes*')

If the tidal volume V is small compared to the fresh water volume R (ie the ratio R/V is large), the fresh water will float on the denser ocean water without experiencing much mixing. Friction at the interface between the two layers will prevent it from spreading over the entire surface of the ocean and establish a boundary or front between fresh water and oceanic water at the surface near the estuary mouth. As a result, a wedge of oceanic salt water is seen to intrude into the estuary. This type of estuary is therefore known as the **salt wedge estuary**.

If the tidal volume is increased over R to reduce the ratio R/V to 0.1 - 1, the estuary changes into a **highly stratified estuary**, also known as the partially mixed estuary with entrainment. The fresh water movement in the upper layer against the stronger tidal current produces strong current shear at the interface. This creates instabilities in the form of internal waves which become unstable and break. When the tops of the breaking waves separate from the interface they inject salt water into the upper layer. The result is a net upward transport of mass and salt known as entrainment. (As a general definition, entrainment is the transport of mass drawn from a less turbulent medium into a more turbulent medium. Note that entrainment is a one- way process; there is no transport of mass from the more turbulent medium to the less turbulent medium.)

If the tidal volume is further increased to a R/V ratio of 0.005 - 0.1 the estuary turns into a **slightly stratified estuary**, also known as the partially mixed estuary. The tidal current is now so strong that water movement becomes turbulent everywhere. In shallow estuaries the turbulence is mainly the result of bottom friction. Current shear between the fresh water trying to make its way towards the sea and the tidal current adds to the turbulence, and the entire volume of the estuary experiences turbulent mixing. As a result, mass and salt are exchanged between the two layers in both directions.

The actual rate of increase depends on the efficiency of the mixing and on the degree of local recirculation of the fresh water between the layers which determines the salinity distribution. It can therefore not be calculated in the simple way that applied to the highly stratified estuary. If the tidal volume is further increased to a R/V ratio below 0.005, turbulent mixing becomes so efficient that locally all salinity differences are nearly eliminated and the estuary turns into the **vertically mixed estuary**. The characteristics of the vertically mixed estuary are: The salinity increases towards the sea but does not vary with depth. Vertical salinity profiles therefore show no salinity change with depth but a gradual salinity increase from station to station as the ocean is approached. The mean flow, which is very weak compared to the strong tidal current, is directed towards the sea at all depths; penetration of salt into the estuary is achieved entirely by turbulent diffusion against the mean flow. The distinction between upper and lower layer can no longer be made.

As we have seen, turbulence conditions determine mixing and therefore the transport of properties in estuaries. Near the surface, turbulence is created by wind and breaking waves and transmits heat in and out the ocean. Turbulence near the bottom is caused by bottom friction of tide and affects deposition, resuspension and movement of sediments. Turbulent motions in stratified flows mix fluid particles from different parts of the flow, therefore enhancing the molecular mixing caused by molecular diffusion. The mixing of salt and fresh water in estuaries is carried out by a combination of shear generated at the surface by wind and waves, shear at the sea bed and turbulence generated by shear at the halocline. Without understanding mixing, it is difficult to understand the dynamics of estuaries and coastal areas. The adequate description of vertical mixing is therefore crucial to any coastal application.

The application of models is a valuable tool in the study and management of estuaries and coastal areas. Modeling constitute a demanding task, since the requirements of a useful model include a complete documentation, a stable architecture that allows several simultaneous users and an easy introduction of new features. However, much insight into the dynamics of the system can be gained through the application of models. In a following step, models can be used in the management and monitoring of coastal areas, a field that has been designed as operational oceanography in the last decades.

A first step in the modeling of a system is the identification of the scales of variability. In figure 1.1, a diagrammatic representation of the time-scales of variability of an estuary is shown. The scale of energy is unquantified. On short time-scales (seconds to minutes), turbulence, waves and internal waves are the characteristic phenomena. These scales are usually resolved by numerical models, so their mean effect on mixing must be parameterized. The next significant time scales are related to tide. In time-scales from hours to one day, tide drives the main part of the response of the system. Characteristic tide periods are semidiurnal and diurnal, with some compound tides like M_4 (6 hours) being important in some areas. Another tidal induced period is marked as lunar cycle, and is consequence of the interaction of tidal harmonics of close frequency (ex: M_2 and S_2). This is also known as the spring-neap cycle and is characterized for the variation of amplitude of tides on a fortnightly period. Between diurnal and fortnight periods, variability is dominated by meteorological time-scales, as the passing of fronts and changes in the regime of winds. The differences in heat fluxes and prevailing meteorological conditions throughout the year induce a seasonal signal, that changes in intensity depending on latitude. In-between fortnight scales and seasonal scales, we can quote phenomena with time-scales of variability of months or even years, such as ENSO (El Niño Southern Oscillation). On a longer-term, variability is difficult to identify due to the lack of oceanographic long-term series, and also to the lack of comprehension of the details of the local impact of climate variability on coastal areas.

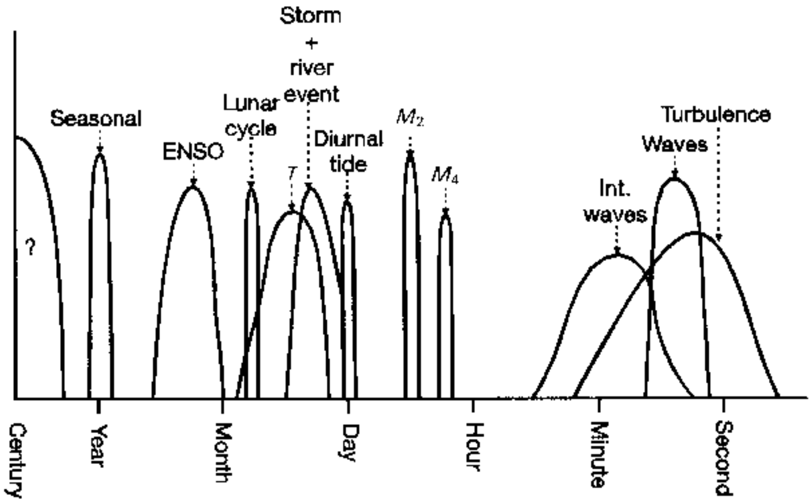

Figure 1.1: Diagrammatic representation of the physical time-scales affecting estuaries. The vertical energy scale is unquantified. From Dyer [1995].

The Galician Rías Baixas are slightly-stratified estuaries and the most characteristic geographical accidents to the south of the Galician coast. They are a well-known site of production of sea species of great economical interest, specially mussels. The most productive Rías are Arousa and Vigo, situated to the north and to the south of the Ría de Pontevedra, the subject of this study. There are not many studies of the physical oceanography of the Ría de Pontevedra. Much of what has been stated for other Rías could however also be applied to this Ría. Their characterization as positive estuaries and the general picture of the seasonal thermohaline cycle are relatively well-known (*Fraga and Margalef, [1979], Nogueira et al. [1997]*). Also, some shorter term events like upwelling relaxation have been the object of study (*Álvarez-Salgado et al. [1993]*). Some modeling efforts have evaluated residual fluxes in the Ría de Vigo and indicate a two-layered pattern (*Taboada et al. [1998]*, *Montero et al. [1999]*), enhanced by upwelling events. In spite of these studies, the hydrodynamics of the Rías is only known in its general trends, and lacks study of the influence of the different forcing on circulation for different spatial and time scales. This makes it difficult to evaluate biogeochemical cycles of bio-elements like carbon, silicon or nitrogen, as well as of potentially harmful ones like heavy metals. Some modeling efforts have been reported in Galician Rias, mainly with 2D models (*Pascual, [1987a, 1987b]*, *Montero et al. [1992], Bermúdez et al. [1998]).* In the last decade, the model MOHID3D has been adapted to simulate Galician Rías hydrodynamics: Ría de Vigo (*Taboada et al., [1998], Montero et al. [1999], Montero, [1999]*), Ría de Pontevedra (*Taboada et al. [2000], Villarreal et al. [2000]*) and other Rías (*Pérez Villar et al. [1999]*). This model does not have a two-equation turbulence closure. The use of two-equation turbulence closures is not widespread in ocean models, in spite of their superior description of physical processes. Apart from their higher computational charge, that is getting more and more affordable with the develop of computers, the use of a two-equation closure requires a proper choice of model parameters and previous testing on a wide range of applications prior to their coupling to a more complex 3D model. Also their performance is dependent on the quality of the available forcing. 1D water column model are a test for embedded turbulence closures and help in the understanding of the behavior of the model in different situations without the demanding requirements of 3D models. A 1D water column model, GOTM (General Turbulence Ocean Model) has been co-developed by the author and several tests of different turbulence closures in real and ideal applications will be presented in this work.

One of the main challenges in the study of the physical oceanography of the Galician Rías is the building of a data base that assembles all of the scattered available information on physical parameters. Many of the studies in Galician rias have focused on biogeochemical properties. However, some physical parameters have been monitored in the last years. There are tidal gauge time series in the main harbors since the first half of the century and also some short term moorings have been carried out in different parts of the Ría and the shelf. Thermohaline variables have been more often measured and some monitoring is done since some years ago. In the Ría de Vigo, thermohaline and chemical parameters are continuously measured in an interior point twice a week from 1987. The Conselleria de Pesca, Marisqueo e Acuicultura (Xunta de Galicia) is also continuously monitoring the Rías to assess water quality. A recently finished project financed by the same organism has set-up a data base of thermohaline, meteorological and current and tidal gauge moorings in all Galician Rías (with surveys of an average duration of six months on each ria). The assemblage and study of these data will lead to a progress in the understanding of the time and spatial scales of variability affecting Galician rias, which constitutes a pre-condition for their adequate management and preservation.

The dissertation will be divided as follows: first, some turbulent closures based on the eddy viscosity principle will be studied and their performance will be compared in some analytical, open sea and estuarine situations. In Chapter 3, the 3D model used in this study will be described. Chapter 4 is devoted to the study of the hydrodynamics of the Ría de Pontevedra. The spatio-temporal scales of variability will be described and illustrated with help of some available data, including thermohaline measurements covering a seasonal cycle. The application of the model to the Ría de Pontevedra will be described and some results will be presented. Finally, some conclusions and a brief outlook are given in Chapter 5.

2 Turbulence

2.1 Introduction: Turbulence and mixing

The ocean is a three dimensional turbulent fluid, with interacting motions and processes at all time and space scales. The flow in the ocean is mostly turbulent and mixing is generally carried out by turbulent processes. The rates of transfer and mixing of flow properties due to turbulence are often several orders of magnitude greater than the rates due to molecular diffusion. The way and rate of mixing in the ocean determines its dynamics and therefore its interaction with biology and its role in the global climate.

Turbulence is an eddying motion with a wide spectrum of turbulent eddies and a corresponding spectrum of fluctuation frequencies. The way how turbulence is transferred between different scales is known as the energy cascade of turbulence. The large eddies interact with the mean flow, and extract energy from it. These eddies correspondingly interact with other eddies and feed smaller scale energy eddies. This process transfers energy from larger to smaller scales. The smallest eddies are of the scale of the viscous forces, so dissipation takes place when turbulence reaches the smallest scales after being transferred from larger scales. We must note however that viscous forces only determine the scale at which energy is dissipated, not the amount of energy that is actually dissipated and the rate at which it is dissipated.[2]

The scale of the phenomenon to study is the flow domain. The larger eddies that extract energy from the mean flow are of the order of the flow domain dimensions. In the context of numerical models, as resolution is limited by computation and storage constraints, a scale is chosen and effects of smaller scales are introduced in the model by parameterizations of the smaller scale eddies. We can distinguish four characteristic ranges for motions in the ocean. The *rotational range* encompasses the largest length and time scales. In this range, motion is primarily comprised of two-dimensional eddy motions acting over length scales greater than 100 meters and time scales of the order of days. This includes ocean basin circulations such as gyres, rings and eddies that are influenced by the effects of the earth's rotation (the Coriolis force). The *buoyancy range* includes motions of a length scale approaching the depth of the

---

[2] This energy cascade classical view was proposed by Richardson [1922]. As pointed in Sander [1998]p. 12, some experimental evidences appear to contradict this classical picture: "Gibson et al. [1970] show that many features measured as turbulence actually have a fossil character: active turbulence starts at small scales... For rotating fluids an inverse energy cascade may also evolve, see Berezin et al. [1991]"

upper ocean mixing layer (from 100's of meters to 1 meter) and includes internal waves and small-scale eddies. In this range, the fluid motion makes a transition from two-dimensional to three-dimensional flow, with periods on the order of minutes to many hours. Buoyancy range motions are affected by gravity and stratification of the water column. The *inertial range* consists of three-dimensional small-scale turbulent motions in which the forces of gravity and molecular viscosity (viscous friction) are dominated by inertial forces. The inertial range extends from several meters to several centimeters, over periods of several seconds to several minutes. The *viscous rang*e is the smallest scale of fluid motions, typically less than a few centimeters. In the viscous range, fluid motions are dissipated by molecular viscosity.

The observed rate of along-isopycnal mixing is significantly greater than across them (*Ledwell et al. [1993]*). As isopycnals are quasi-horizontal in the ocean except in particular zones, like fronts and convection layers, horizontal mixing processes in the ocean have greater space and time scales than that of vertical mixing. Thus, in most parts of the ocean and for eddy-resolving or coastal models, as horizontal turbulent scales are resolved and vertical small-scale are of the order of meters, the problem is to model vertical small-scale processes and their effect of mixing. In ocean global circulation models (OGCM), where a high horizontal resolution is not affordable, the problem of parameterizing quasi-horizontal mesoscale eddies (with length scales from 10 to 100 km) appears. Their bulk effect on the resolved large scales must be parameterized, since these unresolved eddies contain most of the total kinetic energy of the ocean. Some parameterizations have been designed and tested (*Bryan, [1969], Gent and McWilliams, [1990]*, a detailed review of these parameterizations can be found in *Mathieu, [1998]*), but the representation of unresolved horizontal scales is still one of the main challenges in ocean research.

In figure 2.1, a sketch of some mixing processes in the ocean is shown. A review of turbulence and mixing in the ocean can be found in *Caldwell and Moum, [1995].*

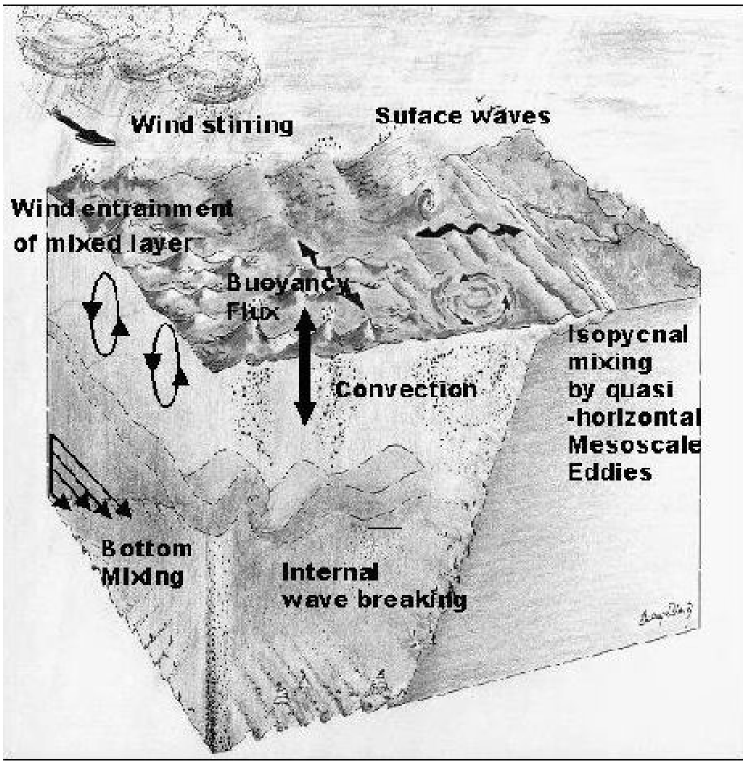

Figure 2.1: Sketch of mixing processes in the ocean. Figure from GOTM web site http://www.gotm.net

Mixing at the surface and mixing at the bottom are boundary induced mixing. A mixed layer is set up where turbulence penetrates the ocean until it is inhibited by stratification. Near the surface, turbulence is created by wind and breaking waves and the heat that is transferred in and out the ocean. Surface turbulence determines the dynamics of the mixed layer of the ocean, where much of the biological activity takes place. Some other processes like Langmuir circulation influence the extent of the mixed layer. Turbulence near the bottom is caused by bottom friction mainly produced by currents. Bottom turbulence affects deposition, resuspension and movement of sediments. In some situations a surface mixing layer extends to bottom or a bottom mixed layer extends to surface, specially in shallow areas, but usually an internal stratified layer exists between a surface and a bottom layer. In the open ocean, where bottom mixing does usually not create an great boundary layer, a surface mixed layer lies above a stratified region. In this internal region, turbulence is inhibited by local stratification, but some mixing processes create turbulence. They have the form of instabilities like internal wave breaking and shear instability.

Boundary layer mixing The ocean is constrained by two boundary layers: a surface boundary layer, in contact with the atmosphere, and a solid boundary layer at the bottom. Boundaries are the sources of much of the turbulence generated in the ocean, and the properties of boundary layers condition mixing.

At the bed, turbulence is generated by interaction of water flows with the bottom, a rigid rough boundary. The effect of bottom stress is greater in shallow seas and is dominant in many tidal estuaries. In the deep ocean, boundary mixing has been regarded as one of the main contributions to the value of observed abyssal diffusivities of O$(10^{-4}m^2s^{-1})$ (for a discussion, see *Caldwell and Moum [1995]*). In coastal areas, tides and other currents are affected by the bottom, that slows down the near bed flow relative to that higher up and turbulence is produced by the flow around bottom roughness elements. In fact, much of the energy that enters the ocean is dissipated in shallow seas by means of generation of bottom turbulence by interaction of tidal currents with the bed. Other turbulence source in shallow waters are surface waves that produce turbulence and enhance the bottom stress felt by the currents by a non-linear interaction with the mean current.

The process of generation of turbulence at the bottom is a frictional process where drag at the sea bed produces a velocity shear: the near bed flow is slowed down in comparison with the flow higher up, and also turbulence is induced by the interaction of flow with the roughness elements of the bed. Although the real boundary condition is null velocity at the bed, the velocity profile near the bed for unstratified conditions can be described by the logarithmic law of the wall or von Karman-Prandtl equation:

$$\frac{u}{u_*} = \frac{1}{\kappa} ln \frac{z}{z_0} \tag{2.1}$$

with u, the modulus of the near bottom velocity, u_* the friction velocity and z_0 the characteristic roughness length of the sea bed, that characterizes the influence of the size of bottom elements on hydrodynamic flow.

Turbulence at the ocean surface boundary layer (OBL) affects the transfer of momentum, heat, freshwater, particles and gases between the ocean and the atmosphere. The main processes that create turbulence at the ocean surface layer are wind stress and surface buoyancy fluxes. Buoyancy fluxes can induce the set-up of unstable stratification at the surface. This generates convection that can be an important contribution to mixing in some regions. Many times, convective motions coexist but are dominated by wind stress acting on the surface. In contrast to other turbulent processes, that produce down-gradient fluxes of density (heat or salt), convection is a counter-gradient process. Measurements (e.g. *Gargett [1989]*) indicate that the full picture of mixing at the OBL is not complete with only wind stress and buoyancy fluxes and there are some other processes acting that enhance mixing. Other contributions are wave breaking and Langmuir circulation. Turbulent measurements in the presence of breaking surface waves indicate that turbulence is greatly enhanced near breaking waves. However, wave breaking does not seem to induce a noticeable deepening of the mixed layer (*D'Alessio et al. [1998]* and references therein). In contrast, Langmuir cells appear to promote a deepening of the surface mixed layer (*Li et al. [1995]*). Langmuir circulations (see e.g. *Weller and Price [1988])* arise if there is a balance between a wind induced Stokes drift gradient (a stabilizing influence) and a temperature driven, vertical density stratification (a destabilizing effect). They are typically manifested as long roll structures of width between 1 and 100m commonly identified from debris or windrows at regions of surface convergence. Langmuir circulation has been regarded as a major effect in plankton dynamics.

Interior mixing In stratified fluids, turbulence is a highly random and intermittent process that is poorly understood. The tendency of stratification is the inhibition of turbulence, although there are some processes that appear in stratified fluids and create turbulence. We will talk of internal mixing as the mixing that is internally generated in the stratified region, sometimes influenced by boundary layer or mean current shear. The ocean is a stratified fluid with different degrees of stratification. In coastal zones, haloclines and thermoclines develop driven by different processes (river freshwater meeting salt water, heat fluxes at the surface, upwelling events, human discharges...). This stratification can be more or less sharp defined depending on the balance of the processes that favor its set-up and those that tend to erode it. Sometimes, a pycnocline is found that lies in-between a bottom boundary layer and a surface boundary layers. In the open ocean, although often haloclines appear, for example, the Mediterranean outflow into the Atlantic or the Levantine Intermediate Water in the Mediterranean Sea, stratification is mainly driven by temperature. A seasonal thermocline can appear as a result of heat and momentum flux at the surface, and its depth depend on the magnitude of this forcing. Between 200-300 m and 1000 m, throughout much of the ocean, temperature diminishes rapidly and this steep layer is called the permanent thermocline. Below this thermocline, there is virtually no seasonal variation and temperature decreases gradually. Mixing in the main thermocline is interior mixing and its adequate understanding is crucial for quantifying the global ocean circulation.

The processes that mix stratified fluids have been reviewed by *Fernando [1991].* They have principally the form of instabilities at the interface and depend on the relative thickness of the velocity interface and the density interface. For small current shear, the density interface is smooth, but as the shear increases, the interface becomes disturbed by waves of different characteristics. When both shear and stratification are present, turbulence evolution depends on the value of the Richardson number (Ri, the squared ratio of stratification to shear). If Ri is less than some critical value, the flow evolution is qualitatively similar to the case of pure shear. If Ri exceeds the critical value, stratification dominates and the flow evolution resembles the case of pure stratification. The critical value of Ri for many ocean situations is near 0.25, the critical value for linear instability (*Kundu, [1990]*), although a unique Richardson number for all distributions of shear and stratification does not exist.

The waves at the interface have different mixing characteristics and can be distinguished in terms of the Richardson number. The Kelvin-Helmholtz waves dominate when the length scales over which velocity and density variations are of the same order (so for $\mathrm{R}_i < 0.25$). If the density interface is sharp ($\mathrm{R}_i > 0.25$), then Holmboe instabilities (characterized by a cusped shape) may develop. The shape of these instabilities is shown in figure 2.2. The development of Kelvin-Helmholtz instability starts with the steepening of the interface, that rolls up and forms billows, into which water from above and below the interface are mixed. With Kelvin-Helmholz waves, equal volumes of water are exchanged between the two layers in a two-way process. So, this process is known as turbulence diffusion and requires that turbulence is present in both layers. Holmboe waves grow in height and become sharper crested. When they break they eject wisps of denser water into the lighter water above. This breaking of Holmboe interfacial waves causes entrainment from the denser layer. Thus, entrainment is a one-way process in which a less turbulent layer 'entrains' a more turbulent layer. Little mixing occurs until the waves break, so entrainment will decrease with R_i.

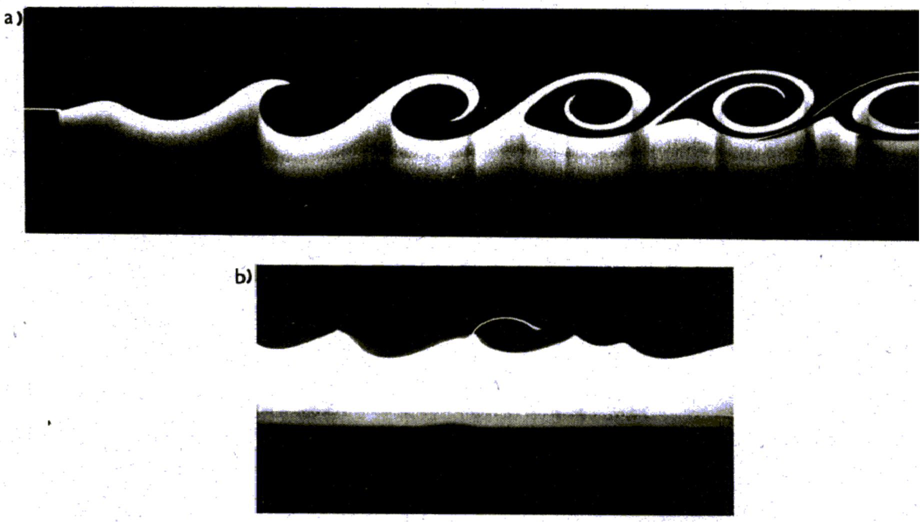

Figure 2.2: Picture depicting what are like to be a) Kelvin-Helmholtz instabilities and b) Holmboe instabilities (courtesy of Dr. Greg Lawrence in Fernando [1991]).

Internal waves In the interface between two fluids of different density, other waves with length scales of meters can appear responding to perturbations on the interface. They are called internal waves. The ocean is not a two-layered fluid, but it is continuously stratified, and internal waves can appear everywhere in it. The maximum period of the internal waves that may occur is limited by the buoyancy frequency. Therefore, the period of the observed internal waves is typically of hours, although also some internal waves have periods comparable or higher than the Coriolis frequency and the effect of Coriolis force on them cannot be ignored. They are known as internal inertia gravity waves. Most of the energy of internal waves in the ocean is centered around tidal and inertial frequencies.

Internal waves generate mixing when they break after encountering critical conditions, such as topographic variations or interaction with shear. For example, in estuaries the change of stratification and layer thickness upstream can induce critical conditions for the breaking of internal waves generated elsewhere. Some estimations (*Geyer and Smith [1987]*) have shown that internal wave interaction with the mean shear may rise the critical Richardson number to 0.33, thus allowing mixing when gradients are above the critical value.

Away from the boundary layer, mixing is thought to be driven primarily by unresolved internal wave shear (*Caldwell and Moum, [1995]*). Internal wave breaking near sloping boundaries has been regarded as a main contributor to the value of diffusivities in interior regions (*Polzin et al. [1997])*.

Double diffusion Double diffusion is another process that affects mixing in the ocean in some stratified situations (for a review see *Schmitt, [1994])*. It is not strictly a turbulent process, in fact its origin is the difference in molecular diffusivities of salt and heat. The molecular diffusivity of heat is about 100 times greater than that of salt. As a result, heat will diffuse faster than salt through the interface between fluids of different densities. An instability will grow in the interface where molecular diffusion occurs. The situations where double diffusion is likely to occur are turbulence-free zones where warm, saltier water lies over cold, less saline water. The tropical and subtropical thermoclines are zones where these conditions meet and double diffusion forces vertical flow to be within tubes typically less than 1 m long where the warmer, saltier water sinks and the colder, less saline water rises. These tube structures are called 'salt fingers' and in regions of active salt fingering mixing is enhanced. Double diffusion processes are also involved in the diffusive-convective staircases that mix cold, fresh water over warm salty water as occurs in the Arctic and adjacent regions (*Padman and Dillon, [1987]*)

In this chapter, we will review the basic assumptions in present turbulence modeling and also introduce the most widespread turbulence models in ocean applications. Finally, an intercomparison of some of them will be done with help of a 1D water column model.

2.2 Reynolds approximation and the turbulence closure problem

Navier-Stokes equations are the equations that describe turbulent fluid motion. There are numerical procedures available for solving these equations with direct numerical simulations (DNS procedures), but the requirements of computing and storage are so stringent that only in some simple situations they can be directly solved. Since the range of scales in a turbulent flow can vary over several orders of magnitude, resolving both the smallest and largest eddies requires a large number of grid points. The smaller turbulent scales are typically of the order of 10^{-3} times smaller than the extent of the flow domain. Therefore, the number of grid points necessary to cover the flow domain is extremely great and grows with the size of the domain, with the consequence that only for small, simple domains direct integration is feasible, even in supercomputers. Nonetheless, although the simulated flows are idealized, DNS simulations have revealed as a useful tool for understanding the basic physics of turbulence and examining models.

The basic assumption in classic turbulence studies is that turbulent motion can be decomposed in a mean flow and a fluctuating part. Leonardo da Vinci already put forward this idea. He realized that usually fluid motion was the balance of two components:

”Observe the motion of the surface of the water, which resembles that of hair, which has two motions, of which one is caused by the weight of the hair, the other by the direction of the curls; thus the water has eddying motions, one part of which is due to the principal current, the other to random and reverse motion”.

[Transcription from Piomelli in Lumley, J.L., 1997. Some comments on turbulence. Phys. Fluids A 4, 203-211.]

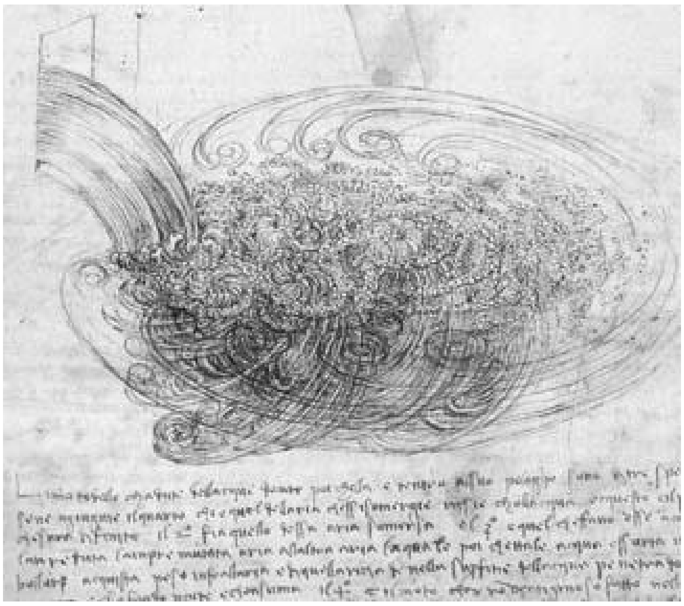

Figure 2.3: Study on turbulence in fluids by Leonardo da Vinci.

Reynolds applied this idea to arrive to a useful form of the equations of motion. He decomposed flow properties into a mean part $\bar{F}$ and a fluctuating part F’:

$$F = \bar{F} + F' \tag{2.2}$$

After applying this decomposition, we arrive to the continuity equation for the mean flow:

$$\partial_i \bar{u}_i = 0 \tag{2.3}$$

and to the Reynolds equations for mean momentum, where hydrostatic and Boussinesq approximations have been assumed:

$$\partial_t \bar{u}_i + \partial_j(\bar{u}_i \bar{u}_j) + 2\varepsilon_{ijk}\Omega_j \bar{u}_k = -\frac{1}{\rho_0}\partial_i \bar{p} - \frac{\rho - \rho_0}{\rho} g\delta_{i3} + \nu\partial_j(\partial_j \bar{u}_i) - \partial_j \overline{u'_i u'_j}, \tag{2.4}$$

with density ρ, pressure p, velocity u_i in direction x_i and the angular velocity vector of the Earth's rotation $\Omega = (0, \Omega\cos\phi, \Omega\sin\phi)$, ε_{ijk} the alternating tensor, ν the molecular diffusivity for momentum and where Einstein convention of summation over repeated indexes in a term applies. The rate of change of horizontal mean velocities results from the balance of advection, Coriolis force, pressure gradient, molecular diffusion and the Reynolds stress terms that represent the cross products of the fluctuating components that are not null after ensemble averaging. If we subtract the averaged from the full momentum equations, we arrive to evolution equations for the turbulent stresses:

$$\begin{aligned}
\partial_t \overline{u_i' u_j'} = & -\overline{u_k}\partial_k \overline{u_i' u_j'} - \left(u_i' u_k' \partial_k \overline{u_j} + u_j' u_k' \partial_k \overline{u_i}\right) - \frac{g}{\rho_0}\left(\overline{u_i'\rho'}\delta_{j3} + \overline{u_j'\rho'}\delta_{j3}\right) \\
& + \overline{\frac{p'}{\rho_0}\left(\partial_j u_i' + \partial_i u_j'\right)} - \partial_k\left(\overline{\frac{p'}{\rho_0}\left(u_i'\delta_{jk} + u_j'\delta_{ik}\right)} + \overline{u_i' u_j' u_k'}\right) \\
& - 2\Omega_l\left(\varepsilon_{ilk}\overline{u_k' u_j'} + \varepsilon_{jlk}\overline{u_k' u_i'}\right) + \nu\frac{\partial^2 \overline{u_i' u_j'}}{\partial x_k^2} - 2\nu\overline{\partial_k u_i' \partial_k u_j'} \qquad (2.5)
\end{aligned}$$

Rate of change = Advection + Shear Production + Bouyancy Production
+ Pressure-strain correlation +Triple correlation term
+ Rotation + Molecular diffusion + Dissipation rate of Turbulent Kinetic Energy

where Einstein convention of summation over repeated indexes in a term applies. This equation involves triple correlations of velocities. This is a general feature: for all correlations of order n of the fluctuations, the temporal evolution includes correlation terms of order n+1. As a result of this coupling, this process goes to infinite and therefore a closure at a certain level n is necessary to solve the system. That is why the evaluation of these Reynolds stresses constitutes what is called the turbulence closure problem. A closure at level n describes how the correlations of order n+1 are prescribed by empirical relations. As described for example in *Sander* [1998], terms like pressure strain correlations must also be approximated. Some other classical approximations are the neglect of rotational terms and the boundary layer approximation. This last approximation permits neglecting horizontal gradients in Eq. 2.5 and is based in the assumption that horizontal scales are greater than vertical scales, that as we noted in the section 2.1 is valid for many ocean applications. An analogous approach to the outlined for the correlation of velocity fluctuations can be taken for the evolution equation of internal energy or tracers. Correlations between velocity fluctuations and tracer or internal energy fluctuation and the autocorrelations of tracers appear in the new equations and must be evaluated to arrive to a closed form of the tracer transport equation.

One way to simulate a geophysical flow of large scale is to use the large eddy simulation (LES) method. This technique lies between the computations of the complete turbulent flow field (like DNS) and the methods based on empirical parameterizations of the turbulent correlations as functions of the mean flow quantities at a lower scale of resolution. Rather than parameterize the smallest turbulence scales, the LES simulations parameterizes their effects on the largest scales of motion, and only those scales are computed explicitly. LES is a valid approach in some situations because the larger eddies contain most part of the energy and transport most of the conserved properties. Even though mixing occurs at the smallest scales, the rate of mixing and the bulk properties of the flow are determined by the larger scales of the motion. Since only the larger scales are resolved, the resolution requirements in LES are significantly smaller than in DNS. Consequently, LES can be used for more realistic geophysical flows. However, like DNS, it is necessarily three-dimensional and time-dependent, which makes it computationally expensive too.

In the next sections, some solutions to the closure problem that relate turbulent correlations to mean flow properties will be reviewed and their application in some oceanic test cases will be described.

2.3 Turbulence eddy viscosity models

2.3.a Eddy viscosity principle

One of the most fruitful ideas for estimating Reynolds stresses has been the eddy viscosity principle, originally proposed in 1877 by Boussinesq. If we assume that turbulence exchanges follow a diffusion law similar to that of molecular diffusion, but with a different constant, we can relate turbulent fluxes to gradients of transported properties. In this way, turbulent stresses can be supposed proportional to the mean flow velocity gradients. For general flow situations, this principle can be written as:

$$-\overline{u_i'u_j'} = \nu_t(\partial_j\overline{u_i} + \partial_i\overline{u_j}) - \frac{2}{3}k\delta_{ij} \tag{2.6}$$

A similar concept can be used to relate turbulent fluxes of heat to the gradients of the mean quantities. The factor $-\frac{2}{3}k\delta_{ij}$, where now k is the kinetic energy of the fluctuating motion, is added to this expression to preserve the positiveness of normal (i=j) stresses (see *Rodi, [1980]* p. 10). This term does not need to be determined, because after replacing the unknown velocity-correlations in (2.5), this part is absorbed by the pressure gradient term in the correlations equation. If the turbulent viscosity from (2.6) is substituted into (2.4), the last terms are written analogously to molecular diffusion terms.

Following the analogy with viscous diffusion, the role of molecules in viscous motion is played by eddies in turbulent motion. The proportionality constants for turbulent diffusion are an eddy viscosity ν_t (for momentum) or an eddy diffusivity ν_t' (for mass). In contrast to molecular diffusivity, that is a intrinsic property of the fluid, eddy coefficients depend on the state of the turbulence in the flow. Because water properties are exchanged with the turbulent movement of particles, the rate of turbulent mixing is considered to be the same for all properties: temperature, salinity and other tracers.

The eddy viscosity principle skips the problem of dealing with the evolution equations for the turbulent stresses and shifts the effort to determining an expression for the eddy viscosity suitable for describing turbulent flows. The simplest way to calculate eddy viscosities is to suppose they are constant and have a typical value dependant on the turbulent state of the flow to be modeled and estimated after direct measurements, empirical considerations or trial/error adjusting to fit observations. If a similar eddy viscosity principle is applied to turbulent diffusion of heat and mass, the different turbulent mixing rate of momentum and that of heat and mass can be parameterized by means of the Prandtl number P$_r$, that relates eddy viscosity ν_t (momentum) to eddy diffusivity $\nu_t^{'}$ (heat, mass):

$$\nu_t^{'} = \frac{\nu_t}{P_r} \tag{2.7}$$

As discussed in the introduction, stable stratification inhibits turbulent mixing, which implies that eddy viscosities and diffusivities must be reduced by stable stratification. This contribution can be introduced as a stratification dependant factor ν_{ts} that modifies eddy coefficients in neutral conditions (no stratification) ν_{t0}:

$$\nu_t = \nu_{t0}\nu_{ts} \tag{2.8}$$

One of the first attempts of considering this effect was done by *Munk and Anderson [1954]*, who proposed an empirical formula for eddy coefficients in stably stratified conditions:

$$\begin{aligned} \nu_t &= \nu_{t0}\,(1+10R_i)^{-1/2} \\ \nu_t^{'} &= \nu_{t0}^{'}\,(1+3.33R_i)^{-3/2} \end{aligned} \tag{2.9}$$

with $\nu_{_{t0}}$ and $\nu_{_{t0}}^{'}$, the eddy viscosity and diffusivity in the non-stratified case and R$_i$ the mean-flow gradient Richardson number, that compares the stabilizing tendency of stable stratification with the destabilizing tendency from vertical shear:

$$R_i = \frac{N^2}{S^2} \tag{2.10}$$

N^2 is the Brunt-Väisällä frequency, that characterizes stratification:

$$N^2 = -\frac{g}{\rho_0}\partial_z\rho. \tag{2.11}$$

and S^2 is the vertical shear stress or Prandtl frequency, that characterizes vertical shear:

$$S^2 = (\partial_z u)^2 + (\partial_z v)^2 \tag{2.12}$$

This expression also provides us with a stratification-dependant form of the Prandtl number:

$$\begin{aligned} P_r &= P_{r0}\frac{(1+10R_i)^{1/2}}{(1+3.33R_i)^{3/2}},\ R_i \geq 0, \\ P_r &= P_{r0},\ R_i < 0 \end{aligned} \tag{2.13}$$

with $P_{r0,}$ the Prandtl number for neutral conditions. This value is not known precisely and several estimations in neutral shear flows indicate a value in the range 0.7 to 1.0 (for a discussion of laboratory, atmospheric, theoretical and numerical estimations, see e.g. *Schumann and Gerz [1995]).*

Other simple parameterization that has been widely used is that suggested by Pacanowski and Philander in 1981 for the tropical ocean:

$$\begin{aligned} \nu_t &= \frac{\nu_{t0}}{(1+\alpha\, max[0,R_i])^n} \\ \nu_t^{'} &= \frac{\nu_t}{1+\alpha\, max[0,R_i]} \end{aligned} \tag{2.14}$$

with ν_{t0} a constant viscosity for "neutral" conditions (chosen by them to be $10^{-5}m^2s^{-1}$, a characteristic value for the tropical ocean) and n and α, two empirical parameters chosen as $n = 2$, $\alpha = 5$. Note that they assume $P_{r0} = 1$, rigorously, a factor $1/P_{r0}$ should multiply the right term on the formula for ν_t'. This expression breaks for instable stratification, so the maximum of 0 and R$_i$ has been introduced to avoid powers of negative numbers. We can also derive a stratification-dependant form of the Prandtl number from this expression.

Most of the expressions that have been proposed for $(\nu_t)_s$ can be synthesized in the formula:

$$\begin{aligned} (\nu_t)_s &= (1+\alpha R_i)^{-\,n} \\ (v_t')_s &= (1+\beta R_i)^{-n^{'}} \end{aligned} \tag{2.15}$$

where the values α, β, n and n' are empirical constants. *Munk and Anderson [1954]* MA () used $\alpha = 10$, $\beta = 3.33$, $n = 1/2$ and $n^{'} = 3/2$, *Pacanowski and Philander [1981]* PP () used $\alpha = 5$, $\beta = 5$, $n = 2$ and n$^{'} = 1$ and *Backhaus and Hainbucher* [1987] and *Salomon et al. [1987]* to $\alpha = 7$ and $n = 0.25$, $\beta = 1$ and n$^{'} = -7/4$.

In figure 2.4, the normalized eddy viscosity (ν_t/ν_{t0}) for the different functions quoted in this section, *Backhaus and Hainbucher* and *Salomon et al. [1987]* BHS (2.15) is plotted against the gradient Richardson number in a logarithmic scale. The eddy viscosity is a decreasing function of the Prandtl number for all of them. As R$_i$ grows the eddy viscosity decreases, which accounts for the inhibiting effect of stable stratification on mixing. MA and BHS are more step-like than PP that decays smoother and predicts less mixing for every R$_i$.

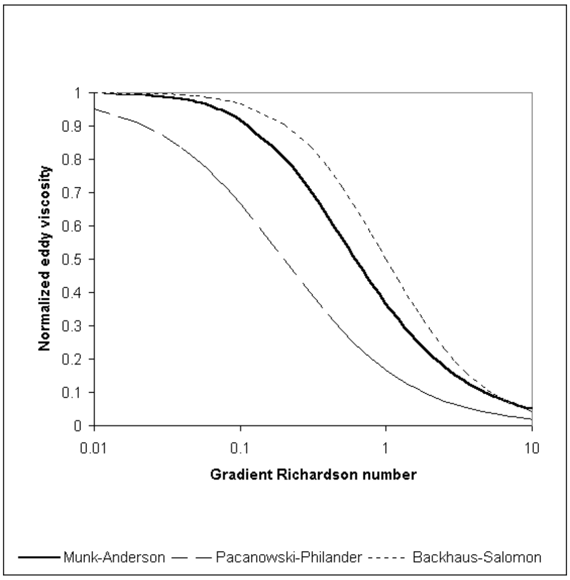

Figure 2.4: Normalized eddy viscosity as function of the gradient Richardson number for the empirical parameterizations described in the text: Munk and Anderson [1954] MA , Pacanowski and Philander [1981] PP and Backhaus and Hainbucher and Salomon et al. [1987] (BHS).

In figure 2.5, the normalized Prandtl number (P_r/P_{r0}) is plotted versus the gradient Richardson number for the Prandtl number expressions that can be derived from the formulas MA (2.9), PP (2.14), and BHS (2.15). In addition to those three expressions, the form proposed by *Schumann and Gerz [1996]* SG is plotted:

$$P_r = P_r^0 \exp\left(-\frac{R_i}{P_r^0 R_f^\infty}\right) + \frac{R_i}{R_f^\infty} \qquad (2.16)$$

with the neutral Prandtl number $P_r^0 = 0.74$ and the limit flux Richardson number $R_f^\infty = 0.25$. All functions have been normalized to this value of $P_r^0 = 0.74$, .that was estimated from

LES results. Also in the figure these LES results by *Schumann and Gerz [1996]* and laboratory data for saltwater by *Rohr [1988]* are plotted. All expressions model the Prandtl number as an increasing function of the Richardson number. As stratification develops, the transference of momentum grows while the transference of mass is not so affected, since pressure fluctuations also transfer momentum. Laboratory data provide an estimation of a lower P_r^0 than LES results. The best fit to LES and laboratory data is shown by the SG expression, that was designed taking into account these data. The MA expression lies closer to SG than the others. Anyway, MA and BHS lie close to SG only for low Richardson numbers. PP formula predicts a too high Prandtl number for all values. Therefore, this expression seems inappropriate for simulating situations with low Richardson number and high spatial resolution. For applications with low resolution as OGCM, the performance of PP can be better than for high resolutions, since mixed layer region (where R$_i$ is low) need not be well characterized, and actually it has been profusely used in global ocean simulations.

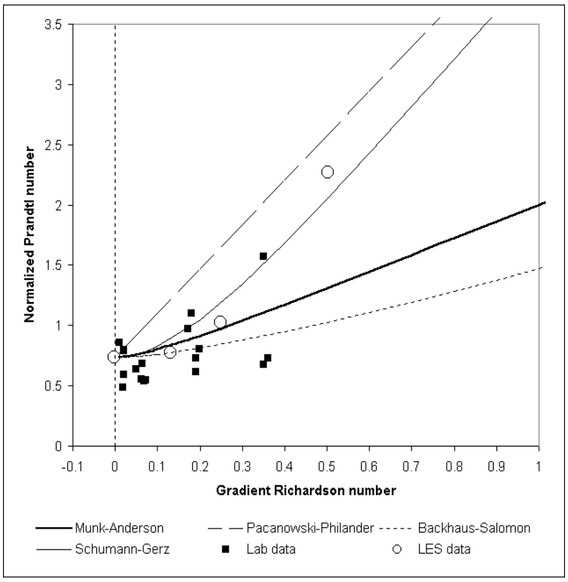

Figure 2.5: Normalized Prandtl number (P$_r$/P$_{r0}$) as function of the gradient Richardson number for the different empirical parameterizations: Munk and Anderson [1954], Pacanowski and Philander [1981] , Backhaus and Hainbucher [1987] and Salomon et al. [1987] and Schumann and Gerz [1996]. Laboratory data from Rohr et al. [1988] and LES data from Schumann and Gerz [1996].

Some other simple models have been used and eddy coefficients have been prescribed as a function of depth, stratification, velocity or other factors. The rather complex KPP (K

Profile Parameterization) model (*Large et al. [1994]*) can be considered as a sophisticated parameterization of eddy coefficients, that prescribes them guided by physical properties and measurements of boundary layers, interior stratified regions or convection zones.

In guiding the parameterization of eddy coefficients, the Kolmogorov and Prandtl hypothesis has been of great utility. Based in dimensional analysis, they postulated that eddy coefficients could be obtained as the product of a velocity scale V and a length scale L that characterize the turbulent motions of larger scale, where the transference of energy from the mean flow occurs:

$$\nu_t \propto VL \tag{2.17}$$

Based in this expression, Prandtl in 1925 proposed the first model to describe the distribution of eddy viscosity. A velocity scale proportional to the mixing length scale times the velocity gradient and a mixing length scale L form what is known as the Prandtl mixing length hypothesis. Under the boundary layer approximation we are using, the velocity scale can be written:

$$V = L\sqrt{(\partial_z u)^2 + (\partial_z v)^2} \tag{2.18}$$

and the eddy viscosity is determined from the expression:

$$\nu_t = L^2\sqrt{(\partial_z u)^2 + (\partial_z v)^2} \tag{2.19}$$

The problem now lies in the determination of the mixing length, and several expressions have been applied for different flows (see *Rodi [1980]*). Some authors have argued that the mixing length scale must be limited by stratification and some expressions have been designed to account for it.

For shallow seas, where the boundary layer is restricted by the water depth, *Bowden and Hamilton [1975]* have used this postulate to prescribe eddy viscosities in a simple manner. They consider the water depth H as the length scale and the magnitude of the depth-integrated mean current $\left|\vec{V}\right|$ as the velocity scale and C_ν as a scaling factor, that may vary for different bottom conditions:

$$(\nu_t)_0 = C_\nu H \left|\vec{V}\right| \tag{2.20}$$

In deeper waters where the boundary layer is only a fraction of the total depth, the mixing length scale may be obtained as a product of depth H and a function of depth $\phi(z)$. *Backhaus and Hainbucher [1989]* substituted the depth-integrated velocity by the velocity in every layer L of the model V_L with a scaling factor of $C_\nu = 2.6 \cdot 10^{-4}$ and reported a good performance in shelf sea simulations.

A physically more appealing velocity scale is the bed friction velocity u_*, that has been widely used in shallow seas (for example *Davies and Xing , [1997]*):

$$(\nu_t)_0 = C_\nu \phi(z) u_* \tag{2.21}$$

This expression is only valid if the bottom boundary layer extends to surface, which is only a good approximation in shallow tidally-dominated seas.

Perhaps the most physically meaningful velocity scale of turbulence is the square root of the turbulent kinetic energy (k or TKE), defined as:

$$k = \frac{1}{2}(\overline{u^2} + \overline{v^2} + \overline{w^2}) \tag{2.22}$$

that represents the mean kinetic energy of turbulent fluctuations (per unit mass). This turbulent kinetic energy can be determined after solving the closure problem, since the trace of equation 2.5 is a transport equation for k. Eddy viscosities and diffusivities will be determined from the expression:

$$\nu_t = c_\mu \sqrt{k} L; \quad \nu_t' = c_\mu' \sqrt{k} L, \tag{2.23}$$

where L is the turbulent macro length scale or the characteristic length scale of the energy containing turbulent motions, and c_μ and c_μ' are dimensionless proportionality factors known as stability functions. As we will see in section 2.3.d, some different expressions that depend on the state of the flow have been proposed for these functions, and the most suitable for every model depends on the level of complexity of the flow in comparison with the velocity and length scales prescribed with the turbulence model. The unresolved physics can be taken into account in the model by means of the stability functions. In fact, the stratification functions we have reviewed can be considered as stability functions for simple models of neutral flows.

Mellor-Yamada in their significant work in 1974 presented a derivation of an equation for a turbulent velocity scale and what can be considered as an equation for a length scale. Other possibility is the k-ε model (*Rodi, [1980]*), where an equation for TKE and an equation for the dissipation rate ε are solved. In the so-called *Mellor and Yamada* model [1974, 1982], the TKE is substituted by the turbulence intensity $q = \sqrt{2k}$. Therefore, the eddy viscosities and stability functions in (2.17) correspond to K_M, K_H, S_M, and S_H used in *Mellor and Yamada* [1974, 1982] in the following way:

$$K_M = \nu_t \quad K_H = \nu_t' \quad S_M = c_\mu/2^{1/2} \quad S_H = c_\mu'/2^{1/2}. \tag{2.24}$$

In the k-ε literature (see *Rodi* [1980, 1987]), the length scale is substituted by the normalized dissipation rate which has here the unit $W\,kg^{-1} = m^2 s^{-3}$:

$$\varepsilon = (c_\mu^0)^3 k^{3/2}/L \tag{2.25}$$

with the constant c_μ^0, that is the value of the stability function c$_\mu$ in neutral local equilibrium. The use of ε instead of L has the consequence that the stability functions in the k-ε literature (*Rodi* [1980, 1987], *Burchard and Bolding [2000]*) are by the factor of $(c_\mu^0)^3$ smaller than those given here. The dissipation rate ε has the advantage that it can be directly measured with the so-called microstructure shear probes, which offers a way of assess the skill of turbulence models (*Simpson et al. [1996], Burchard et al. [1999]*)

2.3.b Turbulent kinetic energy

2.3.b.1 Transport equation

Most of the models used in the literature are based in a transport equation for TKE. As we have already mentioned, a transport equation for k can be obtained as the trace of the equation 2.5. After estimating the unknown correlations in that equation (for a detailed derivation, see

Rodi [1980]),

$$\partial_t k + u\partial_x k + v\partial_y k + w\partial_z k + \partial_z F(k) = P + B - \varepsilon \tag{2.26}$$

The rate of change of TKE is determined from the balance of various terms: advective transport by the mean motion (left-hand side), the diffusive transport (first term on the right-hand side, horizontal diffusive transport is neglected), the shear production term P, the buoyancy production/dissipation term B and the viscous dissipation rate of TKE ε.

Horizontal advection (and diffusion) of turbulence can usually be neglected. An argument supporting this is that turbulent time scales are usually smaller that those of the mean flow that is modeled as driving horizontal advection and diffusion. These terms should only be important near sharp fronts.

The first term on the right-hand side characterizes the diffusive transport due to velocity and pressure fluctuations. Horizontal diffusion can be neglected with similar arguments as in last paragraph and has been not written. The vertical diffusion of turbulence is classically parameterized with an eddy diffusivity principle:

$$F(k) = -\nu_k \partial_z k \tag{2.27}$$

where ν_k represents the diffusivity of turbulence. This term results from the parameterization of the pressure-strain correlations and of the triple correlation terms in the Reynolds stresses equation (Eq. 2.5). As the unknown turbulent fluctuations are modeled in a different way in Mellor-Yamada and $k - \varepsilon$ model, the eddy diffusivity that characterizes diffusive transport in (2.26) is calculated as $\nu_k = \nu_t$ for the k-ε model and as $\nu_k = S_q\sqrt{k}L$ for the Mellor-Yamada-model, with S_q calibrated as $S_q = 0.2$. Some non-local parameterizations for $F(k)$ have been suggested in the literature (*Canuto et al. [1994], D'Alessio et al. [1998])* to account for non-local or countergradient effects on these fluxes in convective regimes.

The shear production represents the transfer of kinetic energy from mean to turbulent motion and is written as:

$$P = \nu_t S^2 \tag{2.28}$$

where the shear frequency S^2 is defined in (2.12)

The buoyancy production represents an exchange between turbulent kinetic energy and potential energy. In stable stratification, turbulence is reduced, with the result that k is damped and its energy transformed in potential energy. In unstable stratification, TKE is produced at the expense of potential energy. Consequently, B can be a source or sink term, and it is written as:

$$B = -\nu_t' N^2 \tag{2.29}$$

with the Brunt-Väisälä frequency N^2 defined by (2.11), that is positive for stable stratification and negative for unstable.

The dissipation term ε represents the rate of viscous dissipation of turbulent kinetic energy into thermal energy and is always a sink term.

2.3.b.2 Boundary conditions

The boundary conditions used in this study are based in the assumption that at the boundary production of turbulence equals dissipation $P = \varepsilon$, i.e. no buoyancy fluxes nor diffusive transport are considered. Dirichlet and non-flux boundary conditions are easily derived from this assumption. If we define a bottom friction velocity u_*^b from the mean flow shear at the bottom:

$$u_*^b = (\nu_t S)^{1/2}|_{bottom} \tag{2.30}$$

and combine it with the relation of Prandtl and Kolmogorov (2.17) and the definition of ε (2.25), a Dirichlet boundary condition for k at the bottom reads:

$$k = \left(\frac{u_*^b}{c_\mu^0}\right)^2, z = -H. \tag{2.31}$$

The analogue surface boundary condition reads

$$k = \left(\frac{u_*^s}{c_\mu^0}\right)^2, z = \zeta, \tag{2.32}$$

with the surface friction velocity $u_*^s = ((\tau_x^s/\rho_0)^2 + (\tau_y^s/\rho_0)^2)^{1/4}$.

The relation $P = \varepsilon$ both at surface and bottom is equivalent to the assumption that diffusive fluxes are null there, which leads to no-flux conditions for bottom:

$$\nu_k \partial_z k = 0, z = -H \tag{2.33}$$

and surface:

$$\nu_k \partial_z k = 0, z = \zeta. \tag{2.34}$$

Generally, the Dirichlet conditions are used with the Mellor-Yamada, and the flux conditions with the k-ε model. *Craig and Banner [1994]* have claimed that the assumption $P = \varepsilon$ in the surface is not valid under breaking waves, and that instead a balance between dissipation and diffusive transport of TKE should stand. This leads to an injection of TKE at the surface written as a flux condition where TKE is proportional to the cube of the surface friction velocity u_*^s :

$$\nu_k \partial_z k = \alpha_w \left|u_*^s\right|^3, z = \zeta \tag{2.35}$$

α_w is the wave energy factor, that is assumed to be constant and equal to 100 for a wide range of wave state conditions. They used this condition in a 1 equation model with a linear increasing profile of mixing length with depth and reported a good fit to observed dissipation rates in the presence of breaking waves. However, up to now, nobody has used this condition in a two-equation model, and their boundary condition for L or ε does not perform well if imposed in a direct way in a transport equation for L or ε (reported by Hans Burchard in *Burchard et al. [1999]*). However, it must be noted that wave breaking enhances turbulence only near the surface, but does not induce a deepening of the mixed layer (see *D'Alessio et al. [1998]*).

2.3.b.3 Algebraic equation

If vertical diffusion in (2.26) is neglected, in steady state conditions, shear and production terms are in balance (local equilibrium assumption) giving:

$$P + B = \varepsilon \tag{2.36}$$

From this expression and knowing L, k can be calculated. Imposing a lower limit to guarantee positiveness, we arrive to:

$$k = \max\left\{\frac{L^2}{(c_\mu^0)^3}(c_\mu S^2 - c'_\mu N^2), k_{\min}\right\} \tag{2.37}$$

This method was proposed originally by *Mellor and Yamada [1974, 1982].* It has been tested on some applications and it has been found that its performance depends on vertical grid spacing and that a noisy pattern appears for small space or large time steps. *Frey [1991]* and *Luyten, et al. [1996]* have shown that the noise disappears by choosing Δz sufficiently large or Δt sufficiently small. A stability condition similar to the obtained for explicit discretization of vertical diffusivity stands (*Davies et al. [1995]*):

$$\frac{\Delta t}{\Delta z^2}\nu \leq \alpha \tag{2.38}$$

with $\alpha = 0.4 - 2$, depending on the stability functions used.

2.3.c Turbulent length scale

Essentially the specification of turbulent length scale is based in empirical considerations. One of them is that its profile decreases linearly near walls:

$$L = \kappa(z + z_0) \tag{2.39}$$

with the von Kármán constant $\kappa = 0.4$, the distance from the boundary, z, and the roughness length of the boundary, z_0. All length scale parameterizations described here will follow that law near fixed boundaries, most of them as well near the surface.

Two different approaches for the determination of the turbulent macro-scale can be distinguished: the first involves a transport equation for the dissipation rate of TKE (ε) or for the product of TKE and the length scale (kL) and the other requires no transport equation and the turbulent macro length scale is directly estimated from algebraic formulae or diagnosed from local characteristics or the flow.

2.3.c.1 Transport equations

The most popular transport equations for the turbulent length scale are the kL equation in the Mellor-Yamada model and the dissipation rate or epsilon equation in the $k - \varepsilon$ model. While a transport equation for TKE can be obtained from scaling arguments, the transport equation for the length scale or equivalently, the dissipation rate, is derived from heuristic arguments. Therefore, the controversy about the physical consistence of these equations (*Mellor and Yamada [1982]*, *Rodi [1980]*) is rather academic, since "both equations are fairly empirical and, with the constants suitable adjusted, perform in a similar manner (*Rodi [1987]*)". From the point of view of performance, *Burchard and Petersen [1999]* have compared both Mellor-Yamada and $k - \varepsilon$ models and have shown that they perform equivalently in some ideal and real cases. *Baumert and Peters [2000]* present a detailed illustration of their structural equivalence in homogenous shear layers.

Epsilon equation The ε-equation without advective transport terms reads:

$$\partial_t \varepsilon - \partial_z(\nu_\varepsilon \partial_z \varepsilon) = \frac{\varepsilon}{k}\left(c_{\varepsilon 1} P + c_{\varepsilon 3} B - c_{\varepsilon 2} \varepsilon\right). \tag{2.40}$$

By means of equation (2.25), the macro length scale L can now be calculated. All terms in this equation are based in empirical assumptions and therefore all contain empirical parameters, but the structure of the equation is similar to the k-equation: the rate of change of ε is a balance of diffusive transport, shear production terms, buoyancy production/destruction and viscous dissipation, although the contributions of the different terms are calibrated with empirical constants.

The eddy diffusivity for ε in equation (2.40) is modeled as:

$$\nu_\varepsilon = \frac{\nu_t}{\sigma_\varepsilon} \tag{2.41}$$

with the Prandtl number for dissipation rate calibrated as $\sigma_\varepsilon = 1.08$ (*Burchard et al.* [1998]).

For non-buoyant situations, the parameters $c_{\varepsilon 1}$, $c_{\varepsilon 2}$, the values can be calibrated. The values $c_{\varepsilon 1} = 1.44$ and $c_{\varepsilon 2} = 1.92$ are widely accepted (*Rodi* [1980]). The standard literature on k-ε models has chosen a positive value for $c_{\varepsilon 3}$ in the ε-equation.(*Rodi* [1987]): a value of 1 for unstable stratified flows, where B is a source term, and a near zero value ($c_{\varepsilon 3} = 0 - 0.2$) for stable stratification, where B is a sink term. However, in stably stratified conditions this standard value fails to predict a length scale. Rodi in 1987 wrote "*it is not clear at present how, with the standard choice of $c_{\varepsilon 3}$, the ε equation performs in situations with collapsing turbulence and what length scales it produces*" (*Rodi [1987]*). *Burchard [1995]*, *Burchard and Baumert* [1995] and *Burchard et al.* [1998] have shown the necessity of a negative value for $c_{\varepsilon 3}$ in stable stratification. The actual value (a typical value would be $c_{\varepsilon 3} = -0.4$) is sensitive to the stability function chosen as shown by *Burchard and Bolding [2000]*. The choice of $c_{\varepsilon 3}$ has a similar effect to the imposition of a lower limit for ε in the transport equation (see section 2.3.c.3), which is necessary for providing a source for dissipation in the case of stable stratification. Therefore, for stable stratification, the value of $c_{\varepsilon 3}$ will be taken from the estimations of *Burchard and Bolding [2000]* for different sets of stability functions, while the classical value $c_{\varepsilon 3} = 1.0$ will be used for unstable stratification to provide for a source of ε in free convection situations ($P = 0, B > 0$).

From the definition of dissipation (2.25) and the near wall profile (2.39), a Dirichlet boundary condition for ε at the boundary can be derived:

$$\varepsilon = \left(c_\mu^0\right)^3 \frac{k^{3/2}}{\kappa(\tilde{z} + z_0)}. \tag{2.42}$$

that depends on the obtained boundary value of k.

By differentiating (2.42) with respect to $\tilde{z}$ and considering $P = \varepsilon$, the non-flux conditions (2.33) and (2.33) for k stand, and an equivalent flux boundary condition for ε

can be obtained:

$$\frac{\nu_t}{\sigma_\varepsilon}\partial_{\tilde{z}}\varepsilon = -\left(c_\mu^0\right)^3 \frac{\nu_t}{\sigma_\varepsilon}\frac{k^{3/2}}{\kappa(\tilde{z}+z_0)^2} \tag{2.43}$$

where $\tilde{z}$ is again the distance from bottom or surface, respectively.

Burchard and Petersen [1999] showed that the performance of the flux condition was better than the Dirichlet, especially for coarse resolution. Numerical problems caused by high gradients near the boundaries are responsible for this bad performance (see *Stelling* [1995] and *Burchard and Petersen* [1999]). Therefore, the flux condition will be used in the simulations.

The kL equation The kL-equation (also without advective terms) in the notation of *Burchard et al. [1999]* reads as:

$$\partial_t(kL) - \partial_z\left(\nu_L \partial_z(kL)\right) = L\left(c_{L1}P + c_{L3}B - \left(1 + E_2\left(\frac{L}{L_z}\right)^2\right)\varepsilon\right). \tag{2.44}$$

The empirical parameters proposed by *Mellor and Yamada [1982]* are $c_{L1} = c_{L3} = 0.9$ and $E_2 = 1.33$. In Mellor and Yamada notation $E_1 = 2c_{L1}$ and $E_3 = 2c_{L3}$ and $B_1 = \sqrt{2} \cdot (c_\mu^0)^{-3}$. The parameters c_{L1} and E_2 were estimated by experiments in neutral conditions. The parameter in the buoyancy term c_{L3} was set by them equal to c_{L1}, since no data were available for specifying it. This value has been subject to great controversy (see section 2.3.c.3).

Similar to eddy diffusivity for TKE, the eddy diffusivity for kL is obtained from an eddy viscosity principle as $\nu_L = c_L\sqrt{k}L$, with c_L estimated by *Mellor and Yamada [1982]* from experiments in neutral conditions. as $S_q = S_l = c_k/\sqrt{2} = c_L/\sqrt{2} = 0.2$

The barotropic length scale L_z has to be prescribed in order to guarantee that L has a linear profile near boundaries. Note that this law was automatically fulfilled by the epsilon equation (2.40). As this function is only required to predict a near wall linear behavior, simple functions can do a good job. Some possible simple profiles have been tested by *Burchard et* *al.* [1998] and showed a good performance, a parabola shaped one:

$$L_z = \kappa \frac{(d_s + z_0^s) \cdot (d_b + z_0^b)}{(d_s + z_0^s) + (d_b + z_0^b)}, \tag{2.45}$$

and a triangle shaped one:

$$L_z = \kappa \quad \min \quad \{d_b + z_0^b, d_s + z_0^s\}. \tag{2.46}$$

Here, d_s and d_b are the distance from the surface and from the bottom and z_0^s and z_0^b are the surface and bottom roughness lengths.

As boundary values for L, the near wall condition (2.39) is used:

$$L = \kappa(d_b + z_0^b), z = -H. \tag{2.47}$$

$$L = \kappa(d_s + z_0^s), z = \zeta, \tag{2.48}$$

where d_s and d_b the distance from bottom and surface, respectively.

Actually, a Dirichlet boundary condition for kL is imposed, that is derived from Eqs. (2.47) and (2.48) and the boundary value of k.

2.3.c.2 Algebraic forms

Instead of solving a transport equation, the vertical profile of L can be calculated from a diagnostic expression. It can be a simple geometric form or a more complicated form. Simple, algebraic expressions have been used both in 1 equation and in 0 equation models, especially in shallow seas, where turbulence is dominated by wind and tide and two mixing layers appear.

Two simple expressions that satisfy the linear profile in the presence of surface and bottom boundaries are the parabolic

$$L = \kappa \frac{(d_b + z_0^b)(d_s + z_0^s)}{(d_b + z_0^b) + (d_s + z_0^s)} \tag{2.49}$$

and the triangle profile

$$L = \kappa \min(d_b + z_0^b, d_s + z_0^s) \tag{2.50}$$

where d_b and d_s are the distances to bottom and surface, respectively and z_0^b and z_0^s the roughness length of bottom and surface boundaries. Other expressions take into account that the position of the maximum in mixing length may not lay in the middle of the water column, as observed to occur in tidal flows. This anisotropy in the profile is obtained by changing the functional form of surface or bottom mixing length, as has been used by *Leendertsee and Liu [1978]* or *Robert and Ouellet* [1987], (note that this function is a distorted parabola):

$$L = \kappa(d_b + z_0^b)\left(1 - \frac{d_b}{D}\right)^{\frac{1}{2}} \tag{2.51}$$

or *Xing and Davies* [1995], that express L in function of simple, algebraic expressions for bottom L_b and for surface L_s mixing length:

$$L = \frac{1}{\frac{1}{L_b} + \frac{1}{L_s}} \tag{2.52}$$

where L_b and L_a are given by the expressions:

$$\begin{aligned} L_b &= \kappa(d_b + z_0^b)e^{-\beta d_b/D} \\ L_{s=}&\kappa(d_s + z_0^s) \end{aligned} \tag{2.53}$$

β is a tuning parameter that tunes the matching of surface and bottom layers, i.e. the position and magnitude of the maximum of L.

In order to take into account free surface effects like breaking waves, some expression were proposed that do not fulfill the logarithmic law of the wall near the surface. Usually a free parameter that allows tuning the profile at the surface is introduced. As an example, we will quote the formula proposed by Nihoul [1982]:

$$L = \kappa(d_b + z_0^b)\left(1 - \delta\frac{d_b}{D}\right) \tag{2.54}$$

where δ is the free parameter that would depend on wave state. For $\delta = 1$, this formula is a parabola, with $L = 0$ at the surface, and for $\delta = 0$, it is a line.

In figure 2.6, these expressions for the profile of the mixing length are plotted as a function of the normalized depth (z/D). Note that the parabola and the triangle profile have a maximum at mid-depth, equidistant to surface and depth boundaries, while Leendertsee and Liu show a maximum closer to the surface, which is useful for tidal dominated flows. The free parameter β in Xing and Davies function allows choosing the position of the transition between the two boundary layers and also the magnitude of the mixing length. It can be used in different conditions after empirically tuning β, but the occurrence of different conditions in a same location or in different points of the same domain restricts the applicability of the parameterization. The Nihoul function for $\delta = 0.5$ illustrates how a non-zero value of mixing length can be imposed at the surface for accounting wave effects.

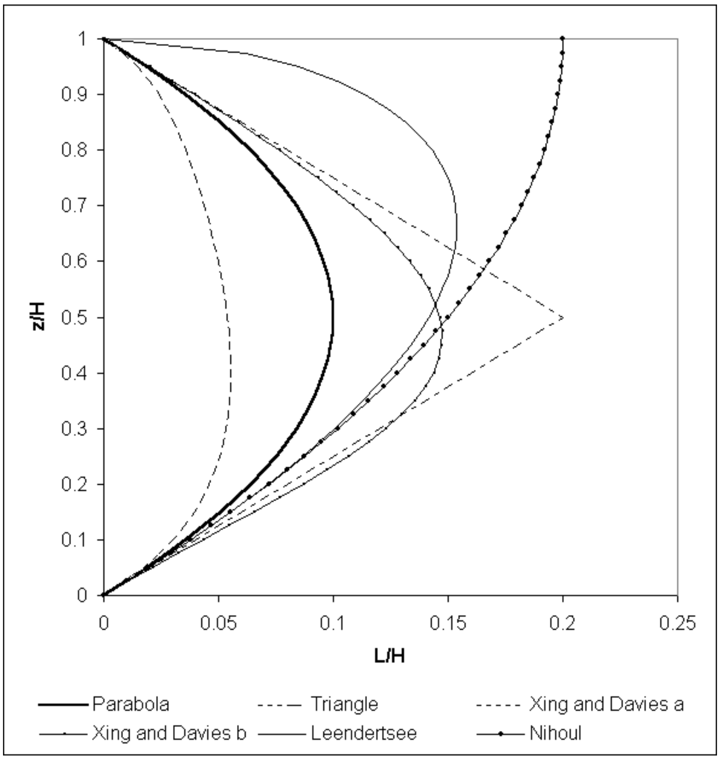

Figure 2.6 : Normalized mixing length as a function of the normalized depth, for several diagnostic profiles that consider the existence of a surface and a boundary layer. Xing and Davies a was plotted for $\beta = -2$ and b for $\beta = 2$. The Nihoul profile was obtained for $\delta = 0.5$.

These expressions only work fine near boundary layers and in well mixed conditions. For the interior region, some formulas have been proposed, as the widely used form of *Blackadar* [1962], that suggests that the turbulent mixing length should depend on local characteristics of the turbulent flow like TKE:

$$l = \frac{\kappa z}{1 + \kappa z / l_0} \tag{2.55}$$

with l_0 given by the expression:

$$l_0 = \gamma_0 \frac{\int_0^D k^{1/2} \tilde{z} d\tilde{z}}{\int_0^D k^{1/2} d\tilde{z}} \tag{2.56}$$

where γ_0 is a constant in the range 0.1 to 0.4. In the presence of two boundaries, the Blackadar mixing length can be written in a form that automatically gives a linear profile of l near walls:

$$l = \kappa \frac{1}{\frac{1}{d_b + z_0^b} + \frac{1}{d_s + z_0^s} + \frac{1}{l_0}} \tag{2.57}$$

For stratified flow, the mixing length is also affected by stratification. A way of including stratification in the algebraic expressions for the mixing length is multiplying it by a stratification correction factor,

$$l = l_0(z) F_s(z) \tag{2.58}$$

Some proposed forms for this factor are based on measurements of the atmospheric boundary layer *Geernaert* [1990]:

$$\begin{aligned} F_s &= 1 - \alpha R_i, \quad \text{for } R_i > 0 \\ F_s &= (1 - \beta R_i)\gamma, \text{ else} \end{aligned} \tag{2.59}$$

with $R_i = N^2/S^2$, the gradient Richardson number, $\alpha = 5 - 10$, $\beta = 15$, and $\gamma = 0.25$. The expression for unstable stratification is known as the KEYPS formula *Panofsky*, [1963] This parameterization of F_s is plotted in figure 2.7. The limiting effect of stable stratification on L is taken into account by $F_s < 1$, while $F_s > 1$ for unstable stratification, as the length scale would grow in these conditions. The value of α can tune the critical R$_i$ number, although for $R_i = 0.25$, α should be 3, and the typical values in the literature plotted in the picture predict a smaller value.

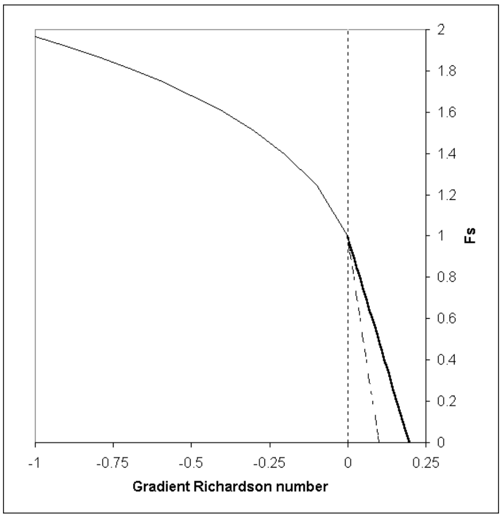

Figure 2.7 : Modification factor for the length scale in the presence of stratification as a function of the Richardson number. The expression for stable stratification is taken from Geernaert [1990], and the factor for unstable stratification is the classical KEYPS formula (Panofsky [1963]). The stable stratification factor is plotted for two values of the empirical parameter α.

Another proposed function for this factor, that also depends on the gradient Richardson number is an exponential function (*Nihoul, [1984]*):

$$F_s = e^{-\alpha R_i}, \ \alpha \approx 0.8 \tag{2.60}$$

An alternative approach has been suggested by *Nihoul and Djenidi* [1987]:

$$F_s = 1 - R_f \tag{2.61}$$

with R_f, the flux Richardson number, that is given as the ratio of the buoyant production term B in the TKE equation to the shear production term P:

$$R_f = \frac{-B}{P} = \frac{c'_\mu N^2}{c_\mu S^2} = \frac{c'_\mu}{c_\mu} R_i \tag{2.62}$$

Similar to the gradient and bulk Richardson number, R_f is negative for unstable stratification, zero for neutral flow and positive for stable stratification. Richardson proposed that $R_f = 1$ is a critical value, because the shear production is balanced by the buoyant consumption of

TKE. If R_f is smaller than 1, stratification is not able to prevent the mechanical generation of turbulence, while for negative values of R_f, the numerator even contributes to the generation of turbulence. So, Richardson expected a turbulent flow for $R_f < 1$, and that the flow becomes laminar for $R_f > 1$. Therefore, the functional form of F_s (Eq. 2.61) versus R_f is similar to that of $F_s(R_i)$ (Eq. 2.59) shown in figure 2.6.

Stability functions-introduced in next subsection (2.3.d)- have a similar effect as this correction factor: they increase mixing for unstable stratification and decrease it for stable stratification. This makes difficult to calibrate a model that uses a stratification-depending functional form of both. Moreover, a calibration of the model with a given mixing length corrected by a stratification factor may no longer be valid if stability functions are changed.

Complex forms A more complex diagnostic mixing length is the one proposed for the atmospheric boundary layer by *Therry and Lacarrère* [1983] and *Bougeault and Lacarrère [1989]* and tested for the ocean by *Gaspar et al. [1990]* and *Blanke and Delecluse* [1993]. Two characteristic lengths one for dissipation L_ε and another for mixing L_k are defined as combinations of two master length scales L_u and L_d obtained in each point as the upward or downward distance that a fluid particle placed at that point must travel to convert TKE in potential energy

$$\begin{array}{l} \int_{z_0}^{z_0+l_u(z_0)}[b(z_0)-b(z)]dz = k(z_0) \\ \int_{z_0-l_d(z_0)}^{z_0}[b(z)-b(z_0)]dz = k(z_0) \end{array} \tag{2.63}$$

L_k and L_ε are then calculated as

$$\begin{array}{l} L_k(z_0) = min[L_d(z_0), L_u(z_0)] \\ L_\varepsilon(z_0) = [L_d(z_0)L_u(z_0)]^{1/2} \end{array} \tag{2.64}$$

The expressions for L_k and L_ε are designed so that they take into account the fact that a strongly stratified region affects diffusion as a wall does, while dissipative phenomena, even near a wall, are affected by the maximum vertical scale of convective motions. Gaspar has lately suggested that L_k should also be calculated as the square root of L_u and L_d. In stably stratified regions with a constant density gradient, a predicted length scale is:

$$L = \frac{\sqrt{2k}}{N} \tag{2.65}$$

In this model, the dissipation rate is calculated by means of the Kolmogoroff expression (see 2.25), where the turbulent macro length scale L is set to L_ε and a different proportionality factor $c_\varepsilon = 0.7$, (tuned by *Gaspar et al.* [1990] to deal with vertical mixing at any depth), is used:

$$\varepsilon = c_\varepsilon k^{3/2} / L_\varepsilon \tag{2.66}$$

The eddy viscosity/diffusivity are calculated from the expression (2.27) using L_k as the macro length scale and two constant stability functions $c_\mu = 0.1$ (as suggested by *Gaspar et al.* [1990]) and the Prandtl number is set to $P_{rt} = 1$. Regarding to the specifications in the TKE equation, the diffusivity of TKE is chosen as in k-ε model $\nu_k = \nu_t$ and a Dirichlet boundary condition for TKE similar to (2.31) and (2.32) is used. The proportionality constant in the Dirichlet condition however is slightly different: they consider 3.75, while in (2.31) and (2.32), the constant is $(1/c_{\mu 0})^2 \simeq 3.23$.

In the algebraic mixing length parameterization used in the ISPRAMIX ocean circulation model (see *Eifler and Schrimpf [1992]* and *Demirov et al. [1998]*), three different regions are distinguished: the surface and the bottom mixed layers and a stably stratified interior layer. After diagnosing the height of each mixed layer by searching for the first point from the boundary where k<k$_{\mathrm{min}}$=10$^{-5}m^2 s^{-2}$, the macro length scale L in every point of both mixed layers is obtained from a *Blackadar* [1962] type formula:

$$L = \frac{\kappa \tilde{z}}{1 + \frac{\kappa \tilde{z}}{c_2 \cdot h_m}} (1 - R_f)^e \tag{2.67}$$

where $\tilde{z}$ is the distance from the interface (surface or bottom). Equation (2.67) predicts an approximation to a linear behavior of L near boundaries and a value proportional to the thickness of the mixed layer far from the interface, $L = c_2 h_m$, where $c_2 = 0.065$ is estimated from experimental data as discussed in *Eifler and Schrimpf* [1992]. The factor $(1 - R_f)^e$, with the flux Richardson number $R_f = -B/P$, accounts for the effect of stratification on the length scale (see Eq. 2.61). The parameter e is here a tuning parameter (personal communication by Walter Eifler, JRC, Ispra, Italy, as quoted in *Burchard et al. [1999]*) which is usually set to $e = 1$. However, during the simulations of the Kato-Phillips experiment, a higher value was necessary in order to predict the expected mixed layer evolution (see section 2.4.a)

Below the top mixed layer and above the bottom friction layer, a suggestion of *Zilitinkevich and Mironov* [1992] is applied to calculate the length scale L_i in the interface between the thermocline and the mixed layer. This formula parameterizes the penetration of the mixed layer into the

stably stratified thermocline by turbulence diffusion:

$$L_i = c_i k^{1/2}/N \tag{2.68}$$

The constant c_i is determined for every specific case (and for both boundary layers) by making use of the requirement that the length scale in the mixed layer L_m and near the thermocline must match at $z = h_m$. Therefore, we have a matching condition to determine c_i for each boundary layer:

$$c_i = (L_m N/k^{1/2})_{z=h_m} \tag{2.69}$$

In the core region of the thermocline, a constant value of L typical of stratified conditions is imposed, where (2.69) would yield too small values. We use $L = 0.01\ m$. Care has been taken that the model behaves well in every possible situation. Thus, if the two boundary layers overlap, we suppose there is no stably stratified region, only two boundary layers, with L calculated from (2.67). The same is supposed if only one mixed layer is detected. In this way, we guarantee that the length scale satisfies the linear profile near both boundaries.

2.3.c.3 Length scale limitation

Both kL and $k - \varepsilon$ models with the standard choice of parameters do not predict a limiting value of length scale in stable stratification. This inconsistency can be removed as suggested by *Galperin et al.* [1988] with the imposition of an upper limit for the macro length scale L in stably stratified flows. Motivated by laboratory experiments and ocean measurements, they suggest:

$$L^2 \leq \frac{0.56k}{N^2} \qquad \text{for } N^2 > 0. \tag{2.70}$$

Note that this expression is similar to Eq. 2.68. Applied to the ε-equation, this corresponds to a lower limit for the dissipation rate ε, which can be calculated by means of using (2.39) as

$$\varepsilon^2 \geq 0.045k^2N^2 \qquad \text{for } N^2 > 0. \tag{2.71}$$

Recently, *Burchard [1999]* has shown that the failure of MY model in predicting a length scale for stable stratification lies in the choice of the empirical parameters in kL equation (2.44). For calibrating the Mellor-Yamada model he used the concept of homogeneous shear layers. Homogeneous shear layers constitute ideal situations far away from boundaries where shear and stratification are constant. There, diffusion terms in turbulent equations can be neglected and a simple set of ordinary differential equations with only time derivatives appears.

$$\begin{aligned} \partial_t k &= P + B - \varepsilon \\ \partial_t(kL) &= c_{L1}P + c_{L3}B - \varepsilon \end{aligned} \tag{2.72}$$

The steady state ($\partial_t k = 0$ and $\partial_t(kL) = 0$) is characterized by the following conditions:

$$R_i = R_i^{st} = \frac{c_\mu}{c'_\mu}\frac{1 - c_{L1}}{1 - c_{L3}} \tag{2.73}$$

$$\frac{B}{\varepsilon} = \frac{c_{L1} - 1}{c_{L1} - c_{L3}} \tag{2.74}$$

A stationary Richardson number then appears that depends on the parameters c_{L1},c_{L3} and on the set of stability functions chosen. The physical sense of this number is that in homogeneous shear conditions, a perturbation in the system will decay until this stationary value of the Richardson number is reached. The actual value of the stationary Richardson number is not known, and it is difficult to measure or estimate it. LES simulations (*Schumann and Gerz [1995]*) suggest a value of $R_i^{st} \leq 0.25$. *Burchard [1995]* and *Burchard and Bolding [2000]* have used a shear-entrainment experiment (the Kato-Phillips experiment) with ocean dimensions (section 2.4.a) for obtaining an estimation of R_i^{st} and subsequently calibrate the parameters in the equation for different stability functions. They propose a value of $R_i^{st} = 0.25,$ .that provides the best fit of results to the theoretical expression by *Price* [1979] for the evolution of the mixed layer. There are experimental evidences in approximate homogeneous shear layers in salt-stratified water by *Rohr et al. [1988]* that provide an estimation of $R_i^{st} = 0.16 \pm 0.06$. There is a discrepancy in this value, that can be related to the downgradient parameterization of TKE flux, that may induce the necessity of a higher value of the Richardson number to reproduce mixed layer dynamics. Although the exact value of R$_i^{st}$ is not known, it is striking that the value $c_{L3} = c_{L1} = 0.9,$ chosen by Mellor and Yamada (in their notation $E_1 = E_3 = 1.8$) does not predict a steady-state, as seen in the second condition for steady-state (*Burchard[1999]*).

For the $k - \varepsilon$ model (from *Burchard, [1995]* and *Burchard and Bolding [2000]*), the equations in homogeneous shear layers are written as:

$$\begin{aligned} \partial_t k &= P + B - \varepsilon \\ \partial_t \varepsilon &= \frac{\varepsilon}{k}(c_{\varepsilon 1} P + c_{\varepsilon 3} B - c_{\varepsilon 2} \varepsilon) \end{aligned} \tag{2.75}$$

Setting $\partial_t k$ and $\partial_t \varepsilon$ equal to zero, we have a condition for equilibrium or steady-state condition:

$$R_i = R_i^{st} = \frac{c_\mu}{c_\mu^{'}} \cdot \frac{c_{\varepsilon 2} - c_{\varepsilon 1}}{c_{\varepsilon 2} - c_{\varepsilon 3}} \tag{2.76}$$

Estimating R_i^{st} allows us to calibrate the value of $c_{\varepsilon 3}$ for every set of stability functions. With the classical value of $c_{\varepsilon 3}$=1.4 in the k-ε literature, no stationary state is predicted for different sets of stability functions, as can be seen in figure 8 of *Burchard and Bolding [2000].*

2.3.d Stability functions

Once the turbulent length scale L and the turbulent kinetic energy k

have been computed, eddy viscosities and diffusivities are obtained with the expression:

$$\nu_t = c_\mu \sqrt{k} L; \quad \nu_t' = c_\mu' \sqrt{k} L, \tag{2.77}$$

where c_μ and c_μ' are dimensionless proportionality factors known as stability functions. They include effects that have not been included in the computation of k and L. For example, often they have the function of increasing mixing for instable and decreasing it for stable stratification. In the literature many different sets of stability functions, we will distinguish between simple stability functions and stability functions based on second-moment closures.

2.3.d.1 Simple stability functions

The simplest set of stability function considers c_μ and c_μ' as constants. No dependence on stratification is considered on them. The stability function for tracers is related to that for momentum via the Prandtl number P_r:

$$c_\mu' = \frac{c_\mu}{P_r} \tag{2.78}$$

Another simple set of stability functions can be derived from the Prandtl number derived from the eddy coefficient formulation by *Munk and Anderson* [1984] (Eq. 2.9):

$$\begin{aligned} P_r = P_{r0} \frac{(1+10R_i)^{1/2}}{(1+3.33R_i)^{3/2}}, \quad R_i \geq 0, \\ P_r = P_{r0}, \quad R_i < 0 \end{aligned} \tag{2.79}$$

where R_i is the gradient Richardson number.

Other type of stability functions depend on the flux Richardson number, as the parameterization of the Prandtl number by *Schumann and Gerz [1995]* :

$$c_\mu = c_\mu^0, \qquad c_\mu' = \frac{c_\mu^0}{P_r} \tag{2.80}$$

with constant c_μ^0 and the Prandtl number P_r given by:

$$P_r = P_{r0} \exp\left(-\frac{R_i}{P_{r0} R_f^\infty}\right) + \frac{R_i}{R_f^\infty} \tag{2.81}$$

with the neutral Prandtl number $P_{r0} = 0.74$ and $R_f^\infty = 0.25$.

The stability functions in the ISPRAMIX model are of the form:

$$c_\mu = constant = 0.5 \tag{2.82}$$

$$c'_\mu = c_\mu f(R_f) = \frac{1}{P_r^0}(1 - R_f)^{1/2} \tag{2.83}$$

The Prandtl number P_r they use is 1/1.4. The function $f(R_f)$ is assumed to lay between the values 0.18 (correspondent to a supercritically stratified situation) and 2 (to prevent it from growing too much in unstable conditions).

A formula that relates $(1 - R_f)$ to the gradient Richardson number R$_i$ can be derived from the definition of the flux Richardson number:

$$R_f = \frac{c'_\mu}{c_\mu} R_i \tag{2.84}$$

after some algebra detailed in *Beckers [1995]* :

$$(1 - R_f) = [(\tilde{R}_i^2 + 1)^{1/2} - \tilde{R}_i]^2 \tag{2.85}$$

with:

$$\tilde{R}_i = \frac{0.5}{P_r} R_i \tag{2.86}$$

2.3.d.2 Stability functions based on second-moment closures

The process for obtaining stability functions from the Reynolds stress equations basically consists in neglecting some terms in the equations to arrive to an algebraic equation, that provides a complex, non-dimensional function of the shear number α_S and the buoyancy number α_N:

$$\alpha_S = \frac{L^2}{k} S^2 \tag{2.87}$$

$$\alpha_N = \frac{L^2}{k} N^2 \tag{2.88}$$

Note that these stability functions contain information about correlation terms that do not influence the obtained distribution of TKE and L, so they introduce more information in eddy coefficients only by solving an algebraic equation. This makes stability functions a key point in the performance of a turbulence model. A detailed discussion on the derivation of stability functions and their role in second-order turbulence closures can be found in *Burchard and Bolding [2000].*

Mellor and Yamada [1974] *Mellor and Yamada [1974]* closed the system by ordering terms from their degree of separation from isotropy and they arrived to the system:

$$2.0424\alpha_S \quad c_\mu + (1 + 15.2958\alpha_N) \quad c'_\mu = 1.0465 \tag{2.89}$$

$$(1 + 2.5392\alpha_S + 3.0636\alpha_N) \quad c_\mu + 8.1142\alpha_N \quad c'_\mu = 0.9888 \tag{2.90}$$

with the following constraints to assure positiveness of c_μ and c'_μ:

$$\alpha_N \geq -0.064$$

$$\alpha_S \leq 1.65 + 25\alpha_N$$

The resulting stability functions are noise-prone, mainly due to these constraints, as noted for example in *Deleersnijder and Luyten [1996].* In spite of this numerical stability draw-back, these functions have been used in many applications, for example, they are the stability functions in the widely used POM (Princeton Ocean Model). A smoothing filter is applied every few iterations to get smooth eddy coefficients.

Galperin et al. [1988] *Galperin et al.* [1988] proposed a set of stability functions based in the *Mellor and Yamada [1982]* set, that showed a robust numerical behavior, with no noise in the resulting solution. If local equilibrium P+B=ε is assumed, a relation between α_N and α_S appears:

$$c_\mu \alpha_N - c'_\mu \alpha_S = (c^0_\mu)^3 \tag{2.91}$$

where c^0_μ is the value of the stability function in neutral local equilibrium conditions, i.e. $B = 0$ and $P = \varepsilon$. Substituting this in Eq. 2.88 and 2.89, a set of stability functions that depend only on the buoyancy number is obtained:

$$c_\mu = \frac{c^0_\mu + 2.182\alpha_N}{1 + 20.40\alpha_N + 53.12\alpha_N^2} \tag{2.92}$$

$$c'_\mu = \frac{0.6985}{1 + 17.34\alpha_N}, \tag{2.93}$$

These stability functions depend only on the buoyancy number and are derived from prognostic equations for Reynolds stresses and heat fluxes under the assumption of a local equilibrium of turbulence in only these equations, therefore they are known as quasiequilibrium stability functions.

This stability functions are only positive for $\alpha_N > \alpha_{\min} = -0.0466$. In the case of convection, much smaller values of α_N may occur. In order to guarantee a smooth transition into this convective regime, α_N is limited by (*Burchard and Petersen, [1999])*

$$\alpha_N = \max\{\alpha_N, \alpha_N - (\alpha_N - \alpha_c)^2/(\alpha_N + \alpha_{\min} - 2\alpha_c)\}. \tag{2.94}$$

In the free convection simulation discussed below, it was sufficient to use $\alpha_c = -0.02$. An upper limit for α_N is given by $\alpha_{\max} = 0.56$.

Kantha and Clayson [1994] *Kantha and Clayson [1994]* suggested an improvement of the *Mellor and Yamada [1994]* stability functions by estimating some correlators from LES results. After algebraizing taking into account the new pressure correlations, a complete set of stability functions similar to those by *Mellor and Yamada [1982]* is obtained. If local equilibrium is assumed, the quasi-equilibrium version is obtained. *Kantha and Clayson [1994]* only showed the quasiequilibrium version, the full version is written down in *Burchard and Bolding [2000]*. The stability functions in the quasiequilibrium form read:

$$\begin{aligned} c_\mu &= \frac{1}{(c_\mu^0)^3} \cdot \frac{0.1682 + 0.03269\alpha_N}{1 + 0.4679\alpha_N + 0.07372\alpha_S + 0.01761\alpha_S\alpha_N + 0.03371\alpha_N^2} \\ c_\mu' &= \frac{1}{(c_\mu^0)^3} \cdot \frac{0.1783 + 0.01586\alpha_N + 0.003173\alpha_S}{1 + 0.4679\alpha_N + 0.07372\alpha_S + 0.01761\alpha_S\alpha_N + 0.03371\alpha_N^2} \end{aligned} \tag{2.95}$$

with $c_\mu^0 = 0.094$.

Canuto et al. [2000] Recently, *Canuto et al. [2000],* after reviewing the closure of pressure-strain correlations making use of the latest available results, have arrived to a new second-moment closure that, as shown by *Burchard and Bolding [2000],* is equivalent to proposing a new set of stability functions. The stability functions resulting from the *Canuto et al. [2000]* closure are as follows (from *Burchard and Bolding [2000]*):

$$\begin{aligned} c_\mu = &\ \frac{1}{(c_\mu^0)^3} \cdot [(0.1070 + 0.01741\alpha_N - 0.00012\alpha_S)/ \\ &(1 + 0.2555\alpha_N + 0.02872\alpha_S + 0.008677\alpha_N^2 + 0.005222\alpha_N\alpha_S - 0.0000337\alpha_S^2)] \end{aligned} \tag{2.96}$$

$$\begin{aligned} c_\mu' = &\ \frac{1}{(c_\mu^0)^3} \cdot [(0.1120 + 0.004519\alpha_N + 0.00088\alpha_S)/ \\ &(1 + 0.2555\alpha_N + 0.02872\alpha_S + 0.008677\alpha_S^2 + 0.005222\alpha_S\alpha_N - 0.0000337\alpha_S^2)] \end{aligned} \tag{2.97}$$

with $c_\mu^0 = 0.077$. These stability functions depend on α_S and α_N and the functional form is similar to the *Kantha and Clayson [1994]* set.

2.3.e Internal mixing and internal waves

A major weakness of local turbulence models is that they do not take into account the increasing effect of mixing of shear instability and internal wave activity in the presence of stable stratification. Some simple methods have been suggested to solve these shortcomings. As we noted in the introduction, turbulence in stratified fluids is a highly intermittent and poorly understood process. These simple models do not intend to model the physics of turbulence in the presence of stratification, but they intend to parameterize the mean effect of these processes on mixing.

2.3.e.1 Limitation of turbulent magnitudes

Galperin et al. [1989], as commented in section 2.3.c.3, argued the necessity of a limiting condition on the mixing length in order to take into account the effect of stable stratification on mixing (Eq. 2.70 and 2.71). This could be seen as a crude but simple way to incorporate internal wave effects into the model. *Luyten et al. [1996b]* found it necessary to impose a limitation on TKE, as the limiting condition on L made no significant change on their results. A similar remark was made by *Gaspar et al. [1990]*. Based in oceanic observations by *Gregg [1987]*, that show that $\varepsilon_{\mathrm{min}} \sim N^{\alpha-1}$ they propose a constant minimum value of TKE, by assuming $\alpha = 1$ for simplicity. This limitation of TKE improved the model results in the stratified layer. The value of $\mathrm{k}_{\mathrm{min}}$ is an empirical parameter, that they tuned to a value of $\mathrm{k}_{\mathrm{min}} = 10^{-6}$ $\mathrm{m}^2\mathrm{s}^{-2}$ by comparing model predictions with experimental dissipation rate data taken at the Irish Sea. *Burchard et al. [1998]* suggest a value of $\mathrm{k}_{\mathrm{min}} = 7.6 \cdot 10^{-6}$ $\mathrm{m}^2\mathrm{s}^{-2}$ for the same set of data.

As we discussed in section 2.3.c.3, the failure of the MY and $k-\varepsilon$ models in predicting a limiting value of L and ε in stable stratification can be solved by tuning the parameters in the equation making use of the homogenous shear layer concept. For the classical parameters, no limiting length scale was predicted and therefore the limitation is only a patch to compensate for the lack of a length scale in stable stratification. It is easily understood now with this view, why a limitation of TKE was also needed by *Luyten et al. [1996b]* to predict realistic values of turbulence at the pycnocline, since length limitation only predicts a limiting value of the length scale, and carries no information about internal wave activity.

2.3.e.2 Internal wave shear

Mellor [1989] suggested to introduce internal wave effect directly in turbulent equations instead of imposing a limiting condition. The basic idea of the model is that internal waves induce an additional shear that increases the mean flow shear. As internal wave energy is known to depend on N^2, internal wave shear is modeled as a term αN^2, that is added to the shear production terms (2.28) in both turbulent transport equations. The production term for stable stratification ($N^2>0$) is:

$$P = \nu_t(S^2 + \alpha N^2) \tag{2.98}$$

where α is a free parameter, that Mellor tuned to a value of 0.7 after estimating the internal wave contribution to shear as the difference between the observed shear profiles and those modeled without internal wave parameterization. The performance of the model was evaluated by testing sea surface temperature (SST) predictions of the model. SST is a parameter sensitive to across isopycnal mixing, as a too low mixing across the thermocline will cause heat to remain in the mixed layer and therefore to a prediction of a too warm SST.

2.3.e.3 Parameterization of eddy coefficients below the mixed layer

Large et al. [1994] parameterized eddy viscosities and diffusivities below the mixed layer of the ocean upon empirical arguments in their KPP model simulations of ocean vertical mixing. *Kantha and Clayson [1994]* adapted this parameterization for use in two-equation turbulence models. The base of the mixed layer is diagnosed in their model by the first point in the layer where k is smaller than a certain value -their choice was $10^{-6}\text{m}^2\text{s}^{-2}$. In this way, the extinction of turbulence that characterizes the end of the mixed layer is estimated. In the region below (or over, if a bottom boundary layer), the value of ν_t and ν_t' is not obtained from model predictions of TKE and L via relations (2.23), but their value is set to the parameterized values.

In the KPP parameterization, eddy coefficients below the mixed layer are regarded as the superposition of three processes: local instability due to resolved vertical shear (SI), internal wave breaking (IW) and double diffusion (DD). Each process is parameterized by them in terms of a vertical diffusivity. The effective interior diffusivity is the sum of the three contributions:

$$\nu_t = \nu_t^{IW} + \nu_t^{SI} + \nu_t^{DD}, \quad \nu_t' = \nu_t'^{IW} + \nu_t'^{SI} + \nu_t'^{DD} \tag{2.99}$$

It should be noted that due to the nature of double-diffusion as reviewed in the introduction (section 2.1), the associated eddy diffusivities of temperature and salinity have different values. For the scenarios we will model, double diffusion is not important and we will assume that there is no contribution to vertical eddy coefficients from this process. However, the introduction of the parameterization of ν_t^{DD} and $\nu_t'^{DD}$ in the model does not introduce further complications.

The other processes in 2.97 have been parameterized based in the available empirical information from measurements and laboratory experiments. Advances in the comprehension of these phenomena may lead to improved parameterizations.. As we described in section 2.1, shear instability occurs locally in stratified fluids when the stabilizing effect of stratification is overcome by the vertical shear. Therefore, the tendency for developing of shear instabilities can be characterized by the gradient Richardson number R$_i$ (Eq. 2.10). The shear instability eddy coefficients are modeled as a strongly decreasing function of the local gradient Richardson number R_i, and is the same for momentum and scalars:

$$\begin{aligned} \nu_t^{SI} = \nu_t'^{SI} &= 0, \quad R_i > R_i^{SI} \\ \nu_t^{SI} = \nu_t'^{SI} = \nu_0^{SI} &\left[1 - \left(\frac{R_i}{R_i^{SI}}\right)^2\right]^3, \quad 0 < R_i < R_i^{SI} \\ \nu_t^{SI} = \nu_t'^{SI} &= \nu_0^{SI}, \quad R_i < 0 \end{aligned} \qquad (2.100)$$

The empirical parameters in this expression are ν_0^{SI}, that was chosen by *Large et al. [1994]* to fall within the range of the maximum diffusivities reported for the seasonal thermocline (*Peters et al., [1988]*) and R$_i^{SI}$, a critical value for shear instability to appear. In the ocean, field measurements usually are in the range 0.4-1. (see literature cited in *Large et al. [1994]),* so no information can be drawn for low Richardson numbers. Laboratory experiments suggest a

step-like function, with eddy diffusivities growing rapidly as R$_i$ decreases below a critical R$_i^{SI}$. This value has been set to 0.7, and the function is smoother than the experimental curve, to avoid instabilities in coarse resolution models. In figure 2.8, the ratio $\nu_t^{SI}/\nu_t'^{SI}$ is plotted versus R$_i$. Also, *Pacanowski and Philander [1981]* PP and *Munk and Anderson [1954]* MA functions are plotted. SI is a step-like function, while the others are monotonously decreasing functions. Compared to PP, SI results in higher diffusivities for values of R$_i$ greater than about 0.4, while PP predicts higher values for R$_i$ > 0.4. It must be noted that SI does not account IW effects on diffusivity that are dominant for great Richardson numbers, and that are accounted for by PP and MA. Munk and Anderson shows lower values than SI for R_i lower than about 0.36 while for higher values, eddy viscosities are considerably higher.

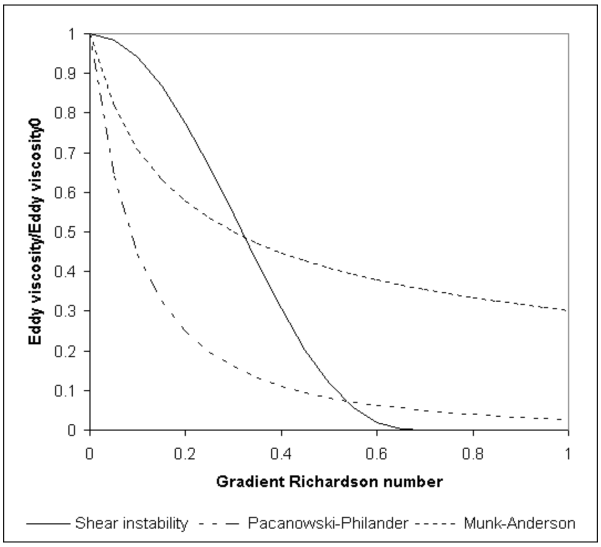

Figure 2.8: Normalized eddy viscosity versus the gradient Richardson number for the parameterization of shear instability induced mixing by Large et al. [1994], Munk and Anderson [1956] and Pacanowski and Philander [1981].

The magnitude of mixing due to internal waves is estimated from the available measurements. The diffusivity due to IW breaking appears to be small, and varies only with the internal wave energy. Results from the North Atlantic Tracer Release Experiment (NATRE) provided values of around $0.11 \cdot 10^{-4} m^2 s^{-1}$ for mixing across density surface in the interior region of the open ocean. Less information exists about the magnitude of IW induced viscosity, but *Peters et al. [1998]* show it to be from 7 to 10 times larger than the diffusivity. In this parameterization, internal wave (IW) induced diffusivities are assumed to be constant for simplicity and have a value:

$$\nu_t^{IW} = 1.0 \cdot 10^{-4}, \quad \nu_t'^{IW} = 0.1 \cdot 10^{-4} \tag{2.101}$$

The unit of all diffusivities in 2.98 and 2.99 is of $m^2 s^{-1}$. *Kantha and Clayson [1994]* assumed a larger value of $\nu_t'^{IW}$ of $5.0 \cdot 10^{-5}\ m^2 s^{-1}$.

This parameterization was designed from oceanic measurements in the thermocline, and it is aimed to parameterize eddy coefficients in the interior region. For low Richardson numbers, observations are introduced in the SI contribution, that is why they chose ν_0^{SI} as the maximum reported value, while for higher Richardson numbers, the SI contribution decays and IW dominates. It has resulted a valuable parameterization to predict a reasonable level of mixing across the thermocline in two equation models (*Kantha and Clayson [1994]*, *Burchard et al. [1999]*) and therefore, to avoid the SST warming that in the model intercomparison by *Martin [1985]* was regarded as one of the main problems of local differential models.

2.4 Applications

These turbulent closures have been introduced in **GOTM** (General Ocean Turbulence Model), a 1D water column model, that was co-developed by the author. GOTM is public domain under the GNU license and can be downloaded from http://www.gotm.net. A full description of the model can be found in *Burchard et al.* [1999]. Different test cases have been prepared and implemented to be run with GOTM. In this chapter, a simple entrainment rate case will be used for a simple qualitative and quantitative comparison of the different turbulence models. The performance of the model GOTM will be tested in an estuarine application were dissipation rate measurements are available and an open ocean case.

2.4.a Kato-Phillips experiment

In this classical experiment, the evolution of the mixed layer in a stably stratified fluid subject to a constant surface stress is studied. To reduce this experiment to ocean dimensions, the values of surface friction velocity u_*^s and $N_{0,}$ the constant initial Brunt-Väisälä frequency are chosen to be of 10^{-2} m s^{-1} and 10^{-2} s^{-1}, respectively, following *Deleersnijder and Luyten* [1994] and *Burchard et al.* [1998]. This simple experiment will allow us to intercompare different turbulence models by inspecting mixing coefficients and turbulent magnitudes after 30 hours. A mixing layer will be computed every instant as the value from the surface were TKE first reaches the value $10^{-5}m^2s^{-2}$, thus assuming that this value characterizes the limit of active mixing and of the mixed layer. This computed mixed-layer depth can be compared with the theoretical solution calculated by *Price* [1979]:

$$D_m = 1.05\ u_*^s N_0^{-1/2} t^{1/2} \tag{2.102}$$

The vertical discretization was of $\triangle$z = 0.5 m and the time step $\triangle$t = 100 s.

Figures 2.9 -2.12 show some results of these experiments with different turbulence closures. Profiles of eddy coefficients, TKE and mixing length scale after 30 hours are computed for every model and also the evolution of the mixed layer compared to the analytical solution (Eq. 2.101) is shown.

In figure 2.9, a transport equation for TKE has been used, while the mixing length is imposed from a diagnostic expression. In the first row, the *Blackadar [1962]* expression is used with a constant stability function derived from the quasiequilibrium stability functions by *Galperin et al. [1988]*. As expected, the model does not provide a good estimation of the mixing length, since length limitation is the only explicit dependence on stratification introduced. In the second row, the dependence on stratification is accounted by using the *Galperin et al. [1988]* stability functions and the mixing length evolution is better reproduced. A maximum of TKE appears at mid-depth, that is not present in the upper row. The macro length scale grows in both situations from the surface until a limit is attained, that is forced by the length limitation constraint. In the third row, the ISPRAMIX turbulence model is used. The eddy coefficients are smaller than those obtained with other models, and also the mixing length is smaller. This can be due to the great dependence on the flux Richardson number that was introduced by using an exponent $\alpha = 3$ in the stratification correction of the length scale (Eq. 2.67). However, this value was chosen because the best estimation of the mixing length evolution was attained. In the forth row, the length scale is calculated with the *Gaspar et al. [1990]* and *Blanke and Delecluse [1993]* method. The mixing layer depth fits well the theoretical prediction and the TKE decreases with depth. The eddy coefficients are bigger than for other models. They present a peak at about 10 m deep, consequence of a too steep transition. The mixing length is bigger than for other models, but it must be noted that the eddy coefficients are not calculated from the Kolmogoroff-Prandtl expression, but using a different expression (see section 2.3.c.2). Thus, the predicted mixing length can not be directly compared to the mixing length obtained with other models.

In figure 2.10 , the effect of some simple stability functions is compared. In the first row, the constant version resulting from the *Galperin et al. [1988]* quasiequilibrium set is used. In the second row, *Munk and Anderson [1948]* stability functions are used. In the third row, the *Schumann and Gerz [1995]* expression is used. Eddy diffusivity is greater than viscosity as a result of their prediction of a Prandtl number greater than unity for the range of Richardson numbers reached in the experiment. The TKE has a maximum at the surface and decreases with depth. The mixing length increases linearly with depth until a maximum and then decreases to the bottom. With the *Schumann and Gerz [1995]* stability functions the greater value of the mixing length is predicted. Mixing layer depth is overestimated in all of them, and Schumann and Gerz provides the best prediction of the three.

In figure 2.11, some different sets of stability functions are compared by using a k-ε model. The value of $c_{\varepsilon 3}$ has been chosen following the calibration procedure indicated in *Burchard and Bolding [2000].* The first row plots the result for *Mellor and Yamada [1982]* full version stability functions, the second for *Galperin et al.[1988]* quasiequilibrium version, the third for *Kantha and Clayson [1994]* quasiequilibrium version and the forth for the stability functions by *Canuto et al. [2000].* For the *Mellor and Yamada [1982]* set, eddy viscosities show a noisy profile that is originated by the positivity constraints that are introduced (*Deleersnijder and Luyten [1994]*). The other stability functions predict a clean pattern, with eddy diffusivity greater than viscosity in the mixing zone for the quasiequilibrium *Galperin et al. [1988]* and *Kantha and Clayson [1994]* stability functions, while with the *Canuto et al. [2000]* set, a bigger diffusivity until around 10 m and a bigger viscosity from there down are obtained. The turbulent kinetic energy for the *Mellor and Yamada [1982]* version has a maximum at mid-depth, that seems unphysical for this experiment, and that is also present in the simulations with *Galperin et al. [1988]* and *Kantha and Clayson* [1994] quasiequilibrium functions. In contrast, this TKE maximum does not appear in the computations with the *Canuto et al. [2000]* stability functions. Regarding to mixing length, all of them show a maximum at mid-depth, the mixing length is increasing from the surface following the linear profile near wall until its growth is inhibited by stable stratification. A more symmetrical profile is predicted by the first three sets. The evolution of the mixed layer for the *Mellor and Yamada [1982]* full version is not satisfactory since mixing is underestimated. The quasiequilibrium versions show a better agreement to the theoretical curve. With the quasiequilibrium *Kantha and Clayson [1994]* stability functions*,* a slightly greater entrainment than for the *Galperin et al. [1988]* is obtained. The *Canuto et al. [2000]* stability functions perform the best. They consider shear influence like *Mellor and Yamada [1982]* and the *Kantha and Clayson [1994]* full version, but at the same time that perform in a stable way.

The *Mellor and Yamada [1982]* two equation closure with *Kantha and Clayson [1994]* quasiequilibrium stability functions is studied in figure 2.12. The prescribed macro length scale in Eq. 2.44 is a linear increasing profile from surface, since no bottom effect will be considered:

$$L_z = \kappa \left(d_s + z_{os} \right) \tag{2.103}$$

In the first row, the empirical coefficient c_{L3} is chosen to be equal to $c_{L1} = 0.9$ and no length limitation is considered. The mixing layer depth is greatly overestimated and the mixing length scale is greater than predicted with other models (note that the horizontal scale is different) and the maximum lies at around 25 m. The TKE exhibits a maximum at mid-depth and a strange minimum in eddy coefficients appears. In the second row, length limitation according to *Kantha and Clayson [1994]* is applied and results are improved. The mixing length now fits better the theoretical prediction, and the eddy coefficients do not have a severe minimum. TKE has a maximum at mid-depth and the effect of the limiting constraint on L is appreciated in the L profile. In the third row, the empirical coefficient c_{L3} is set to 2.765, as suggested by *Burchard [1999]* to predict a limit of L in steady-state conditions (see Section 2.3.c.3). It can be seen that eddy coefficients have a smoother shape and the mixing length attains a limit and also shows a smoother shape. Mixing length is slightly underestimated in comparison to the previous row. In the forth row, the conditions are the same as in the third row, but length limitation is imposed. The results are quite identical to those without length limitation, which illustrates that the limitation of length scale is intrinsically fulfilled after choosing the empirical parameter $c_{L3.}$

From the results we can conclude that the k-ε model shows the best performance. The fact that it automatically fulfills the law of the wall avoids some of the problems that appear in the Mellor-Yamada model. The profiles of mixing length in figure 2.12 seem to be strongly influenced by the imposition of the linear profile from Eq. 2.102 and this can be responsible for the slight discontinuity that can be seen in all eddy coefficient profiles. Regarding to 1-equation models, the performance of the model with the *Blackadar [1962]* length scale depend on the stability functions chosen, as with this method no stratification is considered in the determination of the mixing length. The ISPRAMIX model predicts smaller eddy coefficients and smaller length scale probably due to the stratification factor that multiplies the length scale. It can be considered as a stability function, which indicates that stability functions strongly condition the performance of this model. The results with the *Gaspar et al. [1990]* model predict a good fit of the mixing layer evolution to the theoretical prediction, but a too steep profile appears in the length scale and in the eddy coefficients.

Stability functions play a very important role in the performance of the model in this experiments. With the classical *Mellor and Yamada [1982]* full set, a noisy pattern of eddy coefficients is obtained. This stability functions are used in the turbulence model that is implemented in widely used models like POM (Princeton Ocean Model), that need to use a smoothing filter. The classical quasiequilibrium functions show an unphysical maximum of TKE, that is not a consequence of the 2-equation model, since it also appears in 1-equation model with Blackadar length in figure 2.9. It is likely to be related to the neglect of the effect of shear on the stability functions.

The *Canuto et al. [2000]* stability functions provide the best results, with physically sound predictions of eddy coefficients, TKE and mixing length, and a good fit of mixing length evolution to the empirically derived prediction.

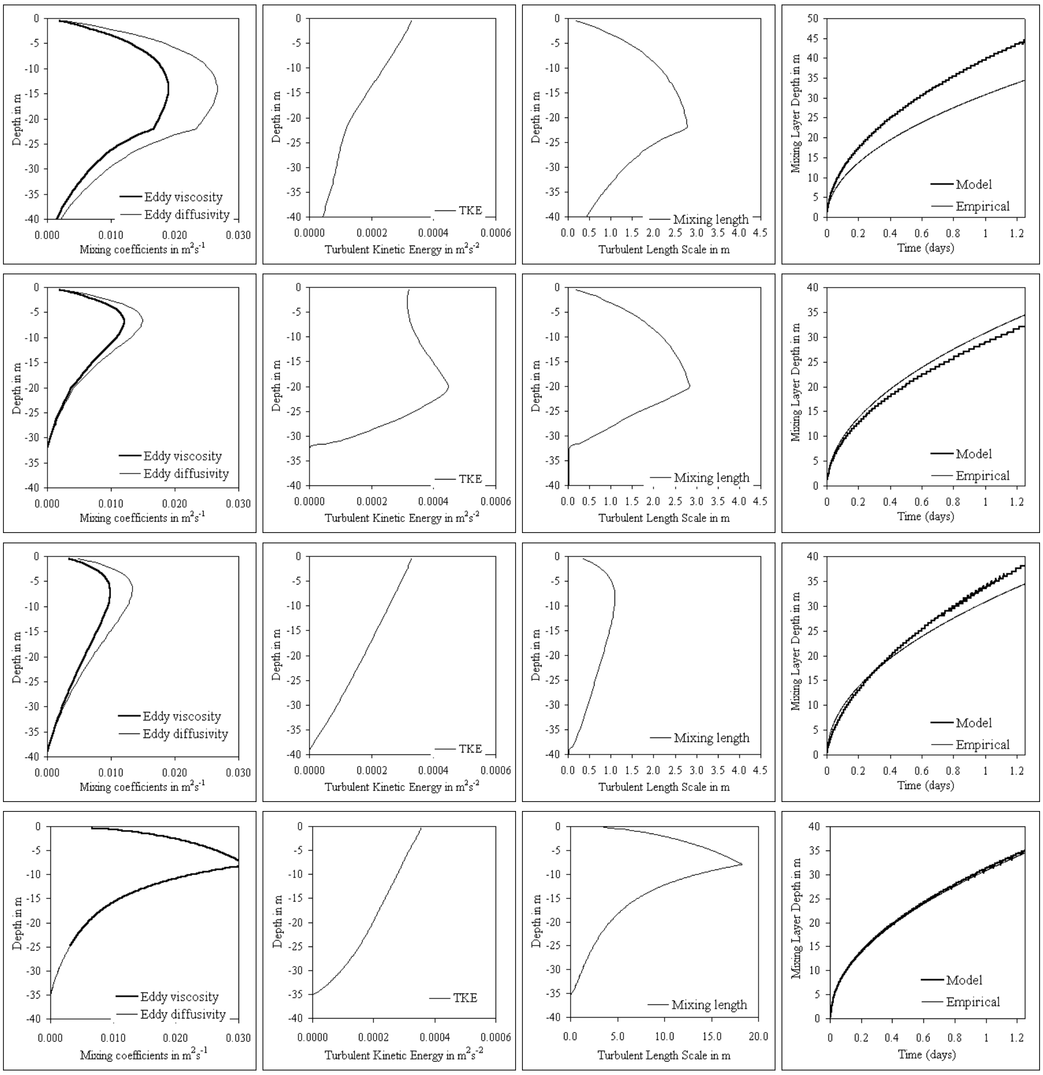

Figure 2 9: Profiles of eddy coefficients (first column), turbulent kinetic energy (second) and mixing length scale (third) after 30 hours and evolution of the mixing length the first 30 hours of the Kato-Phillips experiment. TKE is determined from the TKE equation, while the mixing length is determined from a diagnostic profile First row: Blackadar length scale [1962] with constant stability functions; second row; Blackadar length scale [1962] with Galperin et al. [1988] stability functions; third row: Ispramix model and forth row: Gaspar et al. [1990] model. Note that the scale of the mixing layer depth in the first row is different from the others.

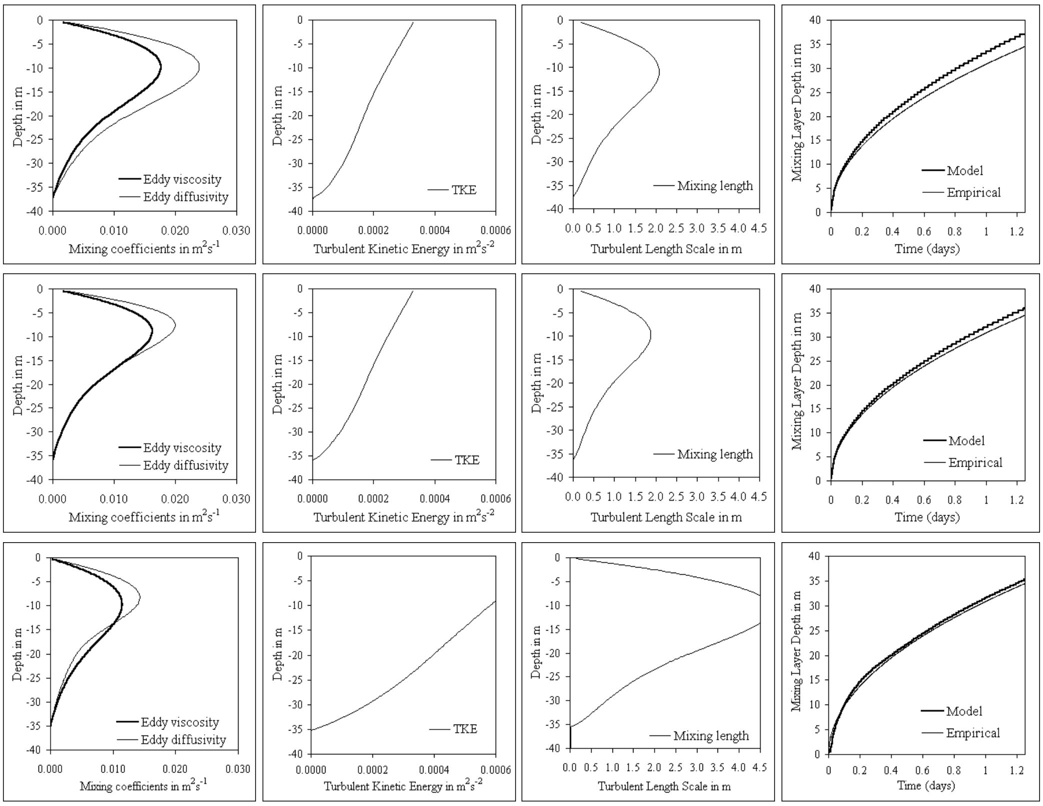

Figure 2 10: Profiles of eddy coefficients (first column), turbulent kinetic energy (second) and mixing length scale (third) after 30 hours and evolution of the mixing length the first 30 hours of the Kato-Phillips experiment. The model is a k-epsilon and in every row a different et of stability functions is chosen. First row: Constant stability functions derived from Galperin et al. [1988]; second row; Munk and Anderson [1956] stability functions; third row: Schumann and Gerz [1995] stability functions.

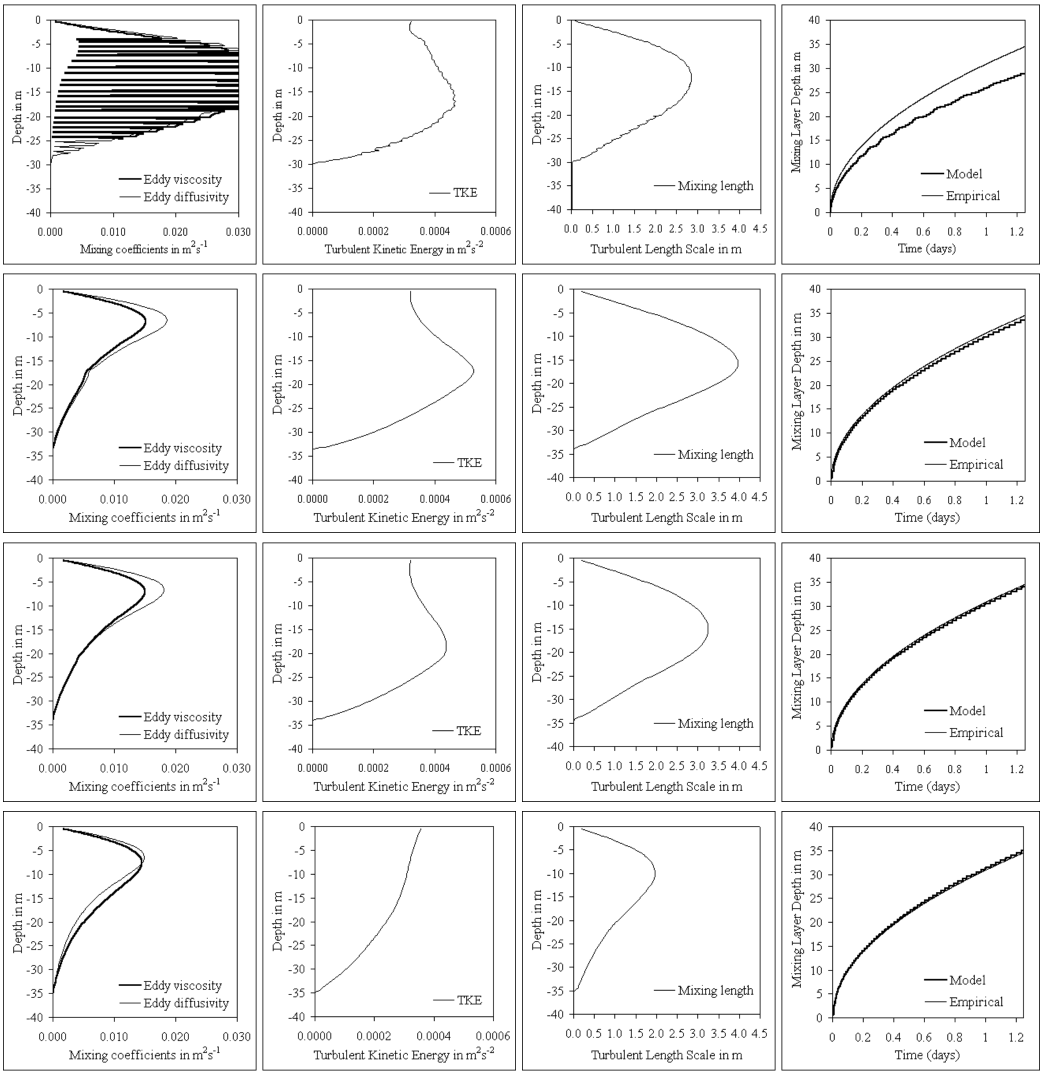

Figure 2.11: Profiles of eddy coefficients (first column), turbulent kinetic energy (second) and mixing length scale (third) after 30 hours and evolution of the mixing length the first 30 hours of the Kato-Phillips experiment. The model is a k-ε and in every row a different stability function is chosen. First row: Kantha-Clayson [1994] quasiequilibrium (with length limitation); second row; Galperin et al. [1988] quasi-equilibrium; third row: Kantha-Clayson quasiequilibrium and forth row: Canuto et al. [2000], full version.

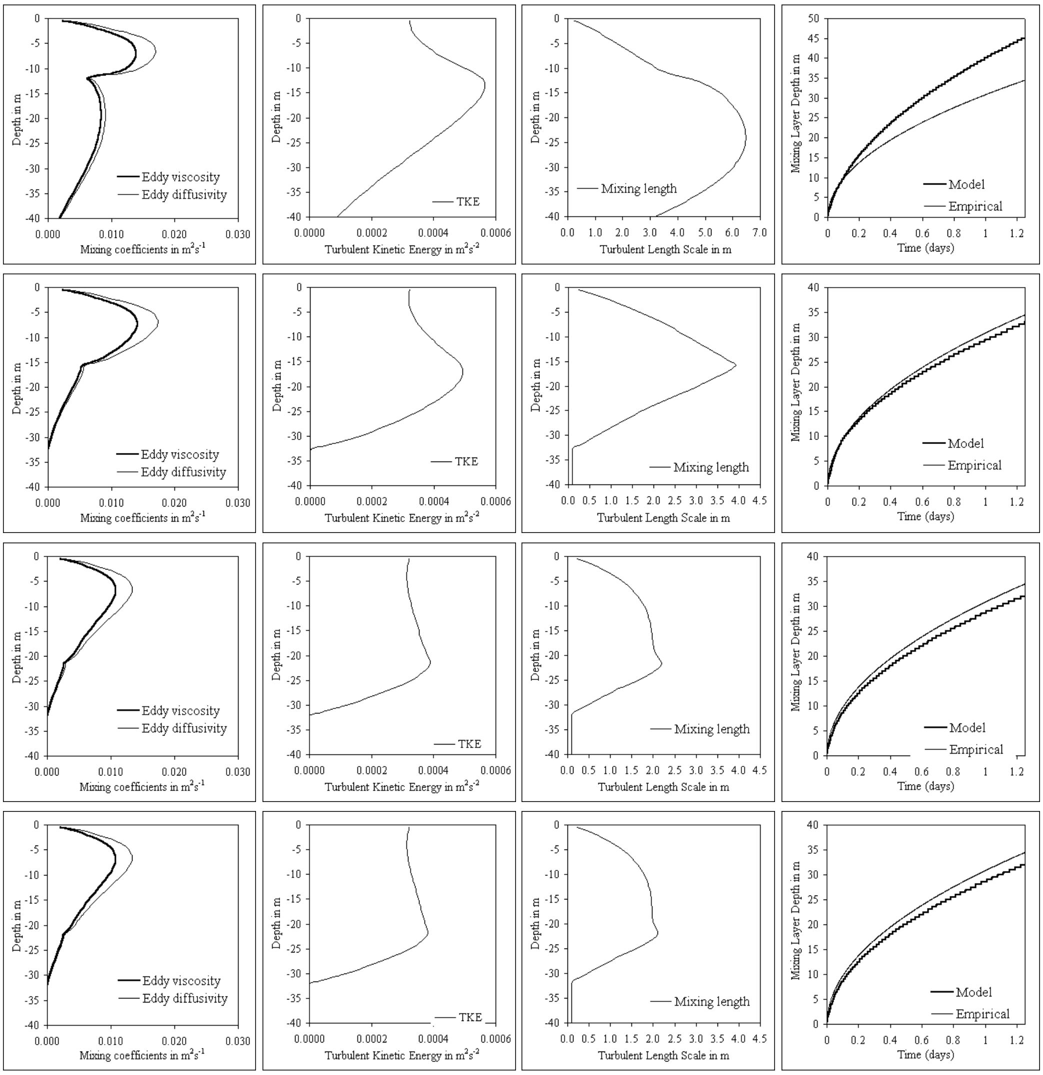

Figure 2.12: Profiles of eddy coefficients (first column), turbulent kinetic energy (second) and mixing length scale (third) after 30 hours and evolution of the mixing length the first 30 hours of the Kato-Phillips experiment. The model is a Mellor Yamada with quasiequilibrium Kantha and Clayson [1994] stability functions. First row: , no length limitation and $c_{L1} = c_{L3} = 0.9$; second row; $c_{L1} = c_{L3} = 0.9$ and length limitation; third row: no length limitation and $c_{L1} = 0.9$ and $c_{L3} = 2.765$ and forth row length limitation and $c_{L1} = 0.9$ and $c_{L3} = 2.765$

2.4.b OWS Papa

The Ocean Weather Station Papa is a site in the Gulf of Alaska in the North Pacific (145^o W 50^o N, see figure 2.13), where measurements of physical and biological parameters have been carried out on a regular basis since 1954.

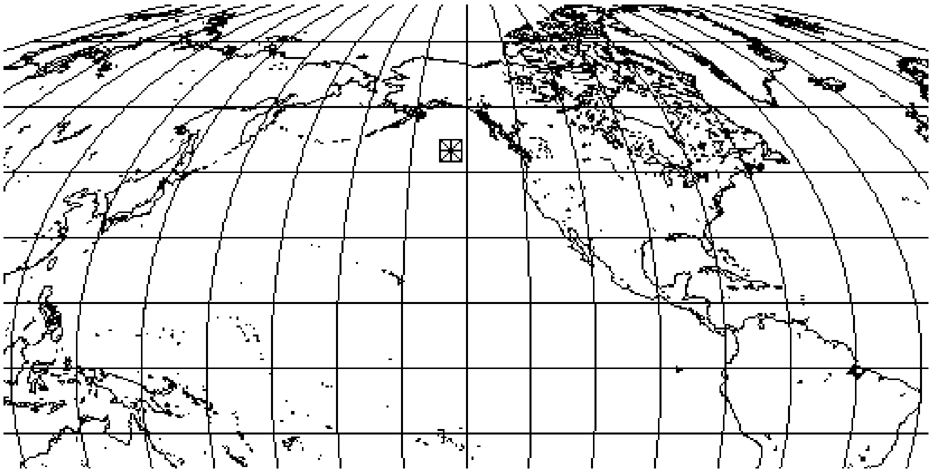

Figure 2.13: Location of the Ocean Weather Station Papa in the North-East Pacific (145^o W 50^o N).

Meteorological parameters every three hours and temperature profiles have been continuously measured. Unfortunately, no velocity, salinity or turbulence measurements are available. However, this site has been used to assess the performance of turbulence models (for example: *Martin, [1985]*, *Gaspar et al. [1990]*, *Large et al. [1994]*, *Kantha and Clayson [1994]*, *D'Alessio et al. [1998]*, *Burchard et al. [1999], Burchard and Bolding [2000]*). One of the advantages of this station is that usually horizontal advection is not important, which allows running a 1D water column model without worrying about 3D effects. The year 1961-62 has been used in many of these studies. In figure 2.14 , the heat content calculated from temperature profiles and the heat content calculated from the meteorological data are plotted, starting in April 1961 and ending in April 1962. We follow *Large et al. [1994]* in starting the simulation at the beginning of the ocean year, April, where the heat content attains a minimum. The annual cycle is clearly seen in the figure, with maximum heat content in the summer. The difference in heat contents from late October 1961 on indicates the existence of advective phenomena. *Large et al. [1994]* states that advection of cold water below the seasonal thermocline is responsible for this difference. The model is initialized with the 25 March instantaneous profile instead of a 5 day average around 15 March as done by *Large et al. [1994]*, but results are comparable. Details on the estimation of heat fluxes and wind stress from the available data can be found in *Burchard et al. [1999].* The average heat flux is of 30 W m^{-2}, the same as obtained by *Large et al. [1994].* The initial salinity profiles are interpolated from the monthly mean profiles from *Levitus [1992]* and afterwards salinity flux is set to zero. *D'Alessio et al. [1998]* have reported sensitivity tests to the treatment of salinity, since a strong halocline exists below a depth of around 125 m. Three different treatments: a) zero salinity fluxes and initial profile from climatology (like in this work), b) keeping the initial salinity profile constant throughout the year and c) estimating the salinity flux from evaporation and precipitation climatologies rendered only slightly different SST profiles. Turbulent quantities are initially set to their minimum values and velocity to zero. The attenuation coefficients are of the type II water in *Jerlov [1968],* following *Large et al. [1994].* A vertical grid space of 1 m and a time-step of 900 s were used in the simulations. The variation of the time step does not induce a major variation in the result.

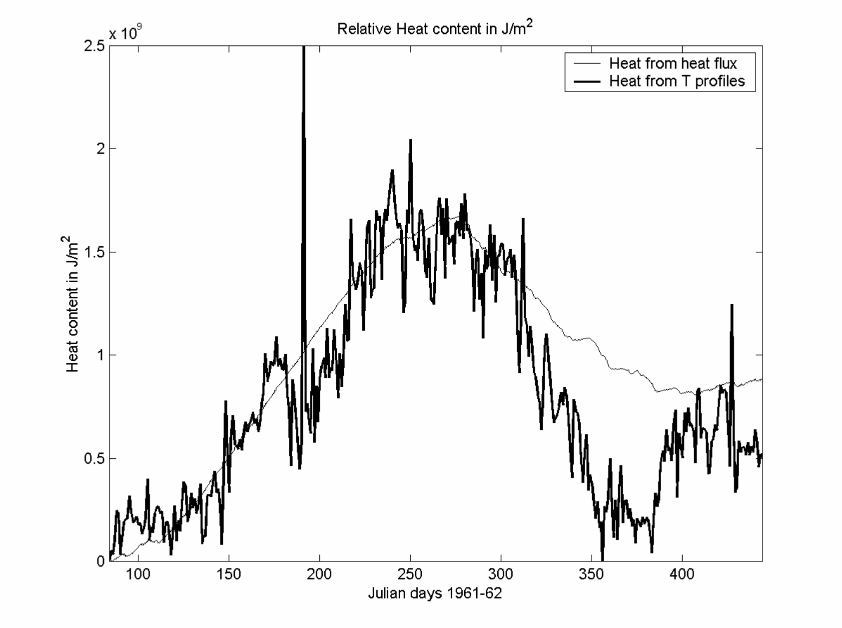

Figure 2.14: Heat content from heat flux and heat content from temperature measurements as a function of the Julian day 1961-62.

In figure 2.15, the observed Sea Surface Temperature (SST) for the ocean year April 1961-April 1962 is plotted. We can see that temperature at the beginning of the simulation is of around 5 C and reaches a peak of 16 C in August. Some peaks are evident in the SST signal that seem to be related to periods of strong heating and low wind, specially when they act on a shallow mixed layer (*D'Alessio et al. [1998]).* The mixed layer depth (MLD) computed from profiles is shown in figure 2.16. The MLD is estimated as the first point from the surface where $T - SST > 0.1.C$. The mixed layer depth gets shallower in the summer, with values of 10 m or less in the summer months. At the beginning of the ocean year, MLD lies at about 100 m. From then on, the mixed layer depth gets gradually shallower, although great variability appears. In August and September, the mixed layer only reaches a shallow depth of 10 m or less.

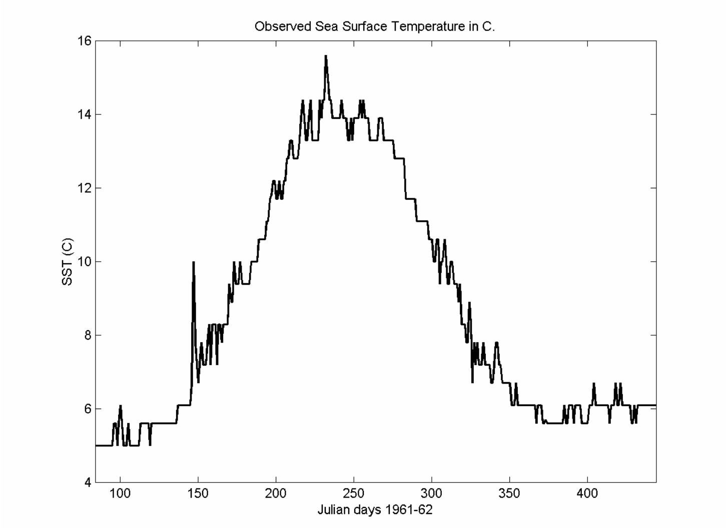

Figure 2.15: Observed Sea Surface Temperature in C at the Station Papa during the year 1961-62.

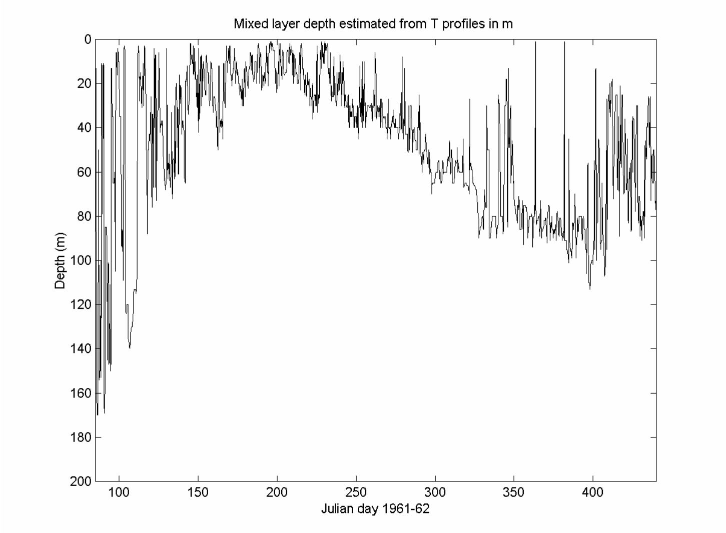

Figure 2.16: Mixed layer depth estimated from temperature profileas at the Station Papa during the year 1961-62.

In figure 2.15, the observed temperature is plotted. In April, temperature is not stratified and temperature values are around 5 C. Surface waters are gradually warming from then on and stratification develops. In late spring a strong seasonal thermocline is marked. Stratification grows at the same time as surface temperature, that reaches a maximum of 15 C at mid-August. In September-October, the thermocline deepens and smoothens and afterwards only a slight stratification of the water column remains. Advection of colder water in the depth layers can be seen from September on.

Martin [1985] performed calculations using several bulk models and the *Mellor and Yamada [1982]* (MY) model and compared the results to observations at station Papa. He tabulated monthly averaged errors and found that MY model was too warm by 2.2 C at the end of the summer, while the bulk models were too cold. This warming of local models like MY was considered to be caused by too small levels of diapycnal mixing. As we reviewed in section 2.3.e, some simple internal wave parameterizations were proposed to remedy this problem. In this section, the k-ε model will be used as a test bed to study the effect of stability functions and internal wave parameterizations on the result. In a first experiment, the model was run with stability functions by *Galperin et al. [1998]* and length limitation according to Eq. 1.70. The buoyancy coefficient $c_{\varepsilon 3}$ in the $\varepsilon-$equation was set to -0.4. The SST predictions are compared to the observed SST in figure 2.19. The measured SST shows an increase from 4 C in April (well-mixed conditions) to 14 C in August and afterwards a decrease. If no IW is considered, the model overpredicts the SST from mid-June with around 2 C difference in summer and early autumn. The IW models of *Luyten et al. [1996]* and *Mellor [1989]* decrease the difference, but still a bias of more than 1 C remains. The *Kantha and Clayson [1994]* parameterization gives the best fit to SST measurements. From November on, all models overestimate temperature, since the model does not take into account the advection of cold water that causes the difference in heat content we have already mentioned. Although the *Kantha and Clayson [1994]* parameterization provided the best results, a too high value of internal eddy diffusivity $\nu'^{IW} = 5 \cdot 10^{-5} m^2 s^{-1}$, greater than the original value of $10^{-5} m^2 s^{-1}$ suggested by *Large et al. [1994]* had to be used. This resulted in a too diffusive thermocline, as pointed by *Burchard et al. [1999].* There is indeed some sensitivity to this parameter, which is assessed in figure 2.21. Also a sensitivity analysis of the influence of the free parameters in *Luyten et al. [1996]* and *Mellor [1989]* parameterizations is shown in figure 2.20.

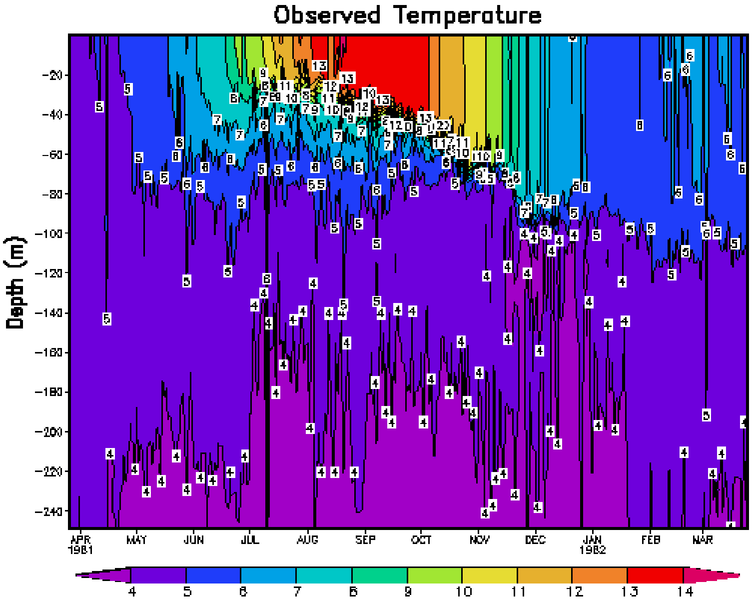

Figure 2.17: Observed temperature in C at the station Papa during the year 1961-62.

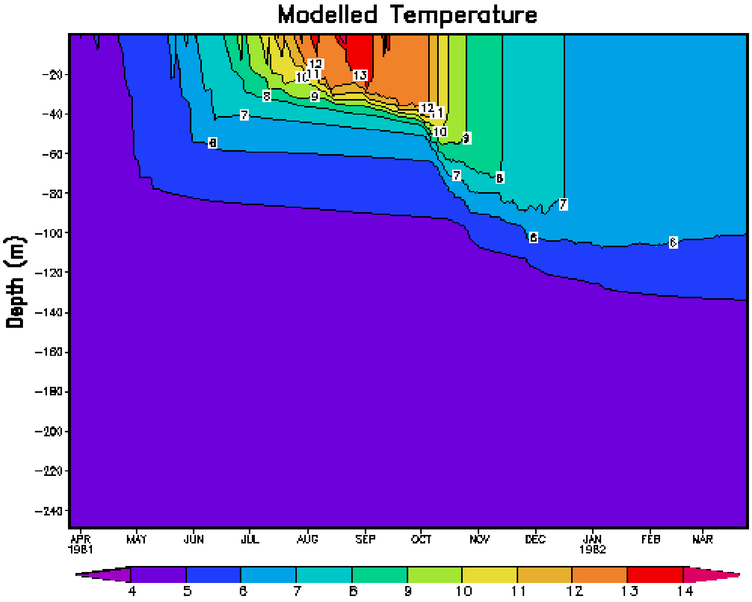

Figure 2.18: Modeled temperature in C for the OWS Papa. k-ε model with stability functions from Canuto et al. [2000].

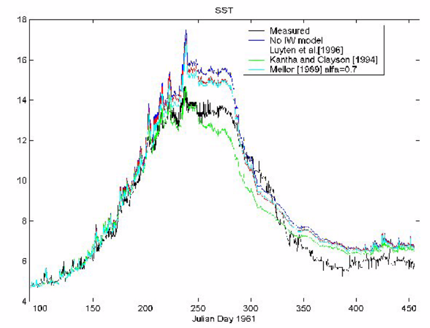

Figure 2.19: Sensitivity of the predicted sea surface temperature to the internal wave parameterization. The model was a k-ε model with stability functions after Galperin et al. [1988].

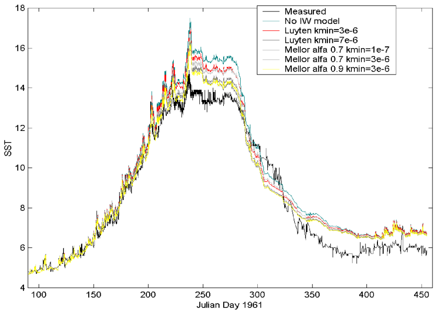

Figure 2.20: Sensitivity of the predicted SST to the free parameters in the Mellor [1989] and Luyten et al. [1996] internal wave parameterizations.

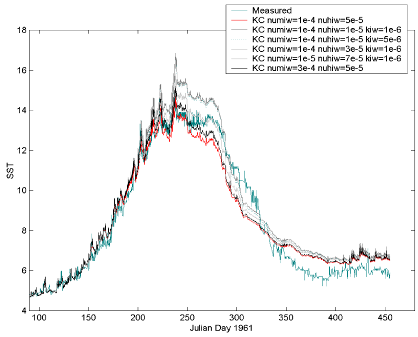

Figure 2.21: Sensitivity of the predicted sea surface temperature to the values of ν^{IW} (numiw) and ν'^{IW} (nuhiw) in the internal wave parameterization by Kantha and Clayson [1994].

The free parameter in the *Luyten et al. [1996b]* parameterization is the value of TKE. As we noted, it has the effect of a tuning parameter. This value has an effect in the predicted SST, and the larger k$_{lim}$, the lower the SST temperature results, although an overestimation is still present for a rather large value of k$_{lim} = 7 \cdot 10^{-6}\ m^2 s^{-2}$. The *Mellor [1989]* model is not very sensitive to the value of α, the tuning parameter for internal wave induced shear, and responds clearer to variations of k$_{lim}$.

The values of ν^{IW} (numiw) and ν'^{IW} (nuhiw) are varied in figure 2.18. Also the value of TKE for switching on the internal wave parameterization is varied. We recall that the values proposed by *Large et al. [1994]* are $\nu^{IW} = 10^{-4} m^2 s^{-1}$ and $\nu'^{IW} = 10^{-5} m^2 s^{-1}$. It is difficult to draw conclusions from this figure, apart from the fact that the model SST prediction is sensitive to the values of the IW eddy coefficients. In contrast, no sensitivity to the value of the set-up TKE is observed: for a TKE five times greater than that proposed by Kantha and Clayson [1994] ($10^{-6} J/kg$) no significant difference is seen. A variation of the value of the diffusivity seems to have more effect in SST than viscosity variations, but with none of the combinations the measured SST can be fitted. This can be interpreted as an indication that diapycnal diffusivity is not the only responsible for the SST measurements-model bias and there is something missing. This is also suggested by the too diffusive thermocline in model results pointed by *Burchard et al. [1999]*.

We discussed in section 2.3.c.3 that an adequate choice of parameters in the k-ε equation makes redundant the imposition of a limit on the length scale in stratified conditions. We have re-run the model without length limitation, with the result that part of the model overestimation in SST comes from the limitation of the length scale. This is not surprising since the length limitation is related to the way that the model behaves in stratified conditions. The right coefficient in the buoyancy term in the ε-equation induces a more realistic behavior of the model.

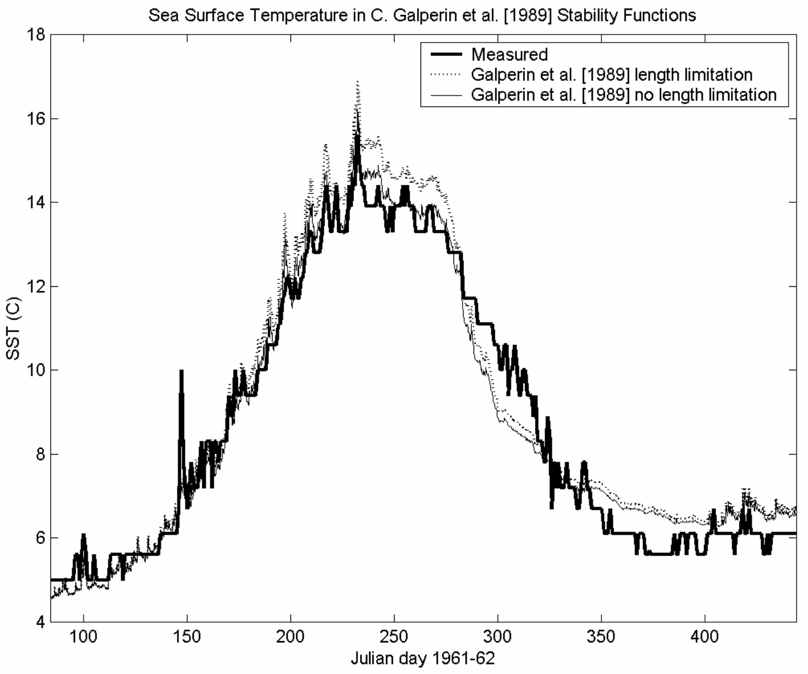

Figure 2.22: Sea Surface Temperature versus the Julian Day 1961-62 for the k-ε model with stability functions after Galperin et al. [1988].

In figures 2.23 and 2.24, the performance of the model with *Kantha and Clayson [1994]* KC and *Canuto et al. [2000]* CA stability functions is evaluated again by comparing predicted with observed SST (*Burchard and Bolding [2000]).* The coefficient in the buoyancy term in the ε-equation was chosen from the estimations of *Burchard and Bolding [2000]*, as we explained in section 2.3.c.3. With both sets of stability functions, the evolution of SST is well reproduced. Until around day 240, the agreement is very good for both, while from around day 270, the difference with observation grows due to the advective phenomena around that time. In the summer (days 210-280), KC overpredicts SST, while the CA stability functions fits the observational SST better. This might be related to the underestimation of the mixing layer by the KC due to their lower steady-state Richardson number R_i^{st} (*Burchard and Bolding [2000]*). Different internal wave parameterizations have been tested. No major difference is seen in the results, although the use of an IW model seems to help KC to predict a slightly deeper mixed layer and therefore a less warm SST. For the CA stability functions, very small differences are evident during some days for all parameterizations, except that by *Mellor [1989].* This parameterization combined with CA forces too much mixing and consequently a cooler SST.

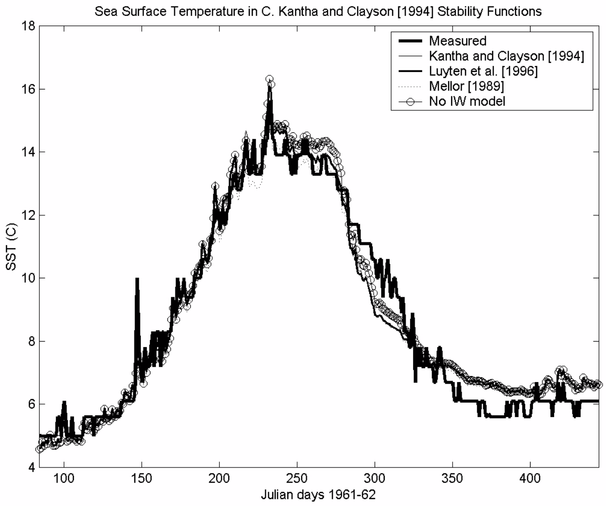

Figure 2.23: Modeled SST in C at the Station Papa during the year 1961-62. k-ε model with stability functions from Kantha and Clayson [1994] and different internal wave parameterizations

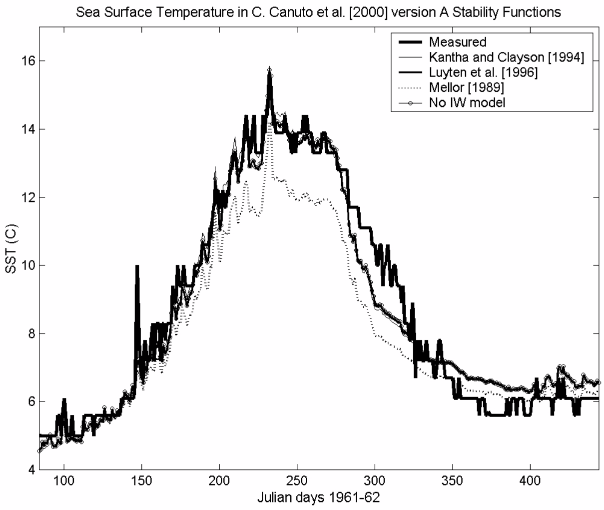

Figure 2.24: Modeled SST in C at the Station Papa during the year 1961-62. k-ε model with stability functions from Canuto et al. [2000] and different internal wave parameterizations

We see that with adequate tuning of the buoyancy term in the $\varepsilon-$equation and with use of the stability functions by *Canuto et al. [2000]*, that consider more pressure-strain correlation effects, the prediction of SST is sensibly improved. No sensitivity to internal wave parameterization is seen, which indicates that the overprediction of SST in local models was not caused by the underestimation of diapycnal mixing, but by a incomplete description of mixed layer physics. Internal wave parameterizations are however needed to predict a reasonable value of eddy coefficients in the interior region.

In figure 2.25, the mixed layer depth estimated from the results of the k-ε model with stability functions of *Canuto et al. [2000]* and IW parametrization by *Kantha and Clayson [1994]*. The mixed layer was computed by the TKE extinction method that we also used in Kato-Phillips simulation. The first point from surface where TKE is smaller than $10^{-5}m^2s^{-1}$ constitutes the estimated mixed layer depth. The evolution of the predicted mixed layer depth is also well predicted, and not much sensitivity to changes in vertical resolution is observed, apart from in summer months, where the mixed layer depth can be of less than 10 m.

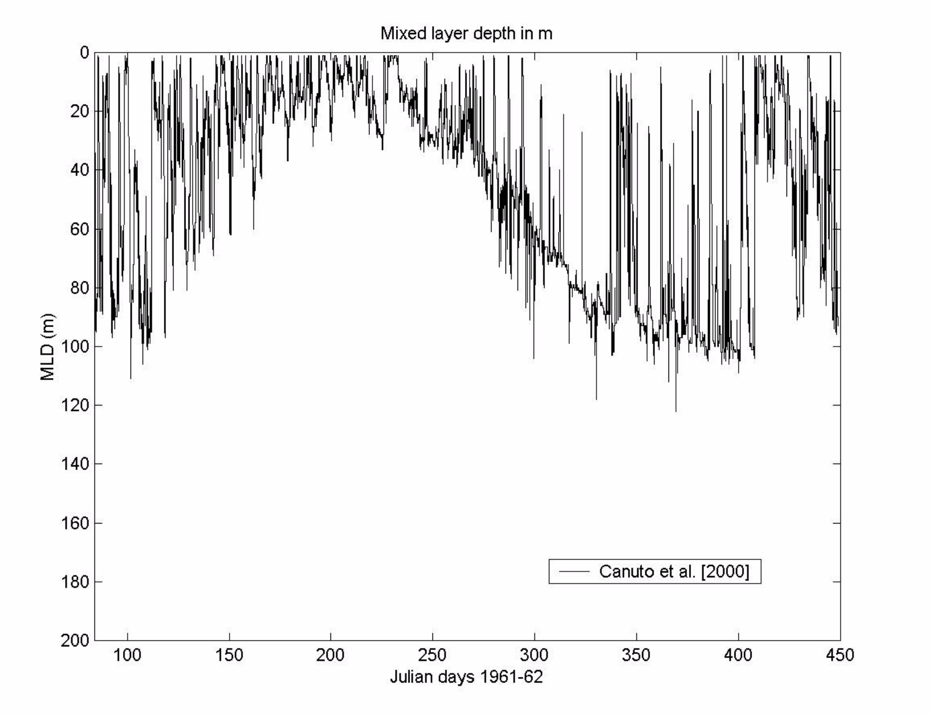

Figure 2.25: Modeled mixed layer depth in m at the Station Papa during the year 1961-62. k-ε model with stability functions from Canuto et al. [2000].

In figure 2.18, the predicted temperature for the CA model with IW parameterization from *Kantha and Clayson [1994]* is plotted. The evolution is well reproduced along the year. Only the cold (4 C) waters that reach up to around 100 m in winter are not modelled, as no advection is considered. The thermocline is not too diffusive since we do not impose the value of $\nu'^{IW} = 5 \cdot 10^{-5} m^2 s^{-1}$ that had to be used by *Kantha and Clayson [1994]* for adequate predicting SST with their modified Mellor-Yamada model. Instead, the original value of $\nu'^{IW} = 10^{-5} m^2 s^{-1}$ proposed by *Large et al. [1994]* was used. In figure 2.26, some modelled temperature profiles are compared to observations for 4 spring and summer days. The model shows a good fit to the observed profile and no great sensitivity to IW parameterization, except for the parameterization of *Mellor [1989]*. Differences are smaller than 0.5 C for all days. Also the model performs well if resolution is diminished and only small differences are apparent. In figures 2.27 and 2.28, profiles of eddy viscosities are shown. Ideally, it would be desirable to have measurements of turbulent magnitudes to evaluate the perfomance of the model. It can be observed that if the *Mellor [1989]* IW model or no IW parameterization is introduced, the values of diffusivities go down to a low value that is in contradiction with the available estimations (see section 2.3.e.3). The use of the *Luyten et al. [1996b]* parameterization results in higher and more realistic values of eddy coefficients. For the *Kantha and Clayson [1994]* parameterization, eddy coefficients in the interior region are imposed to observed values. Some small peaks are observed, but smooth profiles predicted. These peaks are quite small and dissapear when lowering resolution. They seem to be related to the way this parameterization works: we are imposing eddy coefficients, not using the computed values. The developing of direct parameterizations of the values that are actually computed (k and ε) can lead to an improved description of eddy coefficients. However, the results in this chapter indicate that the k-ε model with stability functions from *Canuto et al. [2000]* and parameterization of diapycnal mixing by *Large [1994]* can be used for computing physically sound eddy coefficients that provide the physical forcing for biogeochemical studies.

As a summary, the monthly average SST differences model-measurements and the standard deviation are presented in table 2.1. Also the mean error from April to August is shown. All models use internal wave parameterization by *Kantha and Clayson [1994],* except the *Gaspar et al. [1990],* for which a limitation of TKE is applied. In the first row, the results with the widespread *Gaspar et al. [1990]* model are shown. An underestimation of SST of around 0.5 C in average occurs during all months. In the following two panels, we see quantitatively how length limitation induces a mean error of around 0.3 C from April to August, but with a peak of 0.7 C in August. The *Kantha and Clayson [1994]* and the *Canuto et al. [2000]* model averages are shown in rows 4 and 5. CA is the one that better predicts SST, especially during summer months. The sensitivity to variation in the vertical step can be seen in next rows, where the results for a vertical step of 5 m and of 10 m is shown. The highest difference appears in summer months (around 0.4 C), when mixed layer is shallower and can be of 10 m or less. Finally, the results of the KPP model as presented by *Large et al. [1994]* are shown in the last row. For the same vertical resolution (5 m), the CA and the KPP results are comparable, with CA performing slightly better on summer months. The advantage of the CA model with respect to KPP is that the free parameters in CA model (and in local turbulence models) are estimated from laboratory or analytical work, so they can cope with a broader range of situations without tuning parameters.

OWS Papa SST difference model-measurements (with standard deviation)

Model	April	May	June	July	Aug.	Sept.	Oct.	Nov.	Dec.	April-August
Gaspar dz=1m	-0.32 ±0.25	-0.30 ±0.31	-0.52 ±0.29	-0.52 ±0.27	-0.50 ±0.40	-0.50 ±0.29	-1.42 ±0.47	-0.80 ±0.68	0.18 ±0.33	-0.433±0.32
Galperin LL dz=1m	-0.24 ±0.25	0.08 ±0.31	0.34 ±0.31	0.87 ±0.27	1.19 ±0.38	1.02 ±0.29	-0.49 ±0.74	-0.32 ±0.65	0.57 ±0.31	0.450 ±0.61
Galperin No LL dz=1m	-0.25 ±0.25	0.01 ±0.31	0.08 ±0.28	0.39 ±0.26	0.52 ±0.36	0.38 ±0.29	-0.90 ±0.61	-0.52 ±0.66	0.43 ±0.32	0.150 ±0.41
Kantha and Clayson No LL dz=1m	-0.26 ±0.25	-0.04 ±0.31	-0.00 ±0.28	0.25 ±0.26	0.39 ±0.36	0.24 ±0.29	-0.97 ±0.59	-0.57 ±0.67	0.40 ±0.32	0.065 ±0.37
Canuto dz=1m	-0.28 ±0.25	-0.14 ±0.31	-0.14 ±0.28	0.18 ±0.25	0.26 ±0.35	0.05 ±0.29	-1.11 ±0.55	-0.63 ±0.67	0.35 ±0.32	-0.023 ±0.35
Canuto dz=5m	-0.29 ±0.25	-0.17 ±0.32	-0.29 ±0.29	-0.29 ±0.27	-0.14 ±0.36	-0.13 ±0.28	-1.38 ±0.61	-0.85 ±0.72	0.25 ±0.33	-0.239 ±0.31
Canuto dz=10m	-0.27 ±0.26	-0.21 ±0.25	-0.41 ±0.25	0.57 ±0.29	-0.34 ±0.30	-0.15 ±0.03	-0.15 ±0.15	-0.35 ±0.22	-0.20±0.20	-0.365 ±0.30
KPP dz=5m (from *Large et al. [1994*])	-0.23	-0.16	-0.27	-0.26	-0.33	0.03	-0.32	0.07	0.65	-0.25

Table 2.1: Mean monthly SST difference model-measurements for the station Papa during the year 1961. The standard deviation is indicated. Except for Gaspar et al. [1990] 1-equation model, in the other rows a k-ε model has been used. The internal wave parameterization by Kantha and Clayson [1994] has been used, except in Gaspar et al. [1990] model, where a limitation of TKE was imposed.

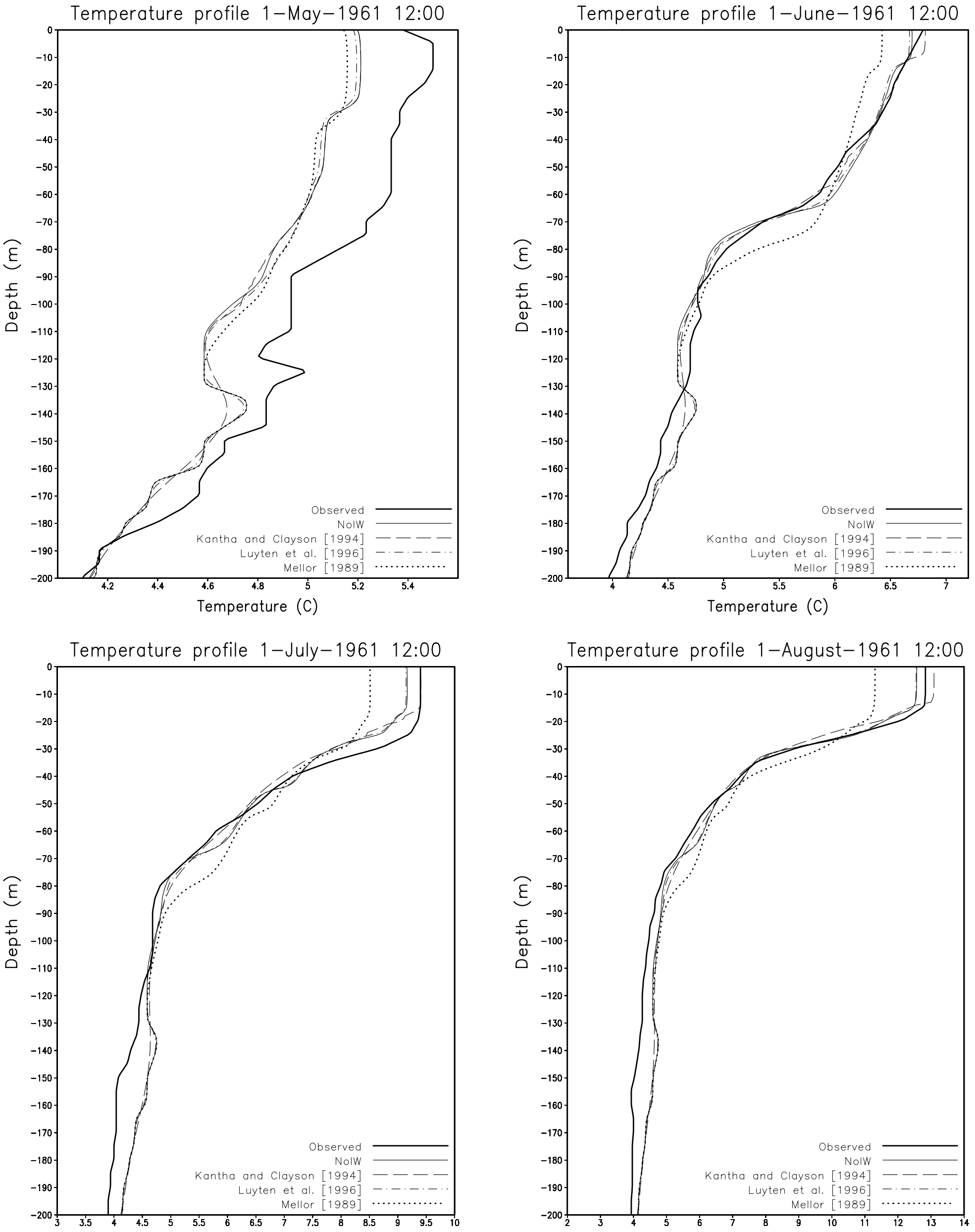

Figure 2.26: Temperature profiles in C for three different spring and summer dates for OWS_Papa. k-ε model and stability functions from Canuto et al. [2000]

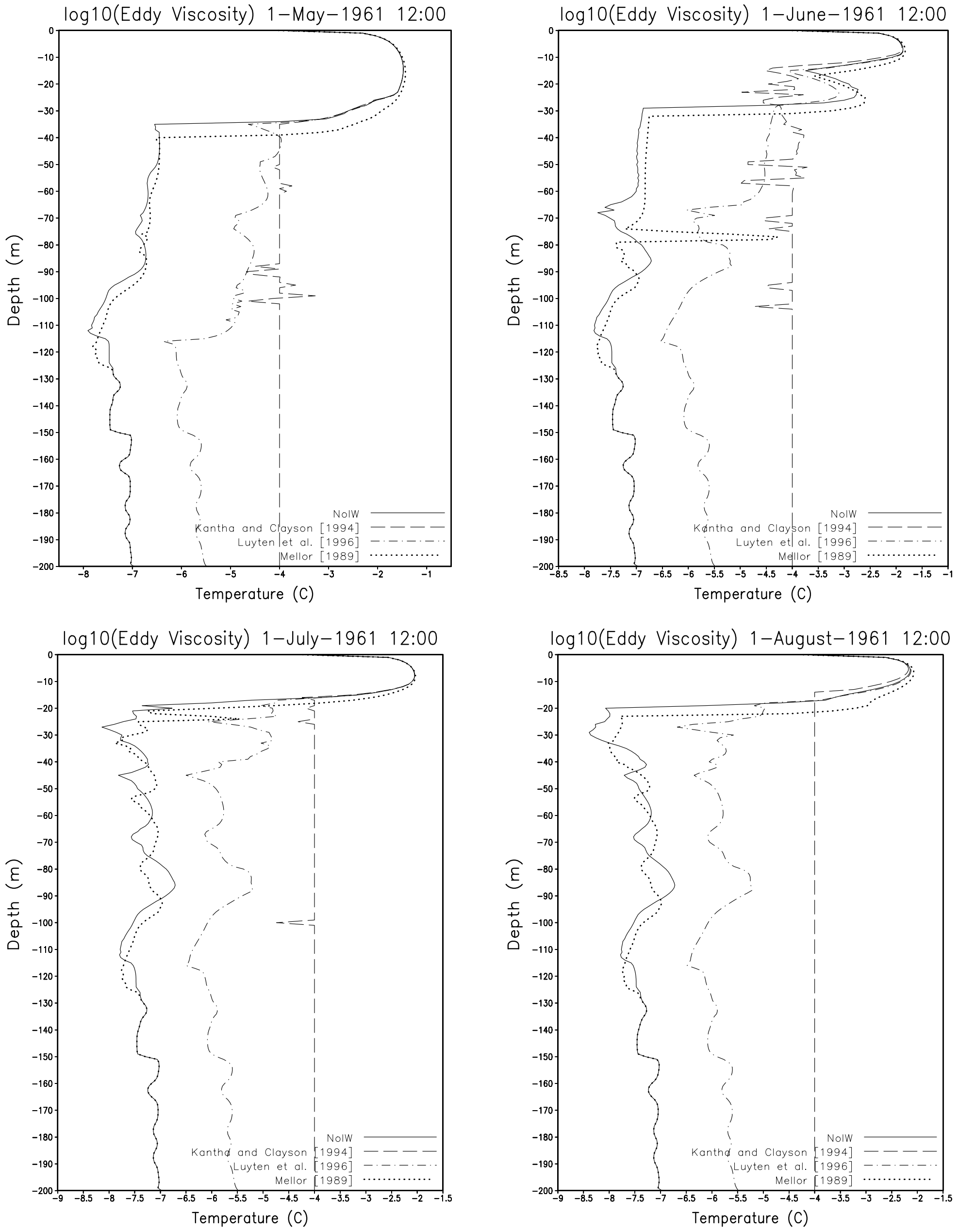

Figure 2.27 : Logarithm of eddy viscosity in $m^2 s^{-1}$ profiles for four spring and summer dates for OWS_Papa. k-ε model and stability functions from Canuto et al. [2000]

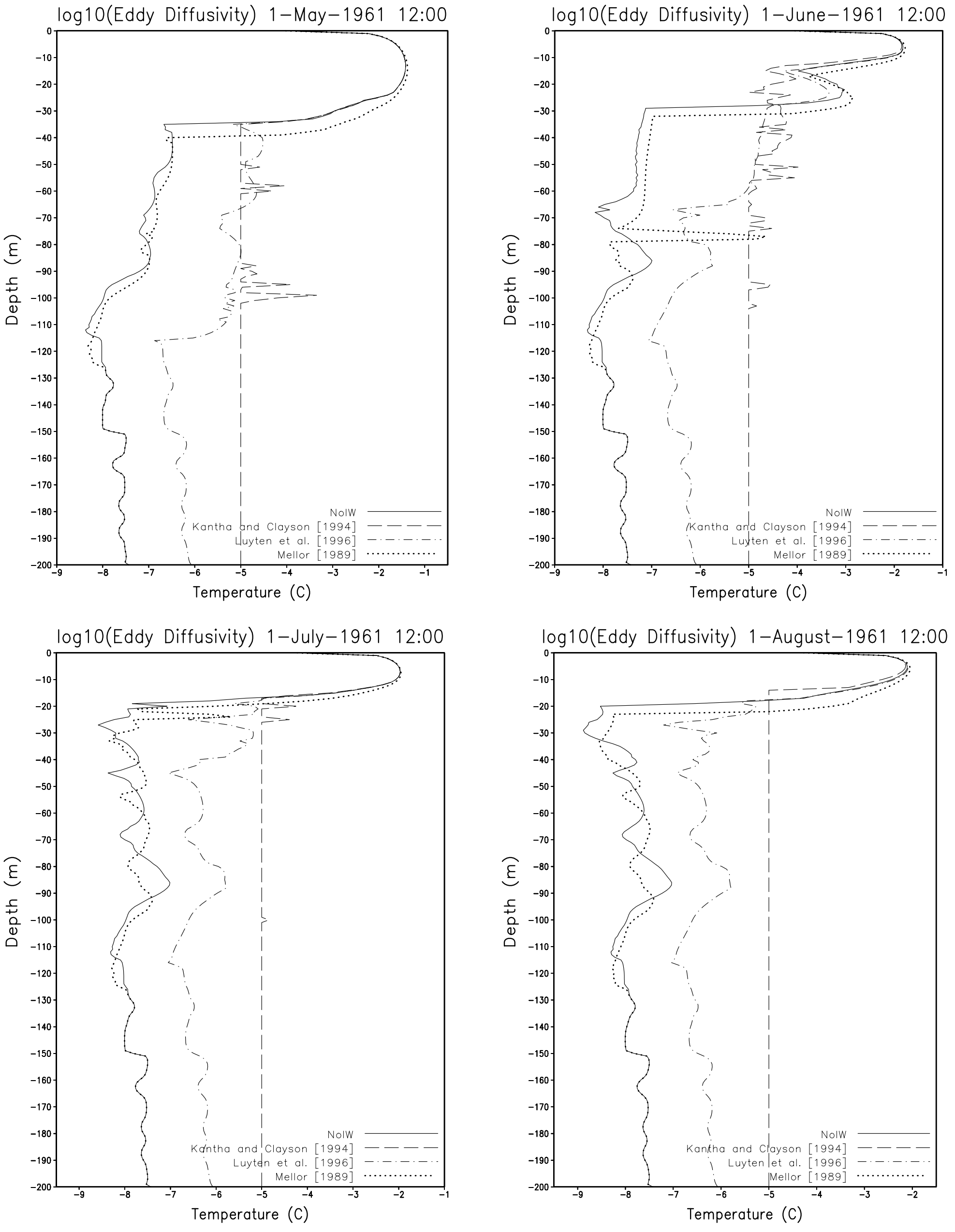

Figure 2.28 : Logarithm of eddy diffusivity in m$^2 s^{-1}$ profiles for four spring and summer dates for OWS_Papa. k-ε model and stability functions from Canuto et al. [2000]

2.4.c Knebel Vig

In-situ measurements of dissipation rate of turbulent kinetic energy have become a near standard technique in the last decades. They have helped in the comprehension of mixing processes in the ocean (*Caldwell and Moum, [1995]*) and constitute the basic tool in turbulence research in natural waters. Classically, the performance of turbulence models was evaluated by contrasting their predictions of SST (Sea Surface Temperature), MLD (Mixed Layer Depth) or salinity and temperature in the column (e.g. *Martin [1985]*) with estimations from real data. Only recently, these microstructure measurements have been contrasted to model predictions in different scenarios: stratified and non-stratified conditions in tidal shelf seas (*Simpson et al. [1996], Burchard et al. [1998], Luyten et al. [1996b]*), the equatorial mixed layer (*Clayson and Kantha [1999]*) or weakly and stratified estuaries (*Burchard et al. [1999], Burchard et al. [2000]*). Comparison of dissipation rate measurements with model predictions is a stringent test for models, although further comprehension of turbulence processes and model performance can be gained from these experiments. An extensive set of measurements must be taken simultaneously with microstructure estimations to be able to compute all of the forcing acting on the system. This is a necessary condition for being able to evaluate the performance of the turbulence model. In this section, the model GOTM has been used to simulate dissipation rate measurements in Knebel Vig, a strongly stratified site during the period of study.

Knebel Vig is a small embayment on the eastern coast of Jutland in Denmark at 56° 13'N, 10° 27'E (figure 2.29). Its shape can roughly be described as quadratic with a side length of 2.5 km. The connection of Knebel Vig to the Kattegatt is a channel less than 1 km wide with a maximum depth of 16 m. Due to the situation in the Kattegat, which connects the Baltic to the North Sea, a strong halocline with a salinity difference of 5 to 10 is existing most of the time. In the framework of the PHASE project, financed by the MASTIII program of the European Commision, dissipation rate measurements have been carried out at a central station in combination with measurements of different forcings from September 7-20, 1997 at different positions in Knebel Vig during a cooling period with strong westerly winds. From September 11 to 13.5, each half hour, 7-10 profiles of dissipation rate have been measured within 10 min at the central station (11 m deep). Since for measuring dissipation rate, the profiler must travel buoyancy driven, two profilers were deployed to get reliable measurements both at the surface and at the bottom. The first profiler was operated in an uprising way by use of a winch, and the other was thrown from a ship, i.e. free falling. Two currentmeters were moored in the area, one at the entrance channel and the other at the measurement point, although unfortunately the currentmeter at the central point did not work. Meteorological measurements of wind speed and direction, relative humidity, cloud cover, solar radiation and air temperature and pressure allowed the computation of momentum and heat fluxes by using bulk formulae (*Kondo [1975]*). Sea surface temperature, also required in these bulk formulae, was taken from the profile casts.

The dynamics of Knebel Vig is determined by meteorological forcing and the dominant conditions in the Kattegat. Tidal range is of about 1 m and river run-off into the embayment is very small. A strong halocline exists during most of the time in the Kattegat as the strong freshwater input in the Baltic causes a two-layered pattern in the connection to the North Sea. Westerly winds induce an inflow of surface waters with low salinity, while easterly winds displace surface waters and cause upwelling of the saltier waters existing below the halocline. Some days before the campaign began, there was a change from easterly to westerly winds, together with a decrease of air temperature. The correlation of wind forcing and currents and thermohaline properties in the inlet can be observed by inspecting figure 2.30 (wind speed and direction and currents at the entrance channel) and figure 2.31 (measured salinity, temperature and dissipation rate of TKE). From the beginning of the period of study, the halocline is rising up to a maximum of 3.5 m below surface on day 11.7. From that moment, there is change in current direction at the entrance channel and a clear two-layer flow is established, with ouflow of bottom water and inflow of surface water. There is a change in wind direction between days 12.2 and 12.5, accompanied by a wind speed maximum of more than 10 $m^3 s^{-1}$. This causes an increase of the velocity shear at the entrance channel on day 12.6. There is an erosion of the halocline from then on, probably induced by this shear increase, although also the peak in near bottom velocity is seen in dissipation rate measurements.

To assess the performance of the model in modelling dissipation rate of TKE, the model was run in such a way that turbulence magnitudes were diagnosed. Temperature and salinity in the model were relaxed to the measured profiles with relaxation time of 30 minutes. As heat fluxes are well known, this relaxation is a good estimation of tracer advection, and the density field is well characterized. Pressure gradients in a 1D model can not be calculated and therefore must be prescribed. Current meter data can be used for recalculating surface slopes following the procedure proposed by *Burchard [1999].* With this method, the pressure gradients are recalculated such that modelled and measured velocities at a certain height above the bottom are identical. The currentmeter moored at the central station failed. Bottom shear stress was estimated from dissipation rate measurements at 1 m near the bed. The log-law relation:

$$\varepsilon = \frac{(u_b^*)^3}{\kappa d_b} \tag{2.104}$$

with κ von Karman constant and d$_b$ the distance to the bottom, can be used for estimating the bottom friction velocity u$_b^*$. If then, a smooth bottom is assumed ($z_0^b = 0.001m$), the current speed at 1 m above the bed can be calculated with the logarithmic law for velocity:

$$u = u_* \kappa \ln \left(\frac{d_b + z_0^b}{z_0^b} \right) \tag{2.105}$$

Near bed current direction could be estimated from currentmeter data, that seemed to give a reliable value of near bottom direction, not of speed.

A k-ε model with stability functions by *Canuto et al. [2000]* was the turbulence closure used in the model simulations. The model set-up we have detailed and the availability of dissipation rate measurements, allow us to examine the performance of the closure in modelling turbulence magnitudes. TKE and dissipation rate are diagnosed in the model from the different forcing and a comparison to real dissipation rate measurements can be done. In figure 2.32, modelled contours of dissipation rate of TKE are presented. In the top pannel, the results with no parameterization of internal mixing are shown. A surface layer and a bottom layer were dissipation rate levels are higher are separated by an internal region were dissipation rate is minimum, both in measurements and in model results. Peaks in near bottom dissipation are well represented, althoug this is influenced by the recalculation of pressure gradients from real dissipation data we have used. The bottom layer extends up to around 4 meters in the model and less in the measurements. Above the halocline, both modeled and observed levels are higher than below. Anyway, the model overestimates dissipation rate levels above the pycnocline by about one order of magnitude. In the internal stratified region between surface and bottom, dissipation rate levels are minimum. The model values decay to the minimum value (less than 10^{-9} W kg^{-1}), while measured levels remain around 10^{-7} W kg^{-1}. *Luyten et al. [1996b]* and *Kantha and Clayson [1994]* parameterizations of internal mixing are shown in the next two panels in figure 2.32. The main features at the bottom and at the surface layers are, as expected, similar in all three panels. A increase of dissipation rate near the pycnocline appears in both internal wave models, although in the *Luyten et al. [1996b]* parameterization, a region of too low values remains. The *Mellor [1989]* parameterization showed very similar results to the *Luyten et al. [1996b]* model, provided that the same minimum of turbulent kinetic energy is chosen (here it was $\mathrm{k_{min}} = 3 \cdot 10^{-6}$ J kg^{-1}). For the *Kantha and Clayson [1994]* parameterization, dissipation rate levels in the interior region are more according to measurements and a smoother transition from the upper to the lower layer is predicted. We must recall that the free parameteres in this model were estimated from open sea data, which might not be realistic for shallower conditions.

In figure 2.33, profiles of dissipation rate for the three parameterizations of internal wave and for no parameterization are compared to measurements for different instants during the simulation. We can see how the *Kantha and Clayson [1994]* approach predicts the more accurate results in the interior region, although discrepancies are still noticeable. The free parameters in the parameterizations ($\mathrm{k_{min}}$ for the *Luyten et al. [1996b]* model and ν^{IW}, ν'^{IW}, ν^{SI} and R_i^{SI}) can act as tuning parameters, although no complete fit can be accomplished by changing them. We can see how at the surface layer, the predicted levels are lower than the measured profiles. For days 12.5 and 13.5, the discrepancy is greater, which can be associated to the high shear levels during those days. In figure 2.34, the results of the k-ε model with stability functions from *Canuto et al. [2000]* and *Kantha and Clayson [1994]* are compared. No major differences can be seen, only maybe a slight greater entrainment is predicted by *Canuto et al. [2000]* stability functions. This can be an indication that the main causes of discrepancy can be some missing processes, not considered by the model. As we noted in section 2.1, at the surface, Langmuir circulation and wave breaking can induce enhanced levels of mixing. In the interior region, tha for this application is a highly stratified shear region, mixing sources are only roughly parameterized via estimations of what could be the average effect on mixing of internal processes, most of them of intermitent nature like internal wave breaking. Advances in the comprehension of stratified shear turbulence in different environments may lead to improved parameterizations. Other effects that can influence dissipation rate measurements and are not considered in the model are sediment dynamics or low Reynolds number flow. However, the measuring of dissipation rate with shear probes, although the most reliable technique for observing turbulence in natural waters, is a complex procedure, and technical problems like the wake or the swaying of the ship might cause unrealistic levels. Consequently, further direct comparisons of measurements of dissipation rate and model results in a wide range of different operation and flow conditions must be undertaken before substantial improvements of turbulence models can be achieved. However, great insight, both in model behavior and in physics is gained from the contrast of model and dissipation rate predictions.

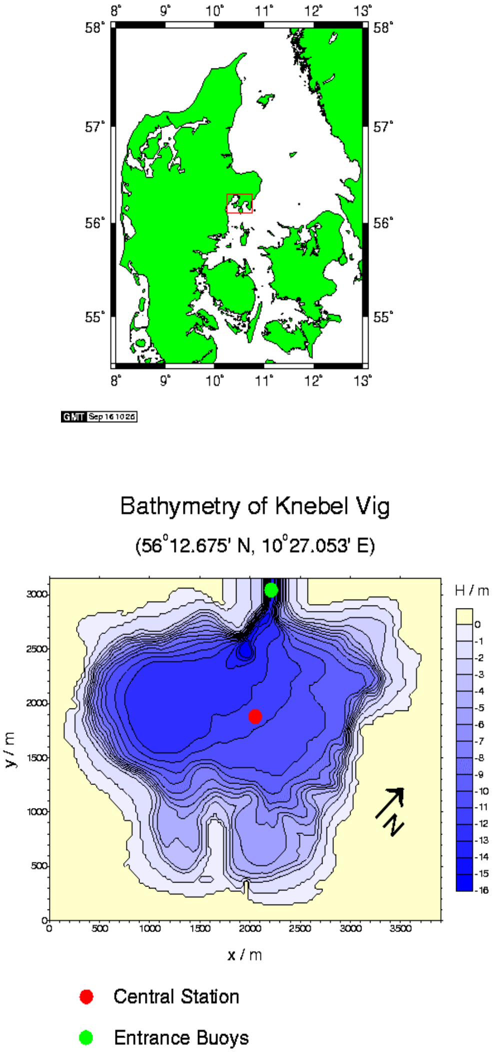

Figure 2.29: Location and bathymetry of Knebel Vig.

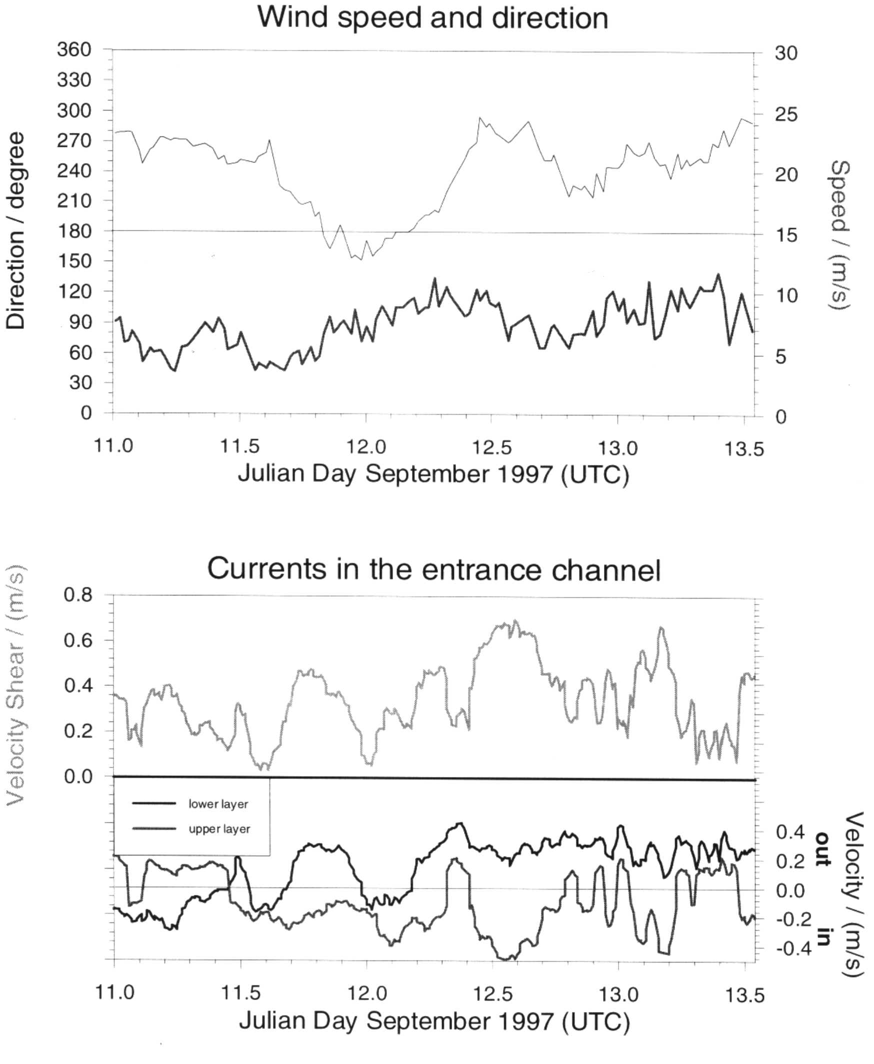

Figure 2.30: Wind speed and direction and currents measured at the entrance channel for the period of study.

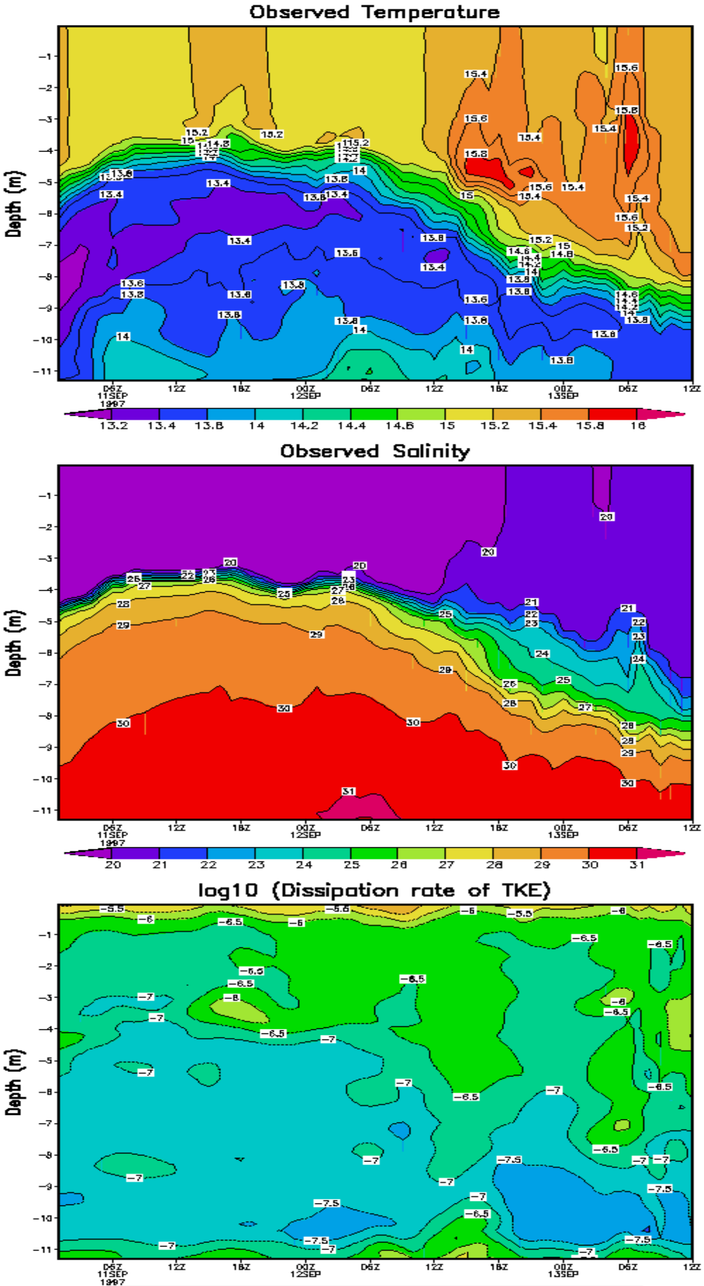
Observed Temperature

Observed Salinity

log10 (Dissipation rate of TKE)

Figure 2.31: Plots of observed magnitudes: temperature (C), salinity and the logarithm of the dissipation rate of TKE (W kg^{-1}).

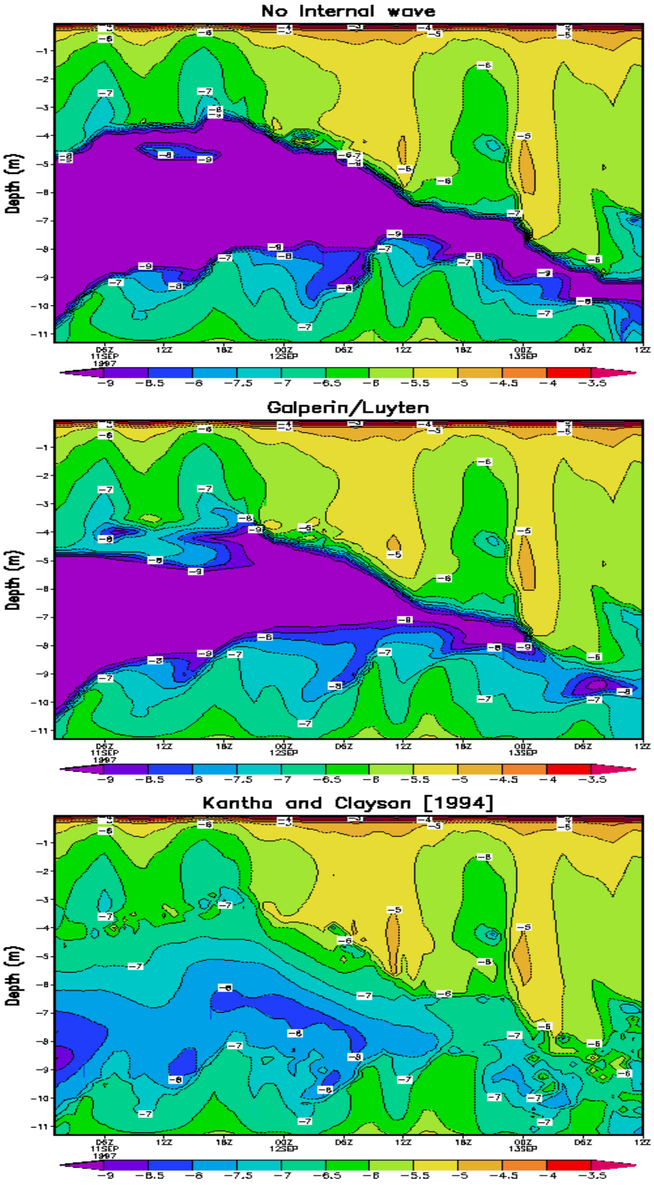

No Internal wave

Galperin/Luyten

Kantha and Clayson [1994]

Figure 2.32: Profiles of dissipation rate of TKE in W kg^{-1} for different instants and for different parameterizations of internal mixing. The turbulence model is a k-ε model with stability functions from Canuto et al. [2000].

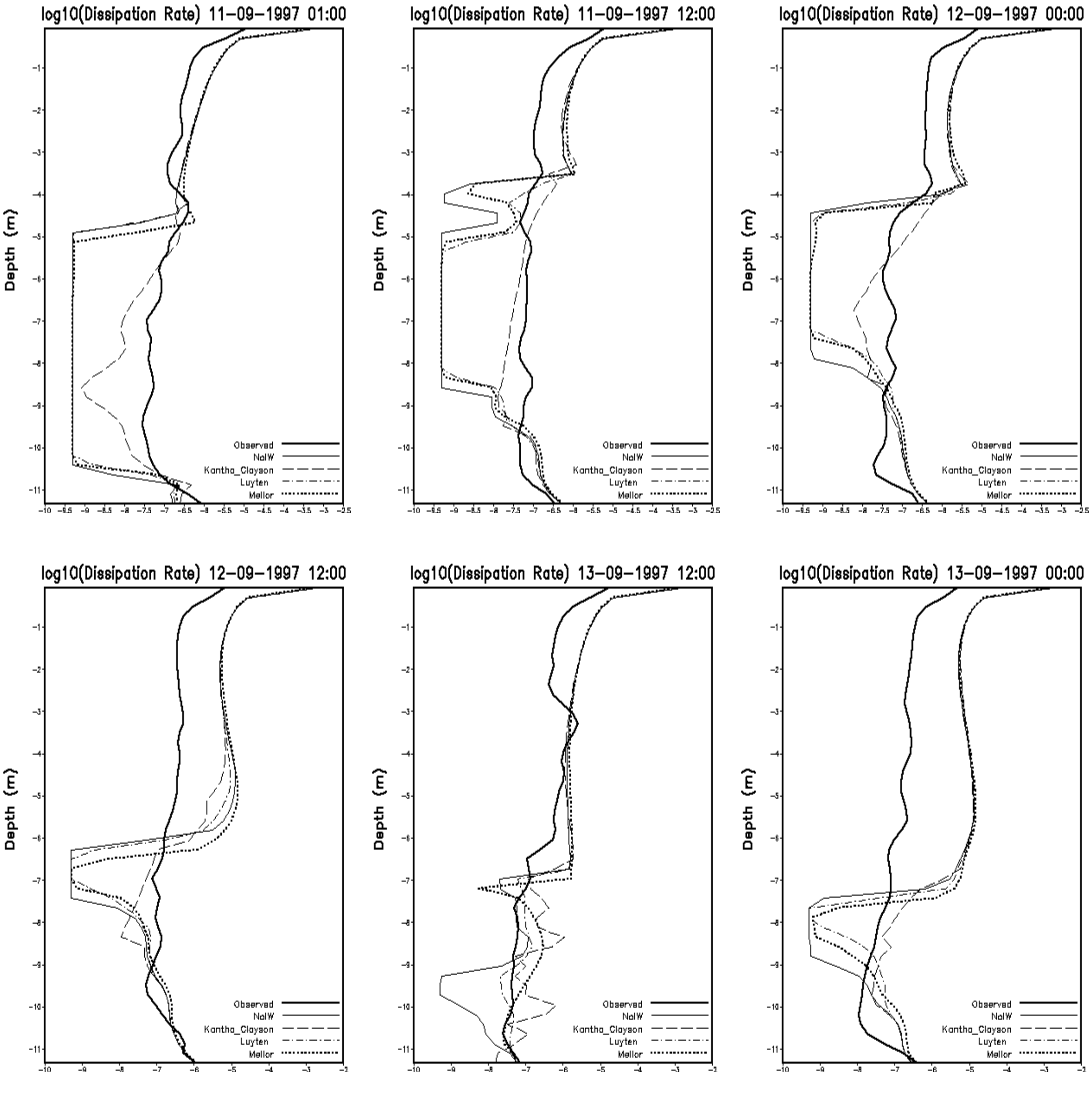

Figure 2.33: Profiles of dissipation rate of TKE in W kg^{-1} for different instants. The effect of the different schemes for parameterizing internal mixing is compared. The turbulence model is a k-ε model with stability functions from Canuto et al. [2000].

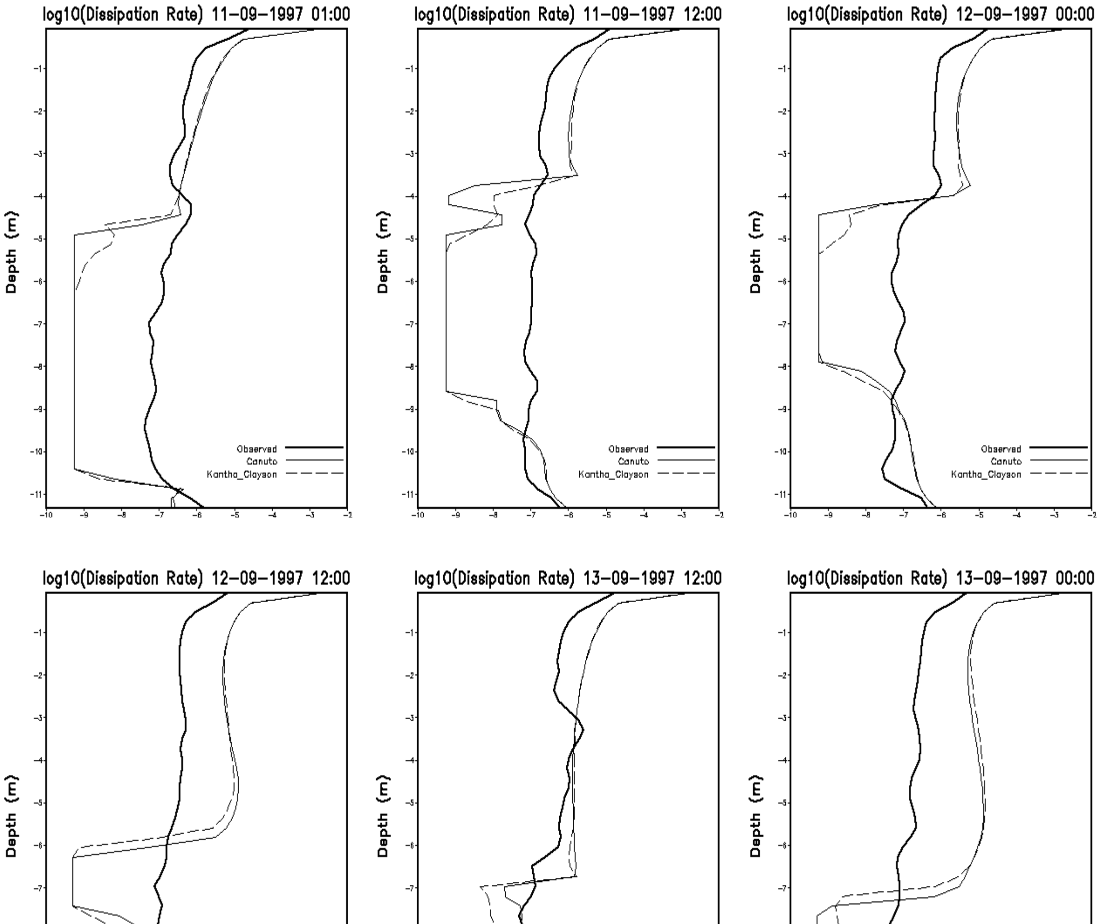

Figure 2.34: Profiles of dissipation rate of TKE in W kg^{-1} for different instants. The effect of the choice of the stability function is shown. The turbulence model is a k-ε model with stability functions from Canuto et al. [2000] or Kantha and Clayson [1994]. No internal wave parameterization is introduced.

3 The 3D model

The 3D model used in this study is MOHID3D, a free surface 3D baroclinic model developed at the Instituto Superior Técnico at the Universidade Tecnica de Lisboa (*Santos, [1995]; Martins, [2000]*). In its initial version (*Santos, [1995]*), a classical finite difference approach was followed in the discretization. Lately, a finite volume discretization has been introduced (*Martins et al. [1998], Martins, [2000]*), that allows the use of a generic vertical coordinate. The initial code was written in standard Fortran77. Now the code has been rewritten in Fortran95 with an object-oriented architecture (*Miranda et al. [2000]*), which has lead to an increase in model robustness and compatibility with other modules (sediment, biochemical, water quality...). The MOHID model has been applied to different coastal and estuarine areas and it has showed its ability to simulate complex features of the flows. Several different coastal areas have been modeled with MOHID in the framework of research and consulting projects. Along the Portuguese coast, different environments have been studied, from river mouths (Douro, Mondego) to coastal lagoons (Ria de Aveiro, Ria Formosa) and broader estuaries (Tagus and Sado estuaries (*Martins et al. [2000]*)). Also the model has been adapted to simulate Galician Rías hydrodynamics (Ría de Vigo (*Taboada et al., [1998], Montero et al. [1999], Montero, [1999]*), Ría de Pontevedra (*Taboada et al.[2000], Villarreal et al. [2000]*) and other Rías (*Pérez Villar et al. [1999]*)). Far from the Atlantic coast of the Iberian Peninsula, some European estuaries have been modeled -Western Scheldt (Holland), Gironde (France) (*Cancino and Neves, [1999]*) and Hellingford (*Leitão, [1997]*)-as well as some coastal estuaries in Brasil (Santos, Fortaleça). Regarding to open sea, MOHID has been applied to the North-East Atlantic region where some processes including the Portuguese coastal current (*Coelho et al. [1994]*), the slope current along the shelf (*Neves et al. [1999]*) and the generation of internal tides (*Neves et al. [1998]*) have been studied and also to the Mediterranean Sea to simulate the seasonal cycle (*Taboada, [1999]*) or the circulation in the Alboran Sea (*Santos, [1995]*).

3.1 Equations

The model solves the three-dimensional incompressible primitive equations. Hydrostatic equilibrium is assumed as well as Boussinesq and Reynolds approximations. All the equations below have been derived taken into account these approximations. The momentum balance equations for mean flow horizontal velocities are, in Cartesian form:

$$\begin{aligned}\partial_t u =& -\partial_x(uu) - \partial_y(uv) - \partial_z(uw) + fv - \frac{1}{\rho_0}\partial_x p \\ &+\partial_x\Big((\nu_H+\nu)\partial_x u\Big) + \partial_y\Big((\nu_H+\nu)\partial_y u\Big) + \partial_z\Big((\nu_t+\nu)\partial_z u\Big), \end{aligned} \tag{3.1}$$

$$\begin{aligned}\partial_t v =& -\partial_x(vu) - \partial_y(vv) - \partial_z(vw) - fu - \frac{1}{\rho_0}\partial_y p \\ &+\partial_x\Big((\nu_H+\nu)\partial_x v\Big) + \partial_y\Big((\nu_H+\nu)\partial_y v\Big) + \partial_z\Big((\nu_t+\nu)\partial_z v\Big) \end{aligned} \tag{3.2}$$

Where u, v and w are the components of the velocity vector in the x, y and z directions respectively, η is the free surface elevation, f the Coriolis parameter, ν_H and ν_t the turbulent viscosities in the horizontal and vertical directions, ν is the molecular kinematic viscosity (equal to 1.3 10^{-6} m^2 s^{-1}), p is the pressure. The temporal evolution of velocities (term on the left hand side) is the balance of advective transports (first three terms on the right hand side), Coriolis force (forth term), pressure gradient (next three terms) and turbulent diffusion (last three terms).

The density ρ is calculated as a function of temperature and salinity by a simplified equation of state (*Leendertsee and Liu, [1978]*)

$$\begin{aligned}\rho =& (5890 + 38T - 0.375T^2 + 3S)/ \\ &((1779.5 + 11.25T - 0.0745T^2) - (3.8 + 0.01T)S + 0.698(5890 + 38T - 0.375T^2 + 3S))\end{aligned} \tag{3.3}$$

that is an approximation for shallow water of the most widely used UNESCO equation (*UNESCO, [1981]*).

The vertical velocity is calculated from the incompressible continuity equation (mass balance equation):

$$\partial_x u + \partial_y v + \partial_z w = 0 \tag{3.4}$$

by integrating between bottom and the depth z where w is to be calculated:

$$w(z) = \partial_x \int\limits_{-h}^{z} udx + \partial_y \int\limits_{-h}^{z} vdy \tag{3.5}$$

The free surface equation is obtained by integrating the equation of continuity over the whole water column (between the free surface elevation η(x,y) and the bottom -h)

$$\partial_t \eta = -\partial_x \int_{-h}^{\eta} udz - \partial_y \int_{-h}^{\eta} vdz \tag{3.6}$$

The hydrostatic approximation is assumed with:

$$\partial_z p + g\rho = 0 \tag{3.7}$$

where g is gravity and ρ is density. If the atmospheric pressure p_{atm} is subtracted from p, and density ρ is divided into a constant reference density ρ_0 and a deviation $\rho^{'}$ from that constant reference density, after integrating from the free surface to the depth z where pressure is calculated, we arrive to:

$$p(z) = p_{atm} + g\rho_0(\eta - z) + g \int_z \eta\rho^{'} dz \tag{3.8}$$

Equation 3.8 relates pressure at any depth with the atmospheric pressure at the sea surface, the sea level and the anomalous pressure integrated between that level and the surface. By using this expression and the Boussinesq approximation, the horizontal pressure gradient in the direction x$_i$ can be divided in three contributions:

$$\partial_{x_i} p = \partial_{x_i} p_{atm} - g\rho_0 \partial_{x_i} \eta - g \int_z \eta \partial_{x_i} \rho^{'} dz \tag{3.9}$$

The total pressure gradient is the sum of the gradients of atmospheric pressure, of sea surface elevation (barotropic pressure gradient) and of the density distribution (baroclinic pressure gradient). This decomposition of the pressure gradient is substituted in Eq. (3.1) and (3.2).

The model also solves transport equations for salinity and temperature:

$$\begin{aligned}\partial_t S = & -\partial_x(uS) - \partial_y(vS) - \partial_z(wS) \\ & +\partial_x\left(\nu_H^{'}\partial_x S\right) + \partial_y\left(\nu_H^{'}\partial_y S\right) + \partial_z\left((\nu_t' + \nu_T^{'})\partial_z S\right) + F_S\end{aligned} \tag{3.10}$$

$$\begin{aligned}\partial_t T = & -\partial_x(uT) - \partial_y(vT) - \partial_z(wT) \\ & +\partial_x\left(\nu_H^{'}\partial_x T\right) + \partial_y\left(\nu_H^{'}\partial_y T\right) + \partial_z\left((\nu_t' + \nu_S^{'})\partial_z T\right) + F_T\end{aligned} \tag{3.11}$$

with $\nu_H^{'}$ and ν_t' the horizontal and vertical eddy diffusivities of salt and temperature (considered to be equal), and $\nu_T^{'}$ and $\nu_S^{'}$ the molecular diffusivities of salt and temperature ($1.1 \cdot 10^{-9}$ and $1.4 \cdot 10^{-7}$ m^2 s^{-1}). The temporal evolution of S and T is the balance of advective transport by the mean flow, turbulent mixing and the contributions of F_T and F_S, the possible sinks or sources of temperature and salinity.

The transport equation of any tracer A that can be coupled to the hydrodynamic, such as sediments, biochemical elements or phytoplankton, has the same structure as salt and temperature equations:

$$\begin{aligned}\partial_t A = & -\partial_x(uA) - \partial_y(vA) - \partial_z(wA) \\ & +\partial_x\left(\nu_H^{'}\partial_x A\right) + \partial_y\left(\nu_H^{'}\partial_y A\right) + \partial_z\left((\nu_t' + \nu_A^{'})\partial_z A\right) + F_A\end{aligned} \tag{3.12}$$

3.2 Discretization

3.2.a Spatial discretization: Finite volume approach

The model uses a finite volume approach (*Chippada et al. [1998]; Martins et al. [1998], [1999], [2000]*) to discretize the equations. In this approach, the discrete form of the governing equations is applied macroscopically to a cell control volume. A general conservation law for a scalar U, with sources Q in a control volume Ω is then written as:

$$\partial_t \int_{\Omega} U d\Omega + \oint_S \vec{F} d\vec{S} = \int_{\Omega} Q d\Omega \tag{3.13}$$

where $\vec{F}$ are the fluxes of the scalar through the surface S embedding the volume. After discretizing this expression in a cell control volume Ω_j where U_j is defined, we obtain:

$$\partial_t (U_j \Omega_j) + \sum_{faces} \vec{F} \cdot \vec{S} = Q_j \Omega_j \tag{3.14}$$

In this way, the procedure for solving the equations is independent of cell geometry. Actually, the cell can have any shape with only some constraints (see *Montero [1999]* or *Martins [2000]*) since only fluxes among cell faces are required. Therefore, a complete separation between physical variables and geometry is achieved (*Hirsch, [1992]*). As volumes can vary in the course of the calculus, geometry is updated in every time step after computing the physical variables. Moreover, the spatial coordinates are independent, and any geometry can be chosen for every dimension. Cartesian or curvilinear coordinates can be used in the horizontal and a generic vertical coordinate with different subdomains can be used in the vertical. This general vertical coordinate allows minimizing the errors of some of the classical vertical coordinates (Cartesian, sigma, isopycnal) as pointed in (*Martins et al. [2000]*).

The volume element used in this work is shown in figure 3.1. Only a vertical degree of freedom is allowed, and the grid is Cartesian orthogonal in the horizontal. The grid is staggered in the horizontal in an Arakawa C (*Arakawa and Lamb, [1977])* manner, i.e. horizontal velocities are located in the center of the west (u-velocity) and south (v-velocities) faces, while elevation, turbulent magnitudes and tracers are placed in the center. Also a staggering in the vertical is used, with vertical velocity w, tracers and turbulent magnitudes vertically placed in the top and bottom faces and horizontal velocities and elevation in the center of the element (in vertical).

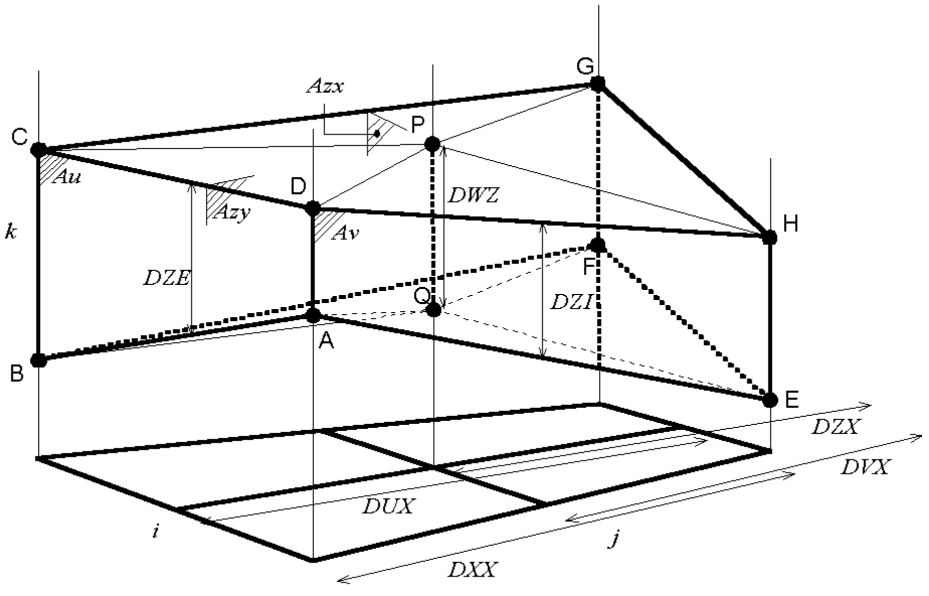

Figure 3.1: Volume element used in the discretization, with indication of surfaces and distances. A denotes surface and D distance. A_{u_i} is the surface where the horizontal velocity u_i is calculated, AX_iX_j is the area of the intersection between the control volume and the plane X_iX_j and D denotes distances between different points in the staggered grid, for example DUX denotes the distance between u points in the x direction.

3.2.b Temporal discretization: semi-implicit ADI algorithm

The temporal discretization is carried out by means of a semi implicit ADI (Alternate Direction Implicit) algorithm, introduced by Peaceman and Racford in 1955 (*Fletcher, [1991]*). This algorithm computes alternatively one component of horizontal velocity implicitly while the other is calculated explicitly. The resulting equation system is a tridiagonal one, that can be solved by Thomas algorithm in a efficient and quick way. This allows to preserve the stability advantages of implicit methods without the draw-backs of computational expensiveness and associated phase errors. A longer time-step can therefore be used. Two different discretizations are coded in the model: a 4 equations one with two time levels per iteration- the S21 scheme (Eq. 3.15) by *Abbott et al. [1973]*- and the 6 equation algorithm by *Leendertsee, [1967]*, more convenient when intertidal zones are to be modeled, since velocities are updated every half time step. In the present study, only the S21 scheme will be used:

$$\begin{aligned} \eta^{t+1/2}(u^{t+1}, u^{t}, v^{t+1/2}, v^{t-1/2}) &\longrightarrow u^{t+1} \longrightarrow \\ w^{*\,t+1/2} \xrightarrow{Geometry\ update} w^{t+1/2} &\longrightarrow S^{t+1/2}, T^{t+1/2} \longrightarrow \\ \eta^{t+1}(u^{t}, u^{t+1}, v^{t+3/2}, v^{t+1/2}) &\longrightarrow u^{t+3/2} \longrightarrow \\ w^{*\,t+1} \xrightarrow{Geometry\ update} w^{t+1} &\longrightarrow S^{t+1}, T^{t+1} \end{aligned} \tag{3.15}$$

Each iteration is divided in two half steps. In the first half step, the free surface elevation η and then one of the horizontal velocities (u) are computed in an implicit way. The required value of the other velocity is taken from the previous time step. A vertical velocity w^* is computed from the continuity equation. Then, geometry is updated and the vertical velocity is corrected. The same process is followed in the next half step, but for the other component of horizontal velocity. In this diagram, salinity and temperature are computed each half step. As internal modes are much slower than external modes, S and T can be updated with a longer time step without losing accuracy and stability.

3.2.c Discretization of the different processes

A sketch of the discretization will be given below. A full description of the discretization may be found in *Martins, [2000]* and *Montero, [1999].*

3.2.c.1 Free surface equation

Free surface elevation is calculated by integrating the continuity equation (Eq. 3.4) over the whole water column. In the finite volume approach, this integration is done via a summation the volume fluxes over all water column cells. For the S21 discretization and the first half time step, it reads:

$$\frac{\eta_{ij}^{t+1/2}-\eta_{ij}^{t}}{\Delta t/2} = \frac{1}{A_{h_{ij}}}\begin{bmatrix} \frac{1}{2}\left(\sum_{kbot}^{k\max} U_{ijk}^{t+1} A_{u_{ijk}}^{t} + \sum_{kbot}^{k\max} U_{ijk}^{t} A_{u_{ijk}}^{t}\right) \\ -\frac{1}{2}\left(\sum_{kbot}^{k\max} U_{ij+1k}^{t+1} A_{u_{ij+1k}}^{t} + \sum_{kbot}^{k\max} U_{ij+1k}^{t} A_{u_{ij+1k}}^{t}\right) \end{bmatrix} + \frac{1}{A_{h_{ij}}}\begin{bmatrix} \frac{1}{2}\left(\sum_{kbot}^{k\max} V_{ijk}^{t+1/2} A_{v_{ijk}}^{t} + \sum_{kbot}^{k\max} V_{ijk}^{t-1/2} A_{v_{ijk}}^{t}\right) \\ -\frac{1}{2}\left(\sum_{kbot}^{k\max} V_{i+1jk}^{t+1/2} A_{v_{i+1jk}}^{t} + \sum_{kbot}^{k\max} V_{i+1jk}^{t-1/2} A_{v_{i+1jk}}^{t}\right) \end{bmatrix} \tag{3.16}$$

where $A_{h_{ij}} = DUX_{ij} \cdot DVY_{ij}$ is the area projected on the horizontal plane. Fluxes are temporally averaged, so the calculus is centered in $t+1/2$. An analogous discretization is carried out for the next half step. The fluxes $U \cdot AU$ and $V \cdot AV$ are obtained from the momentum equation. The discretization of the different terms will be discussed below.

3.2.c.2 Velocity equation

If we discretize equation (3.1) making use of (3.14) and S21 discretization, we arrive to (an equivalent equation is derived for v Eq. 3.2) for every cell u_{ijk} of the grid:

$$\frac{\Omega_{u_{ijk}}^{t}(U_{ijk}^{t+1}-U_{ijk}^{t})}{\Delta t} + \sum_{m=1}^{N\,faces} \vec{F}_m \vec{n} A_m = f_{u_{ijk}} \Omega_{u_{ijk}}^{t} \bar{V}_{ijk}^{t} \tag{3.17}$$

where $\Omega_{u_{ijk}}^{t}$ is the volume of the computation cell for U_{ijk} and $f_{u_{ijk}}$ is the value of the Coriolis parameter for that cell. The value $\bar{V}_{ijk}^{t}$ represents the average value of the v-component of the flow on this cell. The second term on the left hand side represents the fluxes of the forces $\vec{F}_m$ through the surface A_m of the cell m. The Coriolis force is the term on the right hand side and the other terms in the equation are included in the summation on the left hand side.

Coriolis term As we can see on the right hand side of Eq.3.17, the Coriolis term is discretized explicitly, although it is well-known that this implies a restriction on Δt ($\Delta t \leq \frac{2}{f}$, with f the Coriolis parameter). This limitation is not critical for coastal applications -for a latitude of 43^o $\Delta t \leq$ 2000 s$\simeq$ 5 h 30 min, that is much bigger than the time steps chosen in these applications.

The other terms in this formulation are seen as fluxes through the surfaces of the control volume, and therefore enter in the second term on the left hand side.

Advective terms In order to guarantee momentum conservation, fluxes into the element must have null divergence. This is accomplished by using in the convective terms the same fluxes obtained in the last computation of elevation and vertical velocity. Convective fluxes are computed in every face of the cell:

$$
\begin{aligned}
-\sum_{m=1}^{N\,faces} \vec{F}_m \cdot \vec{n} A_m = {} & [(U \cdot ufluxU)^t_{ij+1k} - (U \cdot ufluxU)^t_{ijk} + \\
& (U \cdot ufluxV)^t_{i+1jk} - (U \cdot ufluxV)^t_{ijk} + \\
& (U \cdot ufluxW)^t_{ijk+1} - (U \cdot ufluxW)^t_{ijk}]
\end{aligned}
\tag{3.18}
$$

with $ufluxU_i$ denotes the flux of U_i through the cell of calculus of u. A mixed scheme upwind-central differences is used for computing $ufluxU_i$ (*James, [1987], Santos [1995]*). Horizontal advective fluxes are discretized explicitly as the restriction that surface waves impose on stability is small for the characteristic range of velocities. The vertical advective term can give problems if the layer thickness is small, as can happen in shallow zones with sigma grids. Two solutions to this problem have been introduced in the model: an implicit discretization or neglecting this term in those regions. We will use the first option.

Barotropic pressure gradient The restriction of surface waves on stability lead to the implementation of the semi-implicit algorithm, so this term limits stability and consequently is discretized implicitly. For the cell u_{ijk} and the first semi-step:

$$
-\sum_{m=1}^{N\,faces} \vec{F}_m \cdot \vec{n} A_m = \frac{1}{\rho_0}\left[(P^{t+1/2}_{atm_{ij-1}} - P^{t+1/2}_{atm_{ij}}) + \rho_0 g(\eta^{t+1/2}_{ij-1} - \eta^{t+1/2}_{ij})\right] A^t_{u_{ijk}} \tag{3.19}
$$

This expression, when substituted in the equation for the free surface, results in a tridiagonal system, that is solved by Gaussian elimination. In the equation for velocities, the values of η are already known, which allows the explicit discretization of this term for introduction in momentum equations.

Baroclinic pressure gradient Internal modes do not introduce a stringent restriction on stability, so they can be discretized explicitly. The fluxes induced by this term through the faces of a u$_{ijk}$ cell are:

$$- \sum_{m=1}^{N\,faces} \vec{F}_m \cdot \vec{n} S_m = \frac{g}{\rho_0} \left(\sum_{l=k+1}^{kmax} (\rho'^{t}_{ij-1l} DWZ_{ij-1l}) + \rho'^{t}_{ij-1k} \Delta z^{t}_{ij-1k} \right) A^{t}_{u_{ijk}}$$

$$- \left(\sum_{l=k+1}^{kmax} (\rho'^{t}_{ijl} DWZ_{ijl}) + \rho'^{t}_{ij-1k} \Delta z^{t}_{ijk} \right) A^{t}_{u_{ijk}} \tag{3.20}$$

where Δz^{t}_{ijk} represents the vertical distance from the cell top to the velocity point and arises as a consequence of the vertical staggering of the grid (ρ' is not defined in the same point as the u-velocity).

Horizontal diffusive fluxes Horizontal diffusive fluxes are computed in every vertical face of the cell, applying that fluxes are normal to these faces:

$$- \sum_{m=1}^{N\,faces} \vec{F}_m \cdot \vec{n} A_m = (F^{t}_{ij-1/2k} Azx^{t}_{ij-1k} - F^{t}_{ij+1/2k} Azx^{t}_{ijk}) +$$

$$(F^{t}_{i-1/2jk} \frac{Av^{t}_{ijk} + Av^{t}_{ij-1k}}{2}$$

$$-F^{t}_{i+1/2jk} \frac{Av^{t}_{i+1jk} + Av^{t}_{i+1j-1k}}{2}) \tag{3.21}$$

Fluxes for x direction are:

$$F_{ij-1/2k} = \nu^{t}_{H_{ij-1k}} \frac{U^{t}_{ijk} - U^{t}_{ij-1k}}{DUX_{ij-1}} \tag{3.22}$$

and for the y-direction:

$$F_{i-1/2jk} = \nu^{t}_{H_{i-1/2j-1/2k}} \frac{U^{t}_{ijk} - U^{t}_{ij-1k}}{(DYY_{ij} + DYY_{i-1j})/2} \tag{3.23}$$

where the horizontal viscosity coefficient ν^{t}_{H} is interpolated to the appropriate point.

Vertical diffusion These terms must be discretized implicitly as the restriction imposed by an explicit discretization on the time step is strict for the resolution we will use.

$$- \sum_{m=1}^{N\,faces} \vec{F}_m \cdot \vec{n} A_m = (F^{t+1}_{ijk-1/2} - F^{t+1}_{ijk+1/2}) A^{t}_{h_{ij-1/2}} \tag{3.24}$$

with fluxes given by the equation:

$$F^{t+1}_{ijk-1/2} = \nu^{t}_{ij-1/2k-1} \frac{U^{t+1}_{ijk} - U^{t+1}_{ijk-1}}{DUZ^{t}_{ijk-1}} \tag{3.25}$$

3.3 Boundary conditions

3.3.a Free surface

All advective fluxes across the surface are assumed to be null. This condition is imposed by assuming that the vertical flux of W at the surface is null:

$$Wflux|_{surface} = 0 \tag{3.26}$$

Diffusive flux of momentum is imposed explicitly by means of a wind surface stress $\vec{\tau}_W$:

$$\nu \frac{\partial \vec{v}_H}{\partial z}|_{surface} = \vec{\tau}_W \tag{3.27}$$

Wind stress is calculated according to a quadratic friction law:

$$\vec{\tau}_W = C_D \rho_a \vec{W} \left| \vec{W} \right| \tag{3.28}$$

where C$_D$ is a drag coefficient that is function of the wind speed, ρ_a is air density and $\vec{W}$ is the wind speed at a height of 10 m over the sea surface.

Temperature and salinity advective fluxes are imposed null. Other fluxes of heat and freshwater are introduced as source/sink terms in transport equations (3.10) and (3.11).

3.3.b Bottom boundary

Also at the bottom, advective fluxes are imposed as null and diffusive flux of momentum is estimated by means of a bottom stress, that is calculated by a non-slip method with a quadratic law that depends on the near-bottom velocity. So, the diffusive term at the bottom is written as:

$$\nu \frac{\partial \vec{v}_H}{\partial z}|_{bottom} = C_D \vec{v}_H \left| \vec{v}_H \right| \tag{3.29}$$

C_D is the bottom drag coefficient that is calculated with the expression:

$$C_D = \left(\frac{\kappa}{log\left(\frac{z+z_0^b}{z_0^b}\right)} \right)^2 \tag{3.30}$$

where κ is von Karman constant and z_o^b is the bottom roughness length. This quadratic law is derived from the logarithmic law of the wall near boundaries characteristic of boundary layers, as the bottom velocities are located half a grid box above the bottom. This term is calculated semi-implicitly following *Backhaus [1985]* for the sake of numerical stability.

No fluxes of salinity and temperature are considered at the bottom.

3.3.c Lateral closed boundaries

At these boundaries, the domain is limited by land. For the resolution we are using, this lateral boundary layer is resolved, so a impermeable, free slip condition can be used:

$$\frac{\partial \vec{v}_H}{\partial n} = 0 \tag{3.31}$$

$$\vec{v} \cdot \vec{n} = 0 \tag{3.32}$$

In the finite volume formalism, this conditions are implemented straightforwardly by specifying zero normal water fluxes and zero momentum diffusive fluxes at the cell faces in contact with land.

3.3.d Open boundaries

Open boundaries arise from the necessity of confining the domain to the region of study. The values of the variables must be introduced there such that it is guaranteed that information about what is happening outside the domain will enter the domain in a way that the solution inside the domain is not corrupted. Also, waves generated inside the domain should be allowed to go out. There exists no perfect open boundary condition and the most suitable would depend on the domain and the phenomena to be modeled . A recent review paper comparing open boundary conditions in test cases can be found in *Palma and Matano [1999]*. Some different open boundaries are already introduced in MOHID3D (*Santos, [1995], Montero, [1999]*) and some others like FRS (Flow Relaxation Scheme) are in progress.

3.3.e Moving boundaries

Moving boundaries are closed boundaries that change position in time. If there are intertidal zones in the domain, some points can be alternatively covered or uncovered depending on tidal elevation. A stable algorithm is required for modeling these zones and their effect on hydrodynamics of estuaries. A detailed exposition of the algorithms used in MOHID can be found in *Martins et al. [1999]* and *Martins [1999]*.

In table 3.1 a summary of the characteristics of the model MOHID3D is shown. The program architecture characteristics of the code are summarized in table 3.2.

- Three dimensional
- Navier-Stokes incompressible equations
  with Boussinesq, Reynolds and hydrostatic approximations.
- Free surface.
- Baroclinic
- Finite Volume Discretization:
  - Cartesian Horizontal Coordinates. Arakawa C staggered grid. Vertical staggering.
  - Generic Vertical Discretization.
    (Sigma, Cartesian, Lagrangian, Isopycnical or combination)
- ADI semi-implicit temporal discretization:
  - 4 equations (S21 Abbott).
  - 6 equations (Leendertsee).
- Explicit discretization:
  Coriolis term,
  Baroclinic pressure gradient,
  Horizontal advection,
- Implicit discretization:
  Barotropic Pressure Gradient,
  Vertical Diffusion,
  Vertical Advection,
  Bottom friction
- Turbulence module for vertical mixing with different 0, 1 and 2 equation closures.
- Smagorinsky or Constant Parametrization of Horizontal mixing
- Horizontal Advection Schemes for Tracers: mixed scheme (Upwind-Central Differences), TVD.
- Drying and flooding algorithm for simulating intertidal zones.

Table 3.1: Characteristic of the model MOHID3D.

- Fortran 95.
- Object Oriented Architecture.
- Fully modular.
- Check for errors.
- Generic Subroutine for Transport Equation for Tracers.
- Model parameters and computation options read in by KEYWORDS.
- Different options for initializing fields.
- Different standard output formats (ASCii, HDF, NetCDF COARDS-compliant)
- Pre- and post-processing toolkit
- Graphical User Interface

Table 3.2: Characteristic of the code MOHID2000

4 The Ría de Pontevedra

4.1 The area

The Ría de Pontevedra (fig. 4.1) is a coastal embayment about 20 km long that gets broader in the NE-SW direction. From the river boundary to the island of Ons, the Ría has a mean depth of 31 m, a surface of 141 km^2 and a mean volume is of 3450 Hm^3 (*Ibarra and Prego, [1997]*). The Ría may be considered as an extension of the river Lérez valley where there is tidal influence. From the mouth of the river Lérez, depth increases gradually towards open sea. Near the river mouth, a small island -the island of Tambo- can be seen. The presence of another island (the Island of Ons) at the open sea boundary shelters the Ria from the frequent swell and forces the exchange with the open sea to take part through two entrances. The south entrance is rather broad (7 km) and deep (60 m), while the north one is smaller (3.7 km) and shallow (14 m). The Ría de Aldán is another characteristic feature. It is a small embayment near the south entrance, interesting for having some mussel and octopus culture. At the river mouth, the city of Pontevedra is located. Other important villages are Marín and Sanxexo, on the south and north shore. These settlements increase their populations in summer months, which increases the sewage discharges and the pressure on the ecosystem. Some industries are located near Pontevedra city and there is great concern about the impact of their effluents on water quality on the ria. Hydrodynamic studies, both observational and numerical, are a necessary step in the evaluation and management of a productive and valuable system like a ria.

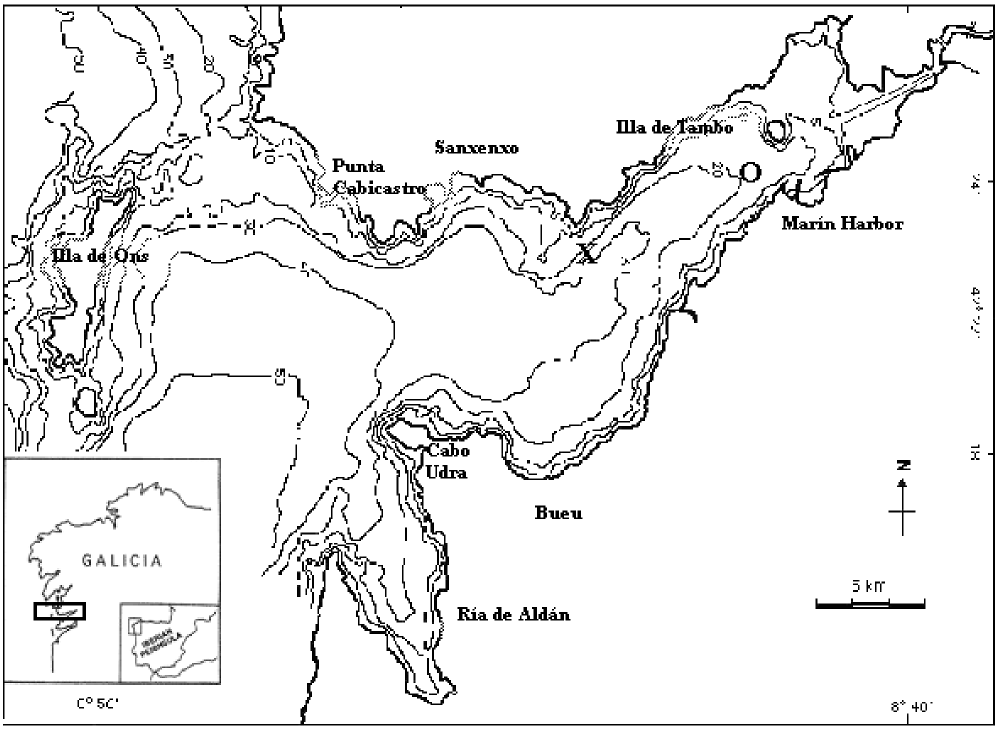

Figure 4.1: Bathymetry of the Ría de Pontevedra and its location in the Iberian Peninsula.

In figure 4.2, the Galician Rias Baixas and the nearby shelf are represented. We can see how to the north and to the south of the ria de Pontevedra, the rias of Arousa and Vigo are located. The Galician shelf is rather narrow and some kilometers offshore, the depth is already of 200 m. To our knowledge, apart from some short-term surveys on the adjacent shelf (*Fraga [1981]*, data from several cruises prior to 1980, *Castro et al. [1994],* data from the Galicia XI cruise 10-14 May 1991), data from 3 days (4 Sep., 21 Sep. and 3 Oct. 1986) in the rias de Pontevedra and Vigo during conditions prior to a red tide event (*Fraga and Prego, [1989]*) and a survey consecutively in the four rias starting north during 4 days (1 day each ria) during a red tide event (*Tilstone et al. [1994]*), there is few published information on the coupled dynamics of the four rias, since many of the studies have focused on one. The topography of the rias has been regarded as a determinant effect in the generation of red tides

(*Tilstone et al. [1991]*) and as an enhancing influence on upwelling (*Castro et al. [1994]*), but further studies are needed to understand how the different rias are coupled.

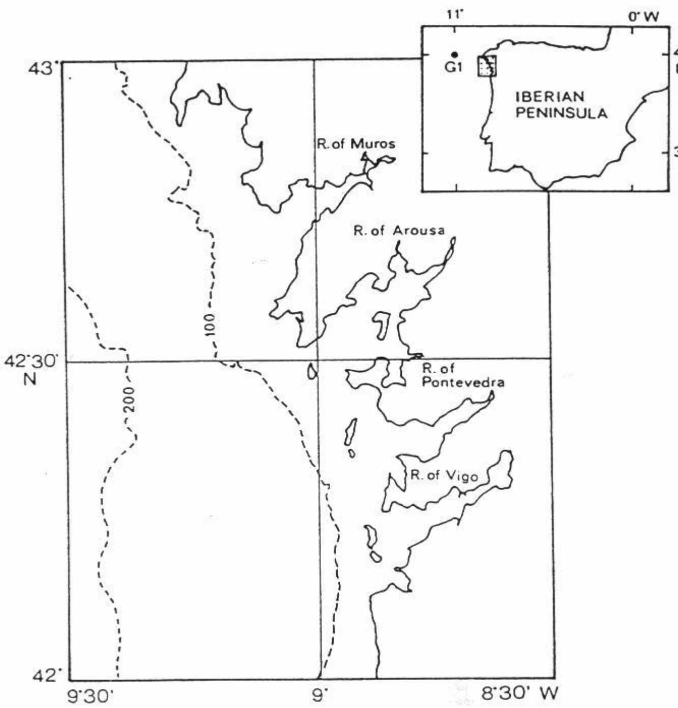

Figure 4.2:Map of the Galician Rías Baixas, showing the relative location of the Ría de Pontevedra.

4.2 Physical Oceanography of the Ría de Pontevedra

Among the Rías Baixas, Vigo and Arousa have been the object of several studies, but only few studies have dealt with the hydrodynamics of the Ría de Pontevedra (*Ruiz-Mateo, [1984], Figueiras et al. [1985],* a review of hydrography, benthic and biogeochemical data by *Ibarra and Prego, [1997]* and the recently submitted *Prego et al. [2000]*). Some of the conclusions drawn up from observations in other Rías are also applicable of this Ría. As the tidal prism is much greater than the river volume flow into the Ría, the tide prevents the river from dominating the circulation. Therefore, the Ría appears to be during most of the year a partially mixed estuary with a two-layered residual pattern, where freshwater flows seawards in the upper layer and water coming from open sea flows upstream in the bottom layer. Anyway, as far as we know, there are no long-term direct measurements of residual circulation in the Rías, although box model (*Otto, [1975], Prego and Fraga, [1992], Rosón et al. [1997]*) and 3D model *(Taboada et al. [1998])* calculations support this picture of mean residual pattern in the nearby Rías (Vigo and Arousa). A transverse (across-channel) component of circulation has been described in some partially mixed estuaries and may play an important role in the dynamics of mixing and sedimentation (*Dyer [1989]*). As far as we know, there are no studies of transverse circulation in Galician Rías, apart from some model results of tidal circulation in the Ría de Vigo (*Montero [1999]*).

4.2.a Forcing

The main forcing factors that affect flows in the area are:

4.2.a.1 Tide

At the Ría de Pontevedra, the tidal forcing is mainly semidiurnal with M2 (amplitude of about 1.1 m) modulated over the spring-neaps cycle by S2 and N2 (of around 0.3 m and 0.2 m amplitude, respectively). The tidal range is about 3 m in average, so the Ría is a mesotidal estuary. In table 4.1, the semiamplitude and phase of the main harmonic constituents in the area are shown. Two tidal gauges were moored in the area during 3 months (1-4-1997 to 30-6-97) in the framework of the project ”Ordenación Integral del Espacio Marítimo Terrestre de Galicia” (”Integral Management of the Maritime-Terrestrial Space from Galicia”), financed by the Consellería de Pesca, Acuicultura e Marisqueo from the Xunta de Galicia. The tidal signal was processed with the Foreman package (*Foreman, [1977]*) to obtain the harmonic constituents. As the tidal gauge series are only three months long, some harmonics can not be resolved and their contribution is assigned to other harmonics. However, longer time series in neighboring harbors[3] indicate that among the unresolved component main constituents only K2 and P1 have a noticeable amplitude. K2 contribution to tide amplitude goes to S2, that has a close frequency. They can only be resolved if a record length longer than 182.6 days (6 months) is available (*Foreman, [1977]).* The first two columns correspond to a tidal gauge near the line Cabicastro-Udra (see figure 4.1), and the last two to a tidal gauge moored near Tambo Islet. Only a short delay is observed between both tidal gauges, so the estuary appears to be synchronous.

Harmonic	Amp(cm)	Phase(deg)	Amp(cm)	Phase(deg)
M_2	110.2533	77.05	110.9065	77.07
S_2	33.1253	101.17	33.3608	100.93
N_2	19.7675	54.85	19.8856	55.31
K_1	8.7363	46.27	8.7488	46.04
O_1	6.5295	321.24	6.5247	321.66
MM	4.0078	136.25	4.1031	129.31
MSF	2.8518	354.33	2.8176	353.22
L_2	2.3094	82.80	2.4850	81.67
Q_1	2.0307	259.51	2.0310	258.07
MU_2	1.2623	69.24	1.2815	68.14
M_3	0.7084	296.73	0.6134	295.20
M_4	0.7952	236.20	0.8198	236.22
NO_1	0.5792	168.72	0.6172	170.86
EPS_2	0.5513	54.96	0.6419	69.86

Table 4.1: Semi-amplitude and phase of main tidal constituents in the area, computed from a 3 month time-series of moored tidal gauges in the area. The first two columns correspond to a tidal gauge near the line Cabicastro-Udra (see figure 4.1), and the last two to a tidal gauge moored near Tambo Islet.

---

[3] Tidal gauge series analysis in Vigo and Vilagarcía de Arousa harbors are available from REDMAR (Red de Mareógrafos del Estado, State Tidal Gauge Network) http:\\www.puertos.es

If, from this values, the form factor (*Dietrich, [1963]*) is computed, the semidiurnal character of the tide is revealed. The form factor is a ratio between the amplitudes of the main diurnal constituents (K_1 and O_1) to the semidiurnal (M_2 and S_2):

$$F = \frac{K_1 + O_1}{M_2 + S_2}$$

The tide is then said to be:

i) semidiurnal if $0 \leq F \leq 0.25$,

ii) mixed if $0.25 < F < 3.00$,

iii) diurnal, if $F \geq 3$.

For the Ría, F=0.1, so the tide has a marked semidiurnal character.

Bottom friction affects the propagation of the tidal wave in a non-linear process which depends on the square of the velocity, and consequently, friction is greater in shallow waters. The frictional distortion of tide can be quantified through the analysis of the contributions of the overtides of M_2 (M_4, M_6, etc) to the tide. The main part of the asymmetry of the tide curve can be represented by the superposition of M_2 and M_4:

$$A = a_{M_2} cos(\omega t - \theta_{M_2}) + a_{M_4} cos(\omega t - \theta_{M_4})$$

where a and θ are the amplitude and phase of tidal height and ω is the frequency of the harmonic constituent. The elevation amplitude ratio (a_{M_2}/a_{M_4}) is a measure of the distortion of the tide and the relative phase of M_4 to M_2 ($2M_4 - M_2 = 2\theta_{M_4} + \theta_{M_2}$) indicates if the system is ebb (phase=$0 - 180^o$) or flood (phase=$180 - 360^o$) dominant. For the Ría at the entrance $a_{M_2}/a_{M_4} = 7.39 \cdot 10^{-3}$, and the relative phase $2\theta_{M_4} + \theta_{M_2} = -82.08$, so this distortion is small and only results in a slight longer duration of flood. Near the river mouth, the distortion is of the same small order of magnitude ($a_{M_2}/a_{M_4} = 7.21 \cdot 10^{-3}$)

4.2.a.2 Wind and meteorological forcing

The climate in this region is determined by the movement of the mean location of the Azores High relative to the Iceland low and Galicia between winter and summer. In the winter, the mean position of the high is to the south from Galicia, which allows fronts to reach the coast and results in SW winds and rain as predominant conditions. In the summer, the mean position is displaced northwards, and anticyclonic conditions with northerly winds and sunny weather are usual. Therefore, we can classify the climate as Atlantic with a summer dry season. Further information about weather situations may be found in the *Atlas Climático de Galicia [1999]*. The annual mean rainfall is of 1300 mm, with a seasonal maximum in winter and a seasonal minimum in the summer. This is illustrated in figures 4.3 and 4.4, where monthly mean precipitation and monthly mean temperature are plotted for two meteorological stations, one near the river boundary (Pontevedra) and one in the middle part of the Ría (Marín). The annual mean temperature is 14.8 C in Pontevedra and 12.9 C in Marín. The mean thermal amplitude range is of 11.5 C in Pontevedra and 9.8 C in Marín. As characteristic of temperate latitudes in the north hemisphere, a clear seasonal cycle is observed, with maximum temperatures in the summer and minimum in the winter, with a rather small variation range 10 C, consequence of the smoothing influence of sea on the climate of coastal areas.

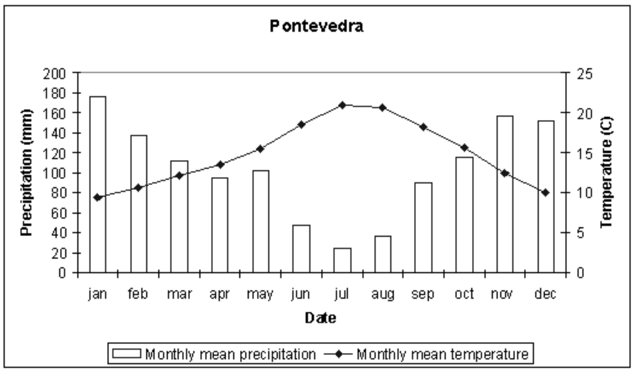

Figure 4.3: Monthly mean temperature and precipitation in Pontevedra. From Atlas Climático de Galicia [1999]

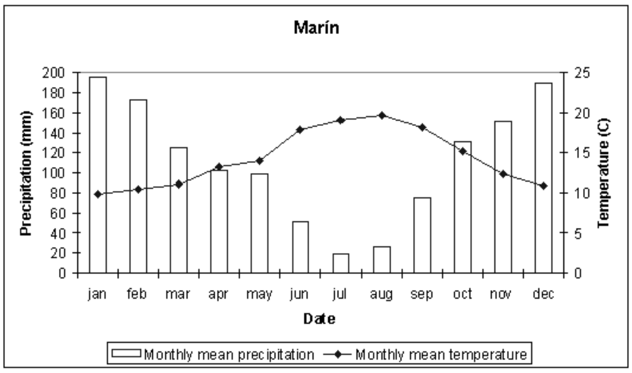

Figure 4.4: Monthly mean temperature and precipitation in Marín. From Atlas Climático de Galicia [1999]

The wind patterns in the estuary are both determined by mesoscale structures and local influences. The mesoscale dynamics results in predominant SW winds in the winter and N winds in the summer. The hilly relief of land around the Ría influences wind flow, causing funneling, and winds to flow predominantly along the main axis of the Ría. The same orientation is showed by breezes and katabatic winds (*Chase, [1974], deCastro et al. [2000]*).

4.2.a.3 Fresh water input

The river Lérez accounts for about 80% of the river discharge into the Ría. In figure 4.5, the mean monthly run-off for the period 1980-1992 is plotted (data from estimations of run-off at the mouth by Prego and Vergara, [1998]). This cycle can be considered as the climatic reference. It oscilates between a maximum monthly average of 80 m^{3}s^{-1} in the winter and a minimum of 4 m^{3}s^{-1} in the summer time, as expected from the different rainfall rate. After some intense rainfall episodes, the run-off may be much bigger, and reach peaks of 300 m^{3}s^{-1}. Some effluents from other minor rivers and city or industry outfalls may have a local importance. Due to the relative low run-offs, the river influence on circulation is mainly baroclinic, not advective. The density gradient between river freshwater and the adjacent coastal waters can support buoyancy driven flows that account for much of the non-tidal variability.

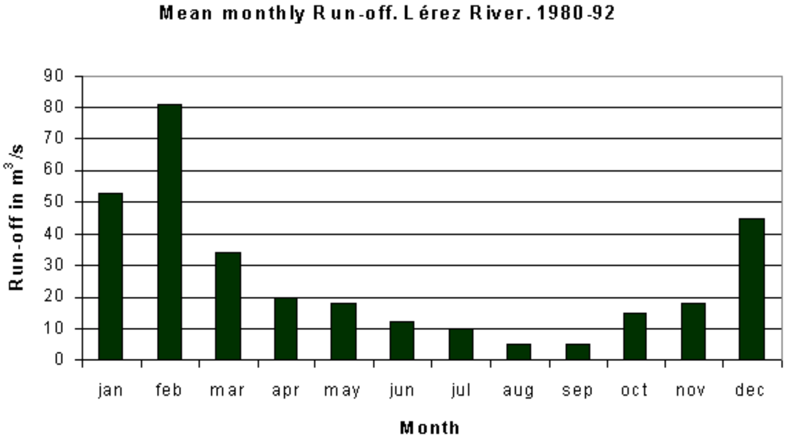

Figure 4.5: Mean monthly run-off in m^3 s^{-1} for the period 1980-1992. Data from Vergara and Prego, [1997]

4.2.a.4 Density forcing

The subsurface water mass outside the Ría is ENACW (Eastern North Atlantic Central Water). *Fraga [1981]* describes the presence of two subsurface water masses on the Galician shelf. To the west, typical North Atlantic Central Water (NACW) appears with TS properties that follow the correlation S=35.586+0.116(T-11). To the north, he describes highly modified NACW, with TS properties described as S=35.565+0.096(T-11). Both water masses are similar to those described in *Fiúza [1984]*. He distinguishes two water masses of different origins. A lighter, relative warm and salty branch following the line connecting 13.5 C, 35.8 and 18.50 C, 36.75, that appears to be formed along the Azores Front at about 35^o N, so it was named as ENACW_{st}, i.e., ENACW of subtropical origin (*Ríos et al. [1992], Fiuza et al. [1998]*). The other branch, a less saline and colder branch follows the line connecting 10 C, 35.40 and 12.20 C, 35.66. Its origin is the Celtic Sea North of 46^o N, so it was named as ENACW of subpolar origin (*Ríos et al. [1992], Fiuza et al. [1998]*). These two segments are connected by a line, which has ranges of temperature and salinity that coincide with the NACW defined by *Helland-Hansen and Nansen [1926].*

Subsurface water masses lie at a mean depth of 100 m from November to January and by March this mean depth is of 50 m. In the summer, when upwelling favorable conditions dominate, this water lies very close the surface or it can even reach surface. Above the mean depth of the water mass, mixed surface waters are found (*Fraga, [1981]*). The Rías Baixas are located near the northern boundary of the Canarian-Portuguese upwelling system. In late spring and summer, upwelling favorable winds are usual, and ENACW is upwelled into the Ría, renewing nutrients. Some authors have estimated that upwelling increases residual circulation inside the Ria de Vigo (*Prego and Fraga, [1992]*).

4.2.b Spatio-temporal variability of thermohaline properties

In the framework of the project *"La hidrodinámica y el ciclo biogeoquímico del silicio"* (*Hydrodynamics and the biogeochemical cycle of silicon*), financed by the CICYT (Comisión Interministerial de Ciencia y Tecnología), the Ría was surveyed fortnightly during one year, from October 1997 to October 1998. CTD casts in seventeen different points in the Ría (figure 4.6), provided a spatial picture of the distribution of salinity and temperature. This CTD coverage was accompanied by measurements of chemical properties in some significant stations in order to link the effect of hydrodynamics in the cycle of key elements as silicon. Nine stations were monitored along the main axis of the Ría, ending at open sea after passing through the south entrance. One station at the north entrance, one near Ons island and one in-between station 0 and 9 completed the monitoring of the outer section of the Ría. In the intermediate region, two transversal sections were monitored: 12-4-11 in the line Sanxenxo-Bueu and 13-6-14 near Tambo Island. The most interior region was monitored with three stations: one to the north of Tambo Island, one to the South and one near the river.

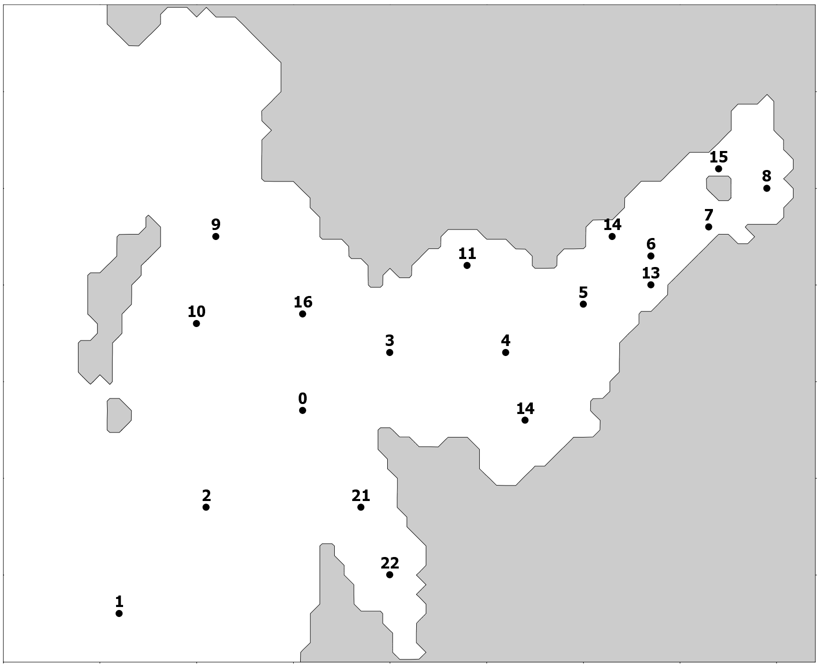

Figure 4.6: Situation of the CTD cast stations during the campaigns Po-97 and Po-98.

4.2.b.1 Annual Cycle

One year, from autumn 1997 to autumn 1998 covered the seasonal cycle, i.e the response of the Ría to the variations of the different forcing along the year. As already discussed, tide has a dominant effect in diurnal and semidiurnal periods, and it has been observed that the spring-neap tidal cycle also influences stratification in coastal areas (*Sharples and Simpson [1995]*). In longer-term scales (days to months), mesoscale atmospheric effects are important. On longer-term scales (annual), the variation of thermohaline properties responds to the variation of heat and freshwater fluxes along the seasons. Differences between years depend on atmospheric and offshore water variations and are difficult to assess in a system like an estuary. We can also quote longer-term scales: interdecadal or even climatic, but not much can be said about these variations in the Ría, as such long-time series of measurements are not available. The annual cycle of rainfall and solar radiation drives the variation of thermohaline properties during the year. We will summarize the evolution observed during the campaign and try to draw some information about the seasonal cycle, although for evaluating it rigorously, several year data would be required.

In figure 4.7, the daily run-off measured at a river gauging station near the river mouth at the limit of tidal influence is plotted for a period from December 1997 to November 1998. This year, the winter maximum was in January and a minimum appeared in August. During December and January, run-off was above 40 $m^3 s^{-1}$. Some intense rainfall episodes increased daily run-off and some peaks are observed in the figure. From late January until March, the year was drier than average, specially February, where run-off decreased under 25 $m^3 s^{-1}$, that is low compared to the climatic mean of 80 $\mathrm{m}^3 s^{-1}$. March was rather dry, especially at the end. April was rainier than average, so run-off resulted in a value ($\sim$40 $m^3 s^{-1}$) above the climatologic (20 $m^3 s^{-1}$). May was also rainy, and run-off was of around 40 $m^3 s^{-1}$, above the climatologic 18 $m^3 s^{-1}$. The climatologic low run-off in summer months also was characteristic of this year.

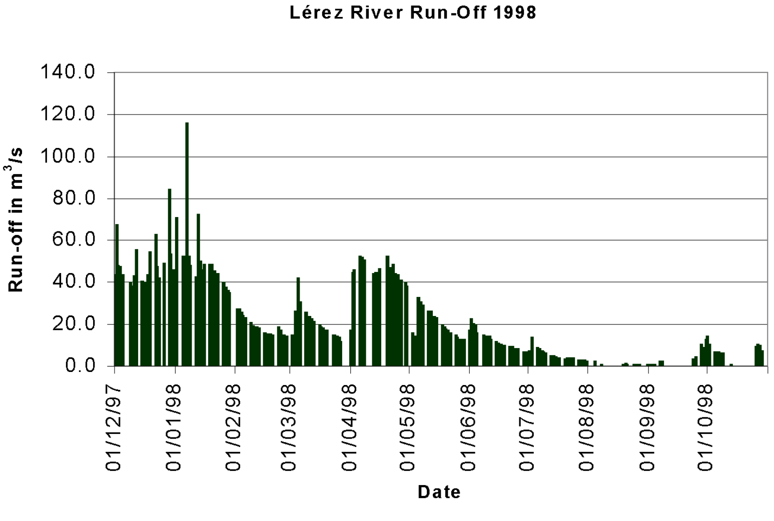

Figure 4.7: Daily river run-off in $\mathrm{m}^3\ \mathrm{s}^{-1}$ measured at the mouth of the River Lérez.

As commented in section 4.2.a.2, northerly winds are prevailing offshore in late spring and summer, and southerly winds appear during the winter. Upwelling is driven by northerly winds that move surface waters offshore, which originates a replacement of these water by bottom waters. The intensity of upwelling-induced flow has been classically estimated from the wind stress by the upwelling index I_w (*Bakun, 1973*):

$$I_w = 1000\frac{\vec{\tau}_N}{f\rho_w} \tag{4.1}$$

with f the Coriolis parameter, ρ_w, a water reference density and $\vec{\tau}_N$, the northerly wind stress, calculated from wind date with the expression:

$$|\vec{\tau}_N| = C_d\rho_a\,|\vec{v}|\,\vec{v}_N \tag{4.2}$$

C_d is a empirical drag coefficient, ρ_a is air density, $|\vec{v}|$ the modulus of the wind speed and $\vec{v}_N$ a normal vector directed to the south. The units of the upwelling index are $m^3s^{-1}km^{-1}$, and it represents a surface water flow per km of coast. Positive upwelling index represent offshore fluxes of surface waters (upwelling), while negative values indicate onshore fluxes (downwelling). In figure 4.8, the upwelling index calculated from geostrophic wind speed obtained from atmospheric pressure fields at the point 43^o N 11^o W (offshore Cape Finisterre) is shown. The main dominating signal in the evolution of upwelling index is the seasonal variation of the winds, that as we noted is driven by the seasonal evolution of large-scale meteorological cells (the Azores high and the Iceland low). The two characteristic seasons determined by this signal are apparent in figure 4.8: a winter (October- March) non-upwelling season with negative upwelling indexes and an upwelling season (March-October) characterized by positive upwelling indexes. The downwelling season lasted this year until early March. From March on, upwelling dominates, although some downwelling events of several days can be observed. Also some upwelling periods are apparent during the downwelling season.

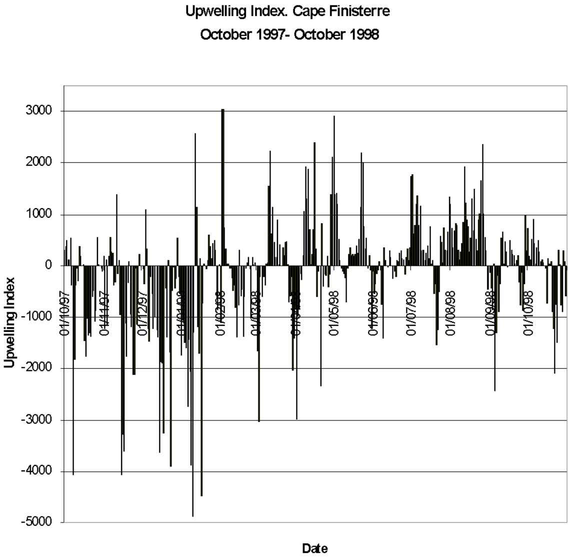

Figure 4.8: Upwelling index for the period October 1997-October 1998, estimated from wind data near Cape Finisterre.

In table 4.2, some information about cruises is shown: date, measured run-off and upwelling or downwelling conditions estimated from the upwelling index during the previous two days, supposing that 2 days is a good estimation of the delay time between this meteorological forcing and the hydrodynamic response. We will see that this estimation of upwelling/downwelling conditions fits well with observed data. This correlation is an indication that temporal scales of response of the estuary to wind forcing on the shelf are short, of around 2 days. *McClain et al. [1986]* estimated an inertia of coastal circulation to wind stress of about 3 days, with slower time scales for relaxation of upwelling.

Cruise	**Date**	**Upwelling-Downwelling**	**I_w($m^3s^{-1}km^{-1}$)**	**Daily run-off (m^3s^{-1})**
1po10	15-10-1997	Upwelling	283	19.4
2po10	29-10-1997	Upwelling	289	24.1
3po11	13-11-1997	Changing	1388, -156	30.1
4po11	26-11-1997	Downwelling	-2120	49.4
5po12	17-12-1997	Downwelling	-2506	39.5
6po12	29-12-1997	Downwelling	-344	84.0
7po01	14-1-1998	Upwelling	1847	49.8
8po01	27-1-1998	Upwelling	626	37.4
9po02	10-2-1998	Low wind	-52	20.5
10po02	24-2-1998	Upwelling	114	16.6
11po03	10-3-1998	Downwelling	-174	22.9
12po03	24-3-1998	Upwelling	276	14.5
13po04	13-4-1998	Upwelling	1293	43.0
14po04	27-4-1998	Low wind	-6	41.0
15po05	12-5-1997	Downwelling	-470	26.0
16po05	26-5-1998	Upwelling	1388	13.5
17po06	9-6-1998	Downwelling	-417	14.0
18po06	23-06-1998	Upwelling	159	9.2
19po07	7-7-1998	Upwelling	1281	7.9
20po07	21-7-1998	Downwelling	-442	3.7
21po08	3-8-1998	Upwelling	959	2.0
22po09	1-9-1998	Downwelling	-466	0.8
23po10	7-10-1998	Upwelling	669	6.3

Table 4.2: Summary of the cruises carried out during the project, with upwelling index and river run-off as information on forcing.

In the next figures (Fig. 4.9-11) the annual evolution of temperature, salinity and density is shown for stations 1, 0 and 6 (for location, see figure 4.6). Note that the cruises were carried out every fortnight, but the last three ones, when only one cruise per month took place. Station 6 (mean depth ~30 m) is located in the interior of the Ría near Tambo Island, station 0 (mean depth ~50m) is located in the main channel in the line Cabicastro Point- Udra Cape and station 1 (mean depth ~65 m) lies at the south entrance. The first noticeable feature is the increase of salinity towards open sea, and the greater river influence at station 6, that results in lower salinity values (Note that the salinity scale for salinity at station 6 is different from that for stations 1 and 0). Temperature at the surface is partially driven by the annual cycle of heat flux. During the first campaign in October 1997, the ria was thermally stratified, with warmer waters at the surface. A gradual cooling is evident during the next cruises and a thermal inversion of the water column develops. For cruise 6, a thermal inversion in the column of more than 1 C is clear, with 14 C at the surface and around 15.5 C at the bottom at station 6. From the first cruise, that represents the end of summer conditions, surface salinity decreases and is responsible for maintaining the stability of the water column. In winter months run-off induces the low surface salinity values and a surface layer of less salty waters until around 20 m. The extent of this surface layer is also influenced by wind. Although downwelling conditions are usual from October to March, some upwelling episodes occur that influence the dynamics. This year, cruises 7 and 8 were characterized by positive upwelling indexes. During cruise 8, although upwelling index is lower than for cruise 7, an intense upwelling episode was measured and ocean waters were detected near the surface. Also, during cruise 10, upwelling conditions were met.

From cruise 11, surface waters are warmed in response to the seasonal increment of solar heat flux. This increase of heat influx drives the heating of the column and induces the set-up of a thermal stratification, that is maximum in summer months. Maximum surface temperatures were found on cruises 17 and 20, when downwelling conditions were met. This heating at the surface during the upwelling season contrasts with the cold waters (ENACW) at bottom waters, that are evident during all campaigns even at station 6. Intense upwelling on cruises 17 and 21 made this water mass reach the surface, even at station 6, breaking the thermocline. Different upwelling and downwelling events can be seen and the dynamics of the system is driven by the sequence of these pulses. Upwelling conditions are characterized by the rising of the colder, saltier waters (ENACW). Upwelling-downwelling sequences are evident by looking at the displacement of the 13.5 C and 35.5 contours at station 1. During cruises 12,13,16,18, 19 and 21, upwelling conditions were met with different intensities. ENACW can be found at the bottom, but they reach a different depth depending on the intensity of upwelling. On cruise 21, upwelling was very intense and ENACW waters are found at the surface. During cruises 14,15,17 and 20, downwelling conditions influence the displacement of the isotherms downwards and of the 35.5 salinity contour downwards. A haline stratification is evident during the whole year. Salinity in the summer months is influenced by the sequence of upwelling and downwelling events of different intensities, that introduce saltier water through bottom layers or surface shelf waters at the surface. Also, some episodic run-off events are responsible for low salinity values at the surface and enhance the stability of the column, as occurs for campaigns 13 and 14, that took place in April, rainier this year compared to the climatologic value.

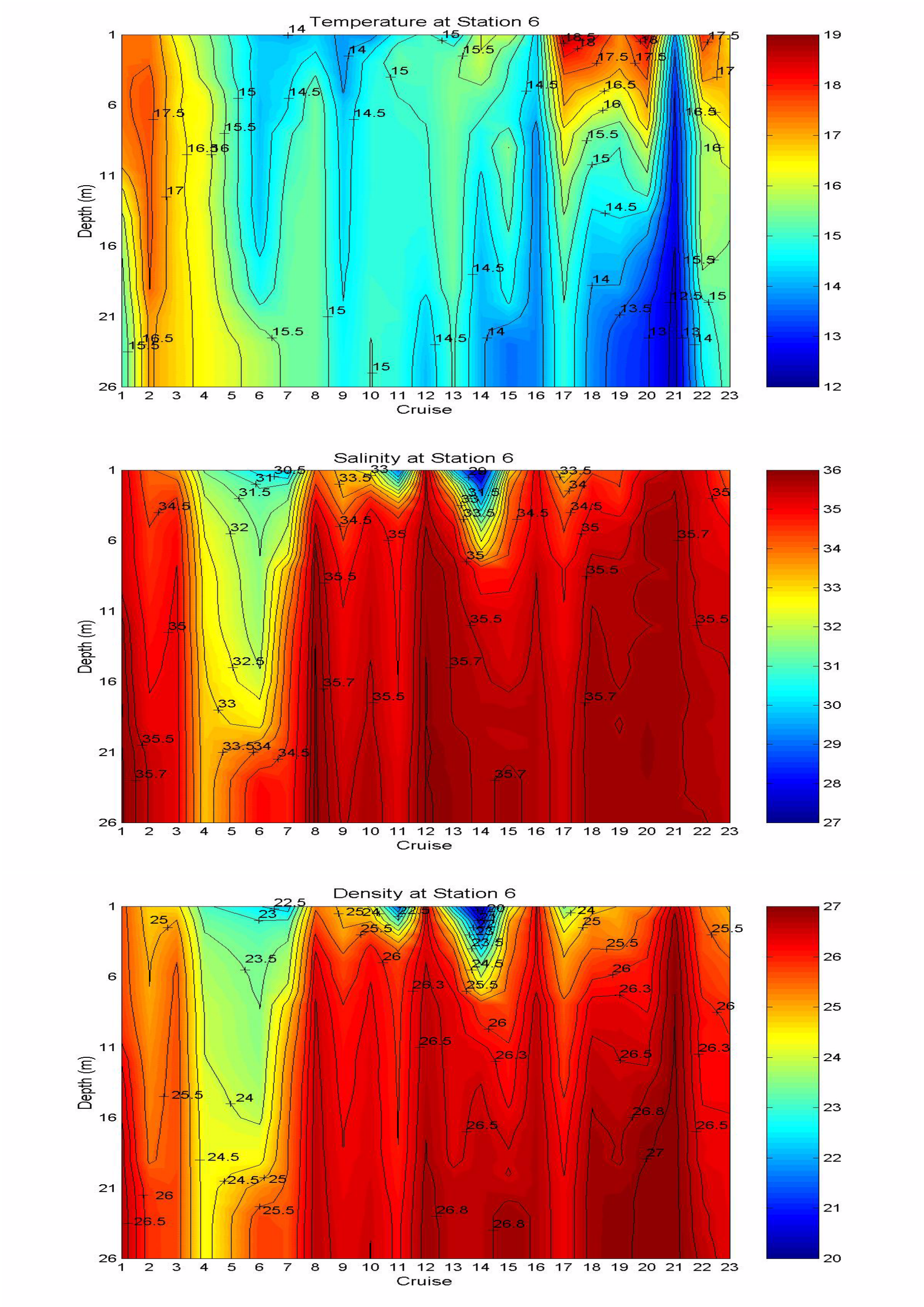

Figure 4.9. : Evolution of temperature in C, salinity and density at station 6 for the campaigns in 1997-1998.

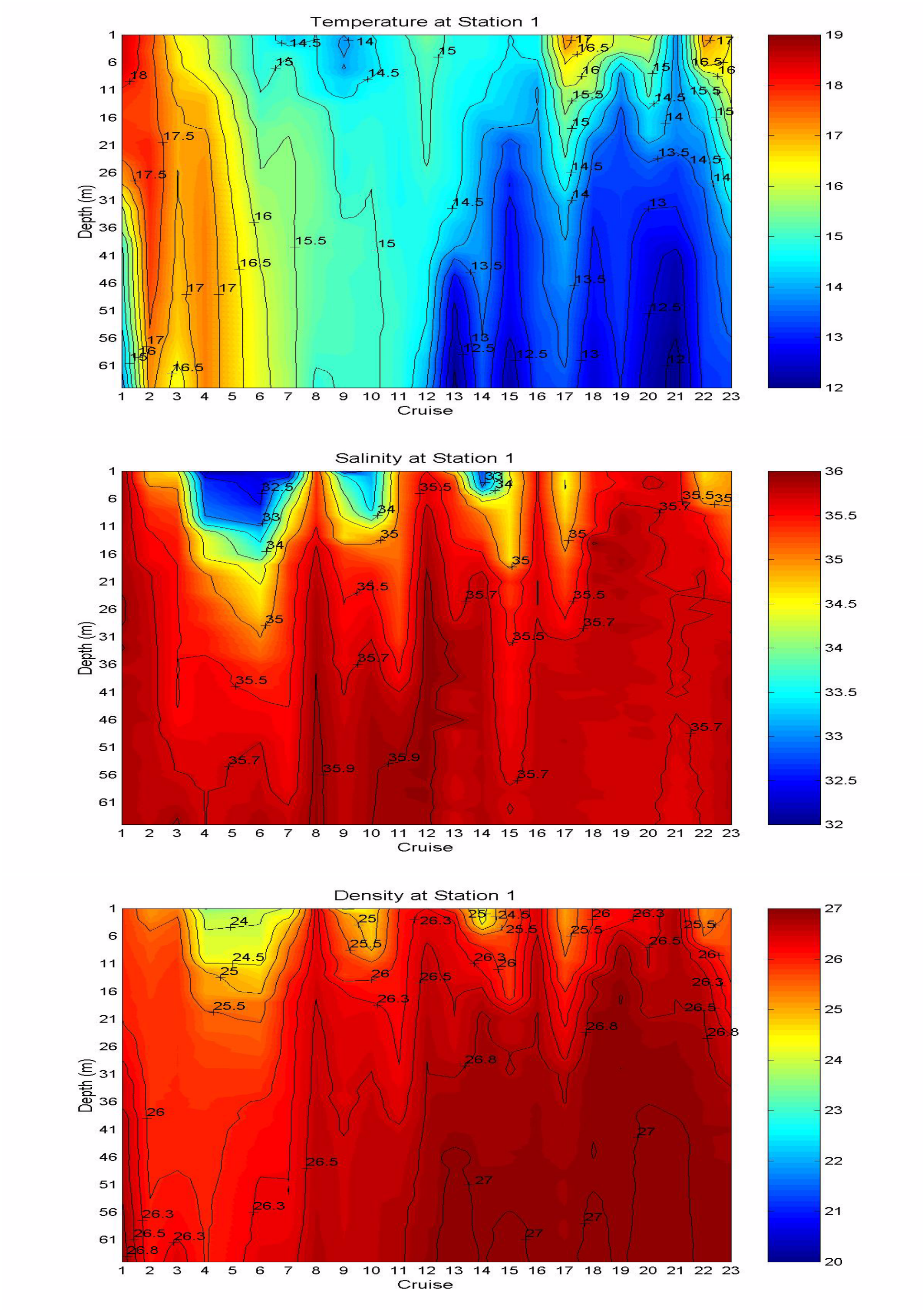

Figure 4.10: Evolution of temperature in C, salinity and density at station 1 for the campaigns in 1997-1998. No data was taken at this station for the campaign 5, so the data are interpolated.

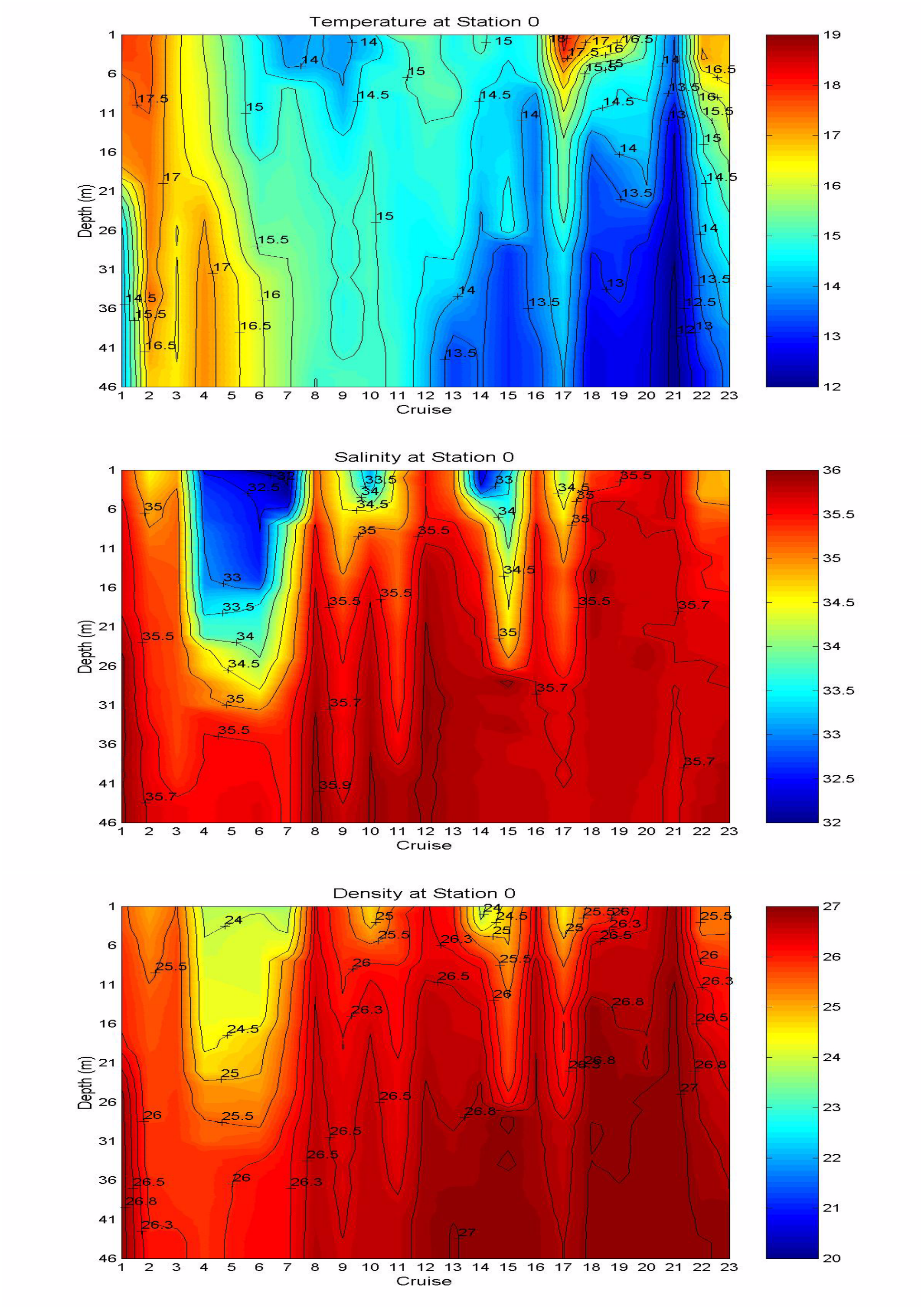

Figure 4.11: Evolution of temperature in C, salinity and density at station 0 for the campaigns in 1997-1998.

In next figures, salinity-temperature diagrams allow us to complete the picture of the annual variability and to assess the processes influencing observations in the period. We will show diagrams for stations 1 and 6 and we will divide cruises in two seasons, that are also evident from the analysis of upwelling indexes: downwelling season (October- March) and upwelling season (April-October).

In figure 4.12, a salinity-temperature diagram for casts in station 6 for the period October-April is plotted. In this picture the autumn and 'downwelling' season cruises (October-March) are shown, together with April cruises. This is done in order to mark the transition from summer to winter conditions. The ST properties of the Eastern North Atlantic Central Water (ENACW) are plotted from the empirical function by *Fraga [1981]* :

$$S = 35.586 + 0.116(T - 11) \tag{4.3}$$

Several studies have found a similar function with linear regression between salinity and temperature from different years (*Álvarez-Salgado et al. [1993], Ríos et al. [1992]).*

For the first date 1po10, the ST pattern is quite different from the next ones: thermal stratification (2.5 C difference between surface and bottom) and only a slight haline stratification. For the second October cruise 2po10, haline stratification is already present and thermal stratification in the column is only of 0.5 C. Temperature is around 17 C. This cruise illustrates the autumnal transition from thermal stratification to haline stratification. From this cruise on, thermal inversion between surface and bottom develops and a gradual water cooling is evident. Surface waters are about 1C colder than bottom until March. The haline stratification of the column gradually grows, although it is driven by variations of run-off, and it is maximum in December and January (near the maximum run-off that year). Also, temperature decreases from 17 C in October to around 14 C in February, maintaining a thermal stratification of 1C. Near the bottom, points are closer, which indicates that density stratification is smaller. A surface mixing layer is seen at surface points that are more apart. From 9po02 on, water starts to warm and stratification decreases. Previous conditions seem to be dominant, but some upwelling favorable conditions were met during some of the cruises. For cruises 7 and 10, ENACW does not appear at station 6 nor at station 1. On cruise 8, an intense upwelling took place and rather homogeneous water was detected, with a temperature of 15.3 C and a salinity of 35.9 at station 6. On cruise 12, upwelling did not homogenize the column, but ENACW were evident at bottom layers both at station 1 and 6. Bottom waters had a temperature of 14.1 C and a salinity of 35.9.

In figure 4.14, the evolution of ST for next cruises is depicted. These can be considered as the upwelling season cruises. Although a strong variability appears, some features can be derived. Surface temperature increases and upwelling episodes are evident through cooler and saltier bottom waters (near the ENACW Salinity-Temperature line). Haline winter stratification is replaced by thermal stratification in these cruises. There is a sequence of upwelling-downwelling events that dominate the response of the system. On cruises 13, 14, 16, 18, 19, 21 and 23 upwelling index was positive. During cruises 12, 20 and 21, bottom waters have ENACW characteristics. Cruises 15, 17, 20 and 22 took place during downwelling conditions and a greater thermal stratification can develop.

For station 1 in figure 4.13 (downwelling season) and 4.15 (upwelling season), evolution is similar. No data were taken at this station during cruise 5po12 due to bad weather conditions. In figure 4.13, haline stratification is smaller than for station 6. Surface waters are saltier than at station 6, as a consequence of the smaller influence of run-off and the greater influence of oceanic waters. In figure 4.15, we see a greater oceanic influence. For clarity, the maximum plotted salinity is of 34.4, although greater values were measured at surface layers. Bottom waters for every cruise have ENACW characteristics.

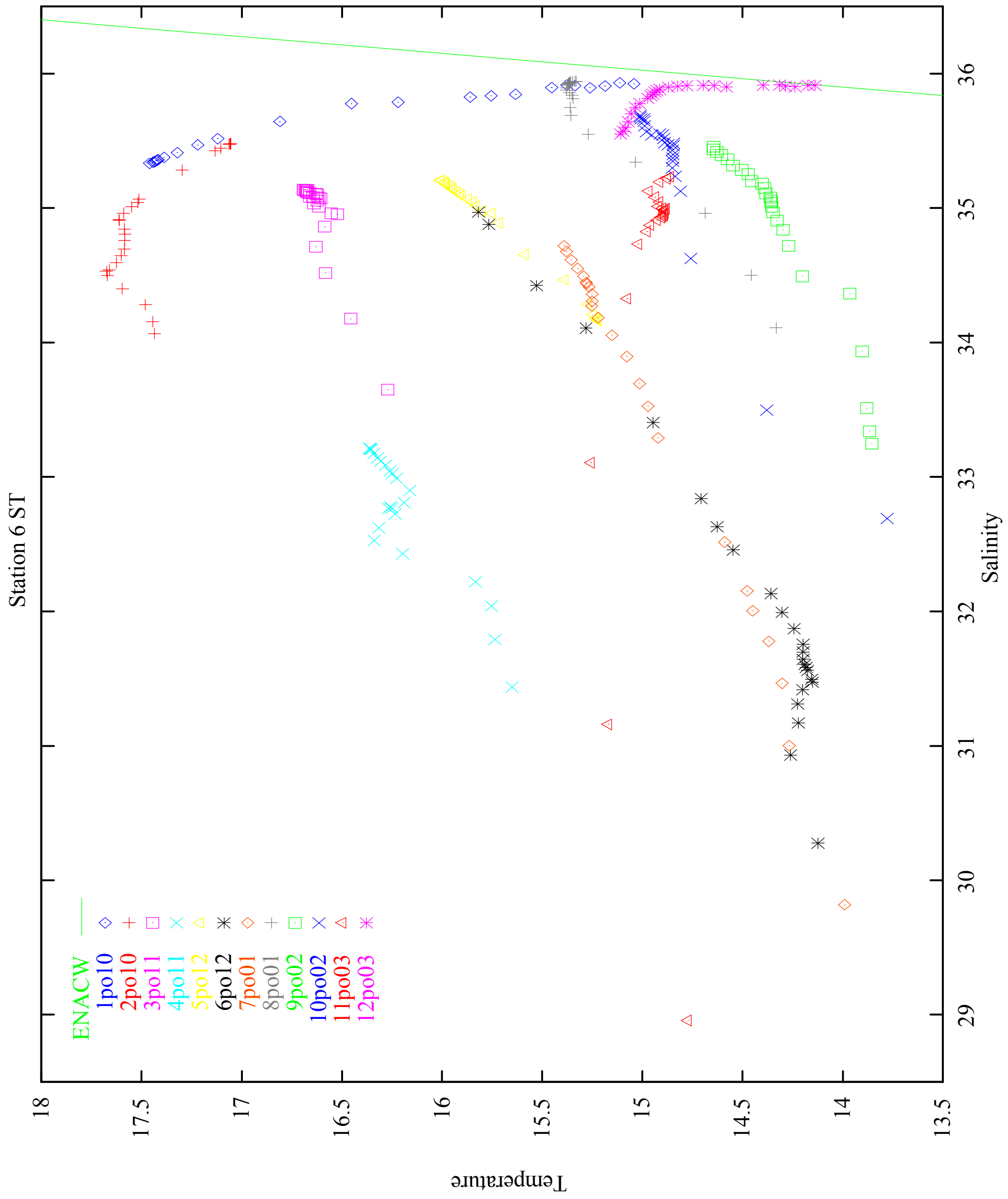

Figure 4.12: Temperature-Salinity Diagram at station 6 for cruises 1po10-12po3 (October 1997-March 1998).

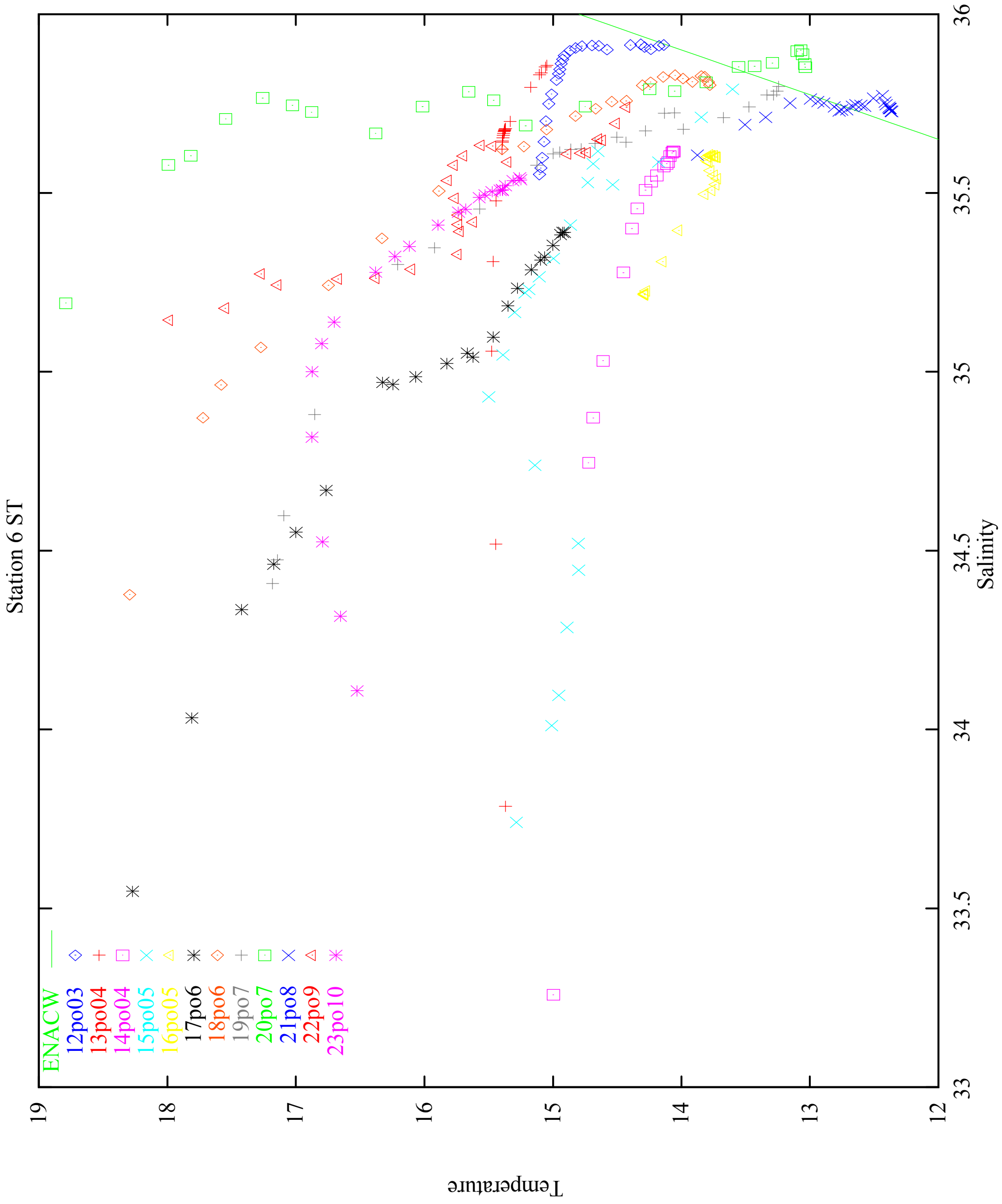

Figure 4.13: Temperature-Salinity Diagram at station 6 for cruises 12po3-23po10 (March 1998-October 1998).

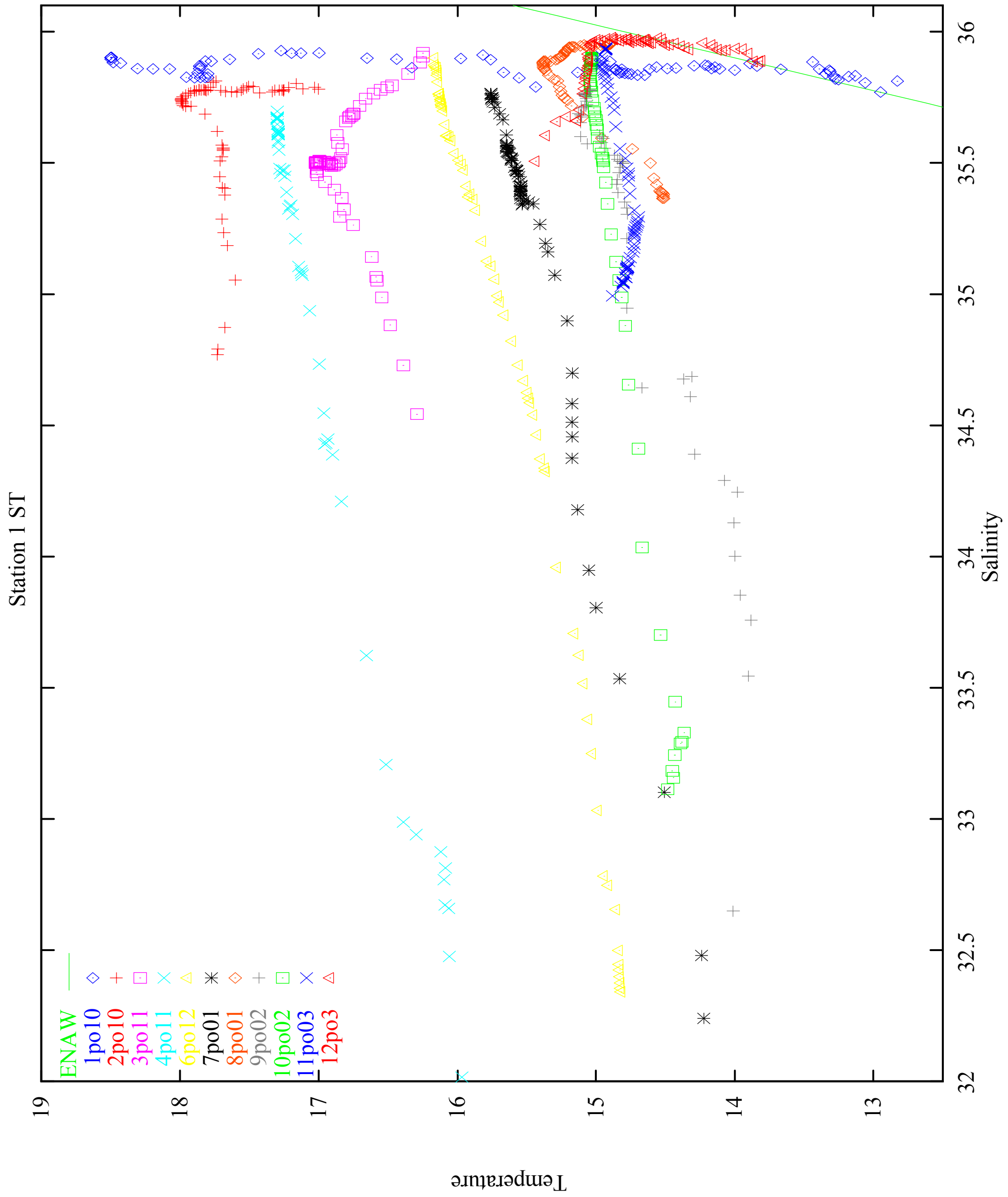

Figure 4.14: Temperature-Salinity Diagram at station 6 for cruises 1po10-12po3 (October 1997-March 1998).

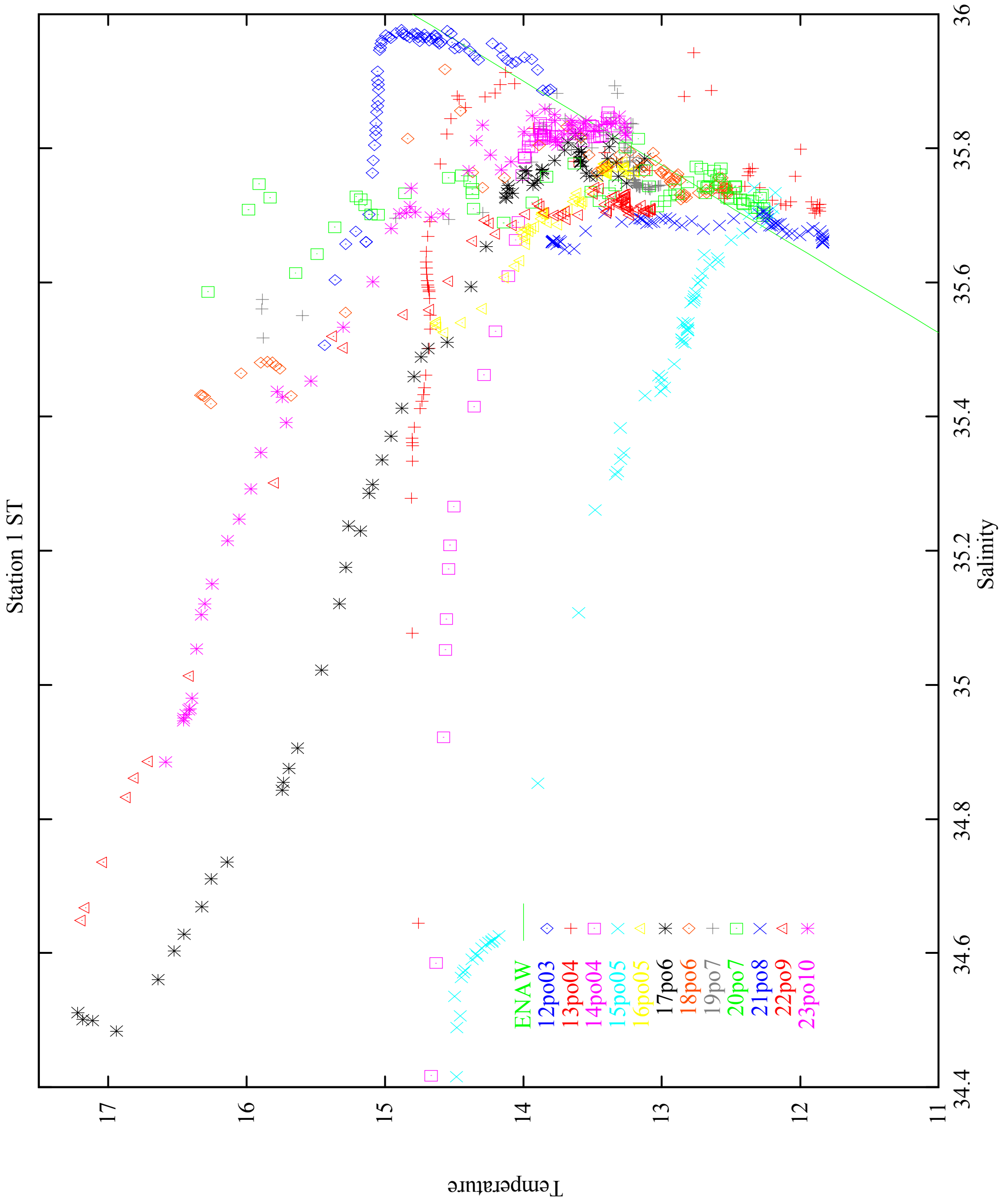

Figure 4.15: Temperature-Salinity Diagram at station 1 for cruises 12po3-23po10 (March 1998-October 1998).

In figure 4.16, salinity-temperature diagrams for data at 50 m and 60 m from casts at station 1 are plotted for all cruises to get an idea of the variability of shelf waters, that are present at the entrance of the ria. The characteristic lines for subsurface water masses according to *Fiuza [1984]* are plotted, together with the functional regression for NACW on the shelf by *Fraga [1981] (* see section 4.2.a.4). Information on date and conditions during the cruises is found in table 4.2. For all cruises, salinity at this depth is around 35.5 and 36.0, as river influence is not strong at this depth. For many of the cruises, ENACW is present at this depth. Cruises 2, 3, 4, 6, 7 and 9 were carried out during winter months (October-February). Temperature is warmer (15-18 C) than in the other cruises, as no ENACW waters are found. As we mention in section 4.2.b, this temperature is warmer than at the surface, which constitutes the thermal inversion characteristic of winter months. Another group is formed by cruises 8, 10 and 11 (and maybe 1 and 9). Warm and saline waters (15 C, 35.95) are found. 8 and 11 cruises coincided with upwelling conditions in the downwelling season, which were related to good weather conditions during February. Probably these conditions resulted in upwelling of waters of the mixed layer offshore that according to *Fraga [1981]* extend to 100 m from November to March (see section 4.2.a.4). According to *Prego et al. [2000]*, these surface waters may have been transported by the poleward current that has been reported in hydrographic and satellite measurements during winter (*Frouin, [1990]*). In the rest of the cruises, water of ENACW characteristics is found. The actual value of ST at this depth is related to local upwelling or downwelling conditions prior to cruises. Thus, in cruises where downwelling conditions were met, points lie above the ENACW lines, for example, cruises 17 and 22. However, this is also influenced by the intensity and the duration of upwelling offshore. *Álvarez-Salgado [1993]* found an increase in salinity from May to October 1989 in a series of survey cruises. Our cruises in the May to October period go from 15 to 23. No clear pattern of variability can be derived from our data. The survey point in their campaigns was located slightly further from the ria, with a depth of 75 m in contrast to our 65 m. Also, the sampling frequency was higher (twice a week compared to fortnightly), which helps in the determination of a tendency in the data. However, interannual variability might be responsible of this difference. In some cruises like 13, 15, 20 and especially 21, ST points are near the ENACW$_{sp}$ line. As we saw in section 4.2.a.4, a subsurface front between ENACW$_{sp}$ and ENACW$_{st}$ is present near Finisterre. Variations in the mean location of this front affect the ST characteristics of the waters outside the ria, and may result in upwelling of waters with ENACW$_{sp}$ characteristics. Evidence of episodic changes in the upwelled water mass were described by *Álvarez-Salgado [1993]* (see their figure 4), although the general trend is an increase of salinity with time. Further surveys on the shelf are necessary to clarify this point.

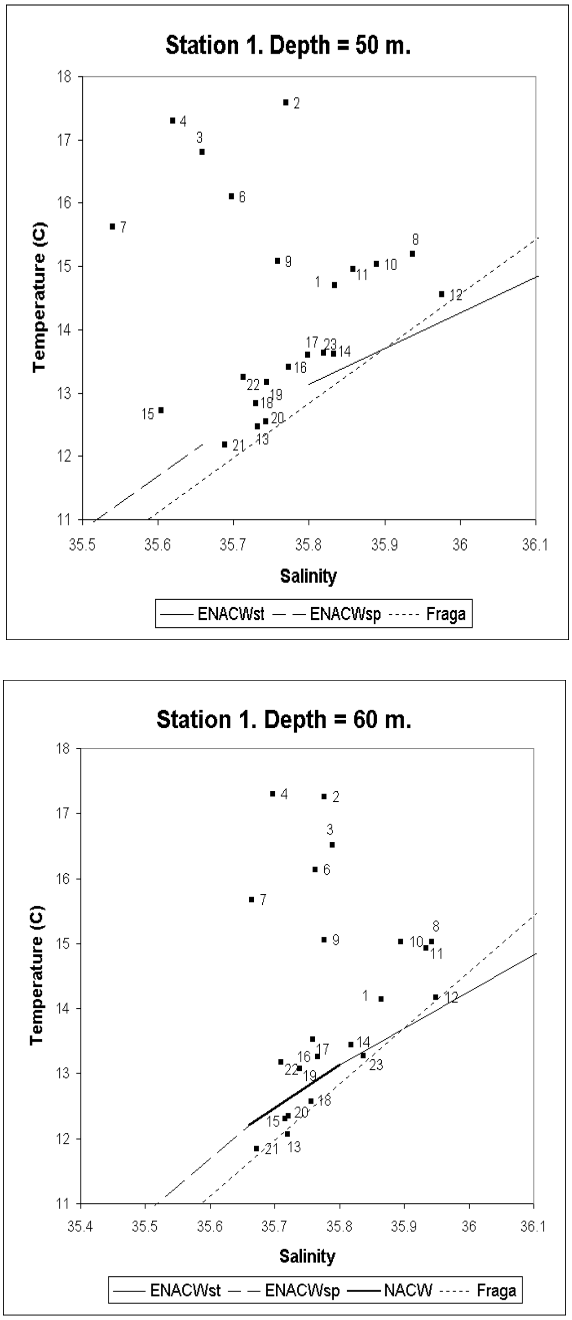

Figure 4.16: ST diagram for points at 50m and 60m at station 1.

Summarizing, several seasonal conditions inside the Ría appear as we will show and also is described in (*Prego et al. [2000]*). In the winter, the small radiation causes a thermal inversion in the column of around -1 C on average and the stability of the column is maintained by salinity, because river run-off is important. From spring on, due to surface heating, a thermal stratification between surface and bottom starts to develop, while haline stratification is reduced, because the decreasing river run-off, but there is a strong variability due to wind, river discharge and upwelling events. In the summer, the thermal stratification reaches its maximum, with upwelling usual conditions that introduce shelf colder waters in deeper layers. Autumn is a transition season, that constitutes the end of the upwelling season and the transition to winter haline stratification. The dominant winds offshore have been shown to play an important role and the hydrodynamics of the ria can be divided in two seasons according to the prevailing conditions. From October to March, downwelling conditions are usual, although some upwelling episodes introduce shelf waters. From March to October, upwelling conditions are often met, and relaxation of these conditions is induced by changing in the wind regime.

As pointed in *Prego et al. [2000]*, most of the studies in the ria de Pontevedra were aimed to the study of biogeochemical properties. The observations by *Figueiras et al. [1985]* for the year 1983-84 support the annual variability we have found. In other Rias Baixas, several studies have focused on the variation of thermohaline properties in an annual or monthly scale. Some hydrographic works were carried out in the ria de Vigo in the 70s (*Mouriño and Fraga [1982] and Mouriño et al. [1984]*). In the ria de Arousa, the work of *Otto [1975]* studied the thermohaline variation and described the annual cycle. Data of a 5 year monitoring in an interior point in the Ría de Vigo were analyzed by *Nogueira et al. [1997]* and the annual signal was established. Also in the ria de Vigo, two points were surveyed every fortnight from May 1994 to September 1995 (*Doval et al. [1998]*). In the upwelling season (*Rosón et al. [1995]*), the ria de Arousa was surveyed twice a week in 10 points. The general trend is similar in all of them and the sequence of upwelling-downwelling events has been observed. This sequences have been related to the appearance of red tides (*Fraga et al. [1988], Fraga and Prego, [1989]* and *Tilstone et al. [1994]*).

4.2.b.2 Along-channel variation

In this section, some representative cruises will be chosen and a description of the longitudinal (along-channel) variation of thermohaline properties will be given. The selected cruises were 4po11, a characteristic winter downwelling cruise, 20po07, a summer cruise where downwelling conditions were met, and 21po8, a summer cruise when the most intense upwelling conditions this year were found.

The location of the stations used for plotting the longitudinal section is shown in figure 4.17. The section, after passing through the south of the Tambo Island, follows the main axis of the Ría and ends at station 1.

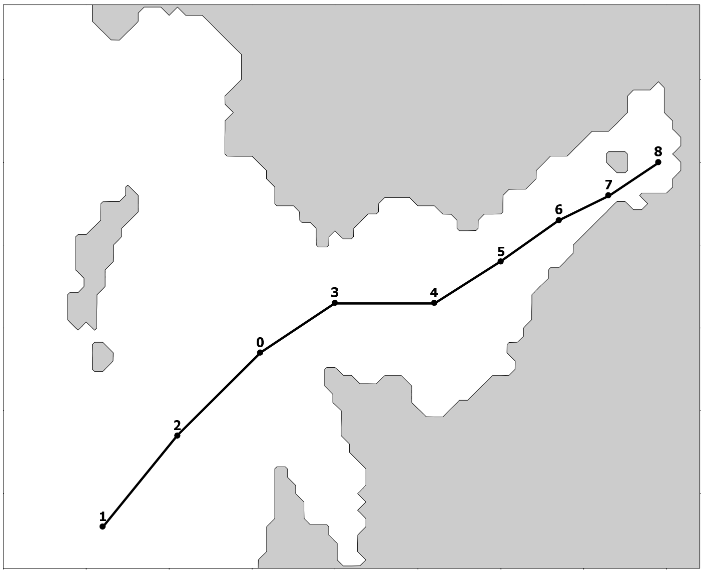

Figure 4.17: Location of stations used in the longitudinal section.

In figure 4.18, the longitudinal section for cruise 4po11 is shown. During this cruise (26-11-1997), river run-off was important (50 $m^3 s^{-1}$) and a negative upwelling index indicated downwelling conditions. Contour plots of temperature, salinity and density are shown. There is a thermal inversion of the water column, with warmer waters at deeper layers. Stability is maintained by salinity, as less dense river waters are found at the surface. The slope of the contours indicates that downwelling is retaining water and denser waters are entering through the open entrance. The river plume influences the low salinity values at the surface.

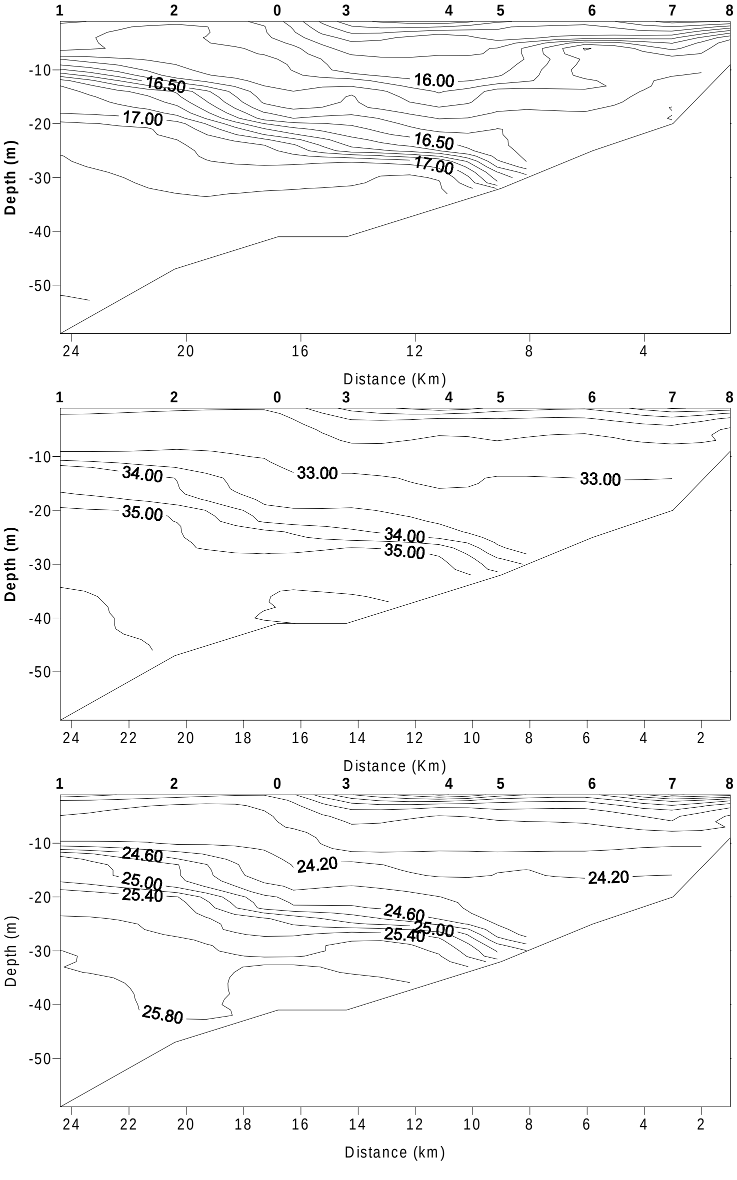

Figure 4.18: Longitudinal section of temperature, salinity and density for the 4po11 cruise.

In figure 4.19, the longitudinal section for cruise 20po07 is shown. During this cruise (21-07-1998), river run-off was very small (3.7 $m^3 s^{-1}$), as characteristic in summer months. A negative upwelling index indicated downwelling conditions. A thermal stratification is evident in temperature contours. Until station 4, surface values are warm and reach 19 C at the surface. Salinity range of variation is not great and a thin slick of stratified fresher water can be seen until station 5 in the first 5 meters or so. Contour lines (specially of temperature and density) suggest that this behavior is a consequence of a retention of water inside the ria due to downwelling. A minimum at the surface exists between station 0 and 2 and the shape of contour lines suggests a sinking of water between station 3 and 4. Below 30 m, ENAWC waters are present in all of the ria and downwelling helps the warming of surface waters.

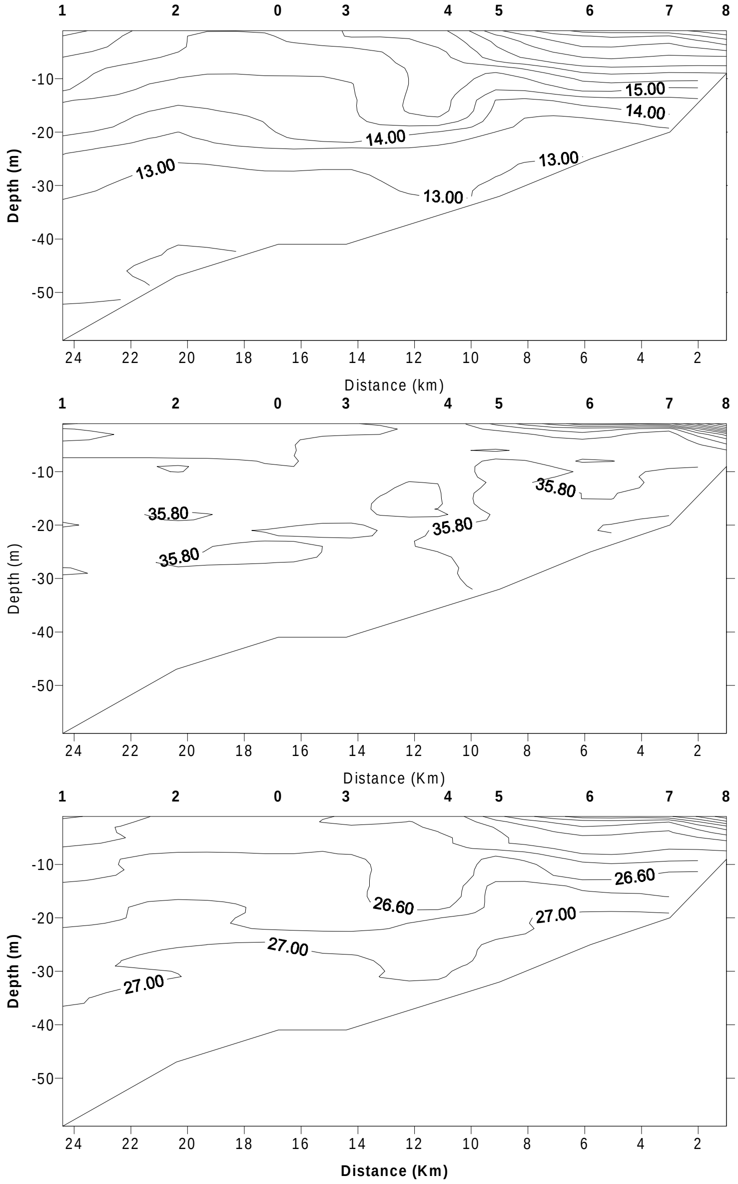

Figure 4.19: Longitudinal section of temperature, salinity and density for the 20po7 cruise.

In figure 4.20, the longitudinal section for cruise 21po08 is shown. During this cruise (03-08-1998), river run-off was very small (2.0 m^3s^{-1}), as characteristic in summer months. A positive upwelling index indicates upwelling conditions. A intense upwelling took place during this cruise. Salinity is uniform around 35.7, but at surface layers until station 4, where the first 5 meters low salinities are influenced by river waters. Temperature at bottom layers is between 12 and 13, which together with salinities of 35.7 is characteristic of ENACW waters. Near the surface, temperature is higher and reaches 14 C. Towards open sea, temperature at the surface increases. Density contours show a layer of ENACW entering the Ria through bottom layers. Over this waters, a thin slick of less dense waters is induced by the river. At the ria entrance, warmer waters induce lower densities.

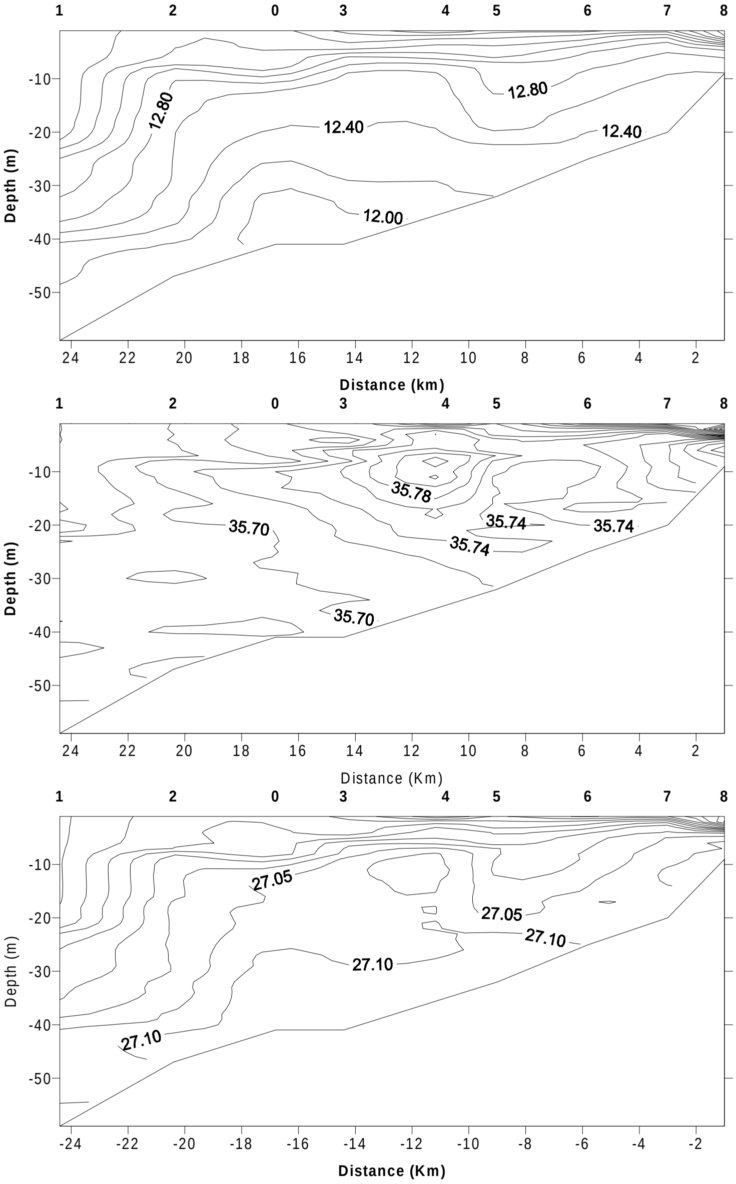

Figure 4.20: Longitudinal section of temperature, salinity and density for the 21po8 cruise.

4.3 Hydrodynamic model study

3D hydrodynamic models are a useful tool for the understanding and management of coastal areas and estuaries. However, they are not a substitute of proper field measurements in the study of the system, although they can provide us with a better understanding of the response of the system to different forcing at different spatial and time scales. This is invaluable in a complex system like the sea, where field research is expensive and dependant on weather conditions and other logistic matters. The application of a 3D model strongly depends on the available data. Many times, the available data base is reduced or incomplete, which makes modeling a complicate task. For modeling purposes, many different data from the same period must be available. When this is not the case or when the hydrodynamics of the system is not well established, as in the case of Galician Rias, simple process studies must be carried out to gain insight on the dynamics of the system before more complex studies, or even real-time forecasts, can be undertaken. In this section, a description of the application of the model MOHID3D to the Ria de Pontevedra, following by some conclusions drawn from process studies, will be made.

4.3.a Application to the Ría de Pontevedra

The bathymetry of the area (figure 4.21) was obtained by digitizing and interpolating to a Cartesian grid the bathymetric charts number 925 and 9251 edited by the Instituto Hidrográfico de la Marina (Army Hydrography Institute, Spain). Some utilities in Visual Basic have been developed and are available for entering the coastline and the bathimetric information on the chart into a file. From the depth and location of the depth points, the grid is constructed by using a series of pre-processing tools. The coastline is transposed to grid information by means of a polygon construction algorithm. The depth points are introduced in the grid and interpolated to get a value in every grid point with help of a set of interpolating routines. Smoothing of the resulting bathymetry is also possible to avoid problems with steep depth gradients in sigma layers. For this application, we have constructed a grid with horizontal dimensions 69x114. This domain was chosen with a shelf zone of around 11 km due to the lack of data on density gradients at the ria entrances, needed as boundary conditions. With this domain, a relaxation zone is introduced and the imposition of for example Levitus data (*Levitus, [1994]*) at that boundary is not so unrealistic, since Levitus data are an average of measurements on the shelf.

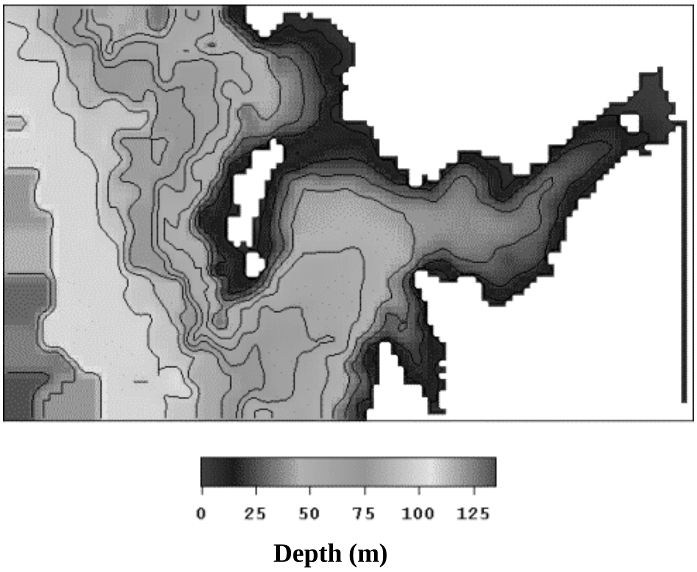

Figure 4.21: Bathymetry used in the computations. The horizontal space step is of 300 m.

Initialization By letting the model run for some tidal cycles with tide, river and open boundary density forcing until a near stationary solution is achieved, the model is spun-up. Velocities and elevations are set to zero in the domain, while temperature and salinity distributions are set to constant values. This process can be sped-up by starting from interpolated real density data as initial distribution. Results are calculated for the subsequent period. The model could also be initialized by interpolating temperature and salinity distributions and gradually switching on the baroclinic term in the hydrodynamic equations with a damping term dependant on Coriolis frequency to avoid inertial or spurious oscillations to appear. However, the performance of this method depends on the quality of the available data and can depend on the interpolation procedure. Some preliminary tests with a bi-linear interpolation and real data in 16 interior points have shown bad performance. As in this study, we will only carry out process studies, there is no need to use this kind of initialization. Such an initialization would be preferable for other more complex situations.

Boundary conditions The model was forced at the open boundary with 18 tidal harmonics calculated from a time series of a tide gauge located at the southern entrance of the Ría (42^o 20.944’ N; 8^o 49.148’ W) and artificially correcting its phase by considering shallow water wave propagation. The density distributions at the open boundary were obtained from the Levitus 94 database (*Levitus [1994]*) and imposed there following a time relaxation approach, when the flux goes into the domain, and allowing convection when flux is outwards. At the river boundary the volume flow is imposed, and river temperature and salinity are fixed. The river boundary was placed in the limit of tidal influence in the river, i.e. 2 km inland from the mouth. Elevation and salinity were set to zero and temperature was imposed equal to air temperature.

The lateral boundary condition at coastal boundaries is a free slip condition. No fluxes at the surface and bottom were considered. Bottom stress is computed using a quadratic wall-function with the roughness length z_0^b as an adjustable parameter. No wind stress at the surface was applied in these simulations.

Parameterization of turbulent diffusion Although the use of a more advanced turbulence model would lead to a better description of vertical mixing, as a first step a simple closure will be used. The vertical eddy viscosity is calculated via the Prandtl mixing length hypothesis (Eq. 2.19):

$$\nu_t = L^2\sqrt{(\partial_z u)^2 + (\partial_z v)^2} \tag{4.4}$$

where the mixing length L is the product of a depth-dependant factor and a stratification dependant factor. In these simulations, the (*Leendertsee and Liu, [1978]*) distorted parabola (Eq. 2.51) is used. As discussed in chapter 2, this expression fulfills the law of the wall near bottom and surface boundaries and shows a maximum at mid-depth, but closer to the surface to represent the greater extent of the bottom mixed layer in tidally dominated flows. The dependence on stratification is empirically introduced as an exponential function of the Richardson number (Eq. 2.60) following (*Nihoul, [1984]*). The vertical eddy diffusivity is assumed to be the same for all scalars and is imposed to be equal to vertical viscosity.

Regarding to horizontal eddy coefficients, they are set to a value of $50\ m^2 s^{-1}$. For the resolution we are considering, the characteristic observed coefficients are of the order of $1\ m^2 s^{-1}$ (*Okubo [1981]*). The value of horizontal diffusion we have chosen is therefore only used for allowing a stable computation. As discussed for example in the review of coastal ocean models by *Mellor and Greatbach [1999],* a zero horizontal diffusion is preferable, although not always possible on numerical stability grounds.

Some of the constants and parameters used in the simulations are summarized in Table 4.3.

Time step	30 s
Horizontal step $\Delta x, \Delta y$	300 m
Grid size xyz	69x114x10
Number of sigma layers	10
Roughness length z_0^b	$2.5\ 10^{-3}$ m
Horizontal eddy viscosity ν_H	$50\ m^2s^{-1}$
Horizontal eddy diffusivity ν_H'	$50\ m^2s^{-1}$
Reference density ρ_0	$1025\ kg\ m^{-3}$

Table 4.3: Constants and parameters used in the computations.

As skill assessment, the model was run for 3 days in a time where data from a Doppler current meter were available. The consistency of the tidal forcing was checked by comparing the results with a tidal gauge inside the ria (symbol O in figure 4.21), near the Illa de Tambo 42^o 24.345’N, 8^o 42.957’W (fig. 4.22). The position of the Doppler was 42^o 22.477’ N; 8^o 46.998’ W (marked with an X in figure 4.21). The mean depth at the mooring point was of 22 m. The observed along-channel component of the flow is contrasted to model predictions in figure 4.23. Wind speed was low during the period of comparison. The velocity has a clear semidiurnal variation and it can be seen that the model performs reasonably well and accounts for much of the variability on a tidal scale.

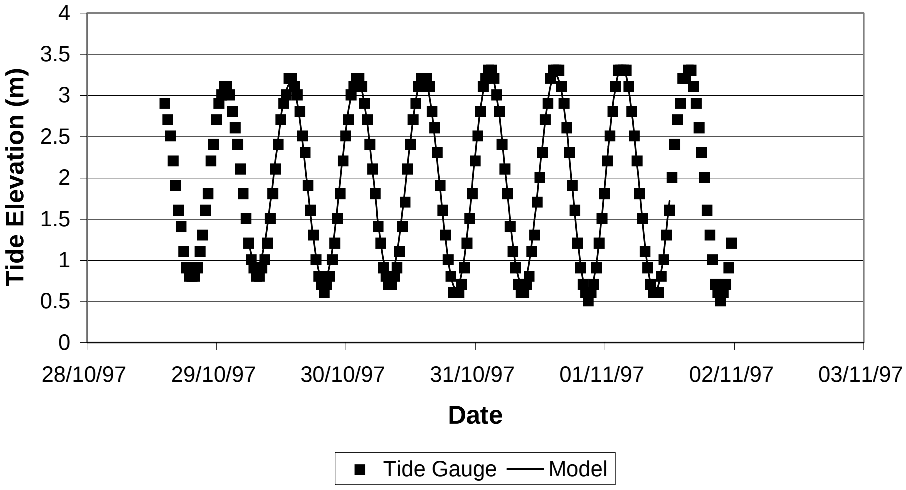

Figure 4.22: Comparison of modeled (solid line) and measured (squares) tide elevation at a point near the Illa de Tambo (42^o 24.345'N, 8^o 42.957'W)

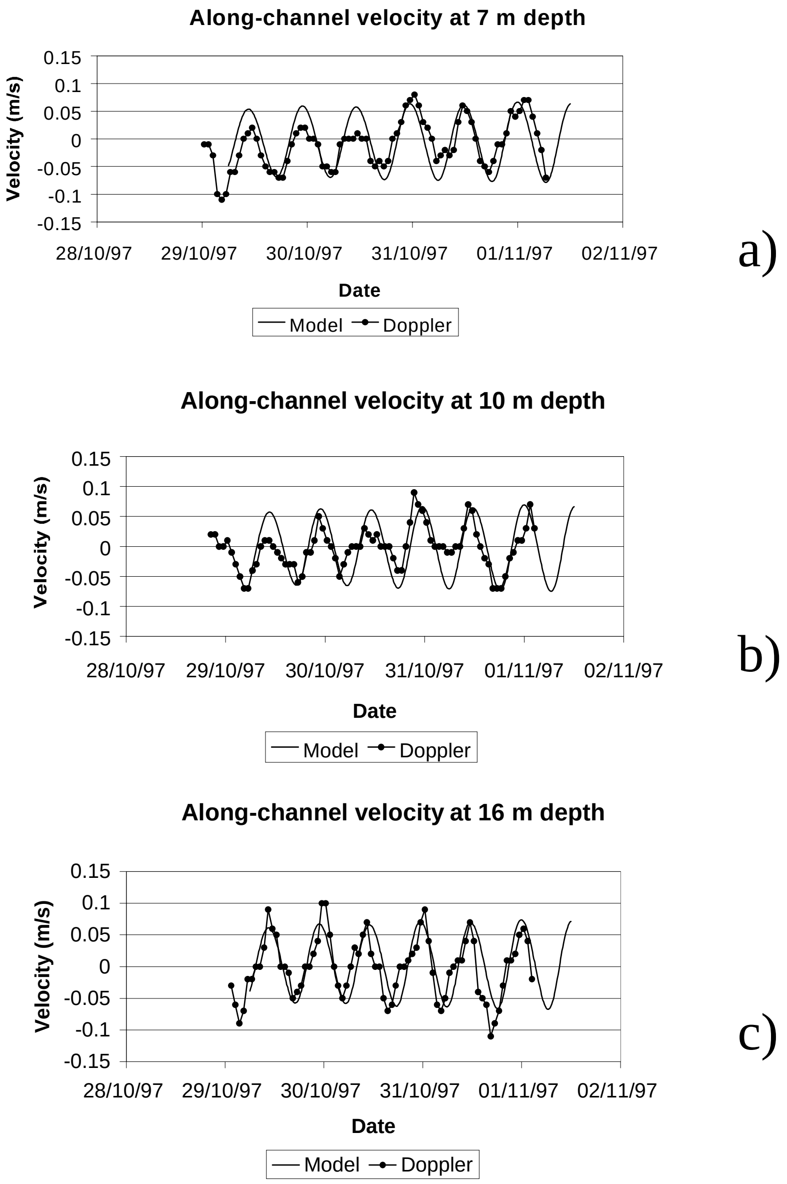

Figure 4.23: Comparison of modeled (solid lines) and 1h low pass filtered measured (line-pointed lines) along-channel currents for three different depths a) 7 m, b)10 m, c) 16 m at the point Areas (42^{o} 22.477' N; 8^{o} 46.998' W).

4.3.b Results

To assess winter conditions, an experiment was run under characteristic estuarine conditions, with a river run-off of 50 m^3s^{-1} and river temperature of 15 C. The density forcing at the open boundary corresponds to the December average Levitus density. No wind forcing was considered. The tidal and residual circulation for a period in-between neaps and springs are studied.

4.3.b.1 Tidal circulation

The tidal circulation pattern for mid-flood and mid-ebb (1.5 m tide elevation) is shown in figures 4.24a and 4.24b, both for the surface layer and for the sigma layer closer to the bottom. The order of magnitude of the observed velocities is of about 0.05-0.1 m s^{-1}, with higher velocities at the surface layer. The maximum obtained velocities are in the main channel, reaching a maximum value of around 0.1 m s^{-1} at the surface layer. Also an acceleration of velocities at the north entrance (velocities of 0.1 m s^{-1}) appears. In the inner zone , to the north of the Tambo island, velocities are small. Only a small intertidal bank exist there, so no change in the observed velocities is expected if these zones are modeled. Velocities to the south of the Tambo Island are bigger than to the north. Passing the Island, the main component of the current results to be along-channel, although in Sanxenxo and Bueu bays, a change in the direction of the flow is observed. Towards open sea and after the line Punta Cabicastro-Cabo Udra, two main streams can be seen in the flow, one flowing to the north entrance and the other towards the south. The velocities in the Ria de Aldán are smaller than those at nearby points of the estuary, and have a different direction, as expected. The influence of the Ons Island is clear and a zone of lower velocities appears. No island wake is apparent for the resolution we are using (300 m).

In figure 4.25, a horizontal section of salinity averaged over a tidal cycle is plotted for a surface layer and for a bottom layer. A noticeable feature is the decrease of stratification in the water column towards open sea. The river plume seems to advance faster at the middle of the channel. It is interesting to note the faster advance of the river plume at the northern shore compared to those at the south shore, that induces a north-south salinity gradient. *Prego* *et al. [2000]* and *Figueiras et al. [1985]* also noted a difference in thermohaline properties between north and south shore. The stratification is greater in the interior zone, that is more influenced by river inflow. From the middle part of the ria, the horizontal along-channel gradient and the stratification decrease. At the surface layer, just after passing the Tambo Island, less dense water appear to the south. Afterwards, the faster advance of the river plume on the north shore is apparent until the Ons Island. At the bottom layer, saltier water appear to the south of the ria, until Tambo Island is reached. This indicates that saltier water flows into the ria mainly through the south, probably forced by Coriolis force, bathimetry and topographic features as Cape Udra and the shape of the ria. The south entrance is saltier than the north entrance. With respect to temperature, it is rather uniform also in measurements during the same period and the slight winter thermal inversion is not reproduced, as no heat fluxes at the surface were considered. Also, the imposed Levitus temperature distribution at the open boundary shows no inversion, because it is the result of a monthly mean. Anyway, the slight thermal inversion observed in some winter cruises is rather uniform throughout the ria and does not induce a thermocline. Consequently it is not expected to substantially enhance residual currents.

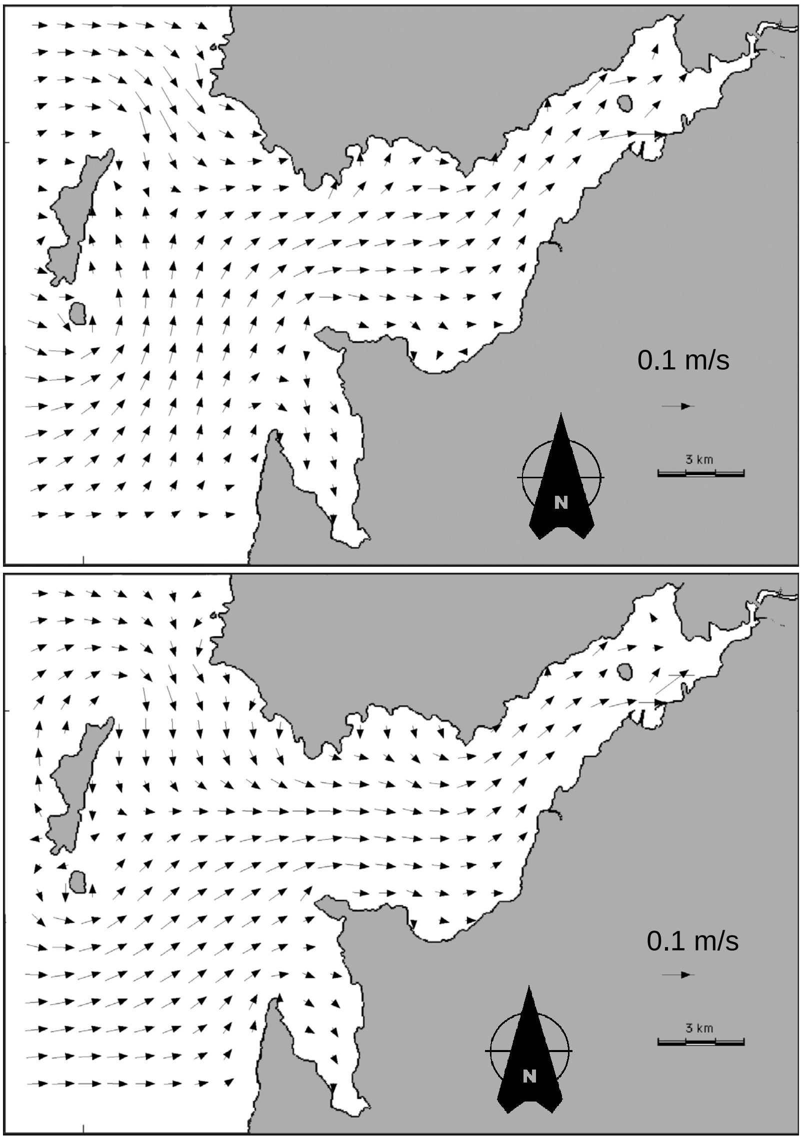

Figure 4.24a: Tidal velocities (in m/s) for a) mid-flow (1.5 m tidal elevation during a period in-between springs and neaps)at surface and bottom layers.

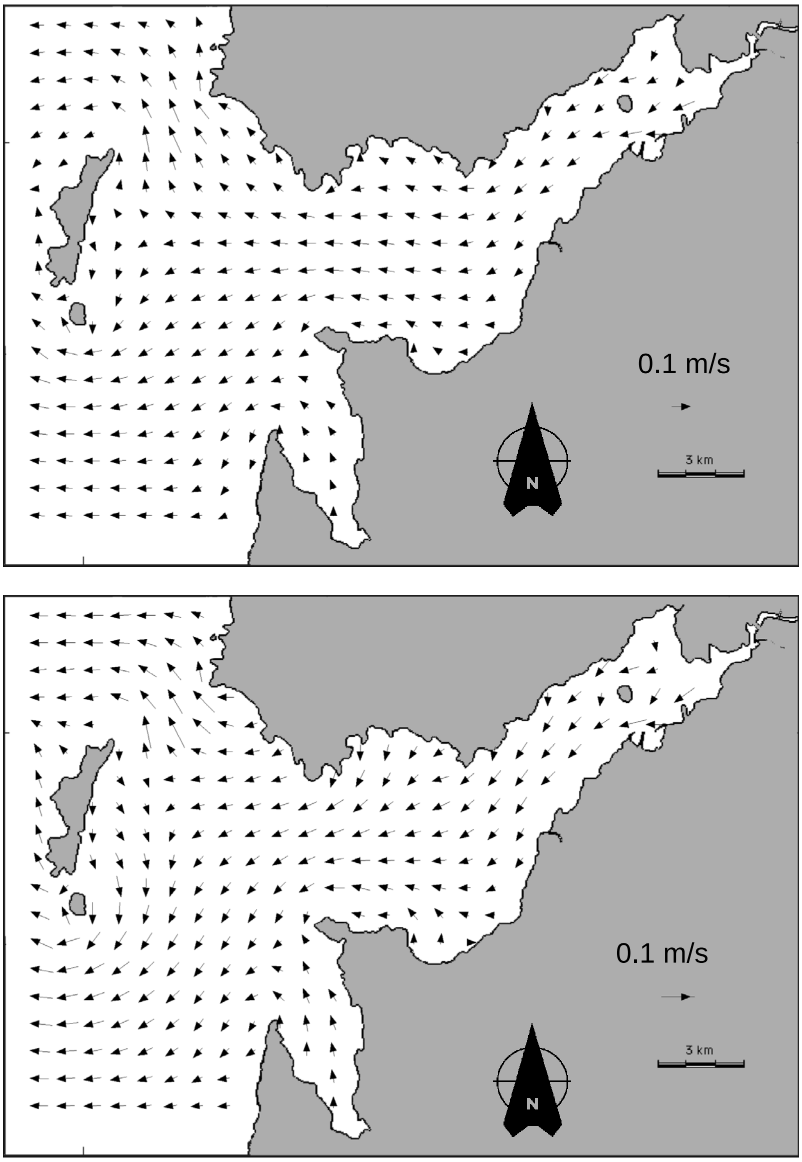

Figure 4.24b: Tidal velocities (in m/s) for mid-ebb (1.5 m tidal elevation, during a period in-between springs and neaps) at surface and bottom layers.

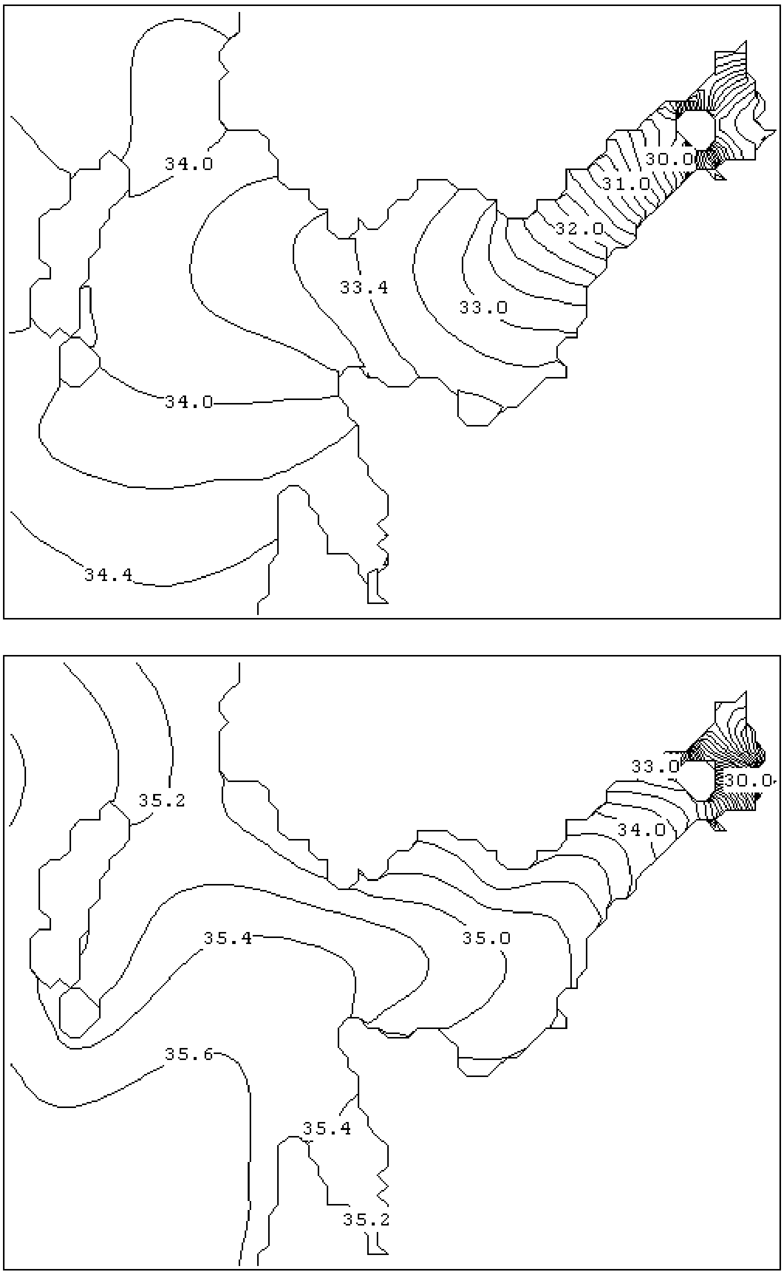

Figure 4.25: Tide-averaged salinity distribution for surface and bottom layers.

4.3.b.2 Residual circulation

To address the influence of the considered forcing on transport, residual velocities were computed by averaging tidal velocities over several tidal cycles. In figure 4.26, the horizontal residual circulation for surface and bottom layer is shown. Residual velocities are about one order of magnitude smaller ($\mathrm{O}10^{-2}$ m s^{-1}) than the tidal ones ($\mathrm{O}10^{-1}$ m s^{-1}). A two-layered pattern is observed, with water leaving the Ría at the surface layer and entering it at the bottom. Near the river mouth, residual velocities are smaller. In this interior region, the main flow runs to the south of the Illa de Tambo, while in the shallow zone to the north-east of the island, no net residual flux is apparent. Gradually these velocities increase and reach their maximum near the line Cape Udra-Punta Cabicastro. In the surface layer a transverse (across channel) component northwards can be observed in the middle part of the Ría. The higher across-channel residual velocities are observed near the south channel. Afterwards, the flow is divided into two branches, one that goes through the north entrance and the other through the south one. In the bottom layer, the flow also decreases to the river mouth. The transversal component is not so intense and faces south, which indicates a cross-channel cell in vertical. This feature will be further explored in the next paragraphs. In the Ría de Aldán, residual circulation velocities are lower than in the adjacent zones and an expected change in the direction of the flow is noticeable, but the two-layered structure is maintained. Near the Ons Island, smaller velocities are found.

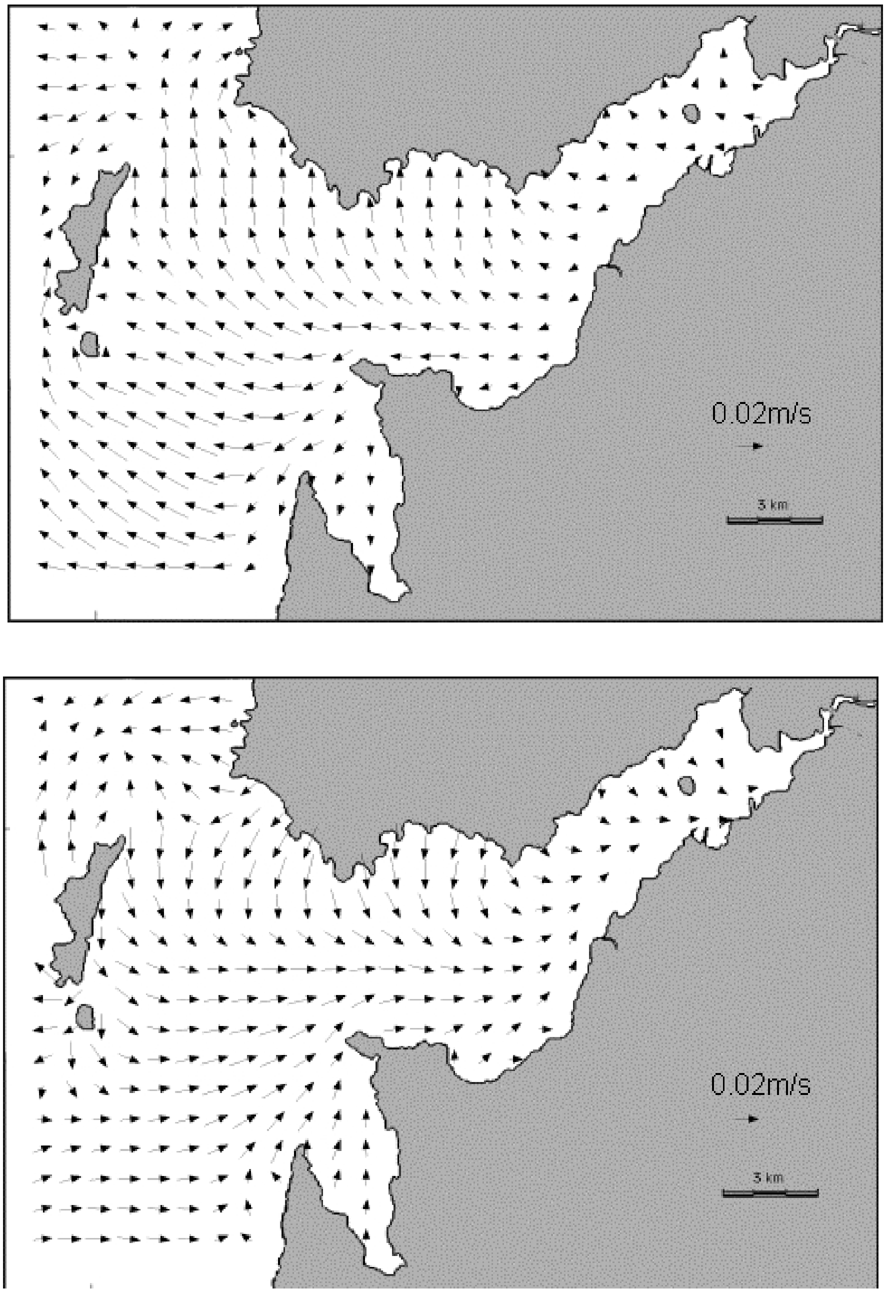

Figure 4.26: Residual velocities (in m/s) for surface and bottom layers

To study in detail the water column structure of residual circulation, an axial (along-channel) section and a transverse (across-channel) section are plotted in figures 4.27 and 4.28 (the location of sections is marked in the map on the left-bottom side). The axial section (figure 4.27) follows the main axis of the ria and illustrates the vertical structure of the two-layered pattern. It has been chosen so that it is equidistant to both shores and so that it follows the main channel. In arrows, the along-channel component of velocity is plotted and in contour lines, the across channel. Positive velocities are defined as to the north and to the east (i.e. inwards the estuary). Note that vertical velocities are around one order of magnitude smaller than horizontal ones. Anyway, also vertical characteristic dimensions are smaller than horizontal, which must also be considered for interpreting results. The discontinuities in the velocity field are due to the specification of the section. In a horizontal view, water flows outwards the estuary at the surface, while in bottom layers a net inflow of water appears. Residual velocities are smaller at the inner part, as noted in figure 4.26. An intermediate layer where along-channel horizontal residual velocities are smaller can be observed. This corresponds to the mean position of the halocline and separates the outflow (surface layer, arrows towards open sea) and inflow (bottom layer, arrows towards river mouth) domains. The separation of inflow and outflow domains is not sharp and they appear to be coupled, as characteristic of a partially mixed estuary. Superimposed to the along-estuary arrows, contour lines of transverse (across-channel) velocities (positive northwards) are plotted. A two-layered structure is observed with net northward transport of water at the surface layer and a southward one at the bottom. A level of zero transverse flow is present at mid-depth. The transverse circulation is weaker near the river.

To obtain a clearer picture of the transverse circulation, this transverse component of the flow is plotted for an across-channel section (figure 4.28). In arrows, the across-channel component of velocity is plotted and in contour lines, the along-channel. The observed circulation is like that in contour lines described in figure 4.27. At the surface, a net northward residual flow is observed. At the north coast, water sinks and starts to flow southwards near the bottom. A surge of water is seen in the south shore, which closes a vertical residual clockwise (facing seawards) eddy. An intensification of downwelling is observed at the north shore and the center of the clockwise eddy is slanted to the north. The along channel circulation is plotted as a contour plot, where positive velocities represent velocities into the estuary. Like in figure 4.27, a surface outflow and a bottom inflow layer are observed, with the level of zero axial residual flow lying at about mid-depth.

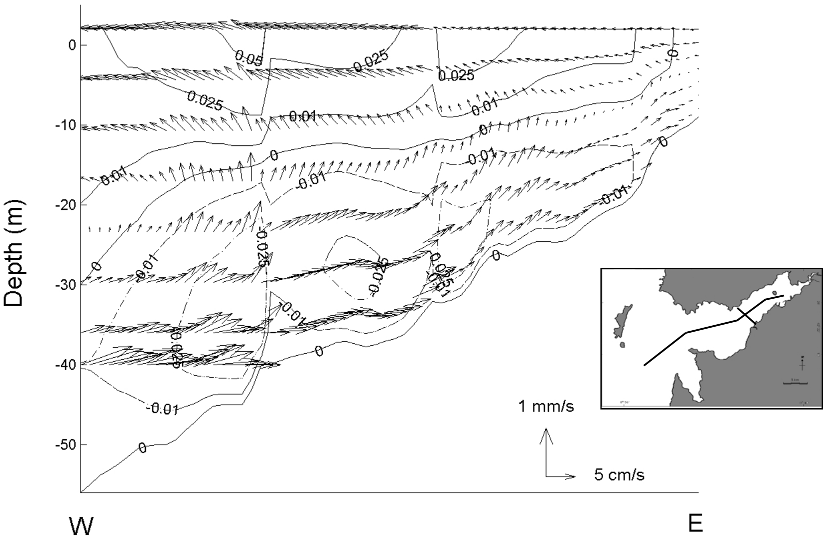

Figure 4.27: Residual currents for an along channel section. In the superimposed contour plot, the modulus of across channel velocity (positive northwards) is depicted.

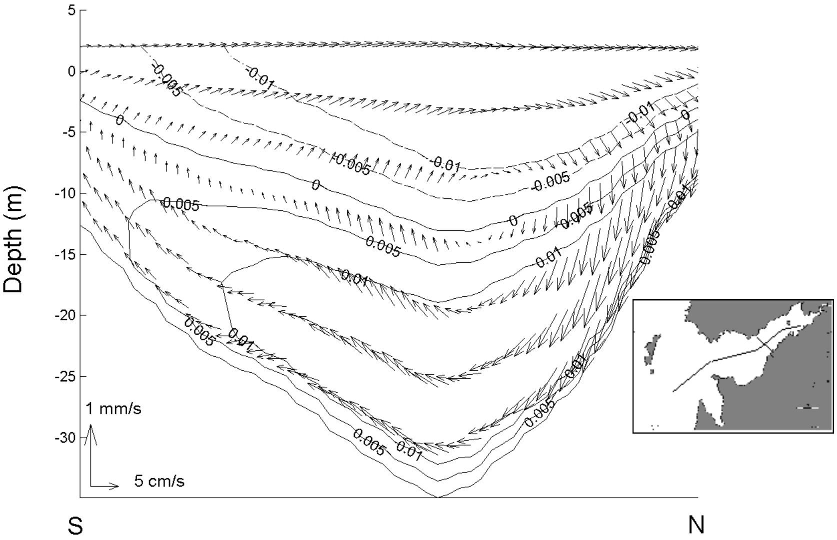

Figure 4.28: Residual currents for across-channel section B (6 km NS distance). In the superimposed contour plot, the modulus of along-channel velocity (negative seawards) is depicted.

In this study, our main aim has been the establishment of the circulation pattern forced by tide and the density gradient between river and coastal adjacent waters, both having characteristic winter values for the Ria de Pontevedra. The use of a 3D model allowed us to obtain the pattern resulting of this forcing combined with topography. A spatial picture of tidal and residual velocities in the ria, not available until the moment, was accomplished. On a tidal scale, only few direct Eulerian and Lagrangian measurements of currents in different points of the ria during a tidal cycle were available (*Ruiz-Mateo, [1984]*). Model tidal velocities are of the same order of magnitude as those observed with a Doppler currentmeter and follow a similar pattern to the few measurements by (*Ruiz-Mateo, [1984]*). The main component of the velocities was obtained as along-channel, with some recirculation in Sanxenxo and Bueu bays. The velocities in the Ria de Aldán have a different direction and lower values than those at nearby points at the estuary.

In figure 4.29, a measured field of salinity during the winter season (end November, cruise 4po11) with a river run-off close to that used in the simulations is shown. The salinity measurements were obtained starting outside the ria during the beginning of the flood tide, and it was finished before the ebb. Therefore, they constitute only an estimation of the tidal averaged salinities. At the bottom layer, the faster advance at the main channel and a north-south gradient of salinity are very similar to model predicted salinity, although model salinity values are lower at the north entrance of the ria. At the surface layer, salinity values predicted by the model are smaller than those observed, although the pattern is also similar. A direct comparison of model and measurements would require considering all of the forcing acting in the ria. The observed low surface salinities can be induced by the characteristic southerly (downwelling favorable) winds in the winter season, that introduce water in the ria through the surface layer and so a retention of fresh water inside the ria can be induced. Downwelling conditions were met on this cruise and also rainfall, not introduced in the model, can account for the lower observed salinities at the surface. Another fact that should be taken into account is that we have considered a uniform density distribution at the open boundary, since the north-south density gradient along the open boundary is not resolved by Levitus data nor there are measurements available. The sensitivity of the results to the density distribution at the open boundary should be assessed when measurements are available.

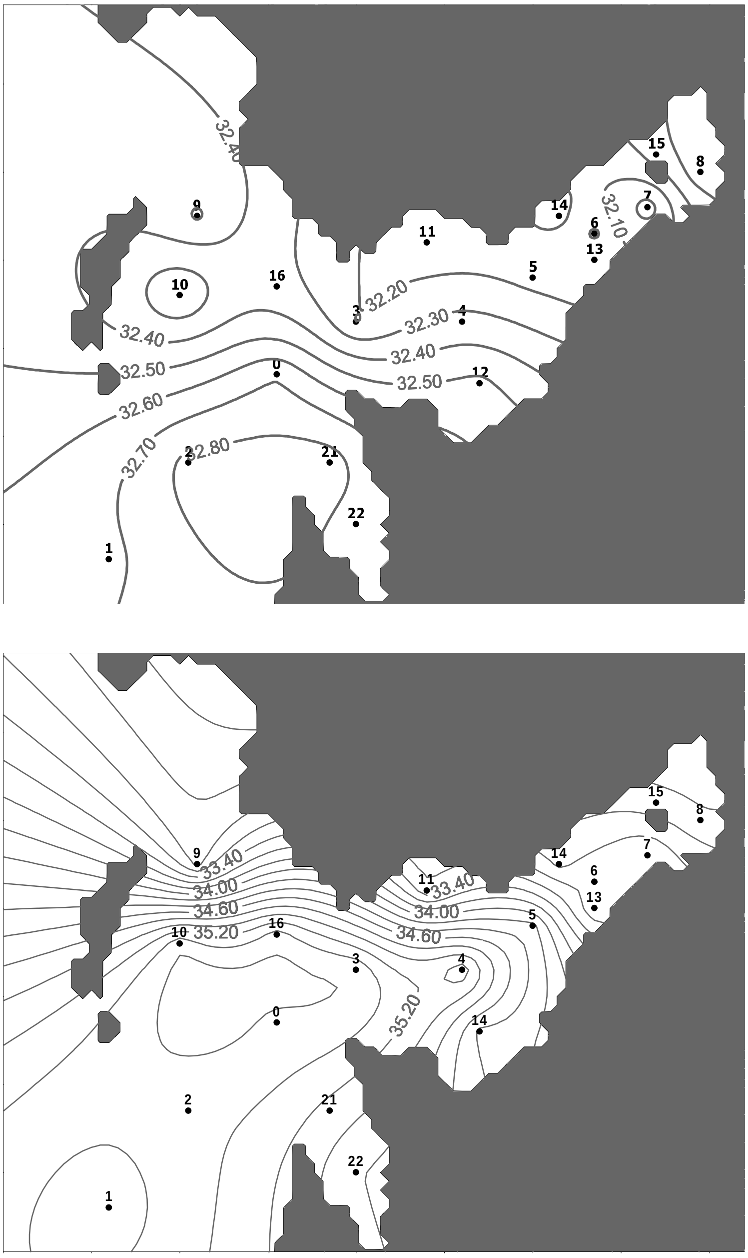

Figure 4.29: Measured surface and bottom fields of salinity in the ria on cruise 4po11.

A two-layered residual circulation is obtained for the applied forcing, with water flowing towards open sea at the surface layer and into the ria through the bottom layer. The computed residual velocities are of the same order of magnitude as those estimated in the Ria de Vigo by (*Prego and Fraga, [1992]*) with a box model and by (*Taboada et al. [1998]*) with a 3D baroclinic model. The fact that in the interior zone the flow goes mainly south from the Illa de Tambo has implications for evaluating the impact of the city and industry outfalls located near the south bank in the zone close to the river mouth. In the ria de Aldán, residual velocities are lower than in other zones of the ria, which indicates that residence times are longer there. In contrast to some box-model estimations in the Ria de Vigo (*Prego and Fraga, [1992]*), residual velocities near the river are smaller than in the outer part of the estuary. The same was obtained by *Taboada et al. [1998]* in their 3D-model simulations of residual fluxes in the same ria. Apart from the fact that the 3D-model considers barotropic and baroclinic pressure gradients in every point for the estimation of residual fluxes, probably, one of the main causes of discrepancy is the imposition of the vertical level of zero residual velocity in the box model from salinity measurements, that influences the subsequent computations. The level of zero residual in the 3D-model evolves in response to variation of flow properties, which is more realistic and influences the predicted fluxes.

In the present simulations, wind forcing was neglected. We pointed in last section that wind induces much of the variability in time scales of days, which can be an important effect on residual flows (*Dyer, [1998]*). It might be that wind forces the reversal of the obtained two-layered pattern, but an study of this effect would require further simulations with different wind forcing complemented with real data.

A transverse (cross-channel) component of residual circulation was described. To our knowledge, there have been carried out no measurements or estimations of this lateral circulation in Galician Rias, but some model results in the ria de Vigo (*Montero, [1999]*), that did not focus on residual circulation. The combined effect of stratification, irregular topography and Coriolis force are supposed to determine its form, a vertical clockwise (facing seaward) eddy. The center of the eddy lies near the level of zero residual flow, and is slanted to the north shore. The combination of this transversal with the longitudinal circulation results in a tendency for the flow to spiral as it propagates along the estuary. This introduces another source of mixing apart from vertical mixing and it might have an important effect in biogeochemical cycles and productivity in the estuary. It must be noted that this level of zero residual flow is at some extent sensitive to the parameterization of vertical turbulent exchange. In fact, there is some sensitivity to the value of α, which characterizes the dependence on stratification in equation 2.60. However, some tests with a constant value of ν rendered a similar pattern, which indicates that the differences in the prediction of vertical eddy coefficients are not determinant in the set-up of this circulation, although they affect details of its intensity and variability. The use of a more advanced turbulence model, for example a k-ε model, that takes into account the sources and sinks of turbulence, is a next step. It would allow us to evaluate efficiently possible variations in the form of this transverse circulation in response to changes in wind, tide and density forcing.

A similar study was carried out in summer conditions, i.e. low river run-off (5 m$^3 s^{-1}$) and Levitus August monthly mean, that corresponds to ENACW in the whole water column, imposed at the open boundary. Tidal currents are not appreciably affected by the change in this forcing, as its intensity is mainly dominated by harmonic forcing. The resulting residual circulation is much smaller than in the winter case. Some box model estimates (*Otto [1975], Prego and Fraga [1992] and Rosón et al. [1997]*), suggest an enhanced residual flow in upwelling conditions. As we showed in section 4.2, summer hydrodynamics seems to be dominated by the sequence of upwelling-downwelling events, where wind forcing plays a dominant role. However, it is expected that in low wind situations, residual circulation in summer months is small. Further experiments must be carried out considering wind forcing for studying the behavior of the ria during the upwelling season.

As we reviewed in section 4.2.b, the published information about Galician Rias has focused on measurements of thermohaline and biogeochemical properties, especially on time scales useful mainly to assess annual variability and only in some points in the ria. Other physical variables like currents and tides must be analyzed to get a better understanding of the hydrodynamics of the ria. The interest of cross-channel measurements of currents is suggested by our results.

4.3.b.3 Application of a 1D model

We showed in chapter 2 that the use of a two equation closure may lead to an improved description of turbulent exchanges. In this section, the ria de Pontevedra is studied with the model GOTM to illustrate the superior physical description of the system provided by a more advanced turbulence model. To date, nothing has been said about the physics of mixing in the Galician rias, and the only available information comes from salinity and temperature measurements, at best with a periodicity of some days. As a first approach to the comprehension of mixing processes, the model GOTM was adapted for the simulation of a point in the estuary. The point was located in the intermediate region of the ria (42^o 22.477' N; 8^o 46.998' W, marked with a X in figure 4.1) with a mean depth of 23 meters. The chosen turbulence closure was a k-ε model with stability functions from *Canuto et al. [2000]*, that in previous sections was shown to be the most physically sound. A dataset obtained in the framework of the project "Ordenación Integral del Espacio Marítimo Terrestre de Galicia" ("Integral Management of the Maritime-Terrestrial Space from Galicia", financed by the Consellería de Pesca from the Xunta de Galicia) was used for estimating some forcing during the period October- November 1997.

Tidal gauge measurements were available to impose the elevation. The elevation is used in the 1D model only for letting the grid evolve. The external pressure gradient was estimated from a series of near bottom velocities following the procedure detailed in *Burchard [1999]*. As we noted in section 2.4.c, the idea is that a time series of velocity can provide an estimation of surface slopes. Although the barotropic pressure gradient is constant in depth and velocity at any depth would be adequate, surface processes greatly influence the velocity at the surface. Therefore, time series of current far from the surface layer are preferable. ACDP data corresponding to an average over the bottom first 4 meters were used in the simulation. Wind stress was calculated from wind measurements at a meteorological station placed at the highest point in the Ons island (about 100m over sea level). The station lacked sensors for measuring parameters needed for heat flux computations. Therefore heat fluxes can not be measured, and will be neglected. At the same time, some cruises were carried out every 3 days and provided CTD casts at a nearby point from where to get temperature and salinity. These casts are used for initializing the model and also for avoiding the model to diverge in the course of the run. This is accomplished by relaxing salinity and temperature to the observed values. The internal pressure gradient should be estimated from continuous measurements of density gradients. Therefore, as a first approach, a salinity flux of -0.00005 m^{-1} was imposed in the first 10 meters to simulate the river effect. From that depth on, the salinity flux is gradually reduced until the bottom, to account for the reduction of river influence towards the bottom. As we noted in section, bottom waters (from 30 m down) are oceanic during much of the year, so the assumption of a non-constant in depth salinity flux is reasonable. In a first run, advection of salinity was considered, but the predicted salinity and temperature values were forced to very non realistic values due to the lack of realism of the imposed internal pressure gradient. An adequate consideration of advection would require continuous measurements of density gradients.

As we showed in section 4.2.b.1, the usual conditions in this seasonal period are a uniform temperature of the column and a haline stratification in the water column. Cruises took place on 22th,27th and 30th October 1997 and 3rd and 6th November 1997. For the first cruise salinity was greater than 35 in the whole column, while for next cruises surface salinity gradually diminishes due to the effect of river-runoff. In figure 4.32, salinity and temperature predictions are contrasted to the observed values. It must be noted that the contour of observed magnitudes was obtained only with 5 values, so the apparent overall disagreement is not so worrying, and some of the observed stratification is induced by contouring. Temperature predictions are acceptable and the range of variation of the observed temperature is small. Salinity at surface layers is underestimated in around 0.3 from around 30th October. A prediction of salinity and temperature observed values would require the knowledge of density gradients and heat and salinity fluxes at the surface.

The main forcing are studied in figures 4.30 and 4.31. Sea surface elevation (figure 4.30) is not used as forcing, but only to adapt the grid size to the movement of the free surface. In figure 4.30, also the bottom velocity, used to estimate the barotropic pressure gradient, is shown. Sea surface elevation is clearly semidiurnal, and a modulation spring-neaps can be seen. The start of the simulation coincided with the end of neap tides, which might be related to the high observed surface salinities, and around 1st November spring tide occurred. Near bottom velocity was characterized by a strong non-tidal variability. It is induced by variations in offshore wind and weather conditions. A diurnal evolution seem to be characteristic of bottom velocity between 29th October and 2nd November. A diurnal component also seems to dominate the variation of wind stress, that is plotted in figure 4.31. During the period of simulation, wind speed values were always smaller than 10 m s^{-1}, except during the peak around 27th October.

In figure 4.33 and 4.34, turbulent magnitudes are plotted. In figure 4.33, the evolution of the logarithm of eddy viscosities and diffusivities is shown. A bottom and a surface layer can be seen, with the maximum of eddy coefficients at mid-depth. The order of magnitude of eddy coefficients is of $10^{-1.5}$ m$^2 s^{-1}$ in the intermediate region and reduces to 10^{-2} m$^2 s^{-1}$ near bottom and it is even smaller near surface. Also the logarithm of the turbulent kinetic energy and the dissipation rate of turbulent kinetic energy are plotted in figure 4.34. By looking at the turbulent kinetic energy, we observe that the mixing induced by tidal friction extends almost to surface. At the surface, wind stress does not induce much turbulence, which is deduced from the rather low values of TKE. This might be induced by the fact that wind data were taken over land, while for computing wind stress we would need winds over sea. Some peaks in bottom turbulence seem to be correlated with bottom velocity and some diurnal peaks coinciding with flood can be observed between 27th October and 3rd November. These peaks coincide with flood and afterwards some periods of reduced turbulence can be observed. Bottom turbulence is reduced, and turbulence created at the surface extincts around 10 m. This induces a reduction of turbulent eddy coefficients that can be seen in figure 4.33 Dissipation rate of TKE is correlated to TKE. High levels of turbulent activity are correlated with high dissipation rates. Therefore maxima of dissipation rate appear for maxima of TKE. Near the surface dissipation levels are low and only in the first meter a relative increase can be observed: dissipation rates are of the order of 10^{-5} and get reduced to 10^{-6} in 1 meter.

A preliminary picture of mixing processes in the ria is presented. For the situation under study, mixing is mainly of tidal origin, with high levels of mixing that reach the surface. Wind mixing is not a major effect in comparison to tidal mixing, although this can be related to an underestimation of wind stress after extrapolating wind data over land to wind data over sea. The response of the system is clearly related to the variability of the bottom velocity, from where slopes of pressure gradients are estimated. This procedure lies in the assumption that advection of momentum is not a major effect on pressure gradients. Some tests carried out in *Burchard [1999]* show that for some estuarine cases, where advection would be supposed to have an effect, this technique provides reliable results. Time series of velocities in Galician Rias have not been analyzed to date, so there is lack of knowledge of the processes that determine its variability. Meteorological forcing must be taken into account. The time scales of this forcing are of the order of days. Further analysis of these time series and its correlation to meteorological variability is required. 1D models are not really made for estuarine modeling, since many measurements are needed for estimating advective terms. However, we have shown how they can help to understand mixing processes in these systems.

As we noted in chapter 2, shear probes are an useful tool in the study of mixing in natural waters. We already quoted some works on dissipation measurements and modeling efforts in shelf sea scenarios like the Irish Sea (*Simpson et al. [1996], Burchard et al. [1998]*), where tidal mixing is important. Our results in Knebel Vig show that direct confrontation of turbulence measurements and model results is a stringent test for models. Knebel Vig, however, was a site with a more reduced tidal range, which accounts for lower bottom turbulence levels. Besides, in spite of its semi-enclosed shape, advection had a major influence after the change in wind direction. To our knowledge, few shear probe measurements of turbulence in estuaries have been carried out. *Peters [1997]* presents measurements of shear and dissipation rates for a point at the Hudson River estuary and founds a complex pattern, with neap to spring transitions during high river flow. We have not observed a neap-spring transition in our application. River flow in the Hudson river is much bigger than in the Ria (the river Lérez shows typical winter values of 50 m$^3 s^{-1}$), so more stratification is introduced. However, our knowledge of density profiles and internal pressure gradients in the ria is very small and this can hide some effects. Consequently, combined measurements of turbulence, meteorological forcing, currents, elevation and density profiles and gradients are necessary to arrive to a comprehension of how different forcing balance and account for mixing levels in the ria.

This 1D model could also be applied to other seasonal conditions to assess variability of mixing in response to different forcing. However, understanding mixing in Galician Rias and in estuaries is a challenging task that requires the combined effort of measurements and model development. We have shown that 1D column models, in particular GOTM, can provide us with ideas to guide further research on mixing in estuaries.

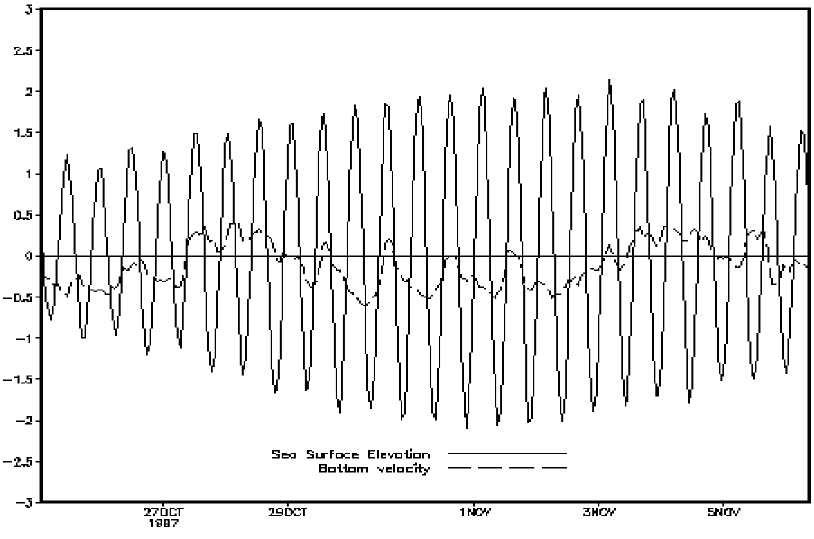

Figure 4.30: Sea surface elevation in m and bottom velocity in m s^{-1} for the period of simulation

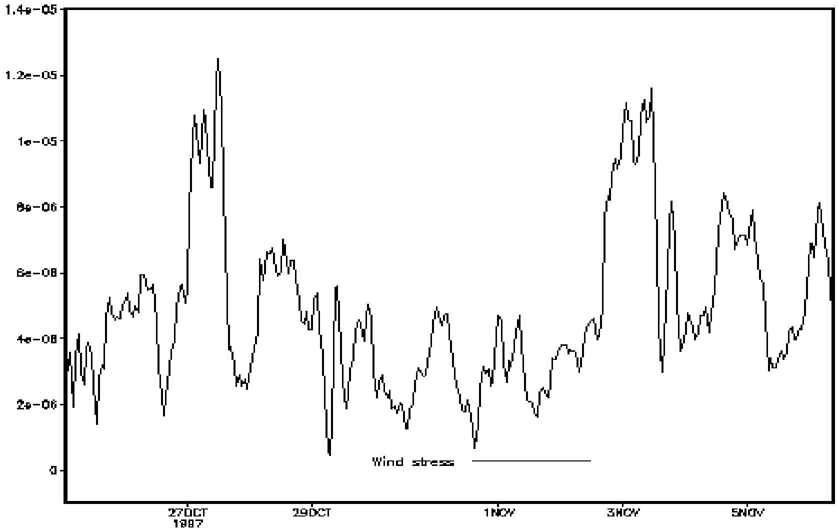

Figure 4.31: Wind stress modulus (normalized by ρ_0) in N m^{-2} for the period of simulation

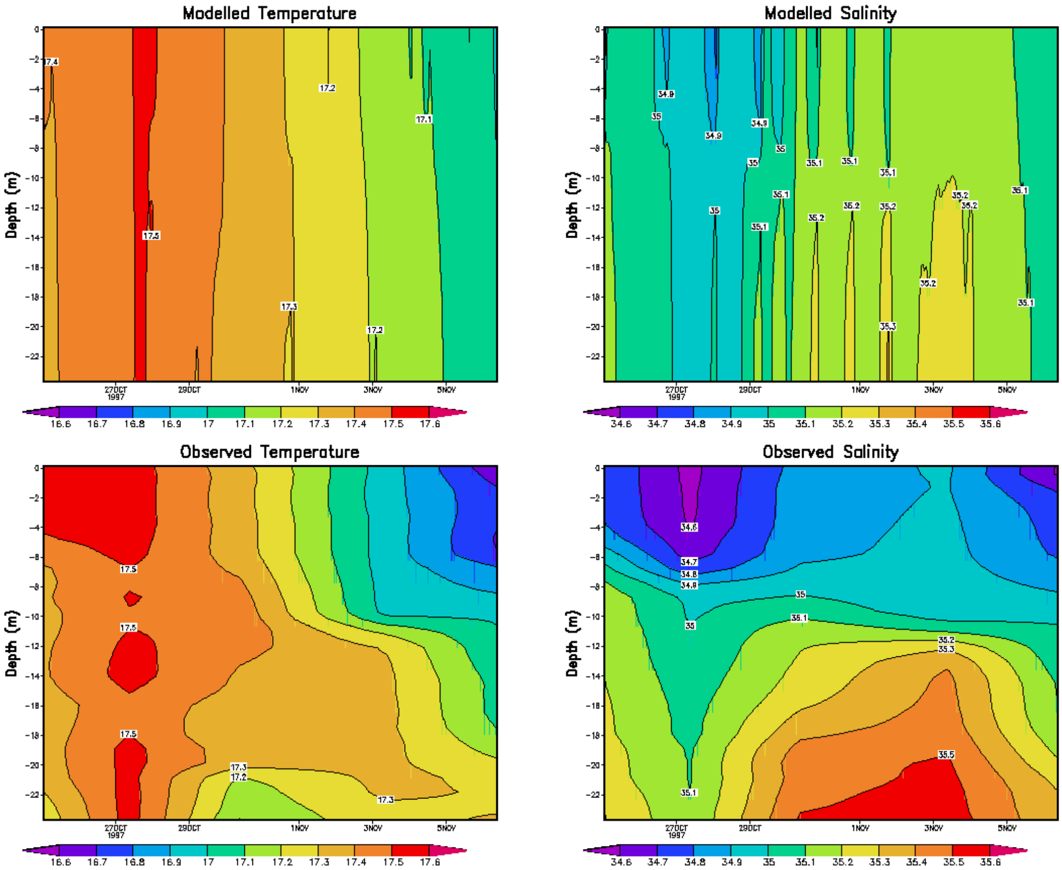

Modelled Temperature

Modelled Salinity

Observed Temperature

Observed Salinity

Figure 4.32: Modeled and observed contours of salinity and temperature.

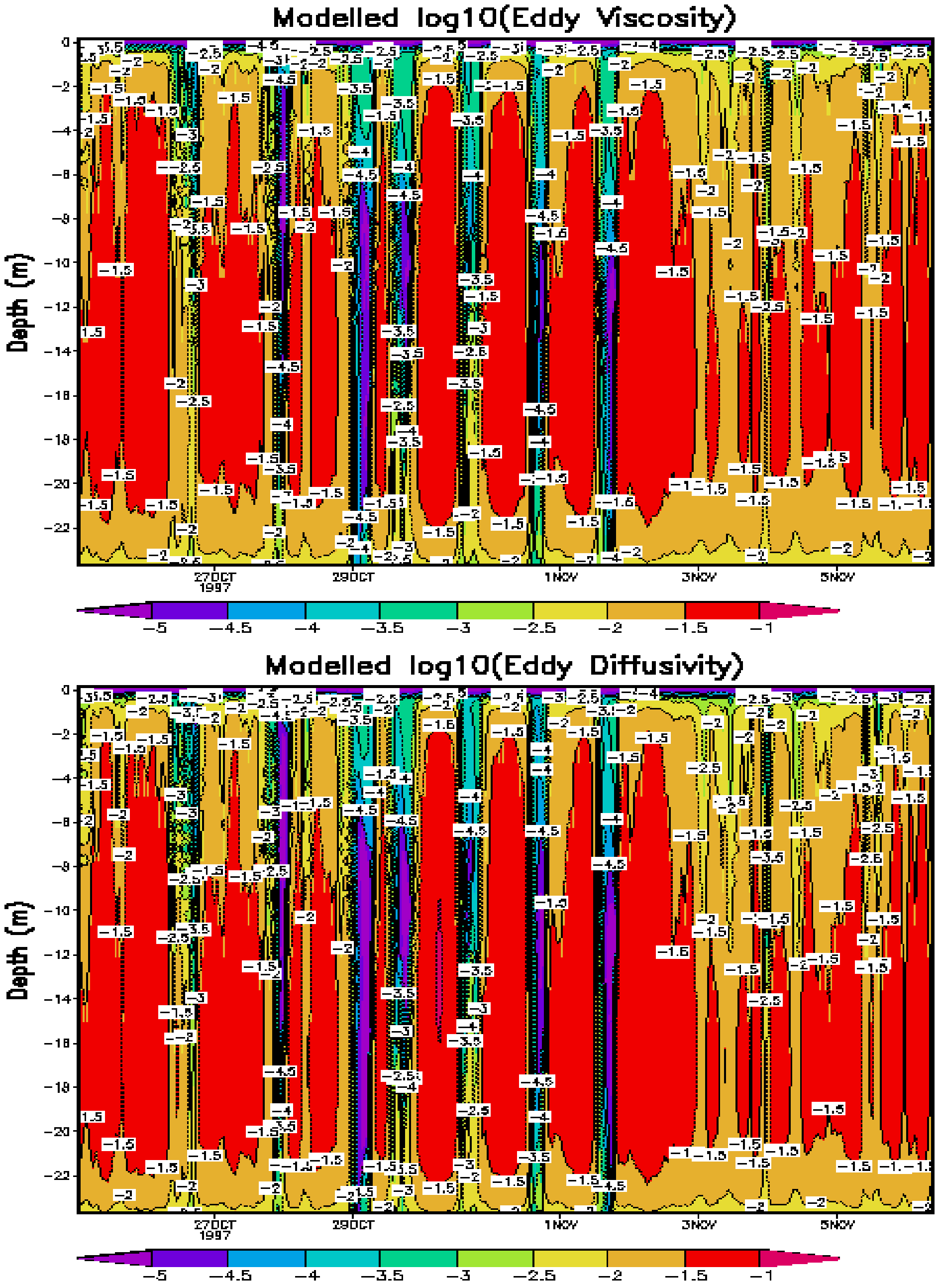

Figure 4.33: Modeled contours of eddy viscosity and diffusivity in m^2s^{-1}

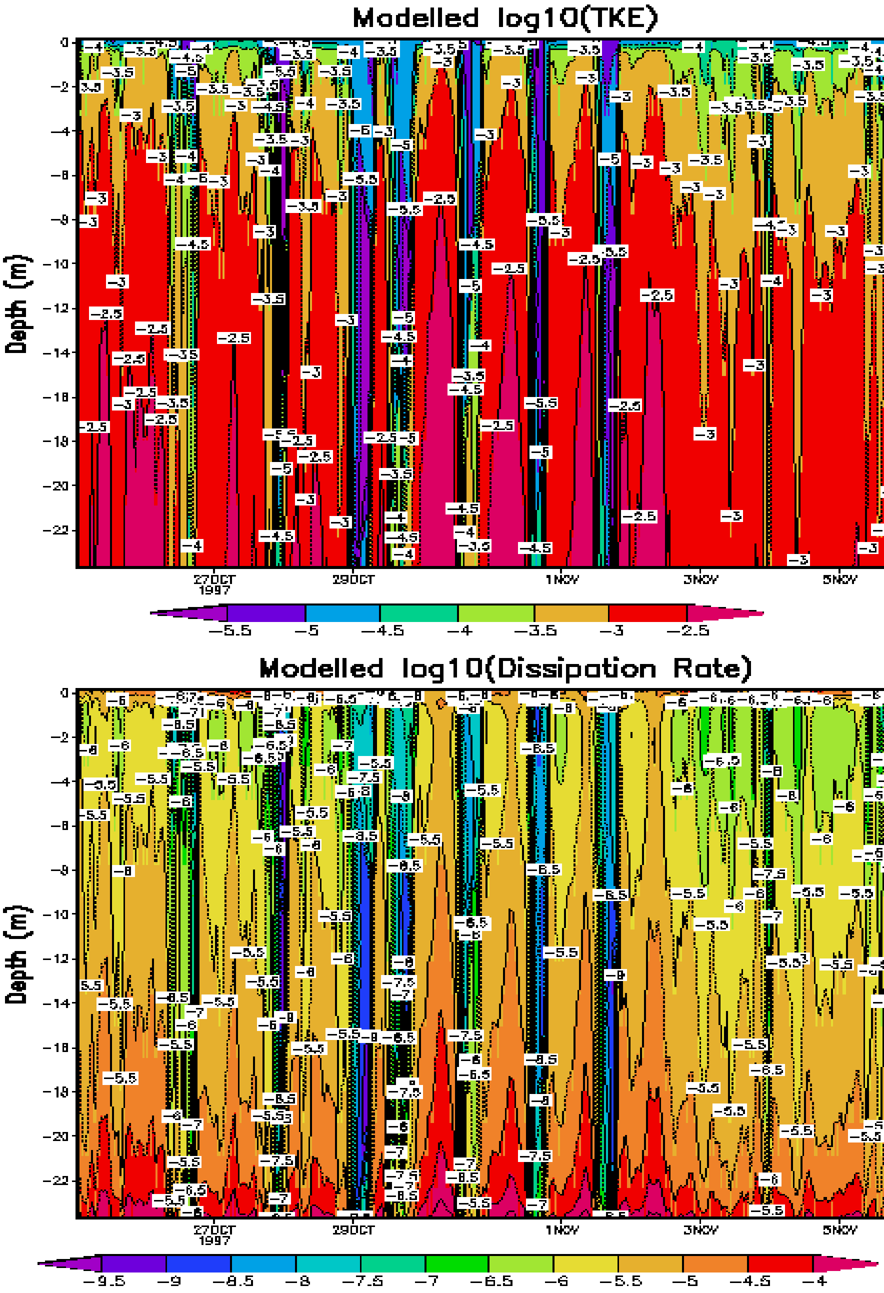

Figure 4.34: Modeled contours of turbulent kinetic energy and dissipation rate of turbulence kinetic energy.

5 Conclusions and outlook

In this study, several steps have been given towards the setting-up of a 3D baroclinic model for the study of the Ría de Pontevedra. The results of a monitoring project of thermohaline and chemical properties in the Ría during the years 1997-1998 and the available information about the Ría have been used to identify the relevant spatio-temporal scales of variability. A 3D baroclinic model has been adapted to the area for the simulation of hydrodinamics and finally, several turbulent closures with different levels of complexity have been coded in the 1D water column model GOTM (General Turbulence Ocean Model) and their performance has been compared in analytical, estuarine and open sea situations. This has provided evidence that the use of a two equation turbulence model can lead us to a major improvement of the description of flows in different environments, including the Ría.

The relevant time scales of variability in the Ría de Pontevedra have been identified and illustrated with help of different available data sets. The main forcing on a short-term scale is the tide, that has a marked semidiurnal character in the estuary. On a longer time scale, the effect of tide is not so important due to its periodical behavior, and meteorological-induced events and the variability in the density gradients between river and shelf waters dominates the response of the system. The annual cycle of variation has been determined with help of thermohaline measurements in different parts of the Ría. These data covered from October 1997 to October 1998. Two seasons have been distinguished driven by the annual cycle of heat flux, rainfall and prevailing winds: a winter season, with haline stratification and dominance of downwelling events and a summer season, where thermal stratification replaces haline stratification and upwelling conditions are usual. Both in the upwelling and in the downwelling season, there is variability in the wind regime that results in upwelling or downwelling events of a typical time scale of some days. The study of the spatial distribution of thermohaline properties in different cruises have lead us to get a picture of the along-channel variability. Near the river mouth, freshwater influence is greater and towards the entrance of the Ría, oceanic influence grows, but the actual distribution is influenced by wind conditions.

A set of different models for the description of turbulence has been assembled and tested on the one-dimensional water column model GOTM. This model has been co-developed by the author and can be downloaded from http://www.gotm.net. All the closures studied are based in the eddy viscosity principle and relate eddy coefficients to mean flow properties. The most simple ones are the 0-equation models, where eddy coefficients are obtained from empirical or ad hoc parameterizations. Most models are based in the Prandtl hypothesis. More information on the evolution of the flow is introduced in the models that consider a transport equation for TKE or two transport equations, one for TKE and one for the turbulent length scale. The performance of some turbulent closures has been tested against analytical predictions and observational data sets.

In an ideal experiment of a constant stratified fluid forced by a constant wind shear, the two equation models perform the best. Among these models, the k-ε results are the most physically sound because it automatically fulfills the law of the wall near boundaries, without additional constraints. The choice of the stability functions has been shown to play a determinant role in the predictions of the model. The classical *Mellor and Yamada [1982]* stability functions do not have a stable numerical behavior, while the quasiequilibrium version derived after them predict an unphysical maximum of the turbulent kinetic energy at mid-depth. The *Canuto et al. [2000]* stability functions solve these problem through their consideration of shear on stability functions and their numerical stability.

The performance of different models for parameterizing dyapicnal mixing was assessed by simulating the annual cycle for the years 1961-62 the Ocean Weather Station Papa on the North Pacific. Classically, it has been found that local turbulence models overestimate the observed Sea Surface Temperature and low rate of dyapicnal mixing has been blamed as the cause of this bad performance. Several simple parameterizations have been designed to account for these effect in the framework of local turbulence models and an improvement of performance was traditionally observed, specially for the *Kantha and Clayson [1994]* empirical parameterization. By using the *Canuto et al. [2000]* stability functions, the SST is no more overestimated. This indicates that the SST overestimation lied in an incomplete description of the physics of the mixing layer and not in the parameterization of diapycnal mixing. However, parameterizations of internal mixing are required to provide a physical value of eddy coefficients in the interior region. Our results indicate that the k-ε model with stability functions from *Canuto et al. [2000]* and parameterization of diapycnal mixing by *Large [1994]* can be used for computing physically sound eddy coefficients that provide the physical forcing for biogeochemical studies.

An application in an estuarine environment (Knebel Vig) where dissipation rate of TKE measurements were available provided an illustration of the possibilities offered by direct intercomparison of turbulence measurements and numerical model predictions. For this application, wind stress, heat fluxes and external pressure gradients forced the model and advection was parameterized by nudging temperature and salinity to the observed values. In this way, turbulent magnitudes are diagnosed, which allows an intercomparison of model predictions and turbulence measurements. We have found that comparison with real dissipation rate data is a hard test for models, although much insight on the physics of the processes and on the performance of the model can be gained. There is a need of further research on modeling stably stratified situations in the framework of two equation closures.

The 3D baroclinic model MOHID3D has been adapted for simulation of flows in the Ría de Pontevedra on a tidal and subtidal scale. The choice and specification of the different parameters has been discussed and some applications with ideal forcing have been carried out. A picture of tidal and residual velocities has been obtained. The combined effect of the density gradient between river and open boundary and bathymetry induces the establishment of a double layered pattern on a subtidal scale. Water flows seawards at the surface layer and downwards at the bottom layer. A lateral component of the subtidal residual component appears in the computations and suggests another mechanism for mixing, that can be important in the understanding of sediment and biogeochemical cycles in the estuary. The same experiment with summer conditions predicted a very small residual circulation, which indicates that other forcing, namely wind, are necessary for adequately simulating circulation in summer conditions. Further comparison with real data is still necessary for running the model in a prognostic way. A monitoring of shelf conditions is crucial for an adequate performance of the model. Also, the interest of measurements of cross-channel variability is suggested by our results.

Finally, the model GOTM has been applied to the ria de Pontevedra. We have shown how in slightly stratified conditions and for the characteristic tidal and wind forcing acting on the estuary, a mixed layer extends to surface. Further analysis of how currents in the estuary respond to subtidal forcing is necessary before conclusions on the variability of mixing in the estuary can be carried out. The assemblage of complete data sets that cover all the physical forcing is a requirement for improving our understanding of mixing processes in the ria.

Two equation turbulence closures are more powerful in simulating complex flows, but they have been not generally used until the moment in real 3D ocean and coastal applications. The main reason has been the extra computing requirements of solving additional equations. Also the choice of parameters and the difficulty of understanding how a more complex turbulence closure influences the results is a difficult task. By using the 1D model as a test bed, we have shown how a k-ε model describes realistically mixed layer behavior. The coupling of two-equation turbulence closures in GOTM to our 3D model will allow us to improve the description of the hydrodynamic of the ria and to assess the impact of variations in forcing on the response of the ria.

6 Bibliography

[1] Atlas Climático de Galicia (Climatical Atlas of Galicia), Coordinated by Antonio Martínez Cortizas and Augusto Pérez Alberti. Consellería de Medio Ambiente. Xunta de Galicia. In Galician,1999.

[2] Abbott, M.B., A. Damsgaardand and G.S. Rodenhuis, System 21, Jupiter, a design system for two dimensional nearly horizontal flows. *J. Hyd. Res*, 1, 1-28. 1973.

[3] Álvarez-Salgado, X.A., G. Rosón, F.F. Pérez and Y. Pazos. Hidrographic variability off the Rías Baixas (NW Spain) during the upwelling season. *J. Geophys. Res.*, 98(C8), p. 14447-14455, 1993

[4] Arakawa, A. and V.R. Lamb, Computational design of the basic dynamical processess of the UCLA General Circulation Model. *Methods of Computational Physics*, 17, pp.174-264. 1977.

[5] Backhaus, J., A three dimensional model for the simulation of shelf sea dynamics. *Dt. Hydrogr. Z.,* 38, 165-187, 1985.

[6] Bakun, A., Coastal upwelling indexes, west coast of North America, 1946-71, *NOAA Tech. Rep. NMFS*, 671, 103 pp., 1973.

[7] Bermúdez, A., A. Dervieux, J.A. Desideri and M.E. Vázquez, Upwind schemes for the two-dimensional shallow water equations with variable depth using unstructured meshes. *Comput. Methods App. Mech. Engrg.*, 155, 49-72. 1998.

[8] Blackadar, A. K., The vertical distribution of wind and turbulent exchange in neutral atmosphere, *J. Geophys. Res. 67, 3095-3102, 1962.*

[9] Blanke, B. and P. Delecluse, Variability of the tropical Atlantic Ocean simulated by a general circulation model with two different mixed-layer physics, *J. Phys. Oceanography, 23,* 1363-1388, 1993.

[10] Bougeault, P. and P. Lacarrère, Parameterization of orography-induced turbulence in a mesobeta-scale model, *Monthly Weather Review*, 117, 1872-1890. 1989.

[11] Bowden, K.F. and P. Hamilton, Some experiments with a numerical model of circulation and mixing in tidal estuaries. *Estuarine and Coastal Marine Science* 3 281-301, 1975.

[12] Bryan, K. A numerical method for the study of the world ocean, *J. Comput Phys.*, 4, 347-376, 1969.

[13] Burchard, H.: Turbulenzmodellierung mit Anwendungen auf thermische Deckschichten im Meer und Strömungen in Wattengebieten, Ph.D. thesis, report GKSS 95/E/30, GKSS Research Centre Geesthacht, Geesthacht, In German, 1995.

[14] Burchard, H., and H. Baumert, On the performance of a mixed-layer model based on the k-ε turbulence closure, *J. Geophys. Res., 100*, 8523-8540, 1995.

[15] Burchard, H.: The 3D hydrostatic equations in a generalized vertical co-ordinate system. Theory and test cases , *Rep. ICCH R22*, 57 pp., ICCH, Hørsholm, Denmark, 1996.

[16] Burchard, H., O. Petersen, and T.P. Rippeth. Comparing the performance of the Mellor-Yamada and the k-ε two-equation turbulence models, *J. Geophys. Res*., 103, 10,543-10,554, 1998.

[17] Burchard, H.: Recalculation of surface slopes as forcing for numerical water column models of tidal flow, *Appl. Math. Mod.*, 23, 737-755, 1999.

[18] Burchard, H. and Petersen, O. Models of turbulence in the marine environment - A comparative study of two-equation turbulence models. *Journal of Marine Systems*, 21, 29-53, 1999.

[19] Burchard, H., K. Bolding and M.R. Villarreal, GOTM, a General Ocean Turbulence Model. Theory, implementation and test cases. Report EUR18745 EN, European Comission, 103 pp., 1999.

[20] Burchard, H. Note on the q^2l equation by *Mellor and Yamada [1982], J. Phys. Oceanography,* submitted 2000.

[21] Burchard, H. and K. Bolding, Comparative analysis of four second-moment closure models for the oceanic mixed layer, to appear in *J. Phys. Oceanography,* 2000.

[22] D. R. Caldwell and J. N. Moum, Turbulence and mixing in the ocean *Rev. Geophys.* Vol. 33 Suppl., AGU, 1995. HTML version in *http://earth.agu.org/revgeophys/caldwe01/caldwe01.html.*

[23] Cameron, W.M. and Pritchard, D.W, Estuaries. In: *The Sea*, (Ed. MN Hill), Vol. 2, Wiley, New York, 306-324, 1963

[24] Cancino, L. and Neves, R. Hydrodynamic and sediment suspension modelling in estuarine systems. Part II: Application to the Western Scheldt and Gironde estuaries, *Journal of Marine Systems* 22, 117-131, 1999.

[25] Canuto, V.M., A. Howard, Y. Cheng and M.S. Dubovikov, Ocean turbulence I: one-point closure model. Momentum and heat vertical diffusivities, *Journal of Physical Oceanography*, submitted, 2000.

[26] Castro, C.G., F.F. Pérez, X.Álvarez-Salgado, G. Rosón and A.F. Ríos, Hydrographyc conditions associated with the relaxation of an upwelling event off the Galician coast (NW Spain), *Journal of Geophysical Research*, 99, 5153-5147, 1994.

[27] De Castro, M., M. Gómez-Gesteira, R. Prego, J.J. Taboada, P. Montero, M.R. Villarreal, P. Herbello and V. Pérez-Villar, Wind and tidal influence on water circulation in a Galician Ria (NW Spain), accepted in *Estuarine, Coastal and Shelf Science*, 2000.

[28] Chase J. Wind-driven circulation in a Spanish estuary, *Estuarine and Coastal Marine Science* 3, 303-310, 1974.

[29] Chippada S., Dawson C., Wheeler M., A godonov-type finite volume method for the system of shallow water equations, C*omputer methods in applied mechanics and engineering*. 151(01): 105-130, 1998.

[30] Clayson, C. and L. Kantha, Turbulent kinetic energy and its dissipation rate in the equatorial mixed layer, *Journal of Physical Oceanography*, 29, 2146-2166, 1999.

[31] Coelho, H., A. Santos, T. L. Rosa and R. Neves: Modelling the wind driven flow off Iberian Peninsula, *GAIA*, 8, 71-78, 1994.

[32] Davies, A.M., P.J. Luyten and E. Deleersnijder, Turbulence energy models in shallow sea oceanography, In: *Quantitative Skill Assessment for Coastal Ocean Models,* D.R. Lynch and A.M. Davies Eds. American Geophysical Union, 1995.

[33] Deleersnijder, E. and Luyten, P., On the practical advantages of the quasiequilibrium version of the Mellor and Yamada level 2.5 turbulence closure applied to marine modelling, *App.*

Math. Modelling, 18, 281-287, 1994.

[34] Dietrich, G., General Oceanography, Interscience Publishers, New York. 588 pp., 1963.

[35] ISPRAMIX, a three dimensional free surface model for coastal ocean simulations and satellite data assimilation on parallel computers, Technical report EUR 18129EN, European Comission, 76 pp., 1998.

[36] Doval, M.D., E. Nogueira and F.F. Pérez, Spatio temporal variability of the thermohaline and biochemical properties and dissolved organic carbon in a coastal embayment affected by upwelling: the Ría de Vigo (NW Spain), *Journal of Marine Systems*, 14, 135-150, 1998.

[37] Dyer, K. R.. Estuarine flow interaction with topography, lateral and longitudinal effects. In: B.J. Neilson et al. (Eds.), *Estuarine Circulation*, Humana Press, Clifton, New Yersey, pp.39-59, 1989.

[38] Dyer, K.R., Response of estuaries to climate change. In: *Climate Change Impact on Coastal Habitation (* Ed. D. Eisma). Lewis Publisher, Boca Raton, Florida. 1995.

[39] Dyer K. R., Estuaries, a physical introduction. 2nd edition, John Wiley & Son Ltd; 210 pages, 1998.

[40] Eifler, W. and W. Schrimpf, ISPRAMIX, a hydrodynamic program for computing regional sea circulation patterns and transfer processes. CEC Report EUR 14856 EN, 1992.

[41] Fernando, H. J. S., Turbulent mixing in stratified fluids, *Ann. Rev. Fluid Mech.*, 23, 455–494, 1991.

[42] Figueiras, F.G., Niell, F.X. and Zapata, M., Hidrografía de la ría de Pontevedra (NO de España) con mención especial al banco de Placeres (Hidrography of the Ría de Pontevedra (NW Spain) with special mention to Placeres bank) . *Investigaciones Pesqueras* 49(3), 451-472. In Spanish, 1985.

[43] Fiúza, A.F. G., Hidrologia e dinamica das aguas costeiras de Portugal, PhD dissertation, 294 pp., University of Lisboa, September 1984.

[44] Fiuza, A.F.G., M. Hamann, I. Ambar, G. Díaz del Río, N. González and J.M. Cabanas , Water masses and their circulation off western Iberia during May 1993. *Deep Sea Research I* 45, 1127-1160, 1998.

[45] Fraga, F.. Upwelling off the Galician coast, Northwest Spain. In: F.A. Richards, (Ed.), *Coastal Upwelling*, American Geophysical Union, Washington, pp. 176-182, 1981.

[46] Fraga, S., D.M. Anderson, I. Bravo, B. Reguera, K.A. Steindiger and C.M. Yentsch. Influence of upwelling relaxation on dinoflagellates and shellfish toxicity in Ría de Vigo. *Estuarine, Coastal and Shelf Science,* 27, 349-361. 1988.

[47] Frouin, R., A.F.G. Fiúza, I. Ambar and T.J. Boyd, Observations of a poleward surface current off the coasts of Portugal and Spain during winter, *Journal of Geophysical Research*, 95, 679-691. 1990

[48] Fletcher, C.A.J., Computational techniques for fluid dynamics. Volume I. 2nd Edition. *Springer Series in Computational Physics,* Springer Verlag, 401 pp., New York, 1991.

[49] Fraga, F. and R. Margalef, Las Rías Gallegas. Estudio y Explotación del Mar en Galicia (Galician Rías: Study and Exploitation of the Sea in Galicia). Cursos y Congresos, Universidad de Santiago de Compostela, p. 101-122, In Spanish, 1979.

[50] Fraga, F. and R. Prego, Condiciones hidrográficas previas a la purga de mar (Hydrographic conditions prior to red tide), *Cuadernos da Área de Ciencias Mariñas.* Seminario de Estudos

Galegos, 4, 21-44, In Spanish, 1989.

[51] M.G. Foreman, Manual for Tidal Heights Analysis and Prediction, *Pacific Marine Science Report* 77-10, Institute of Ocean Sciences, Victoria, B.C., Canada. 1977.

[52] Frey, H., A three-dimensional, baroclinic shelf sea circulation model - 1. The turbulence closure scheme and the one-dimensional test model, *Cont. Shelf Res., 11*, 365-395, 1991.

[53] Galperin, B., L.H. Kantha, S. Hassid, and A. Rosati A quasi-equilibrium turbulent energy model for geophysical flows, *J. Atmos. Sci., 45*, 55-62, 1988.

[54] Gaspar, P., Y. Gregoris and J. Lefevre, A simple eddy kinetic energy model for simulations of the oceanic vertical mixing: Tests at station Papa and long-term upper ocean study site, *J. Geophys. Res.*, 95, 16179-16193, 1990.

[55] Gent, P.R. and McWilliams, Isopycnal mixing in ocean circulation models. *J. Phys. Oceanography,* 20, 150-155, 1990

[56] Geyer, W.R. and Smith, J.D. Shear instability in a highly stratified estuary, *J. Phys. Oceanography*, 17, 1668-1679, 1989.

[57] Gómez-Gesteira, M., Montero, P., Prego, R., Taboada, J., Leitao, P., Ruiz Villarreal, M., Neves, R. and Pérez-Villar, V.. A two-dimensional tracking model for pollution dispersion in A Coruña and Vigo Rías, *Oceanologica Acta* 22(2) 167-177, 1999.

[58] Helland-Hansen, B. and F. Nansen, The eastern North Atlantic. *Geophys. Publ.* 4, 1-76, 1926.

[59] Hirsch, C. Numerical computation of internal and external flows. Vol I: Fundamentals of numerical discretization. *Wiley Series in Numerical Methods in Engineering.* John Wiley and Sons, 515 pp., Chichester. 1988.

[60] Ibarra, E. and Prego, R., La Ría de Pontevedra: Revisión de su conocimiento. (The Ría de Pontevedra: areview of its knowledge) *Monografías de Química Oceánica*, 1, 55-87, In Spanish, 1997.

[61] James, I.D. A general three-dimensional eddy-resolving model for stratified seas. In: *Three-dimensional models of marine and estuarine dynamics*, edited by J.C. Nihoul and B.M. Jamart, Elsevier Oceanography Series 45 Amsterdam, 1-33, 1987

[62] Kolmogorov, A.N., Equations of turbulent motion on an incompressible fluid, *Izv. Akad. Nauk. SSSR, Seria fizicheska Vi.*, 56-58, 1942. (English translation: Imperial College, *Mech. Eng. Dept. Rept. ON/6*, 1968).

[63] Kondo, J., Air-sea bulk transfer coefficients in diabatic conditions. *Boundary-Layer Meteorology, 9*, 91-112, 1975.

[64] Kundu, P.K. Fluid Mechanics, 638 pp. Academic, Calif., 1990.

[65] Kundu, P.K. and R.C. Beardsley, Evidence of a critical Richardson number in moored measurements during the upwellling season off Northern California, *Journal of Geophysical Research*, *96,* 4855-4868, 1991.

[66] Large, W.G, ., J.C. McWilliams, and S.C. Doney. Oceanic vertical mixing: A review and a model with a nonlocal boundary layer parameterization. *Rev. Geophys.* , 32 , 363–403, 1994.

[67] Ledwell, J. R., A. J. Watson, and C. S. Law, Evidence for slow mixing across the pycnocline from an open-ocean tracer-release experiment, *Nature*, 364, 701–702, 1993.

[68] Leendertsee, J.J. and S.K. Liu, A three-dimensional turbulent energy model for non-homogeneous estuaries and coastal sea systems. *Hydrodynamics of Estuaries and Fjords,* J.C.J. Nihoul Ed., Elsevier Publ. Co., Amsterdam, pp. 387-405, 1978.

[69] Leendertsee, J.J., 1967. Aspects of a computational model for long water wave propagation. *Rand Corporation, Memorandum RM-6230-RC*, Santa Monica, 1970.

[70] Leonard, B.P., M.K. MacVean, and A.P. Lock, The flux integral method for multidimensional convection and diffusion, *Appl. Math. Modelling, 19*, 333-342, 1995.

[71] Levitus S.. World Ocean Atlas, an atlas of objectively analysed fields of major ocean parameters, 1994. Online dataset available at http://ingrid.ldgo.columbia.edu/SOURCES/.LEVITUS94

[72] Leitão, P. C. (1996) Modelo de Dispersão Lagrangeano Tridimensional (Three dimensional lagangian dispersion model), Degree thesis Tese de Mestrado em ecologia gestão e modelação dos recursos marinhos. Instituto Superior Técnico, In Portuguese, Dezembro 1996.

[73] Li, M. and C. Garrett, Role of Langmuir circulation in the deepening of the ocean surface mixed layer. *Science*, 270, 1955-1957, 1995.

[74] Luyten, P.J., E. Deleersnijder, J. Ozer, and K.G. Ruddick, Presentation of a family of turbulence closure models for stratified shallow water flows and preliminary application to the Rhine outflow region, *Cont. Shelf Res., 16*, 101-130, 1996a.

[75] Luyten, P.J, Simpson, J.H., and T.P. Rippeth, Comparison of turbulence models for homogeneous and stratified flows with turbulence measurements in the Irish Sea, paper presented at the *MAST Workshop on Turbulence Modelling*, Bergen, Norway, Aug. 8-10, 1996, 1996b.

[76] McClain, C. R., S.-Y. Chao, L. P. Atkinson, J.O. Blanton and F. de Castillejo, Wind-driven upwelling in the vicinity of Cape Finisterre, Spain, *J. Geophys. Res.,* 91, 8470-8486, 1986.

[77] Mathieu, P.P. Parameterization of mesoscale turbulence in a world ocean model, Ph.D. Dissertation, Université Catholique de Louvain, 1998.
Downloadable from http://www.met.rdg.ac.uk/~mathieu/PHD/THESIS.html

[78] Martin, P.J., Simulation of the ocean mixed layer at OWS November and Papa with several models, *J. Geophys. Res.,* 90, 903-916, 1985.

[79] Martins, F., Neves R. and Leitão P.. A three-dimensional hydrodynamic model with generic vertical coordinate. In: V. Babovic & L. C. Larsen (Ed.), *Proceedings of Hydroinformatics '98*, Vol. 2, Balkema, Rotterdam, pp. 1403-1410, 1998.

[80] Martins, H, A. Santos, E. F. Coelho, R. Neves and T. L. Rosa, 1999. Numerical Simulation of Internal Tides. *Journal of Mechanical Engineering Science*, in press.

[81] Martins, F., Leitão, P., Silva A and Neves, R. 3D modeling in the Sado estuary using a new generic vertical discretization approach, submitted to *Oceanologica Acta*, 2000.

[82] Martins, F., Modelação matemática tridimensional de escoamentos costeiros e estuarinos usando uma abordagem de coordenada vertical genérica (Three dimensional mathematical modelling of coastal and estuarine flows using a generic vertical coordinate approach). Ph. D. Dissertation. Instituto Superior Técnico. Universidade Técnica de Lisboa, in Portuguese. 2000

[83] Mellor, G.L., and T. Yamada, A hierarchy of turbulence closure models for planetary boundary layers, *J. Atmos. Sci., 31*, 1791-1806, 1974.

[84] Mellor, G.L., and T. Yamada, Development of a turbulence closure model for geophysical fluid problems, *Rev. Geophys., 20*, 851-875, 1982.

[85] Mellor, G. L. and Yamada, T., Development of a turbulent closure model for geophysical fluid problems, *Review of Geophysical and Space Physics*, 20, 851-875, 1982.

[86] Mellor, G.L. Retrospect on oceanic boundary layer modelling and second moment closure. In: Parametrization of Small-Scale Processes, p. Müller, Ed., *Proceedings of the Hawaiian*

'Aha Hulikoa' Winter Workshop, 251-272. Honolulu, University of Hawaii. 1989.

[87] Mellor, G.L. and R.J. Greatbach, An Overview of coastal ocean models, *Coastal Ocean Prediction*, Coastal and Estuarine Studies, 56, American Geophysical Union, 1999.

[88] Miranda, R., F. Braunschweig, P. Leitão, R. Neves, F. Martins and A. Santos, MOHID2000, A coastal integrated object oriented model, to appear in *Proceedings of Hydrosoft 2000.*

[89] Montero P., Gómez-Gesteira M., Taboada J.J., Ruiz-Villarreal M., Santos A.P. , Neves R.R., Prego R. And Pérez-Villar V., 1999. On residual circulation of Vigo Ría using a 3D baroclinic model, *Boletín Instituto Español de Oceanografía*,, n^o 15. SUPLEMENTO-1, 1999.

[90] Montero, P. Estudio de la hidrodinámica de la Ría de Vigo mediante un modelo de volúmenes finitos (Study of the hydrodynamics of the Ría de Vigo by means of a finite volume model), Ph.D. Dissertation, Universidad de Santiago de Compostela, in Spanish, July 1999.

[91] Montero, M.A., A. Lloret and A. Ruiz-Mateo, Water renovation rate in Bouzas basin. *Hydraulic and environmental modelling: Coastal Waters*. R.A. Falconer et al. Eds, 1, p. 263-276.

[92] Mouriño, C. and F. Fraga, Hidrografía de la Ría de Vigo , 1976-77. Influencia anormal del río Miño. (Hydrography of the Ria de Vigo, 1976-77. Abnormal influence of the river Miño). *Investigaciones Pesqueras*, 46, 459-468, In Spanish, 1982.

[93] MOuriño, C., F. Fraga and F. F. Pérez. Hidrografía de la Ría de Vigo, 1979-80. *Cuadernos da Área de Ciencias Mariñas*, Seminario de Estudos Galegos, 1, Edicións do Castro, A Coruña, 91-103, In Spanish, 1984.

[94] Munk, W.H. and E.R. Anderson, Notes on the theory of the thermocline, *J. Marine Research*, 3, 276-295, 1948.

[95] Neves, R., H. Coelho, P. Leitão, H. Martins, and A. Santos. A numerical investigation of the slope current along the western European margin. In: Burgano V., Karatzas G., Payatakas A., Brebbia C., Gray W. and Pinder G. (Ed.), *Computational Methods in Water Resources* XII, 2, 369-376, 1998.

[96] Neves, R., A. Santos, H. Coelho, H. Martins, P. Leitão and R. Miranda: A Circulation Model for the European Ocean Margin. submitted to *Deep Sea Research*, 1999.

[97] Nihoul, J.A. Oceanography of semi-enclosed seas. *Hydrodynamics of Semi-enclosed Seas,* J.A. Nihoul Ed. Elsevier, Amsterdam, 1-34, 1982.

[98] Nihoul, J. A three dimensional general marine circulation model in a remote sensing perspective. In: *Annales Geophysicae* 2, 3, 433-442, 1984.

[99] Nihoul, J.C. and S. Djenidi, Perspectives in three-dimensional modelling of the marine system, In: *Three-dimensional models of marine and estuarine dynamics*, edited by J.C. Nihoul and B.M. Jamart, Elsevier Oceanography Series 45 Amsterdam, 1-33, 1987

[100] Nogueira, E., F.F. Pérez & A.F. Ríos. Seasonal pattern and long-term trends in an estuarine upwelling ecosystem (Ría de Vigo, NW Spain). *Estuarine Coastal and Shelf Science* 44, pp. 285-300, 1997.

[101] Okubo, A., Oceanic diffusion diagrams, *Deep-Sea Research*, 18, 789-802, 1971

[102] Otto, L., Oceanography of the Ria de Arosa (NW Spain). *Konik.Meteor International Medelingen en Verlan*, No. 96, pp: 210, 1975.

[103] Padman, L. and T. M. Dillon, Vertical fluxes through the Beaufort Sea thermohaline staircases, *J. Geophys. Res.* 92, 10799-10806, 1987.

[104] Palma, E. and R. P. Matano, On the implementation of passive open boundary conditions for

a general circulation model: The barotropic mode. *Journal of Geophysical Research*, 103, 1319-1342, 1998.

[105] Patankar, S.V., Numerical Heat Transfer and Fluid Flow, McGraw-Hill, New York, 1980.

[106] Paulson, C.A., and J.J. Simpson, Irradiance measurements in the upper ocean, *J. Phys. Oceanogr., 7*, 952-956, 1977.

[107] Pascual, J.R., The vertical and horizontal M2 tide in the Ría de Arosa (Galicia, Spain NW). *Rev. de Geofísica*, 43, Univ. Complutense Madrid, p.57-64. 1987a

[108] Pascual, J.R., Un modelo de circulación inducida por el viento en la Ría de Arosa. *Bol. Inst. Esp. Oceanografía*, 4, 107-120. In Spanish, 1987b.

[109] Pérez-Villar, V. (Coordinator) ”Ordenación Integral del Espacio Maritimo-Terrestre de Galicia: Modelización informática” (Integrated Management of the Galician Maritime-Terrestrial Space: Numerical Modelling). Final report by the Grupo de Física Non Lineal, Consellería de Pesca, Marisqueo e Acuicultura. Xunta de Galicia. 1999.

[110] Peters, H., Observations of stratified turbulent mixing in an estuary: neap to spring variations during high river flow, *Estuarine, Coastal and Shelf Science*, 45, 69-88, 1997.

[111] Polzin, K.L. J.M. Toole, J.R. Ledwell and R.W. Schmitt, Spatial variability of turbulent mixing in the abyssal ocean, *Science*, 276, 93-96, 1997.

[112] Prandke, H., and A. Stips, Investigation of microstructure and turbulence in marine and limnic waters using the MST profiler , CEC-JRC, Space Applications Institute, Technical Note No.I.96.87, 90pp., 1996.

[113] Prandtl, L., Über ein neues Formelsystem für die ausgebildete Turbulenz (On a new formalism for developped turbulence), *Nachr. Akad. Wiss., Göttingen, Math.-Phys. Klasse*, 6, In German, 1945.

[114] Prego, R. and F. Fraga, A simple model to calculate residual flows in a Spanish Ría. Hydrographic consequences in the Ría of Vigo. *Estuarine Coastal and Shelf Science*, 34, pp. 603-615, 1992.

[115] Prego, R., M. deCastro, M. Gomez-Gesteira, J.J. Taboada, P. Montero, M.R.Villarreal, V.Perez-Villar and A. Dale. Micro-scale hydrography of the Pontevedra Ria (NW Spain). *Journal of Geophysical Research* (submitted). 2000.

[116] Price, J. F., On the scaling of stress-driven entrainment experiments, *J. Fluid Mech., 90*, 509-529, 1979.

[117] Ríos, A. F., F. F. Pérez and F. Fraga. Water masses in the upper and middle North Atlantic Ocean east of the Azores. *Deep Sea Research* 39(3/4), pp. 645-658, 1992.

[118] Robert, J.L. and Y. Ouellet, A three-dimensional finite-element model for the study of steady and non-steady natural flows. In: *Three-dimensional models of marine and estuarine dynamics*, edited by J.C. Nihoul and B.M. Jamart, Elsevier Oceanography Series 45 Amsterdam, 359-372, 1987

[119] Rodi, W., Turbulence models and their application in hydraulics, report, *Int. Assoc. for Hydraul. Res.*, Delft, Netherlands, 1980.

[120] Rodi, W., Examples of calculation methods for flow and mixing in stratified flows, *J. Geophys. Res., 92*, 5305-5328, 1987.

[121] Rohr, J.J., E.C. Itsweire, K.N. Helland and C.W. Van Atta. Growth and decay of turbulence in a stably stratified shear flow, *J. Fluid Mech. 195*, 77-111, 1988.

[122] Rosati, A., and K. Miyakoda, A general circulation model for upper ocean simulation, *J. Phys. Ocean., 18*, 1601-1626, 1988.

[123] Rosón, G, F.F. Pérez, X. A. Alvarez-Salgado, and F.G. Figueiras, Variation of both thermohaline and chemical properties in an estuarine upwelling ecosystem: Ria of Arousa. I. Time evolution. *Estuarine, Coastal and Shelf Science*, 41, 195-213, 1995.

[124] Rosón, G, X. A. Alvarez-Salgado, and F.F. Pérez, A non-stationary box model to determine residual fluxes in a partially mixed estuary, based on both termohaline properties: Application to the Ria of Arousa (NW Spain). *Estuarine, Coastal and Shelf Science*, 44, 249-262, 1997.

[125] Ruiz Mateo, A., Dinámica Marina de la Ría de Pontevedra (Marine Dynamics of the Ría de Pontevedra), *Cuadernos de Investigación* C-13, CEDEX, MOPU, pp.1-22, In Spanish, 1984.

[126] Pacanowski, R.C. and S. G. H. Philander, Parametrization of vertical mixing in numerical models of tropical oceans, *J. Phys. Oceanogr.*, 11, 1443-1451, 1981.

[127] Santos, A. Modelo Hidrodinâmico Tridimensional de Circulação Oceânica e Estuarina (Three dimensional hydrodynamic model of Ocean and Estuarine Circulation), Ph. D. Dissertation. Instituto Superior Técnico. Universidade Técnica de Lisboa, in Portuguese. 1995.

[128] Sander, J., Dynamical Equations and turbulent closures in geophysics, *Continuum Mech. Thermodyn.* 10 1-28, 1998.

[129] Schmitt, R. W., Double diffusion in oceanography, *Ann. Rev. Fluid Mech.*, 26, 255–286, 1994

[130] Schumann, U., and T. Gerz, Turbulent mixing in stably stratified shear flows, *J. App. Meteorol.* 34, 33-48, 1995.

[131] Sharples, J. and J. Simpson, Semi-diurnal and loger period stability cycles in the Liverpol Bay ROFI, *Continental Shelf Research*, 15, 295-313, 1995.

[132] Simpson, J.H., W.R. Crawford, T.P. Rippeth, A.R. Campbell, and J.V.S. Cheok, The vertical structure of turbulent dissipation in shelf seas, *J. Phys. Oceanogr., 26,* 1579-1590, 1996.

[133] Smith, J.D., and S.R. McLean, Spatially averaged flow over a wavy surface, *J. Geophys. Res., 82*, 1735-1746, 1977.

[134] Stelling, G.S., Compact differencing for stratified free surface flow, *Advances in Hydro-Science and -Engineering, 2*, March 22-26, 1995, Bejing, China, 378-386, 1995.

[135] Taboada J.J., Prego R., Ruiz-Villarreal M., Montero P., Gómez-Gesteira M., Santos A. and Pérez-Villar V. Evaluation of the seasonal variations in the residual patterns in the Ría de Vigo (NW Spain) by means of a 3D baroclinic model, *Estuarine Coastal and Shelf Science* 47, pp. 661-670, 1998.

[136] Taboada, J.J. Aplicación de modelos numéricos al estudio de la hidrodinámica y del flujo de partículas en el Mar Mediterráneo (Application of numerical models for the study of hydrodynamics and particle fluxes in the Mediterranean Sea), Ph. D. Dissertation, Universidad de Santiago de Compostela. In Spanish, November 1999

[137] Taboada, J.J., M. Ruíz-Villarreal, M. Gómez-Gesteira, P. Montero, A. P. Santos, V. Pérez-Villar and R. Prego, Estudio del transporte en la Ría de Pontevedra (NO España) mediante un modelo 3D: Resultados preliminares, In: *Estudos de Biogeoquímica na zona costeira ibérica*,Eds. A. Da Costa, C. Vale and R. Prego, Servicio de Publicaciones da Universidade de Aveiro in press 2000.

[138] Therry, G. and P. Lacarrère, Improving the eddy kinetic energy model for planetary boundary layer description, *Boundary Layer Meteorology, 17*, 63-88, 1983.

[139] Tilstone, G.H., F.G. Figueiras and F. Fraga, Upwelling-downwelling sequences in the generation of red tides in a coastal upwelling system, *Marine Ecology Progress Series*, 112, 241-253, 1994.

[140] M. Tomczak, Shelf and Coastal Oceanography,
Web site: http://www.es.flinders.edu.au/~mattom /ShelfCoast/index.html, 1996 - 2000

[141] Vergara, J. and R. Prego, Estimacion de los aportes fluviales de nitrato, fosfato y silicato hacia las Rías Gallegas (Estimation of river inputs of nitrate, phosphate and silica into Galician Rías). *Procesos Biogeoquímicos en Sistemas Costeros Hispano-Lusos. VIII Seminario Ibérico de Química Marina,* R. Prego and J.M. Fernández Ed. Excma. Diputación de Pontevedra, Pontevedra, p.33-40. In Spanish, 1997.

[142] Villarreal, M.R., P. Montero, R. Prego, J.J. Taboada, P. Leitao, M. Gómez-Gesteira, M. deCastro and V. Pé rez-Villar, Water Circulation in the Ria de Pontevedra under estuarine conditions using a 3d hydrodynamical model, submitted to *Est. Coast. and Shelf Sc.,* 2000.

[143] UNESCO, Tenth Report on the joint panel on oceanographic tables and standards. *UNESCO technical papers in marine science,* N. 36, 24 pp., 1981.

[144] Weller, R. A., and J. F. Price, Langmuir circulation within the oceanic mixed layer, *Deep Sea Res.*, 35, 711–747, 1988.

[145] Xing, J. and A.M. Davies, The influence of mixing length formulation and stratification upon tidal currents in shallow seas, *Estuarine, Coastal and Shelf Science, 42,* 417-456, 1996.

[146] Zilitinkievich, S.S. and D. Mironov, Theoretical model of the thermocline in a freshwater basin, *J. Phys. Oceanography, 22*, 988-996, 1992.